BRNO UNIVERSITY OF TECHNOLOGY
VYSOKÉ UČENÍ TECHNICKÉ V BRNĚ

CENTRAL EUROPEAN INSTITUTE OF TECHNOLOGY
STŘEDOEVROPSKÝ TECHNOLOGICKÝ INSTITUT

CMOS COMPATIBLE PIEZOELECTRIC RESONATOR WITH FET STRUCTURE FOR GRAPHENE MONOLAYER PROPERTIES MODULATION

CMOS KOMPATIBILNÍ PIEZOELEKTRICKÝ REZONÁTOR S FET STRUKTUROU PRO ŘÍZENÍ VLASTNOSTÍ GRAFENOVÉ MONOVRSTVY

DOCTORAL THESIS
DISERTAČNÍ PRÁCE

AUTHOR AUTOR PRÁCE	**Ing. Imrich GABLECH**
SUPERVISOR VEDOUCÍ PRÁCE	**Ing. Jan PEKÁREK, Ph.D.**
CO-SUPERVISOR ŠKOLITEL SPECIALISTA	**prof. RNDr. Tomáš ŠIKOLA, CSc.**

BRNO 2018

Abstract

This work proposes a new structure allowing characterization of graphene monolayer properties under precisely specified conditions. It combines MEMS piezoelectric resonator with Hall Bar/FET structure. This approach allows changing graphene properties separately or together via two methods. The mechanical way is based on induced strain from the resonator which is graphene monolayer situated on. It brings the opportunity to measure graphene properties induced by the changes of mechanical strain and frequency of forced vibrations without the influence from external electric field. The second way uses FET structure to influence graphene monolayer using an electric field from bottom gate. There is no limit to measure concentration in units of ppb in terms of structure design. This approach of fabrication CMOS-compatible and biocompatible tunable frequency-modulated piezoelectric MEMS resonators with graphene monolayer can be very useful in many fields for molecule level detection.

Abstrakt

Práce je zaměřena na výzkum nové struktury umožňující charakterizaci fyzikálních vlastností grafenu při přesně řízených podmínkách. Návrh spojuje MEMS piezoelektrický rezonátor spolu s Hall Bar/FET strukturou. Tento přístup umožňuje měnit vlastnosti grafenu odděleně nebo společně dvěma metodami. Mechanický způsob je založen na relativní deformaci způsobené rezonátorem, na kterém je umístěna grafenová monovrstva. Navrhovaná struktura umožňuje měřit vlastnosti grafenu vyvolané pouze změnou mechanického pnutí a frekvencí nucených kmitů bez vlivu vnějšího elektrického pole. Druhý přístup přidává možnost ovládat fyzikální vlastnosti grafenu pomocí elektrického pole FET struktury. Tato technika využívá grafenovou monovrstvu jako laditelný sensor pro molekulární detekci. Měření koncentrace v jednotkách ppb není konstrukčně ničím limitováno. Realizované frekvenčně laditelné piezoelektrické MEMS rezonátory s monovrstvou grafenu budou využitelné v mnoha oblastech pro detekci na molekulové úrovni. Výsledné struktury budou vyrobeny v souladu s požadavky na bio- a CMOS kompatibilitu.

Key words

MEMS, piezoelectric resonator, aluminum nitride, graphene, strain, FET, CMOS-compatibility, biocompatibility

Klíčová slova

MEMS, piezoelektrický rezonátor, nitrid hlinitý, grafen, relativní deformace, FET, CMOS kompatibilita, biokompatibilita

Bibliographic citation

GABLECH, I. *CMOS compatible piezoelectric resonator with FET structure for graphene monolayer properties modulation.* Brno: Brno University of Technology, Central European Institute of Technology BUT, 2018, 150 p., Supervisor: Ing. Jan Pekárek, Ph.D., Supervisor specialist: prof. RNDr. Tomáš Šikola, CSc.

DECLARATION

I certify, that I performed dissertation work independently, under the supervision of Ing. Jan Pekárek, Ph.D. All technical literature and other information sources presented in this work are properly cited in the text and listed in the reference list.

Brno . . . .
(author’s signature)

ACKNOWLEDGEMENT

I would like to thank to my supervisor Ing. Jan Pekárek, Ph.D. and my supervisor specialist prof. RNDr. Tomáš Šikola, CSc. for their effective methodological, pedagogical and technical support and other valuable advices during work on my dissertation. Also, I would like to thank to Ing. Jan Prášek, Ph.D. and to assoc. prof. Ing. Pavel Neužil, Dr., DSc. for professional support and technical advices.

Last, but not least, I would like to thank to my family. My thanks belong especially to my mother Jaroslava and wife Evelína for their patience and support during my studies at the Technical University in Brno.

Brno . . . .
(author’s signature)

CEITEC
Středoevropský technologický institut
BRNO | ČESKÁ REPUBLIKA

VYSOKÉ
UČENÍ
TECHNICKÉ
V BRNĚ

This work was carried out with the support of CEITEC-Central European Institute of Technology with intensive help of research infrastructure financed by project CZ.1.05/1.1.00/02.0068 from European Regional Development Fund.

Part of the work was carried out with the support of CEITEC Nano Research Infrastructure (ID LM2015041, MEYS CR, 2016–2019), CEITEC Brno University of Technology.

MINISTERSTVO ŠKOLSTVÍ,
MLÁDEŽE A TĚLOVÝCHOVY

EVROPSKÁ UNIE
EVROPSKÝ FOND PRO REGIONÁLNÍ ROZVOJ
INVESTICE DO VAŠÍ BUDOUCNOSTI

2007–13
OP Výzkum a vývoj
pro inovace

Table of Contents

Introduction

Present day's requirements for devices dimensions, their accuracy, speed, low fabrication and operating costs, reliability and lifetime are more demanding. These reasons make microelectromechanical systems (MEMS) very important in not only technical fields. As the miniaturization of electronic devices is increasing the MEMS devices decreasing their dimensions into units or tens of micrometers. Some applications need smaller structures which belong to category of nanoelectromechanical systems (NEMS) having better accuracy and smaller dimensions than MEMS. On the other side, the fabrication is much more difficult, longer and more expensive which is not desirable for using in ordinary devices around us. Therefore, the MEMS technology is still used and developed for applications such as sensors (gravimetric, acoustics, thermal, pressure, position, acceleration), waveguides, optical or electronic circuit switches, labs on a chip, energy harvesters, resonators, and many more. These miniaturized systems are often used in common modern electronic devices to power or control them and/or to monitor their environment.

High sensitive molecular sensors are very important in large field of applications such as health care for measuring and monitoring of cells, enzymes, amino acids or to monitor toxic (CO), greenhouse (CO_2) and explosive gases (CH_4, C_4H_{10}, etc.) and many other gasses in environment and industry. These factors lead research and development to fabrication of more precise, reliable and low-power consumption sensors with very fast response.

Combination of well-defined MEMS structure with graphene monolayer brings the opportunity how to get molecular sensor with high sensitivity and fast response. Its sensitivity is usually dependent on a detection principle. The electric readout of active layer properties implemented on the MEMS resonator offers different approach how to detect adsorbed molecules instead of conventional gravimetric method with the possibility to mechanically modulate active layer properties.

This work is focused on fabrication of CMOS-compatible and biocompatible tunable frequency-modulated piezoelectric MEMS resonators including Field-effect transistor (FET) structure for graphene monolayer utilization. Idea of this sophisticated structure is based on simple piezoelectric cantilever beam which is suitable for strain inducing of 2D materials. Such structure can be used for molecular detection.

1 State of the art

MEMS is a process technology used to create small integrated systems that combines mechanical and electrical components. The dimensions of MEMS can vary from units of micrometers up to units of millimeters. For instance, the width of human hair is usually from 70 μm to 100 μm. In general, MEMS consist of mechanical microstructures, microsensors, microactuators and microelectronics which are integrated onto the one silicon chip (see **Figure 1**) [1].

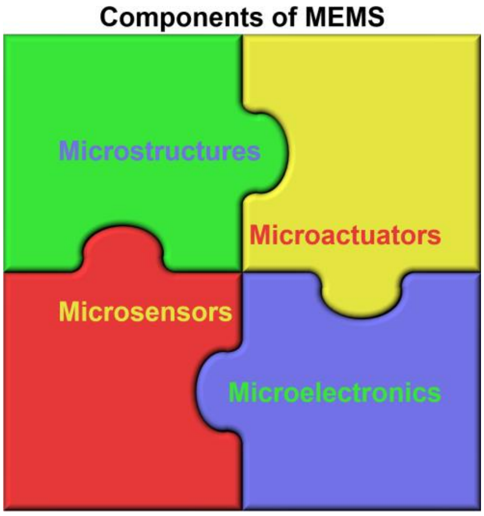

Figure 1: Schematic overview of MEMS components.

The fabrication of MEMS uses standard integrated circuit (IC) techniques. The most of MEMS devices are prepared using low temperature physical vapor deposition (PVD) [2] and/or chemical vapor deposition (CVD) [3,4] techniques with consequent dry or wet etching processing. Wet etching usually employs various solutions while dry etching uses etchant gases or plasmas to remove materials. The MEMS are mostly created on silicon wafer and released using surface and/or bulk micromachining techniques which make these devices mechanically sensitive. Surface micromachining is realized as etching of sacrificial layer on top of the substrate (see **Figure 2A**) and the bulk micromachining is direct etching of substrate (see **Figure 2B**) [5].

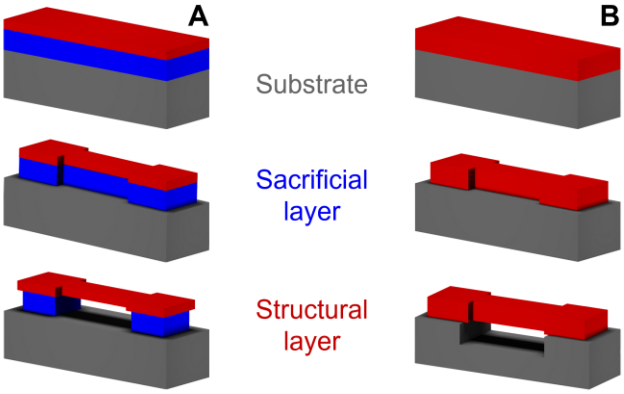

Figure 2: Microfabrication techniques: A) Surface; B) Bulk.

MEMS technology is growing multidisciplinary field in last few decades. It provides utilization for many devices such as electrostatic, magnetic, electromagnetic, pneumatic and thermal actuators, motors, valves, gears, cantilevers, diaphragms, and tweezers. These devices are used for sensing of many physical and chemical phenomena such as pressure, temperature, mass flow, velocity, sound and chemical composition. They are also used as actuators for linear and angular motions or as simple components which take part in microfluidics, lab on a chip devices, droplet generators, heat engines and micro pumps (see **Figure 3**) [6,7].

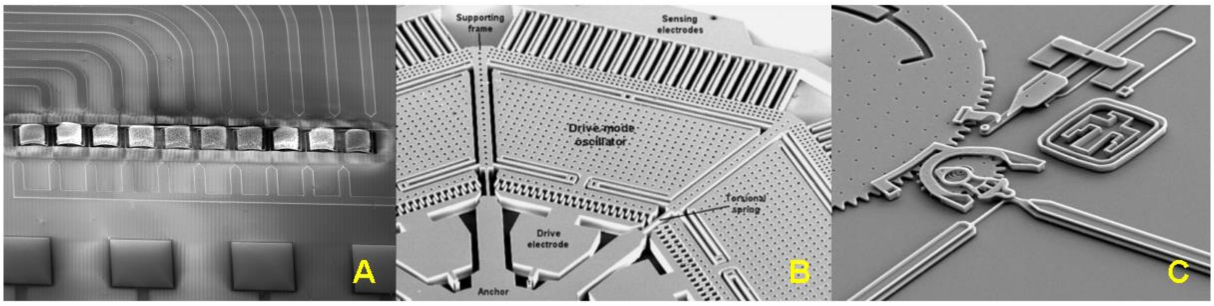

Figure 3: MEMS devices: A) Microbolometer array with carbon nanotubes for thermal imaging; B) Vibratory gyroscope [8]; C) Rotary bearing surfaces and interlocking gears [9].

Cantilevers are one of many the groups of devices that belong to MEMS technology. They are mainly used for mass sensitive detection. In general, the cantilever with smaller dimensions is more sensitive to small changes. It leads to development of NEMS but the fabrication of such device is still difficult and cannot be utilized for commercial fabrication [10]. Cantilevers are sensitive to physical, chemical and biological effects which cause the cantilever bending or change in vibration frequency [11].

One of the principal of the sensing mechanism of cantilever is static mode. Cantilever bends due to external influence which can be chemical or physical effect (see **Figure 4**). These effects take place on the surface of cantilever with active layer which can adsorb various types of molecules. Adsorption of molecules on the active layer results in production of compressive stress due to the increase of mass and cantilever deflects down. A good example can be a thin polymer coating on the surface of cantilever which can swell after absorption of molecules from surrounding environment. Such change of surface results in downward deflection of cantilever, as well. This type of cantilever sensing can be also used for molecular detection in liquid or biochemical environment [12,13]. Another possibility of measurement is detection of contractions of adsorbed material on cantilever surface which cause upward bending [14].

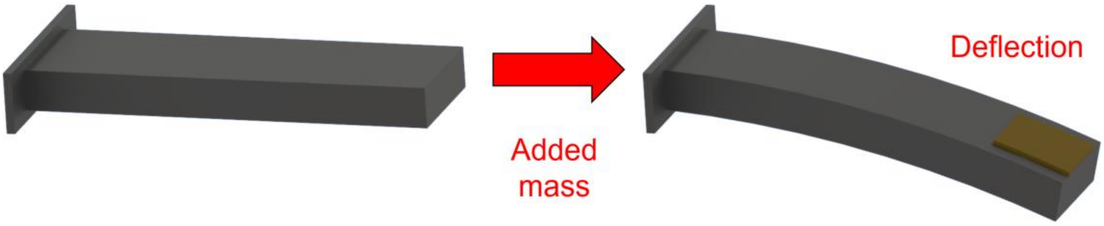

Figure 4: Schematic view of cantilever in static mode.

Deflection of cantilever in static mode is usually evaluated by using one of the three detection principles, namely optical, piezoresistive and capacitive. Common case of optical detection uses laser and position sensing photodetector or interferometer which monitor the displacement of cantilever. Piezoresistive method is based on piezoresistive material which forms piezoresistor embedded in cantilever. Maximal sensitivity can be reached when piezorezistor is located close to one of the surface of cantilever. Since the strain is caused by the deflection of cantilever, then the resistance of piezoresistor changes and it can be measured. Capacitive evaluation is often used for devices with gap between two electrodes. Deflection of cantilever or membrane changes distance between these electrodes which results in change of capacity value that can be measured [13,15,16].

Another principal of sensing mechanism of cantilever is dynamic mode. Cantilever is driven at its resonance frequency in this mode. When any quantity of mass is added or removed from oscillating cantilever, its resonance frequency changes. In general, increasing mass of microstructure causes downshifting of resonance frequency (see **Figure 5**). Changes of mass can be directly derived from shifts in resonance frequency using simple electrical circuit. It is possible to determine exact amount of mass from frequency shift if mass was added on known position of microstructure [17]. Cantilever can be considered as a microbalance with ability to detect mass lower than one picogram [12]. In some cases, the detection limit can be in tens of attograms [18].

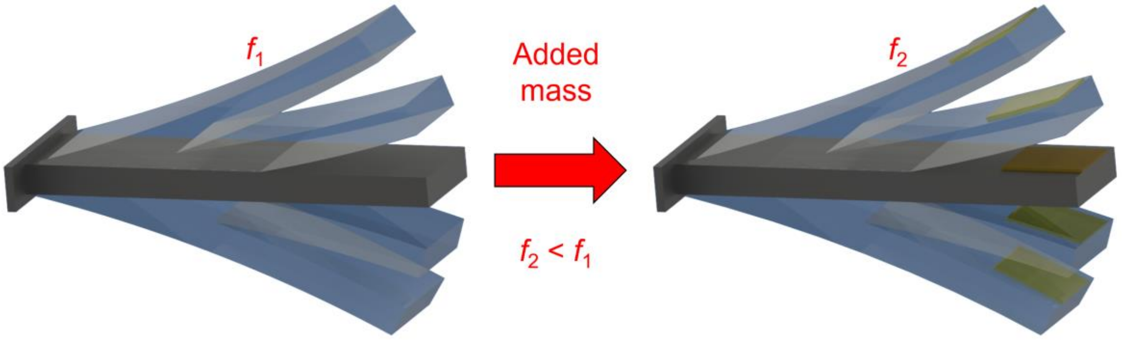

Figure 5: Schematic view of cantilever in dynamic mode.

One of the often used group of devices working in dynamic mode are piezoelectric cantilever resonators. These devices are commonly used for mass sensing [19]. They can be utilized as well as actuators [20]. Methods mentioned above in this chapter can also be used for detection of changes in resonance frequency and phase. Next determination method is impedance measurement. Microcantilever is excited by tracking generator of the spectrum analyzer in demanded frequency range. Impedance is measured as a function of the frequency. Advantage of this method is that the excitation electrical signal is directly used also for detection at the same time. This measurement gives a possibility to determine the electrical parameters of resonator such as capacitance, conductance, phase etc. These parameters depend on actuating voltage and frequency. Significant changes of these parameters mostly occur at frequencies corresponding to the resonant modes [21]. Since the gravimetric sensors evince high sensitivity and relatively easy handling, many researches are dedicated to their functionalization with various modern materials. One of these materials are graphene and other 2D materials such as silicene, germanene, stanene, phosphorene, arsenene and antimonene [22-24]. Properties of these materials can be utilized for various sensors or can be modified by several electrical or mechanical effects [25,26].

The graphene as a unique material is used to sense physical and chemical properties of materials. Several types of nanosensors employing graphene were reported for gas and vapor sensing. Graphene is often employed in applications such as resistive sensors [27], FETs [28], surface acoustic wave (SAW) sensors [29], quartz crystal microbalance (QCM) sensors [30], MEMS or NEMS gravimetric sensors [31], MEMS or NEMS infrared (IR) detectors [32] and semiconductor modified hybrid sensors [33].

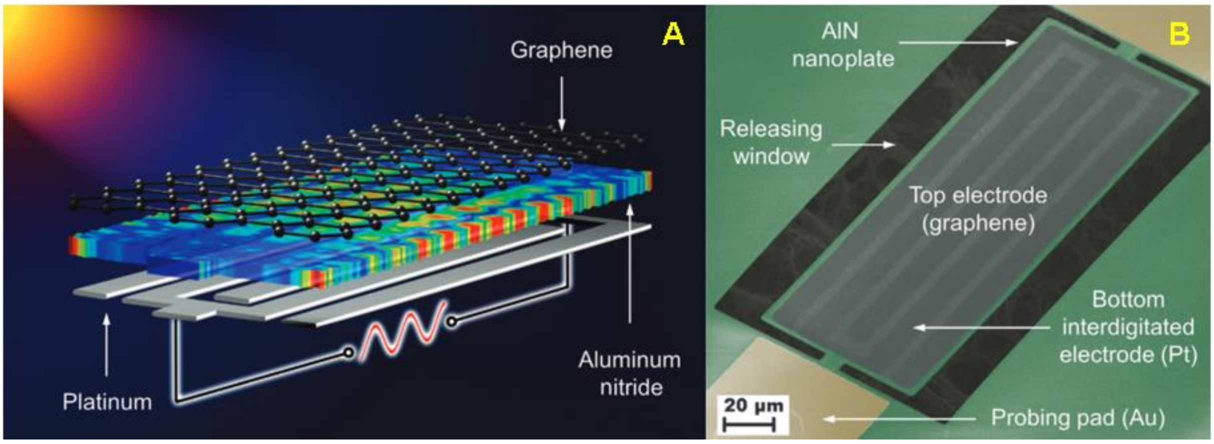

Figure 6: Graphene-AlN NEMS resonant infrared detector: A) Schematic view; B) Colored scanning electron microscope image of fabricated device [32].

A single layer of carbon atoms in the sp^2 hybridization arranged in a honeycomb lattice called graphene (see **Figure 7**) was proposed by Wallace in 1946 [34] and prepared by Geim and Novoselov in 2004 [35]. It was an extensively studied material with numerous interesting properties [36-38]. This material has unique features such as exceptional thermal, mechanical, and optical properties. As a monoatomic layer, it also possesses unusual mechanical flexibility and ambipolar electrical charge transport [38].

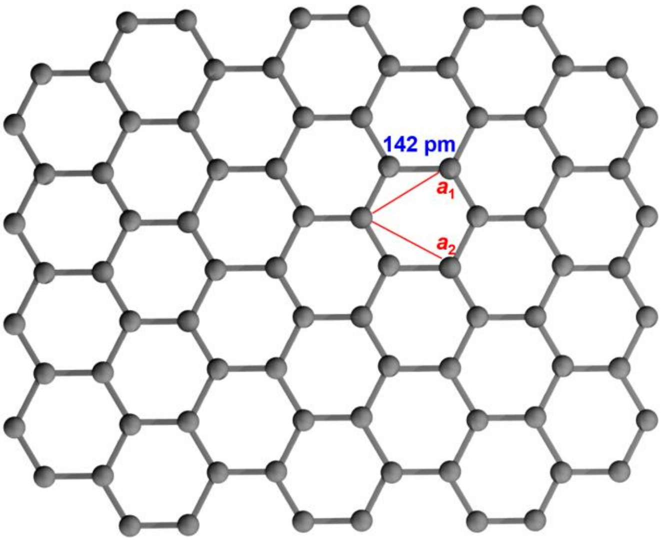

Figure 7: Graphene honeycomb structure [39].

Nowadays, sensors based on carbon nanotubes (CNTs) or graphene evince the highest resolution of all nanosensors. Nanosensors based on graphene give a possibility to detect individual molecules that adsorb or desorb from the surface. Graphene´s exceptional sensitivity was promoted by Andre Geim: “Graphene has the ultimate sensitivity because, in principle, it cannot be beaten, you cannot get more sensitive than a single molecule” [40]. Every atom of the graphene can be considered as a surface atom, thus there is a possibility of interaction with one molecule of the target substance [27]. Free electron concentration of graphene changes with attaching or detaching molecules. Such molecules change electrical conductivity based on fact whether they are donors or acceptors. The detection of the concentration of adsorbed molecules is feasible through this change of the conductivity.

Electronic properties such as electrical charge mobility of graphene can be greatly influenced by induced strain. Graphene stretching results in changes of the bond length between neighboring atoms in its lattice. This has a strong effect on the electronic and transport properties of graphene. This influence is not yet completely understood and it is an interesting avenue with many options [41]. Measurement of graphene properties as a function of the controlled induced strain can be used for determination of the strain influence on the electrical graphene properties. Electron mobility is the most essential part of any electronic device and altering it means that we can tailor the device parameters. The electrical conductivity and mechanical strength of graphene in the in-plane direction are much higher than those in the out-plane direction. Thus, the anisotropy in physical properties can be obtained by the orientation of graphene [42].

Uniaxial strain on graphene was experimentally studied by bending of graphene on a deformable substrate (see **Figure 8**) and using Raman spectroscopy to probe its phonon modes [43,44]. The uniaxial strain moves the relative positions of the Dirac cones and has a significant influence in the intervalley double-resonance processes (D and 2D peaks).

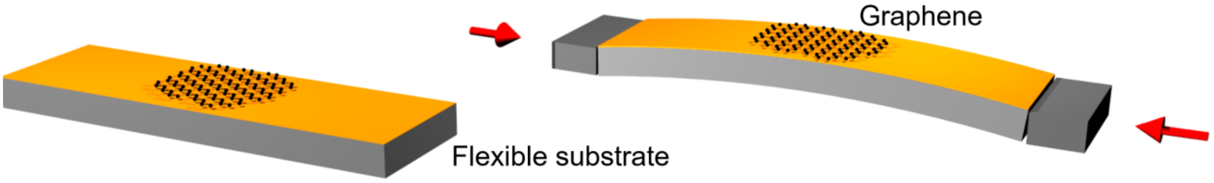

Figure 8: Schematic of uniaxial straining of graphene on a flexible substrate.

The biaxial strain is more suited to study the strain effects on the double-resonance processes due to mimicking the realistic experimental conditions where the graphene is supported by a planar substrate. Biaxial strain in the graphene can be intentionally induced and controlled by three commonly used methods:

1. The graphene is clamped across a hole in a substrate and it is mechanically stretched by pushing the graphene into the hole using an atomic force microscopy (AFM) tip (see **Figure 9**) [45] or electrostatically [46].

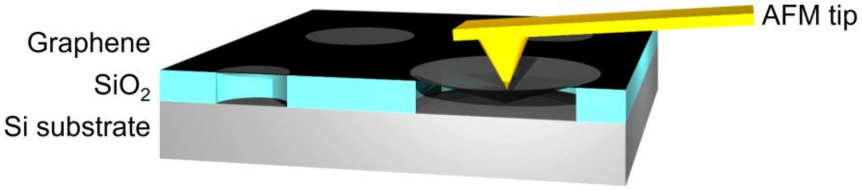

Figure 9: Schematic of suspended graphene membrane nanoindentation.

2. The graphene is placed on a material with different thermal coefficient of expansion and it is subject of temperature changes causing graphene to stretch (see **Figure 10**) [47].

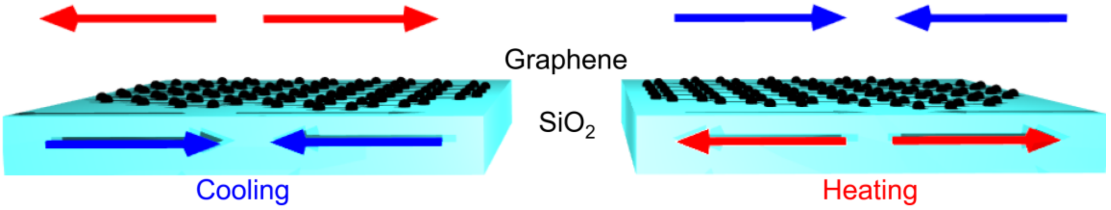

Figure 10: Schematic of thermal expansion and contraction of graphene on thermally heated or cooled SiO_2 substrate.

3. The graphene can be transferred onto a piezoelectric substrate which is controllably shrank or elongated by applying a bias voltage. It results in graphene having a uniform biaxial strain (see **Figure 11**) [48].

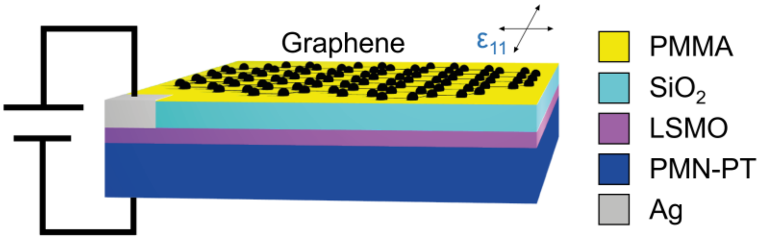

Figure 11: Schematic of the electro-mechanical device for in-plane biaxial strain inducing to the graphene.

Graphene is known as an excellent material capable to sustain reversible elastic tensile strain as large as 25 % [49].

This feature can be used to control of graphene electrical properties either statically or dynamically by integrating them with resonators. It can lead to the novel applications of graphene [49]. These resonators based on MEMS or NEMS can be made of various materials. They can significantly impact the final structural properties, such as residual stress, stiffness, strain, resonance frequency, and quality factor. Electrically controlled resonators allow adjustment of forced vibrations frequency and its amplitude. The structure should be fabricated by planar technology as it is a standard MEMS/NEMS process. The planar process compatibility offers the monolithic integration of a sensing part and readout circuits [50]. Biocompatibility would further increase its attractiveness as it can be used in health care to measure and detect cells, enzymes, amino acids, deoxyribonucleic acid (DNA), ribonucleic acid (RNA), etc. [51].

Resonators based on piezoelectric materials such as AlN can be prepared by planar technology and they can be also biocompatible. AlN has desirable properties, such as good mechanical stiffness, high elasticity, and low thermal coefficient of expansion. Its crystal orientation and low misorientation of individual crystallites can be improved by Ti underlayer. These features are the most important factors influencing the quality of thin film and the value of AlN piezoelectric coefficients. The key piezoelectric coefficient d_{33} achievable with common PVD techniques is usually up to 6 $\mathrm{pC \cdot N^{-1}}$ which is sufficient for MEMS/NEMS applications [52].

2 Aims of doctoral thesis

This doctoral thesis will be focused on design and fabrication of structure allowing characterization of graphene monolayer properties under precisely specified conditions. Structure will be realized as tunable MEMS piezoelectric resonator with Hall Bar/FET structure. The entire structure will be fabricated on a Si wafer substrate using CMOS-compatible processes. This structure allows modulation of graphene electronic properties. It can be achieved by controlling of gate voltage of FET structure and mechanical strain induced by piezoelectric resonator. Proposed unique geometry decouples the electric field effects on the graphene monolayer from the piezoelectric resonator. Such device gives a possibility how to modulate the frequency of forced vibrations and the displacement without directly applying an electric field on the graphene, contrariety to graphene-based sensors on membranes. The strain from resonator displacement and the applied electric field between the sensing electrodes and the gate electrode will change the electrical properties of graphene. This approach leads to tuning of sensing properties of the graphene monolayer (see **Figure 12**).

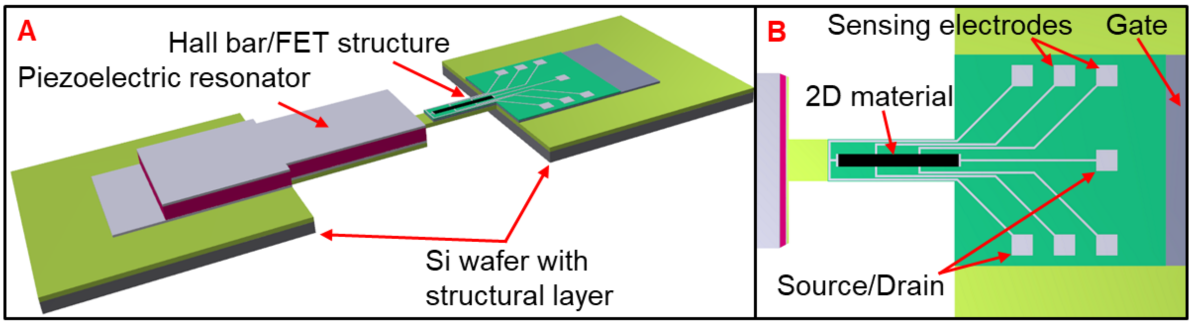

Figure 12: Fundamental concept and principle of proposed structure (not to scale): A) Complete structure that allows modification of 2D material using electrical field and mechanical strain; B) Detail of mechanically stretchable part with Hall Bar/FET structure shows position where 2D material will be situated.

The piezoelectric resonator will be fabricated on a Si wafer covered with the low-stress SiO_2. Ti serves as a bottom electrode and also as an excellent seed layer for deposition of piezoelectric AlN layer. Top electrode is made of Al. These materials were chosen because of their significant properties and CMOS compatibility which are suitable for desired application. The part for graphene monolayer properties modulation including gate, source, drain, and sensing electrodes will be realized with CMOS-compatible materials and processing. Gate electrode will be fabricated from Al due to its good mechanical and electrical properties. Gate insulating layer will be made of low-stress SiO_2. Sensing electrodes must be fabricated of material that is compatible with XeF_2 etching process. Thus, Au cannot be used and must be replaced with other materials that guarantee good electrical contact to graphene. It is possible to use Pt or Ni, etc. The whole structure will be released by removal of bulk Si by a dry isotropic XeF_2 etching method.

3 Crystallography of underlayer for piezoelectric thin film

3.1 Motivation of the article

One of the most important step in device design and its fabrication is to select the ideal underlayer for piezoelectric layer. It must fulfill certain necessities. Very important is also good conductivity because it must serve as a bottom electrode. The similar lattice parameters, crystallographic orientation, misorientation of individual crystallites and surface roughness are no less crucial for consequent growth of AlN piezoelectric layer. The next important is CMOS and biocompatibility of materials which allow wider integration to other devices or systems realized in silicon technology.

I chose the Ti because it meets above mentioned criteria. I realized this deposition using radio frequency inductive-coupled plasma (RFICP) Kaufman ion-beam source which is not conventional method in comparison to magnetron sputtering or evaporation techniques. This machine was also the only one available instrument which allows to deposit thin films in well-controlled conditions. It brings the opportunity how to fabricate high quality layers but the optimization is more problematic then for previously mentioned techniques. I started the optimization process which was focused on preparation of (001) preferentially oriented Ti thin films on SiO_2 which is the most used material for MEMS applications where the Si bulk etching is realized using XeF_2 vapor.

3.2 Conclusion on the article

In this part of my research, I optimized the sputtering process to achieve (001) preferentially oriented Ti on SiO_2 which was important for preparation of consequently deposited AlN piezoelectric layer. The optimized layer with demanded crystallographic orientation had also smoother surface than 1 nm which is excellent and the value of $\approx 5°$ of misorientation of individual crystallites was also good. It is also well-known that the deposition of AlN requires higher deposition temperatures up to ≈ 300 °C. Therefore, I investigated the influence of increased temperature in vacuum furnace to prove that there are no changes after thermal treatment. The residual stress which have to be controlled in MEMS applications, was not solved in this paper but the following paper was aimed to it.

3.3 Contribution

I performed all depositions and thermal treatment processes. I did X-ray diffraction (XRD) measurements in Bragg-Brentano setup and AFM surface roughness analyses. I also contributed to the analysis of the results and to the writing of the manuscript.

3.4 Article 1

The article **Preparation of (001) preferentially oriented titanium thin films by ion-beam sputtering deposition on thermal silicon dioxide** [53] was published in **Journal of materials science** (2014 IF 2.371) in **December 2015.**

J Mater Sci (2016) 51:3329–3336
DOI 10.1007/s10853-015-9648-y

Preparation of (001) preferentially oriented titanium thin films by ion-beam sputtering deposition on thermal silicon dioxide

Imrich Gablech[1,2] · **Vojtěch Svatoš**[1,2] · **Ondřej Caha**[3,4] · **Miloš Hrabovský**[1,5] ·
Jan Prášek[1,2] · **Jaromír Hubálek**[1,2] · **Tomáš Šikola**[1,5]

Received: 6 August 2015 / Accepted: 6 December 2015 / Published online: 21 December 2015

Abstract We propose the ion-beam sputtering deposition providing Ti thin films of desired crystallographic orientation and smooth surface morphology not obtainable with conventional deposition techniques such as magnetron sputtering and vacuum evaporation. The sputtering was provided by argon broad ion beams generated by a Kaufman ion-beam source. In order to achieve the optimal properties of thin film, we investigated the Ti thin films deposited on an amorphous thermal silicon dioxide using X-ray diffraction, and atomic force microscopy. We have optimized deposition conditions for growing of thin films with the only (001) preferential orientation of film crystallites, and achieved ultra-low surface roughness of 0.55 nm. The deposited films have been found to be stable upon annealing up to 300 °C which is often essential for envisaging subsequent deposition of piezoelectric AlN thin films.

Introduction

Titanium has been a frequently used material in microelectronics and MEMS technology. Titanium thin films have been used as sensing electrodes, buffer, or adhesive layers. The advantages of titanium thin films are good electric conductivity, extraordinary chemical resistivity, thermal stability, high hardness, high melting point, and lower number of crystallographic imperfections [1–5]. Crystallographic orientation of titanium thin films has to be controlled during the deposition process to obtain specific properties (e.g., mechanical, chemical) suitable for an eventually required application [6, 7]. Some of recent MEMS devices use the piezoelectric effect for energy harvesting or sensing purposes [8]. Titanium has been often utilized in MEMS technology as a compatible material for fabrication of thin conductive underlying electrodes on which the piezoelectric layers are deposited [6].

The crystallographic orientation of titanium thin films is crucial for properties of consequently deposited piezoelectric layers [9]. Obviously, the properties of these layers (AlN, ZnO), namely electromechanical properties, are significantly affected by the crystallographic orientation, surface morphology, and the roughness layers beneath [10]. There have been many papers published investigating the degree of orientation which is strongly dependent on the texture and roughness of underlying material [11, 12]. Titanium thin films have been usually deposited by the physical vapor deposition (PVD) particularly magnetron sputtering [13] or e-beam evaporation [4]. Obviously, different deposition parameters result in various film properties. Considering the surface roughness, low process pressure during deposition (i.e., $<5 \times 10^{-3}$ mbar) usually results in a smooth film surface (i.e., R_{rms} <10 nm). At higher deposition pressure (i.e., $<14 \times 10^{-3}$ mbar), the

---

✉ Imrich Gablech
imrich.gablech@ceitec.vutbr.cz

[1] Central European Institute of Technology, Brno University of Technology, Technická 3058/10, 61600 Brno, Czech Republic

[2] Department of Microelectronics, Faculty of Electrical Engineering and Communication, Brno University of Technology, Technická 3058/10, 61600 Brno, Czech Republic

[3] Central European Institute of Technology, Masaryk University, Kamenice 753/5, 62500 Brno, Czech Republic

[4] Department of Condensed Matter Physics, Faculty of Science, Masaryk University, Kotlářská 2, 60200 Brno, Czech Republic

[5] Institute of Physical Engineering, Brno University of Technology, Technická 2896/2, 61669 Brno, Czech Republic

titanium RMS surface roughness of 45 nm was achieved. Consequently, a negative effect on the piezoelectric coefficients of AlN layers deposited on Ti thin film due to a porous surface was observed [10]. The magnetron sputtering is the most frequent method for titanium thin films deposition [14]. Titanium thin films deposited by the magnetron sputtering generally possess (100), (001), and (101) crystallographic orientations of crystallites parallel to the surface [1]. Without a special modification of the magnetron sputtering process (closed-field unbalanced magnetron sputtering, pulsed magnetron sputtering), the number of various and independent deposition parameters capable of optimizing deposited layers is limited [15, 16]. Due to the lack of the process control parameters, it is often an issue to achieve thin films of desired properties for specific application.

In this paper, we report on a deposition of Ti thin film with the (001) preferential crystallite orientation growth on amorphous thermal silicon dioxide using a 3-grid radio frequency inductive-coupled plasma (RFICP) Kaufman ion-beam source. As generally known, the Kaufman ion-beam source provides more efficient control and optimization of the deposition process compared to the conventional deposition method [17, 18]. Here, ion-beam flux, energy, and ion-beam geometry, can be controlled independently. We have studied the influence of deposition parameters on properties of Ti thin films especially on their preferential crystallographic orientation and topography.

Experimental details

Deposition process

The deposition of titanium layers was done on substrates (20 × 20) mm diced from 4-inch P-type silicon wafer with the (100) crystallographic orientation and the resistivity of 6–12 Ω cm covered with thermal silicon dioxide (ON Semiconductor). The thickness of silicon dioxide was approximately 1 µm. Before the sputtering process, we cleaned all substrates in the standard piranha solution (96 % H_2SO_4 + 30 % H_2O_2 in the 3:1 ratio) for 5 min, rinsed in deionized water (18.7 MΩ cm), and dried them by compressed nitrogen.

The deposition process was done using the ion-beam sputtering apparatus (Bestec) equipped with RFICP Kaufman ion-beam source (Kaufman & Robinson—KRI®) with the molybdenum 3-grid dished focused ion optics (4 cm in diameter and with 45° ellipse pattern) providing an Ar ion beam bombarding the Ti target under an incidence angle of 45°. The 99.9996 % pure argon gas was used during the deposition process. Titanium of 99.995 % purity (Porexi) was sputtered from a (100 × 100) mm target. Reduction of the ion-beam space charge was provided by KRI LFN 2000 charge neutralizer (KRI®). Before each deposition process, the sputtering chamber was evacuated to pressure of 5×10^{-9} mbar using a turbomolecular HiPace 1200 turbopump (Pfeiffer Vacuum) with the pumping speed of 1200 l/s for argon backed by TriScroll® 300 series dry scroll vacuum pump (Agilent Technologies). The schematic illustration of the apparatus setup including all significant dimensions and angles is shown in Fig. 1.

The operation parameters of the deposition process are beam voltage (BV) determining energy of the ion beam at the target, acceleration voltage (AV) controlling the extraction and the optical parameters of the beam, beam current (BC) equal to the ion-beam current at the target, radio frequency power (RFP) supplied to the discharge, argon flow rate, and substrate temperature. During all deposition experiments, the substrate was rotating with the speed of 5 rpm. A particular setup of the major parameters for individual deposition experiments is listed in Tables 1 and 2. In all deposition experiments, the substrate was not heated up and its temperature was affected only by the energy of sputtered material. The substrate temperature did not exceed the value of 100 °C. The Inficon SQM-242 card with a quartz crystal sensor was used to monitor the deposition parameters as thickness and rate of deposition.

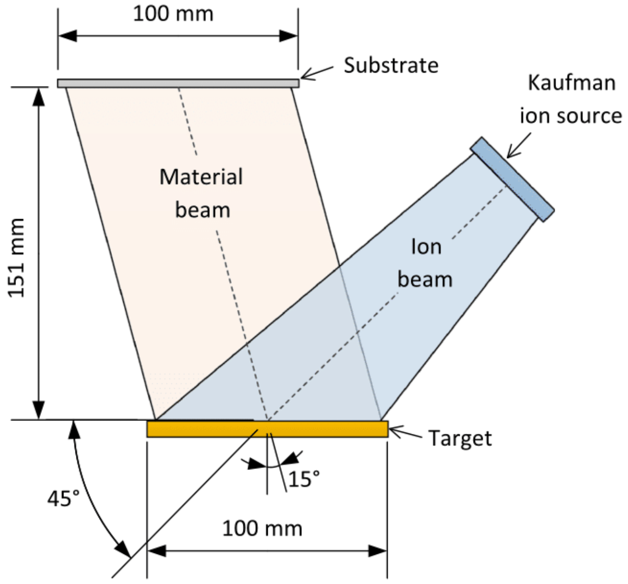

Fig. 1 Schematic of sputtering apparatus geometry with Kaufman ion-beam source

Table 1 Ion-beam source experimental setup (BV, AV, BC, RFP, Ar flow) and deposition pressure and rate

Sample no.	BV (V)	AV (V)	BC (mA)	RFP (W)	Ar flow (sccm)	Process pressure (mbar)	Deposition rate (Å/s)
1–1	200	−100	6.0	74	2.2	2.1×10^{-4}	0.04–0.06
1–2	400	−80	13.0	73	2.4	2.2×10^{-4}	0.15–0.18
1–3	500	−100	18.0	86	2.6	2.3×10^{-4}	0.24–0.26
1–4	600	−120	23.0	94	2.8	2.4×10^{-4}	0.32–0.34
1–5	700	−140	29.0	107	3.0	2.5×10^{-4}	0.42–0.44
1–6	800	−160	36.0	118	3.3	2.6×10^{-4}	0.56–0.58
1–7	900	−180	43.0	130	3.6	2.7×10^{-4}	0.70–0.72
1–8	1000	−200	50.0	140	3.9	2.9×10^{-4}	0.84–0.86
1–9	1200	−240	65.0	168	4.4	3.1×10^{-4}	1.18–1.20
1–10	1200	−600	82.0	188	5.3	3.5×10^{-4}	1.49–1.51

Table 2 Ion-beam source setup deposition pressure and rate in experiments on optimization of the film structure with respect to the (001) preferential crystallographic orientation

Sample no.	BV (V)	AV (V)	BC (mA)	RFP (W)	Ar flow (sccm)	Deposition pressure (mbar)	Deposition rate (Å/s)
2–1	200	−100	6.0	73	2.1	1.9×10^{-4}	0.04–0.06
2–2	200	−120	6.0	74	2.1	1.9×10^{-4}	0.04–0.07
2–3	200	−140	7.0	73	2.1	1.9×10^{-4}	0.05–0.07
2–4	200	−160	7.0	74	2.1	1.9×10^{-4}	0.05–0.07
2–5	200	−180	8.0	74	2.2	2.0×10^{-4}	0.06–0.07
2–6	200	−200	8.0	73	2.2	2.0×10^{-4}	0.07–0.08
2–7	200	−220	9.0	74	2.2	2.0×10^{-4}	0.07–0.09
2–8	200	−240	9.0	74	2.2	2.0×10^{-4}	0.07–0.09

Diagnostic methods

X-ray diffraction (XRD) technique was used for crystallography analysis. These analysis were done with X-ray diffractometer (SmartLab, Rigaku) containing a linear D/teX Ultra detector and working in the Bragg–Brentano (BB) focusing geometry. Pole figures were measured using parallel beam setup with multilayer parabolic mirror as a collimator and a scintillation detector. The surface roughness (R_{RMS}) of deposited layers was investigated by Atomic Force Microscopy (AFM, Dimension Icon, Bruker) in the ScanAsyst®-Air mode using the corresponding probe (ScanAsyst-Air) with the cantilever spring constant of 0.4 N m^{-1} and tip radius of 2 nm.

Annealing procedure

The deposited samples were exposed to an annealing procedure using the annealing oven (Vakuum Praha). The annealing procedure was done for three temperatures 100, 200, and 300 °C at the pressure of 5×10^{-7} mbar. The annealing protocol was set with following parameters: heating rate 5 °C per minute; peak temperature was held for 60 min; cooling rate 5 °C per minute.

Results and discussion

In the first series of experiments, we set the absolute values of BV and AV in the ratio 5:1 to reduce the flux of electrons according to the rule of electron-backstreaming limit experimentally determined by the manufacturer [19]. The higher ratios of BV and AV cause flowing of electrons (secondary electrons, neutralizing electrons) through ion optics into the ion source affecting the discharge. Utilizing the feedback control, we set BC appropriately to BV and AV according to a recommendation in the KRI® datasheet. These values of the ion-beam current were optimum ones at which a direct impingement of beam ions into the accelerator and decelerator grids were suppressed.

The first sample (Sample 1–1) was deposited using higher AV because it was not possible to keep stable plasma discharge, and the last one (Sample 1–10) was deposited at maximum possible voltage settings of ion-beam source. In Table 1, different settings of deposition parameters together with the resultant deposition pressure and deposition rate are listed.

We used XRD in the BB setup with the 2θ angle ranging from 20° to 90° to perform the phase analysis of all deposited layers. We detected diffraction peaks belonging to (100), (101), and (001) crystallographic planes. For

(001) crystallographic plane, second-order diffraction 002 was measured since the first-order diffraction is forbidden. However, in the following text we will note it as (001). The corresponding X-ray diffractogram is depicted in Fig. 2. The diffractograms show also the slight peak at 2θ of 68° to 70° which originates from the silicon substrate and sometimes a very weak peak corresponding to the fourth-order diffraction on the Ti (001) plane at 83°. The obtained results show that crystallographic orientation of sputtered layer depends mainly on ion energy which is given by BV. In case of low ion-beam energies (200 eV and 400 eV, samples 1–1 and 1–2, respectively), the required (001) preferential crystallographic orientation of the crystallites with a small contribution of (100) planes parallel to the surface was obtained. On the other hand, the (100) plane orientation was much more represented at higher ion-beam energies, namely in the range of BV from 500 to 1000 V (Samples 1–3 to 1–8). At the highest ion-beam energy (BV of 1200 V, sample 1–9 and 1–10), the (101) plane orientation was observed along with the (001) and (100) ones.

The second series of experiments was aimed at finding the optimal deposition conditions in order to achieve the only (001) preferential orientation of crystallites in the Ti films parallel to the surface. We were changing AV (affecting ion extraction and ion-beam formation, and thus the ion-beam space charge as well) from −100 to −240 V at the fixed BV of 200 V (i.e., at the constant ion-beam energy of 200 eV). All deposition parameters are summarized in Table 2. The obtained X-ray diffractograms for all prepared samples are shown in Fig. 3.

As can be seen in Fig. 3, at an AV value of −220 V (sample 2–7), it is clear that the preferential (001) orientation of thin film was achieved. The other settings of the AV resulted in a minor peak in the diffractogram proving the presence of (100) plane. This behavior was probably attributed to distinct values of space charge potential depending on the AV setting, and providing different energies of charge-exchange argon ions which are leaving the beam and bombarding the substrate surface [17]. In this way, these factors can assist in the growths of thin films and modify their properties similarly to ion-beam-assisted techniques [20]. These results of performed optimizations showed the possibility of producing the titanium layer with only one preferential (001) plane orientation. We have determined the lattice parameters of the optimized thin films; the c lattice parameter was ascertained $c = 4.72$ Å while the lattice parameter was determined by grazing incidence diffraction $a = 2.95$ Å. The tabulated values of these parameters are $a = 2.951$ Å and $c = 4.695$ Å [21].

Carrying out identical experiments for four times, we proved a good repeatability of the results. In all four cases, we obtained the identical diffractograms of thin films prepared in the independent experiments with the same deposition parameters leading to the (001) preferential orientation as sample 2–7.

Full width at half maximum (FWHM) of the diffraction peak belonging to (001) planes was 0.4° for all samples with good reproducibility. This width corresponds to the average coherently diffracting domain of 22 nm calculated using Scherrer formula [22]. This value is underestimating the real average crystallite size since the internal strain is neglected. The higher order diffractions were too weak to be detected with sufficient statistics and further analysis was not possible.

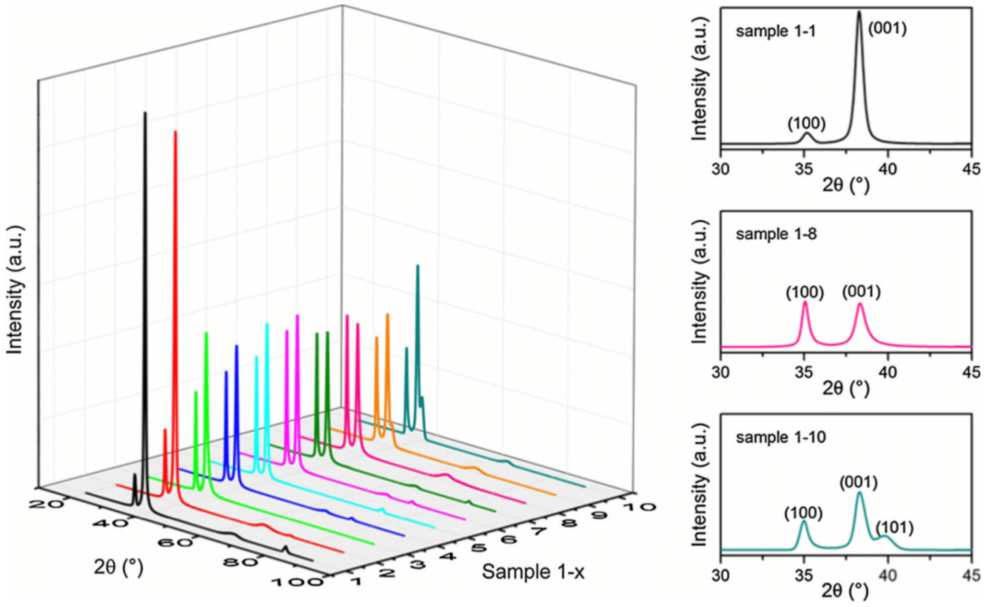

Fig. 2 X-ray diffractograms of deposited thin films obtained with different BV and AV; 3D plot of diffractograms of all samples prepared at deposition parameters listed in Table 1 (*left*), three detailed diffractograms showing the samples with the most distinguished crystallographic orientations of the films (*right*)

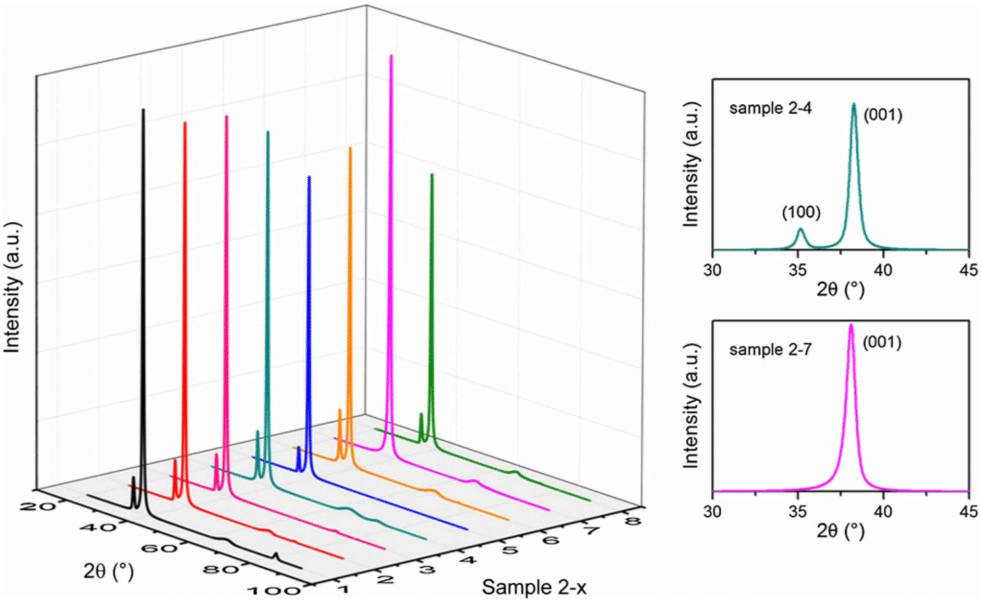

Fig. 3 X-ray diffractograms of thin films deposited at the fixed BV of 200 V and different AVs; 3D plot of diffractograms of all samples prepared at deposition parameters listed in Table 2 (*left*), two detailed diffractograms showing the samples with most presented (100) crystallographic orientation (sample 2–4) and the layer with only (001) orientation (sample 2–7) (*right*)

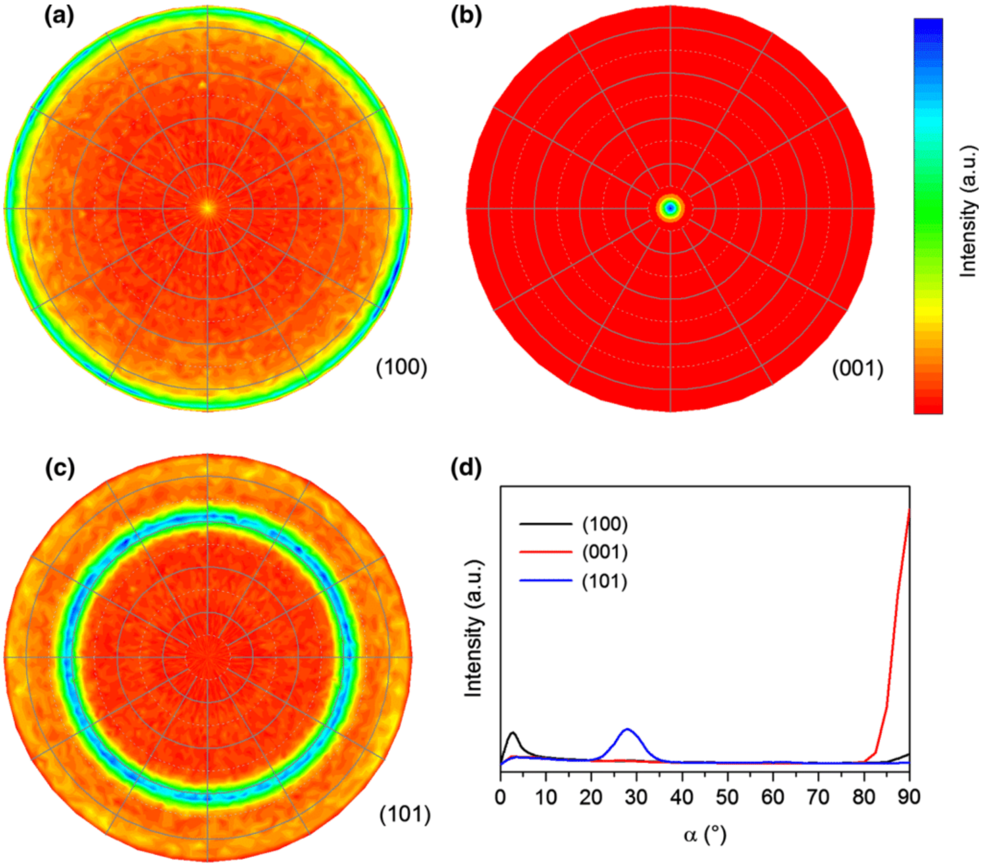

Fig. 4 Pole figures of the sample 2–7 with the optimized preferential orientation; **a** (100) plane angular (i.e., polar and azimuthal) distribution, **b** (001) plane angular distribution, **c** (101) plane angular distribution **d** azimuthally averaged intensity profiles extracted from the preceding pole figures plotted as a function of the crystallographic plane inclination with respect to the sample normal

Further, we performed the pole figure analysis of the optimized sample (i.e., the sample 2–7) for the diffraction angles belonging to (100), (001), and (101) diffraction planes to determine their preferential orientation. The pole figures shown in Fig. 4 are the stereographic projections of the diffracted intensity plotted with respect to the sample coordinates, i.e., pole figure center corresponds to the crystallographic planes parallel to the surface while the edge of the circle corresponds to the planes being perpendicular to the surface. In the previously shown Bragg–

Brentano scans, one can detect only crystallographic planes parallel to the surface. The experimental results show the (001) planes are predominantly oriented parallel to the sample surface, while (100) planes are predominantly perpendicular to the surface. The average misorientation of individual crystallites determined from FWHM of the pole figure peak is 5° (see Fig. 4b, d). Accordingly, the (100) planes being perpendicular to (001) planes reveal their maximum intensity at the edge of the pole figure as shown in Fig. 4a, d. The weak maximum at the pole figure center in Fig. 4a is caused by the fact that the diffraction peaks belonging to (100) and (001) planes are partially overlapping in the angle 2θ and they are not completely separated with used experimental resolution (see Fig. 4d). The angle between the (101) and (001) crystallographic planes in the Ti lattice is 61.3° which perfectly corresponds to the

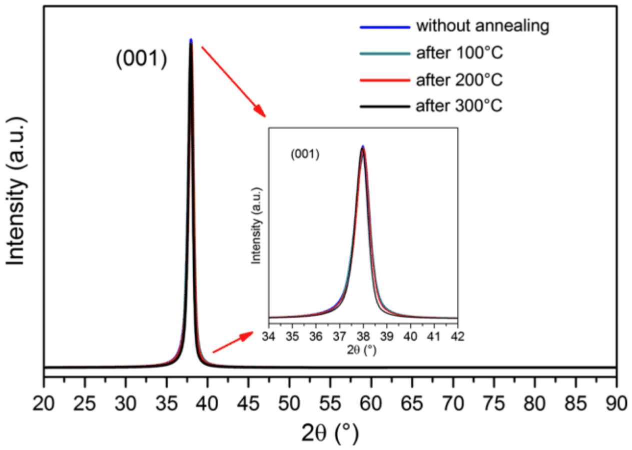

Fig. 5 X-ray diffractograms obtained after each annealing step up to 300 °C for 1 h

Table 3 Measured R_{RMS} surface roughness of samples prepared with different BV and AV settings

Sample no.	BV (V)	AV (V)	R_{RMS} (nm)
1–1	200	−100	0.72 ± 0.08
2–7	200	−220	0.55 ± 0.07
1–2	400	−80	0.73 ± 0.09
1–4	600	−120	0.76 ± 0.09
1–6	800	−160	0.76 ± 0.12
1–8	1000	−200	0.75 ± 0.09
1–9	1200	−240	0.66 ± 0.08
1–10	1200	−600	0.67 ± 0.08

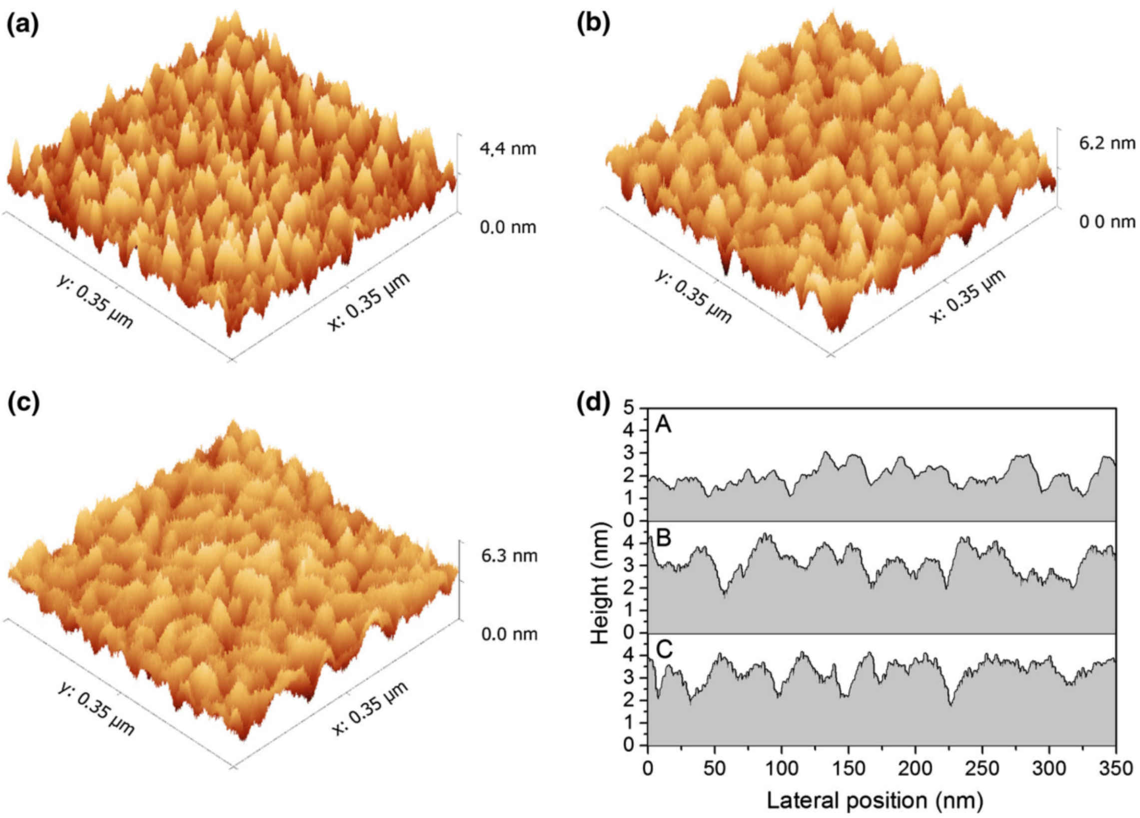

Fig. 6 Surface topography obtained by AFM; **a** the sample 2–7 with the (001) preferential crystallographic orientation; **b** the sample 1–8 with the (100) and (001) crystallographic orientations; **c** the sample 1–10 with (100), (001), and (101) crystallographic planes; **d** profiles corresponding to the three shown AFM surface topography

observed maximum in the pole Fig. 4c. All the three pole figures have a perfect rotational symmetry which means the orientation of the individual crystallites in the azimuthal direction is random with no indication of any preferred azimuthal direction. However, we expected such behavior since the substrate was rotating during the Ti deposition and therefore no unique azimuthal axis is present.

Consequent deposition of some layers such as AlN or ZnO over a titanium film often requires process temperatures up to 300 °C [8]. Considering this fact, we exposed several samples (sample 2–7) with the optimized (001) preferential crystallites orientation to an annealing process in vacuum of 5×10^{-7} mbar. The annealing process was supposed to simulate conditions similar to those needed for deposition of these binary thin film compounds on a titanium layer and thus to learn its possible thermal instability. The consequent XRD analysis (see Fig. 5) shows no obvious changes in the crystal lattice after three different annealing processes which were carried out for three maximum temperatures 100, 200, and 300 °C.

We used the AFM in the ScanAsyst® mode to determine the surface topography and roughness of deposited thin films. Figure 6a shows topography of the sample 2–7 containing titanium crystallites with the preferential orientation (001) with surface roughness of only 0.55 nm. Topography of the sample 1–8 containing crystallites with both (100) and (001) crystallographic planes (see Fig. 2) parallel to the surface is shown in Fig. 6b. This sample has one of the highest surface roughnesses with a value of 0.75 nm. We attribute this fact to the equal distribution of these two crystallographic orientations recognizable as sharp peaks (001) combined with the rounded elongated islands (100). Figure 6c shows the topography of the sample 1–10 where the major contribution to the crystallographic structure comes from the crystallographic orientation 001 along with (100) and (101) planes. We presume this fact is reflected in a surface roughness of the value 0.67 nm which is lower compared to the previous sample. The individual AFM profiles of these three samples (sample 2–7, 1–8, 1–10) are depicted in Fig. 6d.

The results of the AFM measurement are listed in Table 3. The table contains the values of RMS surface roughness including its standard deviations for each sample with corresponding BV and AV. It is obvious that the sample 2–7 possessing the (001) preferential orientation has the lowest surface roughness.

Conclusion

We have presented the optimized deposition process of the (001) preferentially oriented titanium thin film using the Kaufman ion-beam source. The performed experiments have shown that both the low energy and the low ion-beam current are necessary for deposition of highly oriented Ti thin films with the only (001) preferential orientation of films crystallites parallel to the surface.

The crystallites with the (100) orientation parallel to the surface were present in the thin films deposited at higher ion-beam energies (BV of 400 V and higher), and those with the (101) plane parallel to the surface in the films deposited at the highest value of ion-beam energy (BV of 1200 V). The R_{RMS} roughness of all deposited films was less than 1 nm according to the AFM measurements which confirms an ultra-smooth character of surface. The lowest value of surface roughness is only 0.55 nm. We have shown that the surface roughness of thin films depends on the preferential crystallographic orientation.

The observed behavior and properties of the Ti thin films are attributed to specific deposition conditions provided by the Kaufman ion-beam source which generally are not achievable with the conventional magnetron sputtering.

Acknowledgement We acknowledge the support by the European Regional Development Fund (project No. CZ.1.05/1.1.00/02.0068). The work was also carried out with the support of the CEITEC Nano Core Facility under the CEITEC—open access project, ID number LM2011020, funded by the Ministry of Education, Youth and Sports of the Czech Republic under the activity “Projects of major infrastructures for research, development and innovations.”

References

1. Chawla V, Jayaganthan R, Chawla AK, Chandra R (2009) Microstructural characterizations of magnetron sputtered Ti films on glass substrate. J Mater Process Technol 209(7):3444–3451. doi:10.1016/j.jmatprotec.2008.08.004
2. Chen C-N (2012) Fully quantitative characterization of CMOS–MEMS polysilicon/titanium thermopile infrared sensors. Sens Actuators B 161(1):892–900. doi:10.1016/j.snb.2011.11.058
3. Doll JC, Petzold BC, Ninan B, Mullapudi R, Pruitt BL (2010) Aluminum nitride on titanium for CMOS compatible piezoelectric transducers. J Micromech Microeng 20(2):25008. doi:10.1088/0960-1317/20/2/025008
4. López JM, Gordillo-Vázquez FJ, Fernández M, Albella JM (2001) Influence of oxygen on the morphological and structural properties of Ti thin films grown by ion beam-assisted deposition. Thin Solid Films 384(1):69–75. doi:10.1016/S0040-6090(00)01804-6
5. Tsuchiya T, Hirata M, Chiba N (2005) Young’s modulus, fracture strain, and tensile strength of sputtered titanium thin films. Thin Solid Films 484(1–2):245–250. doi:10.1016/j.tsf.2005.02.024
6. Tran AT, Wunnicke O, Pandraud G, Nguyen MD, Schellevis H, Sarro PM (2013) Slender piezoelectric cantilevers of high quality

AlN layers sputtered on Ti thin film for MEMS actuators. Sens Actuators A 202:118–123. doi:10.1016/j.sna.2013.01.047

7. Jackson N, O'Keeffe R, Waldron F, O'Neill M, Mathewson A (2013) Influence of aluminum nitride crystal orientation on MEMS energy harvesting device performance. J Micromech Microeng. doi:10.1088/0960-1317/23/7/075014
8. Jackson N, Keeney L, Mathewson A (2013) Flexible-CMOS and biocompatible piezoelectric AlN material for MEMS applications. Smart Mater Struct. doi:10.1088/0964-1726/22/11/115033
9. Xiong J, Gu H-s HuK, M-z Hu (2010) Influence of substrate metals on the crystal growth of AlN films. Int J Miner Metall Mater 17(1):98–103. doi:10.1007/s12613-010-0117-y
10. Ababneh A, Alsumady M, Seidel H, Manzaneque T, Hernando-García J, Sánchez-Rojas JL, Bittner A, Schmid U (2012) c-axis orientation and piezoelectric coefficients of AlN thin films sputter-deposited on titanium bottom electrodes. Appl Surf Sci 259:59–65. doi:10.1016/j.apsusc.2012.06.086
11. Iriarte GF, Bjurstrom J, Westlinder J, Engelmark F, Katardjiev IV (2005) Synthesis of c-axis-oriented AlN thin films on high-conducting layers: Al, Mo, Ti, TiN, and Ni. IEEE Trans Ultrason Ferroelectr Freq Control 52(7):1170–1174. doi:10.1109/tuffc.2005.1504003
12. Boeshore SE, Parker ER, Lughi V, MacDonald NC, Bingert M (2005) Aluminum nitride thin films on titanium for piezoelectric microelectromechanical systems. In 2005 IEEE ultrasonics symposium, vol 1–4. New York, pp. 1641–1643
13. Jung MJ, Nam KH, Shaginyan LR, Han JG (2003) Deposition of Ti thin film using the magnetron sputtering method. Thin Solid Films 435(1–2):145–149. doi:10.1016/S0040-6090(03)00344-4
14. PalDey S, Deevi SC (2003) Single layer and multilayer wear resistant coatings of (Ti, Al)N: a review. Mater Sci Eng A 342(1–2):58–79. doi:10.1016/S0921-5093(02)00259-9
15. Jing FJ, Yin TL, Yukimura K, Sun H, Leng YX, Huang N (2012) Titanium film deposition by high-power impulse magnetron sputtering: influence of pulse duration. Vacuum 86(12):2114–2119. doi:10.1016/j.vacuum.2012.06.003
16. Henderson PS, Kelly PJ, Arnell RD, Bäcker H, Bradley JW (2003) Investigation into the properties of titanium based films deposited using pulsed magnetron sputtering. Surf Coat Technol 174–175:779–783. doi:10.1016/S0257-8972(03)00397-9
17. Harper JME, Cuomo JJ, Kaufman HR (1982) Technology and applications of broad-beam ion sources used in sputtering. 2. Applications. J Vac Sci Technol 21(3):737–756. doi:10.1116/1.571820
18. Kaufman HR, Cuomo JJ, Harper JME (1982) Technology and applications of broad-beam ion sources used in sputtering.1. Ion-source technology. J Vac Sci Technol 21(3):725–736. doi:10.1116/1.571819
19. Catalog The Kaufman & Robinson Inc. (2013) RFICP 40 ion optics supplement: molybdenum three-grid dished focused 4-cm diameter 45° ellipse
20. Sikola T, Spousta J, Dittrichova L, Nebojsa A, Perina V, Ceska R, Dub P (1996) Dual ion-beam deposition of metallic thin films. Surf Coat Technol 84(1–3):485–490. doi:10.1016/S0257-8972(95)02823-4
21. PDF-2 database entry 00-044-1294, ICDD-JCPDS
22. Patterson AL (1939) The scherrer formula for X-ray particle size determination. Phys Rev 56(10):978–982

4 Residual stress in titanium removing

4.1 Motivation of the article

The most important factor in MEMS fabrication is the value of residual stress in thin films. If the value is higher than 1 GPa it can even cause cracking and buckling of the layer so it is very important to control and reduce value of residual stress. Ti belongs to the group of materials which naturally suffer from compressive residual stress and the controlling is moderate. Here plays a role the main disadvantage of RFICP Kaufman ion beam source deposition which is higher kinetic energy of deposited material in comparison to magnetron sputtering or evaporation. High kinetic energy of sputtered material also increases the value of compressive stress.

After the study of stress removal, the only possible way how to reduce it was the controlling of deposition temperature. It was not possible to use secondary RFICP Kaufman ion-beam source to direct substrate bombardment which provides continual cleaning since the Ti is good oxygen getter and there is also present ultra-low O_2 concentration in 7N Ar gas. I controlled the deposition temperature in range from ≈ 100 °C to ≈ 300 °C to achieve the stress-free (001) preferentially oriented Ti layer. This temperature is acceptable in terms of CMOS compatibility because the lowest possible value of upper limit is ≈ 450 °C which is given by Si-metal interface (e.g. ≈ 450 °C for Si-AlSiCu, ≈ 475 °C for Si-Al, etc.). Increased temperature has significant influence on residual stress after the deposition process is complete and the sample is cooled down due to thermal expansion.

4.2 Conclusion on the article

In this part of my research, I found optimal deposition conditions where layer has no residual stress and also the crystallographic quality of (001) preferentially oriented Ti on SiO_2 was improved. The misorientation was even the best for the stress-free sample with a value of 4.4°. This sample has the lowest roughness over all deposited Ti samples I prepared during my research. Value of lowest roughness was of only 0.58 nm. Such a thin film is ideal for consequent deposition of AlN piezoelectric layer. As prepared Ti layer can be used for various MEMS application where above mentioned properties are required.

4.3 Contribution

I performed all depositions. I also did XRD measurements in Bragg-Brentano and Parallel beam setup and all AFM analyses. I also contributed to the analysis of the results and to the writing of the manuscript.

4.4 Article 2

The article **Stress-free deposition of [001] preferentially oriented titanium thin film by Kaufman ion-beam source** [54] was published in **Thin Solid Films** (2016 IF 1.879) in **September 2017.**

Thin Solid Films 638 (2017) 57–62

Contents lists available at ScienceDirect

Thin Solid Films

journal homepage: www.elsevier.com/locate/tsf

Stress-free deposition of [001] preferentially oriented titanium thin film by Kaufman ion-beam source

Imrich Gablech [a,b,*], Ondřej Caha [c,d], Vojtěch Svatoš [a,b], Jan Pekárek [a,b], Pavel Neužil [a,b,e], Tomáš Šikola [a,f]

[a] Central European Institute of Technology, Brno University of Technology, Purkyňova 123, CZ-61200 Brno, Czech Republic
[b] Brno University of Technology, Faculty of Electrical Engineering and Communication, Department of Microelectronics, Technická 3058/10, CZ-61600 Brno, Czech Republic
[c] Central European Institute of Technology, Masaryk University, Kamenice 753/5, CZ-62500 Brno, Czech Republic
[d] Masaryk University, Faculty of Science, Department of Condensed Matter Physics, Kotlářská 2, CZ-60200 Brno, Czech Republic
[e] Northwestern Polytechnical University, 127 West Youyi Road, Xi'an, Shaanxi, PR China
[f] Brno University of Technology, Institute of Physical Engineering, Technická 2896/2, CZ-61669 Brno, Czech Republic

ARTICLE INFO

Article history:
Received 2 March 2017
Received in revised form 10 July 2017
Accepted 14 July 2017
Available online 15 July 2017

Keywords:
Ion-beam sputtering deposition
Kaufman ion-beam source
Titanium thin film
[001] preferential orientation
Residual stress
Rocking curve

ABSTRACT

We proposed a method to control and minimize residual stress in [001] preferentially oriented Ti thin films deposited by a Kaufman ion-beam source using a substrate temperature during deposition (T) as the parameter. We determined the residual stress, corresponding lattice parameters, and thickness of deposited films using X-ray diffraction and X-ray reflectivity measurements. We showed that the Ti film deposited at $T \approx 273$ °C was stress-free with corresponding lattice parameters a_0 and c_0 of (2.954 ± 0.003) Å and (4.695 ± 0.001) Å, respectively. The stress-free sample has the superior crystallographic quality and pure [001] orientation. The Ti thin films were oriented with the c-axis parallel to the surface normal. We also investigated root mean square of surface roughness of deposited films by atomic force microscopy and it was in the range from ≈ 0.58 nm to ≈ 0.71 nm. Such smooth and stress-free layers are suitable for microelectromechanical systems.

1. Introduction

Ti is a commonly used material in planar technologies either for the fabrication of integrated circuits, microelectromechanical systems (MEMS) or microfluidic systems. Ti has a reasonably good electrical conductivity, an excellent thermal stability, high hardness, high melting point, high elasticity and a very low concentration of crystallographic imperfections [1]. Ti belongs to a group of biocompatible materials and is also compatible with the complementary-metal-oxide-semiconductor (CMOS) process; thus, it is capable of being used in fabrication lines dedicated to CMOS production and research [2]. Ti thin films are used in MEMS applications such as cochlear implants [3], infrared bolometers [4–6], flexible and wearable heartbeat sensors [7], piezoelectric energy harvesters [8], microfluidic devices [9], and piezoelectric resonators [10]. Layers used in MEMS technologies are typically required to have minimal residual stress as this significantly affects the mechanical [11] and electrical [12] properties of a final device. Once the stress level exceeds a certain limit it can even cause damage to the structural integrity of the device [13].

Ti thin films are usually deposited by processes such as physical vapor deposition, including thermal and electron beam evaporation, pulsed laser deposition, or sputtering, either magnetron or ion-beam based. Each technique results in the formation of layers with different properties, such as crystallographic parameters, roughness, residual stress, electrical sheet resistance, and thermal coefficient of resistance [14]. Control of the Ti crystallographic orientation is of crucial significance as it directly affects its properties and, together with surface roughness, it is important for properties of layers subsequently deposited on top of the Ti layer, such as AlN piezoelectric material [10,15,16]. The magnetron sputtering technique allows residual stress control by modulating Ar gas pressure, magnetron power, or substrate deposition temperature (T) [17]. Unfortunately, these parameters cannot be set independently from each other. The other extended technique employing the assisted ion-beam source for concurrent substrate ion-beam bombardment during the layer growth allows only limited control of residual stress [18].

Here, we report on the preparation of stress-free highly [001] oriented Ti thin films deposited using a 3-grid radio frequency-inductively coupled plasma (RFICP) Kaufman ion-beam source. The major advantage of this ion-beam source type is a well-defined process control that allows us, contrary to conventional deposition techniques, to set parameters like ion-beam energy and atomic sputtering direction independently, and also in one order magnitude lower operational pressure compared with magnetron sputtering [1]. On the other hand, its disadvantage is a

---

[*] Corresponding author at: Central European Institute of Technology, Brno University of Technology, Purkyňova 123, CZ-61200 Brno, Czech Republic.
E-mail address: imrich.gablech@ceitec.vutbr.cz (I. Gablech).

http://dx.doi.org/10.1016/j.tsf.2017.07.039
0040-6090/

rather more complex control of residual stress. In our work, we concentrated on the investigation of the control of residual stress by T and its influence on crystallography and surface roughness of a Ti layer deposited on a plasma enhanced chemical vapor deposited (PECVD) SiO_2 layer.

2. Experimental details

2.1. Titanium deposition process

For all experiments, we used p-type Si wafers with diameter of ≈100 mm, crystallographic orientation of [100], thickness of ≈375 μm, and specific resistivity in the range from ≈6 Ω cm to ≈12 Ω cm covered with PECVD SiO_2 with a thickness of ≈200 nm. These wafers were diced into individual substrates with dimensions of ≈20 mm × ≈20 mm.

The Ti layers were deposited by an ion-beam sputtering system inside a vacuum chamber with the RFICP Kaufman ion-beam source (Kaufman & Robinson—KRI®) with a ≈ 4 cm diameter Mo 3-grid dished focused ion optics with an ≈45° ellipse pattern. We used an Ar ion-beam with purity of 99.99999% to provide the bombardment of an ≈100 mm × ≈100 mm Ti target with the purity of 99.995% under an incidence angle of ≈45°. Reduction of the ion-beam space charge was provided by a KRI LFN 2000 charge neutralizer (KRI®). The vacuum chamber was evacuated to the pressure of $\approx 5 \cdot 10^{-7}$ Pa before each deposition process. The final Ti thickness (t_f) of (80 ± 1) nm was monitored in-situ by quartz crystal microbalance method and subsequently verified by X-ray reflectivity (XRR) measurement.

The deposition parameters were selected under conditions determined in our previously reported work [1]. We set the ion-beam energy to ≈200 eV, acceleration voltage to ≈−220 V to control the extraction and optical parameters of the ion-beam, ion-beam current to ≈5 mA at the target, radio frequency power to ≈70 W supplied to the plasma discharge, Ar flow to ≈2.2 sccm, and T was used as the parameter. We performed a contact temperature measurement using a type K thermocouple during the sputter deposition process to investigate the T caused by the combination of deposited material energy and the built-in substrate heater. The lowest value of T was ≈105 °C which is generated only by the deposited material flux with no additional heating. We controlled the T in the range from ≈105 °C to ≈295 °C with an accuracy of ±3 °C. The pressure during the all depositions was constant with the value of $\approx 9 \cdot 10^{-3}$ Pa.

2.2. X-ray scattering methods

We characterized the Ti layers by several X-ray diffraction (XRD) methods (Fig. 1). We used a Rigaku SmartLab system with a Cu X-ray tube.

We used the standard Bragg-Brentano setup (Fig. 1A) to determine the lattice parameter (c) of the planes parallel to the surface. The lattice parameter (a) in the perpendicular direction was measured in a grazing-incidence setup (Fig. 1B) using a parabolic multilayer mirror as a monochromator and parallel plate collimator with a divergence of ≈0.15° and ≈0.11° in the incident and the scattered beam, respectively. We performed this measurement at an angle of incidence (α_i) of 0.3°, which is close to the critical angle of total external reflection of 0.298°. The diffracted signal was integrated over the exit angle (α_f) from 0° up to 2°. We extracted values of lattice parameters by curve fitting using Rigaku PDXL2 software.

We measured the t_f in the XRR configuration using a two bounce Ge (220) channel cut monochromator.

We determined the preferential orientation of the Ti lattice via the pole figures measurement. We performed the measurement with the parallel beam and the parallel plate collimator as in the grazing incidence setup (Fig. 1B). The diffractometer with an in-plane arm allowed to map the full half space above the sample's surface. The background of pole figure was measured 2° off the peak position.

We measured the curvature (Fig. 1C) of the Si substrate before (R_0) and after (R) Ti deposition to determine the elastic stress of Ti layers. The curvature radius was determined from the dependence of Bragg angle (θ) on the substrate position. Its slope is inversely proportional to the curvature radius of crystallographic planes. The stress of a Ti layer (σ_f) can be calculated by the Stoney formula (Eq. (1)) for [001] oriented Si [19]:

$$\sigma_f t_f = \frac{h^2}{6} \cdot \frac{1}{s_{11} + s_{12}} \cdot \left(\frac{1}{R} - \frac{1}{R_0}\right) \qquad (1)$$

where h is the substrate thickness and s_{11} and s_{12} are the components of the Si elastic compliance tensor. We used a four bounce Ge (220) Bartels-type monochromator and measured the position of Si 004 diffraction peak dependence on the sample position.

2.3. Surface roughness measurement method

We determined the root mean square of surface roughness (R_{RMS}) from surface scanning by atomic force microscope (AFM) Dimension Icon by Bruker in the ScanAsyst®-Air mode. We used the ScanAsyst-Air probe with a cantilever spring constant of $\approx 0.4\ \mathrm{N \cdot m^{-1}}$ and tip radius of ≈2 nm.

3. Results and discussion

3.1. Crystallography and stress characterization

We performed phase analysis measurement using XRD in the Bragg-Brentano setup with the 2θ angle in the range from 30° to 85° for all layers with T as the parameter. The interval from 60° to 78° was excluded

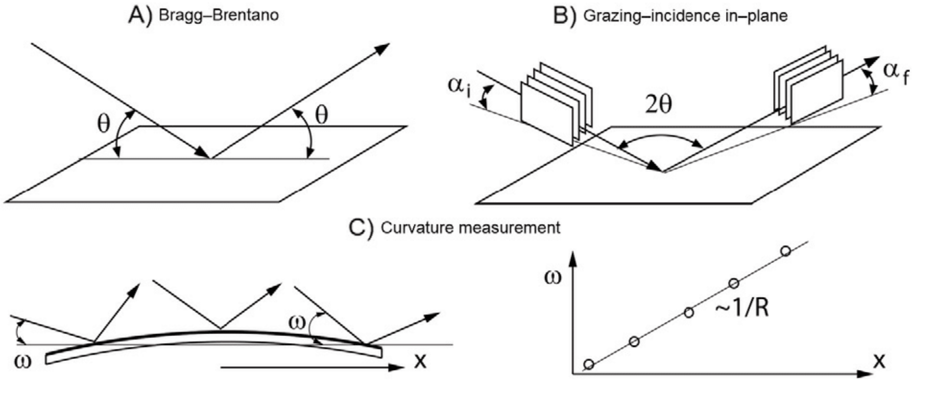

Fig. 1. Setup of the XRD experimental methods: A) Bragg-Brentano setup to measure the out-of-plane c lattice parameter; B) In-plane diffraction for a lattice parameter determination was measured with the parallel plate collimator and analyzer shown in the figure; C) Curvature measurement determines average σ_f in the layer. The angle of incidence with respect to the mean surface is noted as ω.

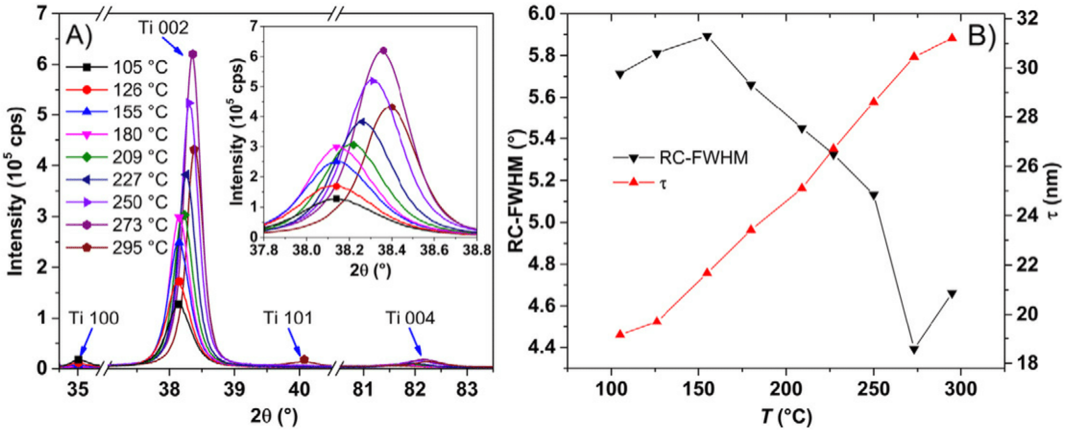

Fig. 2. A) X-ray diffractograms of deposited thin films obtained at different *T*. The range from 60° to 78° was excluded due to Si 400 diffraction with intensity of several orders of magnitude higher than of the Ti peaks; B) RC-FWHM and τ dependence on *T*.

to avoid the high intensity of Si 400 diffraction in this range. We detected the diffraction peaks that belongs to the (100), (001) and (101) crystallographic planes. We detected the 2nd order 002 and the 4th order 004 diffraction peaks since the 1st order diffraction is forbidden (Fig. 2A) for the (001) crystallographic plane (Fig. 2A). We used XRD in the parallel beam setup to determine the rocking curve (RC) width (Fig. 2B). We calculated the minimal average crystallite size (τ) using the Scherrer equation [20] (Eq. (2)) from the full width at half maximum (FWHM) of the 002 diffraction peak in the Bragg-Brentano setup (Fig. 2B):

$$\tau = \frac{K \cdot \lambda}{\beta \cdot \cos(\theta)} \tag{2}$$

where K is the Scherrer constant, λ is the X-ray wavelength, and β is the line broadening at half the maximum intensity. The 004 diffraction peak was not resolved at all samples, thus the inhomogeneous strain induced peak widening could not be determined.

The Bragg-Brentano analysis results proved that the crystallites in all deposited layers had the [001] preferential orientation. We also observed a small contribution of the (100) plane belonging to the samples deposited with *T* from ≈105 °C to ≈155 °C. Only one (001) crystallographic plane was presented for samples deposited in the range from ≈180 °C to ≈273 °C. The small contribution of the (101) plane was presented for the highest *T* ≈ 295 °C.

T increased from ≈155 °C to ≈273 °C, resulting in increased diffraction peak intensity and decreased RC width. We observed the highest diffraction intensity with the lowest FWHM value of ≈0.27° and the lowest RC width with FWHM ≈4.4° at *T* ≈ 273 °C. Increasing *T* from ≈105 °C to ≈295 °C also resulted in the increase of τ from ≈19 nm to ≈31 nm.

The dependence of the lattice parameters on *T* is shown in Fig. 3B. The strain ε_{ij} was calculated (Eq. (3)) using experimental and tabulated values of the lattice parameters:

$$\varepsilon_{xx} = \frac{a_{exp} - a_0}{a_0}, \varepsilon_{zz} = \frac{c_{exp} - c_0}{c_0} \tag{3}$$

where *x* and *z*, respectively, are the in-plane and out-of-plane coordinates, a_{exp}, c_{exp} the experimental lattice parameters and a_0, c_0 the tabulated values of the unstrained lattice. Then assuming in-plane isotropy, the in-plane and out-of-plane stress components can be calculated as (Eq. (4)):

$$\sigma_{xx} = (C_{11} + C_{12}) \cdot \varepsilon_{xx} + C_{13} \cdot \varepsilon_{zz}, \sigma_{zz} = 2C_{13} \cdot \varepsilon_{xx} + C_{33} \cdot \varepsilon_{zz} = 0 \tag{4}$$

where C_{ij} are the components of the Ti elastic stiffness tensor [21], the in-plane σ_{xx}, and the out-of-plane σ_{zz} stress components equal zero since the surface is stress-free. However, the tabulated values of the lattice parameters vary in a relatively broad range and, therefore the uncertainty of the calculated stress would be in the order of GPa and, therefore, not acceptable for MEMS applications. Thus, we measured the σ_f via the curvature of the substrate; the measured σ_f dependence on *T* is plotted in Fig. 3A. The σ_f has the same qualitative dependence as the *a* and opposite one as the *c* in agreement with the previous equations (Eq. (4)).

The Ti thin film deposited at *T* ≈ 273 °C exhibits the zero residual σ_f value within the experimental precision of 0.1 GPa. Corresponding a_0 and c_0 of this unstrained Ti film are (2.954 ± 0.003) Å and (4.695 ± 0.001) Å, respectively and their ratio *c*/*a* is (1.5891 ± 0.0015). Using these values of Ti lattice parameters, we calculated the average amplitudes of σ_{xx} and σ_{zz} using formulas (Eq. (3)) and (Eq. (4)). We obtained values which were in good agreement with the ones determined by the

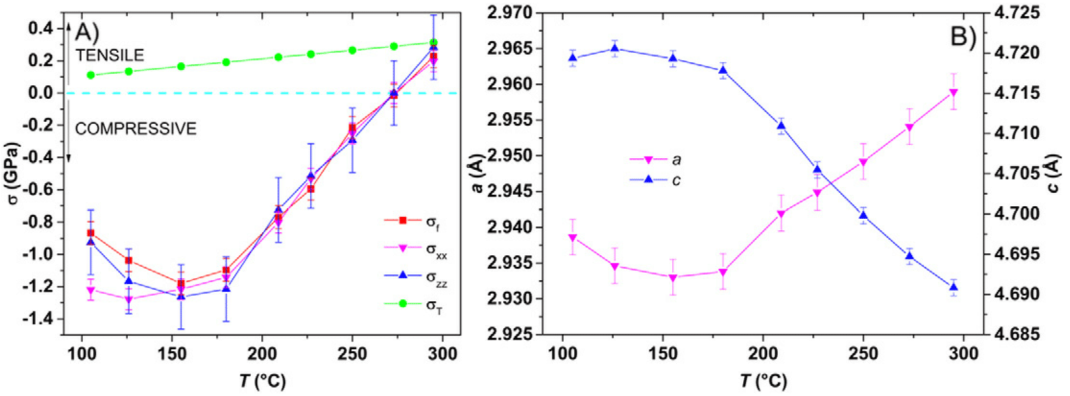

Fig. 3. A) Stress σ dependence of measured σ_f and calculated σ_{xx}, σ_{zz}, and σ_T values (Eq. (4)) on *T*; B) Dependence of measured *a* and *c* of deposited Ti thin films on *T*.

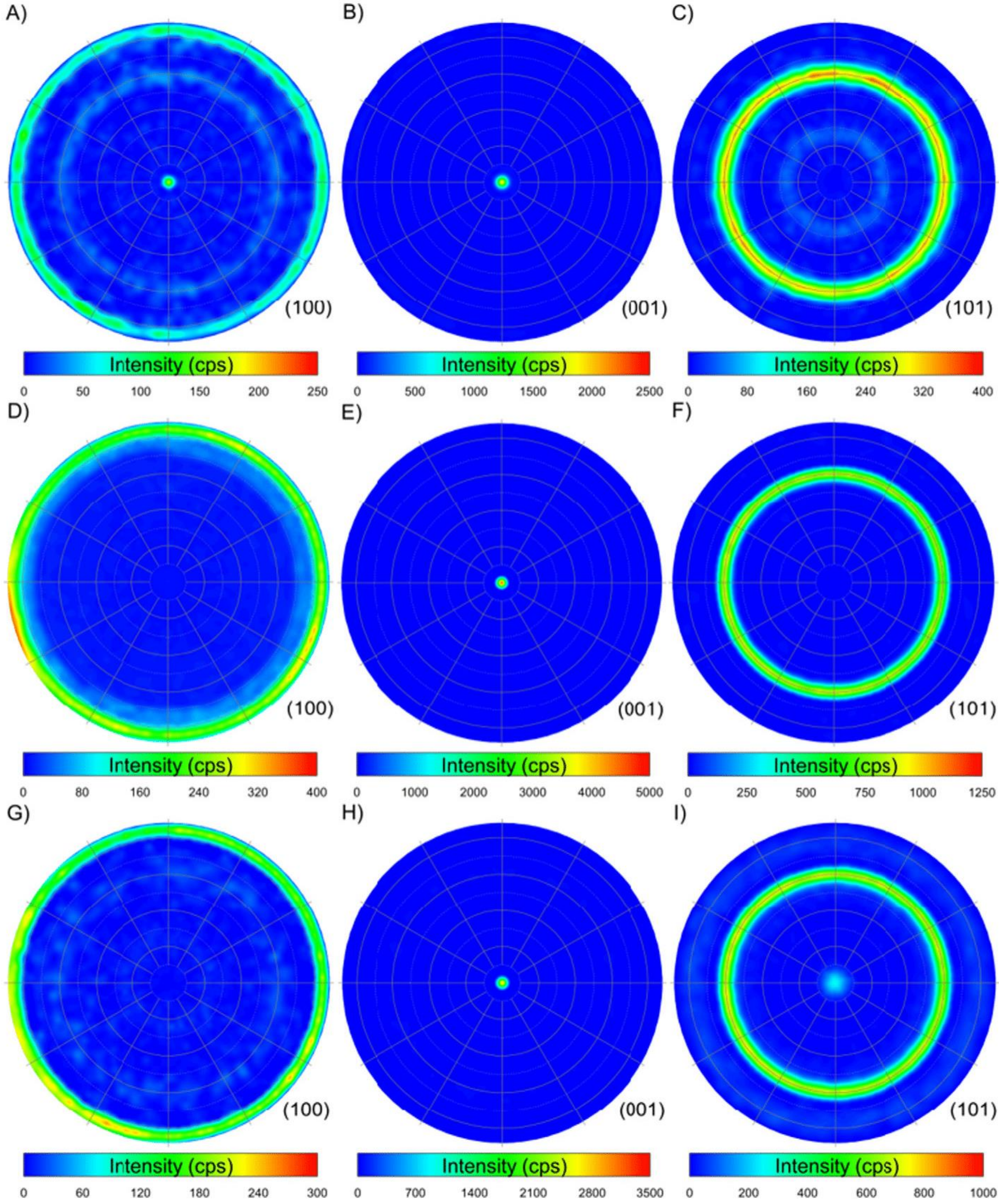

Fig. 4. Pole figures of three diffractions 100, 002 [second order diffraction on the (001) crystallographic planes], and 101 are plotted in the left, center, and right column, respectively: A, B, C) The sample grown at $T \approx 105$ °C with the compressive stress; D, E, F) The sample grown at $T \approx 273$ °C with no residual stress; G, H, I) The sample grown at $T \approx 295$ °C with tensile stress.

independent curvature measurements (Fig. 3A). The tensile stress for the layers deposited at high T can be explained by the different thermal expansion of Si and Ti material. The Ti thermal expansion coefficient is larger than for the Si by $\approx 6 \cdot 10^{-6}$ K^{-1}. This corresponds to a thermally induced stress (σ_T) of ≈ 0.3 GPa for the $T \approx 295$ °C, which is in good agreement with the experimental value (Fig. 3A). The layers deposited at lower T were compressively stressed, with the highest stress value reached at $T \approx 155$ °C. Higher T resulted in stress relaxation. The layer deposited at $T \approx 295$ °C was grown as stress-free and the tensile stress was induced during cooling down to the ambient temperature.

3.2. Pole figure analysis

The Bragg-Brentano setup showed the crystallographic planes parallel to the surface. We performed pole figure analyses to obtain full information of the preferential orientation of the layer. The pole figures were measured on three selected samples with different symmetric diffraction patterns and stress (Fig. 4). The first one was grown at $T \approx 105$ °C exhibits the (100) and (001) crystallographic planes oriented preferentially in crystallites parallel to a surface and the stress was compressive. The second, grown at $T \approx 273$ °C, was purely [001] oriented and stress-free. The third one has the (001) and (101) planes parallel to a surface and the layer possess tensile stress.

The sample grown at optimal $T \approx 273$ °C (Fig. 4D, E, F) shows that the (001) crystallographic planes are oriented in crystallites exclusively parallel to the sample surface, noted as a peak in the center of the circular stereographic projection. The (100) planes are randomly oriented perpendicular to the surface, shown as a ring at the outer circle boundary, the (101) planes are oriented with a theoretical angle of ≈61° with respect to the surface. The other samples show the major contribution of the [001] orientation giving rise to the result equivalent to the optimal T. The samples grown at low and high T show an additional minor contribution of another orientation. The sample grown at a lower $T \approx 105$ °C shows the (100) planes in two preferential orientations: parallel to the surface [[100] oriented crystallites] and perpendicular to the surface [[001] oriented crystallites]; the ring at angle of ≈60° with respect to the surface corresponds also to the [100] orientation since 60° is an angle between various equivalent [17] crystallographic planes (Fig. 4A, B). The (101) planes also show two orientations (Fig. 4C): the more intensive ring at angle of ≈61° corresponds to the crystallites with the [001] orientation and the weaker one at ≈29° corresponds to the [100] oriented crystallites. The sample deposited at $T \approx 295$ °C has the major [001] orientation of crystallites and minor contribution of the [101] orientation (Fig. 4G, H, I). The 100 pole figure shows except of the most intensive ring perpendicular to the surface two weak rings at angles of ≈29° and ≈64° corresponding to the angles of the (100) planes with respect to the (101) equivalent planes.

The pole figures analysis confirmed that the deposition at $T \approx 105$ °C with a compressive stress has mixed [001] and [100] orientation. The stress-free Ti thin film exhibits only [001] orientation at optimum growth $T \approx 273$ °C. The highest $T \approx 295$ °C results in a tensile stress and preferential orientations [001] and [101].

All XRD analyses showed the sample grown at the optimal T has [001] preferential orientation, with the narrowest rocking curve RC with RC-FWHM of ≈4.4° and big crystallites with size of ≈30 nm. Thus, we concluded this sample had the superior microstructure quality from all samples.

3.3. Surface roughness characterization

We performed AFM topography scans by using the ScanAsyst®-Air mode to study the surface roughness of Ti thin films deposited at different T. The obtained amplitude of R_{RMS} with T as the parameter indicates a certain correlation with the curve that describes the dependence of RC-FWHM on T as shown in Fig. 2B.

Nevertheless, all samples had a rather smooth surface with R_{RMS} in the range from ≈0.58 nm to ≈0.71 nm (Fig. 5A). The surface topography of the stress-free sample deposited at $T \approx 273$ °C and having the lowest R_{RMS} value is shown in Fig. 5B.

4. Conclusions

We presented a method to modulate the residual stress in [001] preferentially oriented Ti thin films deposited using the Kaufman ion-beam source by changing T. The experiments showed that T has an essential influence on the residual stress and lattice parameters of deposited Ti thin films. At low T, compressive residual stress was obtained, which decreased with increasing T from ≈155 °C up to ≈273 °C, when zero residual stress was achieved. The corresponding lattice parameters for this stress-free film were $a_0 = (2.954 \pm 0.003)$ Å and $c_0 = (4.695 \pm 0.001)$ Å. At $T \approx 295$ °C, the tensile residual stress was measured due to differences in thermal expansion coefficients of the Ti and Si substrate. The layers have a very well defined preferential orientation, with the c-axis oriented perpendicular to the surface with a negligible contribution of other orientation at T between ≈155 °C and ≈273 °C. At T lower than ≈155 °C, [100] oriented crystallites are present, whereas at T higher than ≈273 °C [101] oriented crystallites were detected. The sample grown at $T \approx 273$ °C showed not only zero residual stress, but also a superior crystallographic quality and the lowest R_{RMS} value of ≈0.58 nm among the whole sample series.

Acknowledgment

We acknowledge the support of CEITEC Nano Research Infrastructure (ID LM2015041, MEYS CR, 2016–2019), CEITEC Brno University of Technology and Grant Agency of the Czech Republic under the contracts GA13-19947S, GA16-11140S and GACR 17-20716S. Authors I. Gablech and J. Pekárek also acknowledge the Brno University of Technology support FEKT/STI-J-17-4136.

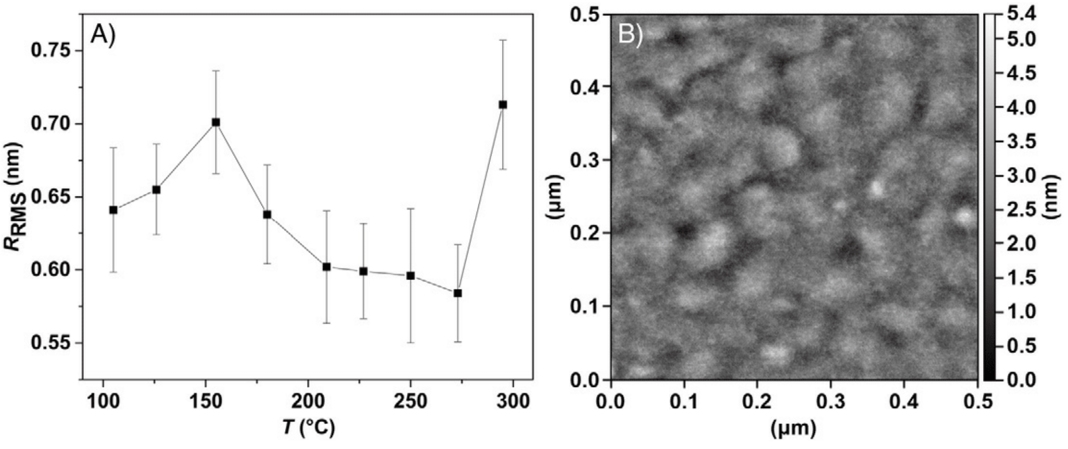

Fig. 5. A) Dependence of measured R_{RMS} values of Ti thin films on T; B) Smooth Ti surface achieved at $T \approx 273$ °C and with the [001] preferential crystal orientation.

References

[1] I. Gablech, V. Svatoš, O. Caha, M. Hrabovský, J. Prášek, J. Hubálek, T. Šikola, Preparation of (001) preferentially oriented titanium thin films by ion-beam sputtering deposition on thermal silicon dioxide, J. Mater. Sci. 51 (2016) 3329–3336.

[2] N. Jackson, L. Keeney, A. Mathewson, Flexible-CMOS and biocompatible piezoelectric AlN material for MEMS applications, Smart Mater. Struct. 22 (2013) 9.

[3] K. Knisely, C. Zhao, K. Grosh, A MEMS AlN transducer array with flexible interconnections for use as a cochlear implant, AIP Conf. Proc. 1703 (2015) 100004.

[4] P. Neuzil, T. Mei, A method of suppressing self-heating signal of bolometers, IEEE Sensors J. 4 (2004) 207–210.

[5] P. Neuzil, Y. Liu, H.H. Feng, W.J. Zeng, Micromachined bolometer with single-crystal silicon diode as temperature sensor, IEEE Electr. Device L 26 (2005) 320–322.

[6] P. Neuzil, T. Mei, Evaluation of thermal parameters of bolometer devices, Appl. Phys. Lett. 80 (2002) 1838–1840.

[7] Y. Khan, A.E. Ostfeld, C.M. Lochner, A. Pierre, A.C. Arias, Monitoring of vital signs with flexible and wearable medical devices, Adv. Mater. 28 (2016) 4373–4395.

[8] G. Urban, J. Wöllenstein, J. Kieninger, A. Sharma, O.Z. Olszewski, J. Torres, A. Mathewson, R. Houlihan, Eurosensors 2015Fabrication, simulation and characterisation of MEMS piezoelectric vibration energy harvester for low frequency, Procedia Eng. 120 (2015) 645–650.

[9] M.W. Ashraf, S. Tayyaba, N. Afzulpurkar, Micro Electromechanical Systems (MEMS) based microfluidic devices for biomedical applications, Int. J. Mol. Sci. 12 (2011) 3648–3704.

[10] J.C. Doll, B.C. Petzold, B. Ninan, R. Mullapudi, B.L. Pruitt, Aluminum nitride on titanium for CMOS compatible piezoelectric transducers, J. Micromech. Microeng. 20 (2010) 8.

[11] R.C. Chang, F.Y. Chen, C.T. Chuang, Y.C. Tung, Residual stresses of sputtering titanium thin films at various substrate temperatures, J. Nanosci. Nanotechnol. 10 (2010) 4562–4567.

[12] M. Khan, M. Islam, A. Akram, Z.M. Qi, L.B. Li, Residual strain and electrical resistivity dependence of molybdenum films on DC plasma magnetron sputtering conditions, Mater. Sci. Semicond. Process. 27 (2014) 343–351.

[13] H.-C. Seo, I. Petrov, H. Jeong, P. Chapman, K. Kim, Elastic buckling of AlN ribbons on elastomeric substrate, Appl. Phys. Lett. 94 (2009), 092104.

[14] W. Kern, K.K. Schuegraf, K. Seshan, Handbook of Thin Film Deposition Processes and Techniques, William Andrew Publishing, New York, 2001.

[15] A.T. Tran, G. Pandraud, F.D. Tichelaar, M.D. Nguyen, H. Schellevis, P.M. Sarro, The extraordinary role of the AlN interlayer in growth of AlN sputtered on Ti electrodes, Appl. Phys. Lett. 103 (2013) 221909.

[16] M. Patru, L. Isac, L. Cunha, P. Martins, S. Lanceros-Mendez, G. Oncioiu, D. Cristea, D. Munteanu, Structural, mechanical and piezoelectric properties of polycrystalline AlN films sputtered on titanium bottom electrodes, Appl. Surf. Sci. 354 (2015) 267–278.

[17] V. Chawla, R. Jayaganthan, A.K. Chawla, R. Chandra, Microstructural characterizations of magnetron sputtered Ti films on glass substrate, J. Mater. Process. Technol. 209 (2009) 3444–3451.

[18] Y. Watanabe, N. Kitazawa, Y. Nakamura, C. Li, T. Sekino, K. Niihara, Mechanical properties and residual stress in AlN films prepared by ion beam assisted deposition, J. Vac. Sci. Technol. A 18 (2000) 1567–1570.

[19] G.C.A.M. Janssen, M.M. Abdalla, F. van Keulen, B.R. Pujada, B. van Venrooy, Celebrating the 100th anniversary of the Stoney equation for film stress: developments from polycrystalline steel strips to single crystal silicon wafers, Thin Solid Films 517 (2009) 1858–1867.

[20] A. Guinier, X-ray Diffraction in Crystals, Imperfect Crystals, and Amorphous Bodies, Dover Publications, 1994.

[21] A. Goldmann, 2.11.3 Ti (Titanium) (Z = 22): Datasheet from Landolt-Börnstein—Group III Condensed Matter Volume 23C1: "Noble Metals, Noble Metal Halides and Nonmagnetic Transition Metals" in SpringerMaterials, in: A. Goldmann (Ed.), Springer-Verlag Berlin Heidelberg, (doi:http://dx.doi.org/10.1007/10714318_18).

5 Electrical properties of titanium thin film

5.1 Motivation of the article

Ti also plays a role of bottom electrode in piezoelectric resonator and it is important to know the fundamental electrical properties of metal such as resistivity (ρ) and thermal coefficient of resistivity (α). Knowledge of these parameters should be useful for different applications where the increased device working temperature or monitoring of temperature changing are required.

This paper was realized as the summary of previous two articles with additional measurement of the important electrical parameters. All electrical measurements were done using 4-probe method to achieve high precision results. Therefore, the ρ and α were determined from measured voltage-current curves.

5.2 Conclusion on the article

Obtained results prove high quality of Ti layers because the measured ρ and α of 80 nm thick layer nearly correspond to bulk material constants. This proves the quality and purity of Ti because impurities reduce the ρ and mainly the α. Additionally, the XPS analyses were not successful but the presence of oxygen and carbon impurities can be also estimated from XRD as peak shifts and also as presence of (100) and (101) along the (001) orientation or even from presence of TiO_x diffractions. All these results prove that the content of impurities is marginal. This optimized Ti layer was also used for another application such as IR microbolometer or device for cells temperature measurement prepared by our group. Ti was used as heater up to ≈ 850 °C to direct CVD grown on membranes with substrate at ambient temperature in IR microbolometer. This Ti layer was subsequently used for temperature change measurement as well. We also published few papers where we used optimized Ti. These articles which have certain similarity to fabrication processing of device are described below in this work.

5.3 Contribution

This article is summary of two previous publications but extended of electrical measurements and evaluation of them. I performed all electrical measurements and results evaluation. I also contributed to the writing of the manuscript.

5.4 Article 3

The article **Preparation of [001] oriented titanium thin film for MEMS applications by Kaufman ion-beam source** [55] was published in proceedings of the international WOS indexed conference **NANOCON 2017** in **October 2017.**

PREPARATION OF [001] ORIENTED TITANIUM THIN FILM FOR MEMS APPLICATIONS BY KAUFMAN ION-BEAM SOURCE

GABLECH Imrich[1,2], CAHA Ondřej[3,4], SVATOŠ Vojtěch[1,2], PRÁŠEK Jan[1,2], PEKÁREK Jan[1,2], NEUŽIL Pavel[1,2], ŠIKOLA Tomáš[1,5]

[1] Brno University of Technology, Central European Institute of Technology, Brno, Czech Republic
[2] Brno University of Technology, Faculty of Electrical Engineering and Communication, SIX Centre, Department of Microelectronics, Brno, Czech Republic
[3] Masaryk University, Central European Institute of Technology, Brno, Czech Republic
[4] Masaryk University, Faculty of Science, Department of Condensed Matter Physics, Brno, Czech Republic
[5] Brno University of Technology, Faculty of Mechanical Engineering, Institute of Physical Engineering, Brno, Czech Republic

Abstract

We propose the sputtering deposition providing titanium thin films with controlled properties such as preferential crystallography and residual stress using Kaufman ion-beam source. The titanium thin films with thickness of ≈ 80 nm were deposited on [001] Si wafer covered by SiO_2 deposited by plasma-enhanced chemical vapor deposition. To achieve the required crystallography and stress properties, we investigated the different beam voltage of Kaufman ion-beam source and controlled the substrate temperature during deposition using a built-in heater. We used two X-ray diffraction methods to determine the planes parallel to the sample surface and residual stress. We also measured the current-voltage curves to determine the resistivity (ρ) and the thermal coefficient of resistivity (α) of titanium thin films at different substrate temperatures using 4-probe measurement setup. We showed that it is possible to prepare stress-free titanium thin films with pure [001] orientation at the lowest beam voltage of 200 V and substrate temperature of ≈ 273 °C. The corresponding lattice parameters a_0 and c_0 were (2.954 ± 0.003) Å and (4.695 ± 0.001) Å, respectively. Electrical parameters of this sample as ρ and α were $(9.2 \pm 0.1)\cdot 10^{-7}$ Ω·m and $(2.6 \pm 0.2)\cdot 10^{-3}$ K^{-1}, respectively. We found out that these layers are well suitable for micro-electro-mechanical systems where the pure [001] orientation, no residual stress and low ρ and high α are essential. We found that ρ and α are dependent on each other. The ρ value was ≈ 2× higher than the bulk material value, which is an excellent result for a thin film with the thickness of ≈ 80 nm.

Keywords: titanium thin film, [001] orientation, stress-free, thermal coefficient of resistivity, resistivity

1. INTRODUCTION

Titanium is a commonly used material in microelectronics, microelectromechanical systems (MEMS) or microfluidic systems due to its low value of electrical resistivity of $4.2\cdot 10^{-7}$ Ω·m. It also possesses an extraordinary chemical resistance, an excellent thermal stability, high melting temperature of 1668 °C, high hardness, and a very low number of crystallographic imperfections [1-5].

Titanium belongs to a group of biocompatible materials and is also compatible with the complementary-metal-oxide-semiconductor (CMOS) processes; thus, it is commonly used for device fabrication using lines dedicated to CMOS production and research [6]. In a thin film format it is used in MEMS devices such as infrared bolometers [7], flexible and wearable heartbeat sensors [8], cochlear implants [9], piezoelectric resonators [3], piezoelectric energy harvesters [10], and microfluidic devices [11].

Titanium thin films are typically deposited by the physical vapor deposition (PVD) methods including thermal and electron beam evaporation, pulsed laser deposition, or sputtering, either magnetron or ion-beam based.

Different deposition parameters and techniques result in various film properties such as crystallographic parameters, roughness, residual stress, electrical sheet resistance, and thermal coefficient of resistance [12].

Layers used in MEMS technologies are typically required to have minimal residual stress as this significantly affects the mechanical [13] and electrical [14] properties of the final device because the excessive stress level can negatively affect the device performance and even cause damage to its structural integrity [15]. The crystallographic orientation of thin titanium thin films is also crucial for properties of consequently deposited piezoelectric layers such as AlN [16].

Here, we report on a deposition of stress-free highly [001] oriented titanium thin film growth on SiO_2 using a 3-grid radio frequency inductive coupled plasma (RFICP) Kaufman ion-beam source. The most important advantage of the Kaufman ion-beam source is a well-defined process control. To achieve the required crystallography and stress properties, we investigated the different beam voltage of Kaufman ion-beam source and controlled the substrate temperature during deposition using a built-in heater. In our work, we concentrated on the investigation of the control of residual stress by the substrate temperature (T) and its influence on properties of titanium thin films especially on their preferential crystallographic orientation, resistivity (ρ) and thermal coefficient of resistivity (α).

2. EXPERIMENTAL PART

2.1. DEPOSITION PROCESS

We deposited the (80 ± 1) nm thick Ti thin film on substrates (20 × 20) mm. The substrates were cut out of p-type Si wafers with diameter of ≈ 100 mm, crystallographic orientation of [100], thickness of ≈ 375 µm, and specific resistivity in the range from ≈ 6 Ω·cm to ≈ 12 Ω·cm covered with SiO_2 layer deposited by plasma-enhanced chemical vapor deposition with a thickness of ≈ 200 nm. The Ti thickness was monitored by calibrated quartz crystal microbalance method during deposition process.

The Ti layers were deposited by the RFICP Kaufman ion-beam source (Kaufman & Robinson - KRI®) with an ≈ 4 cm diameter Mo 3-grid dished focused ion optics with an ≈ 45° ellipse pattern. We used an Ar ion-beam with purity of 99.99999% to provide the bombardment of a ≈ 100 mm × ≈ 100 mm Ti target with the purity of 99.995% under an incidence angle of ≈45°. Ion-beam space charge was reduced by KRI LFN 2000 charge neutralizer (KRI®). The vacuum chamber was evacuated to the pressure of $\approx 5{\cdot}10^{-7}$ Pa before each deposition process. To reach the required thin film parameters, we published earlier, we changed the beam voltage (BV) in the range from 200 V to 1200 V [17] and T was changed in the range from ≈ 105 °C to ≈ 295 °C [18].

2.2. BEAM VOLTAGE AND TEMPERATURE INFLUENCE

In the first series of experiment, we changed the BV value in the range from 200 V to 1200 V at the constant temperature of ≈ 105 °C which is given by the flux of deposited material. In the second series of experiment, the T was changed in the range from ≈ 105 °C to ≈ 295 °C with constant ion-beam source BV determined from the first series of experiment. Other corresponding parameters such as acceleration voltage, beam current, radio frequency power, Ar gas flow, and space charge neutralization were set according to the KRI® datasheet recommendations [19]. In the second series of experiment, we changed the T in the range from ≈ 105 °C to ≈ 295 °C.

We used XRD in the Bragg-Brentano (BB) setup with the 2θ angle ranging from 30° to 90° to perform the phase analysis of all Ti thin films. The interval from 60° to 78° was excluded to avoid the high intensity of Si 400 diffraction in this range. We detected diffraction peaks belonging to [100], [101] and [001] crystallographic planes. For [001] crystallographic plane, second order diffraction 002 and fourth order diffraction 004 were measured since the first order diffraction is forbidden. The corresponding X-ray diffractograms for different BV and for different *T* are showed in Figure 1A and Figure 1B, respectively.

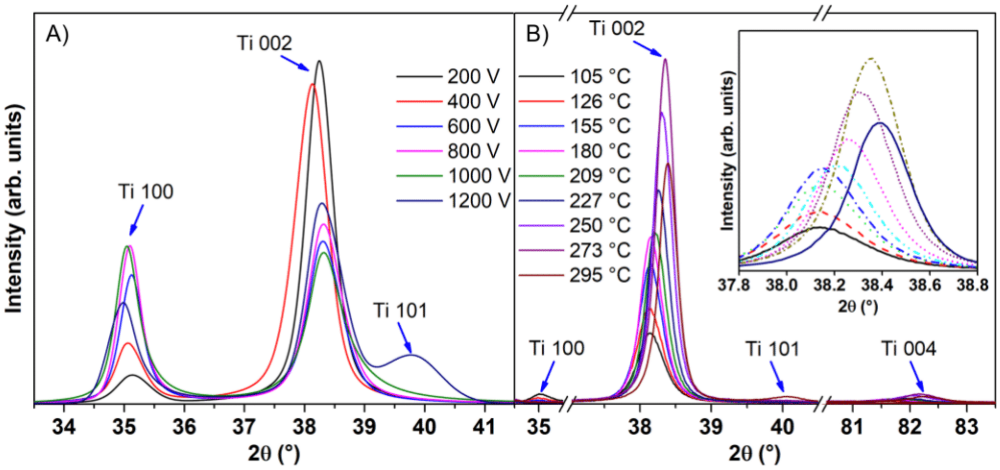

Figure 1: X-ray diffractograms in BB setup of deposited Ti thin films showing the influence: A) of different BV in the range from 200 V to 1200 V at constant *T* of ≈ 105 °C; B) different *T* in the range from ≈ 105 °C to ≈ 295 °C at constant BV of 200 V. The range from 60° to 78° was excluded due to Si 400 diffraction with intensity of several orders of magnitude higher than of the Ti diffraction peaks.

The obtained results for different BV (Figure 1A) show that there are changes in crystallography of deposited layers. In case of low BV of 200 V and 400 V, we achieved [001] preferential crystallographic orientation with small contribution of [100] planes parallel to the sample surface. On the other hand, the (100) contribution raised with higher BV, mainly in the range from 600 V to 1000 V. We also detected the small contribution of [101] plane orientation along with the [100] and [001] ones for the sample prepared at the highest BV of 1200 V.

Since the sample prepared at the lowest BV of 200 V had the [001] preferential orientation with the smallest compound of [100] orientation, we fixed this BV value and other ion-beam source parameters and changed the *T* (Figure 1B). The *T* has influence on peak shift, which corresponds, to residual-stress in thin film, which is described in the next chapter. We also found out that the increasing *T* towards to ≈ 273 °C has positive influence on X-ray diffraction intensity, [100] plane removing and peaks have lower full width at half maximum (FWHM). Only the sample prepared at ≈ 295 °C has higher FWHM and there was detected the small compound of [101] plane parallel to the sample surface. The FWHM value of stress-free sample was ≈ 0.27 °.

2.3. DETERMINATION OF RESIDUAL STRESS

We measured the residual stress σ_f as substrate curvature (Figure 2A) and we also calculated the in-plane σ_{xx} and the out-of-plane σ_{zz} residual stress (Figure 2A) using the determined lattice parameters from peak position (Figure 2B). In-plane lattice parameters *a* were determined from measurement using parallel beam setup and the out-of-plane lattice parameters *c* were determined from measurement in BB setup (Figure 1B). We presented this method for residual stress characterization earlier [18].

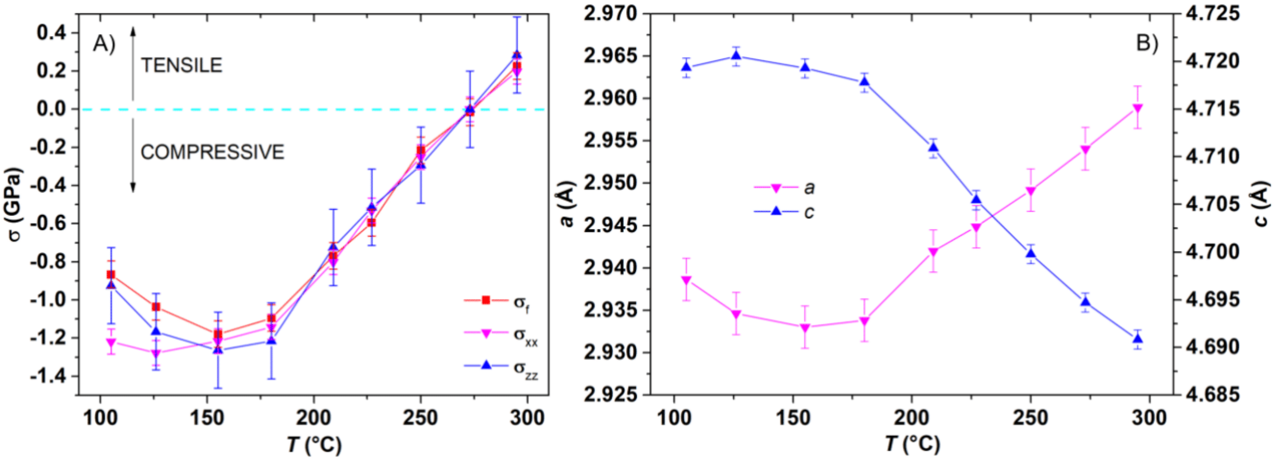

Figure 2: A) Stress dependence of measured σ_f and calculated σ_{xx}, σ_{zz}, values on *T*;
B) Dependence of measured *a* and *c* of deposited Ti thin films on *T*.

We found out that the Ti thin film deposited at BV = 200 V and $T \approx 273$ °C has the zero residual σ_f value within the experimental precision of ≈ 0.1 GPa with the corresponding $a_0 = (2.954 \pm 0.003)$ and $c_0 = (4.695 \pm 0.001)$ Å. From the Figure 2A is obvious that the calculated values of σ_{xx} and σ_{zz} are in good agreement with measured σ_f determined from independent curvature measurement. The compressive residual stress is reduced with increasing *T* towards to tensile stress reached for the sample prepared at the highest *T* of ≈ 295 °C. Only first and second sample have lower compressive stress then next one which could be due to different ratio of impurities which were not removed at low *T* [20].

2.4. DETERMINATION OF ELECTRICAL CONDUCTIVITY AND THERMAL COEFFICIENT OF RESISTIVITY

In case of demanded applications, we determined α and ρ to prove if the Ti thin films are useful for MEMS applications, where these electrical parameters are important for correct functionality. Both parameters were determined from measurement based on 4-probe method. We measured all samples 5× to get more accurate values. We determined the ρ from current-voltage curves, which were measured in the range from -0.5 V to 0.5 V at constant temperature of ≈ 22 °C. The α parameter was additionally extracted as slope of resistivity dependent on sample temperature in the range from ≈ 25 °C to ≈ 110 °C.

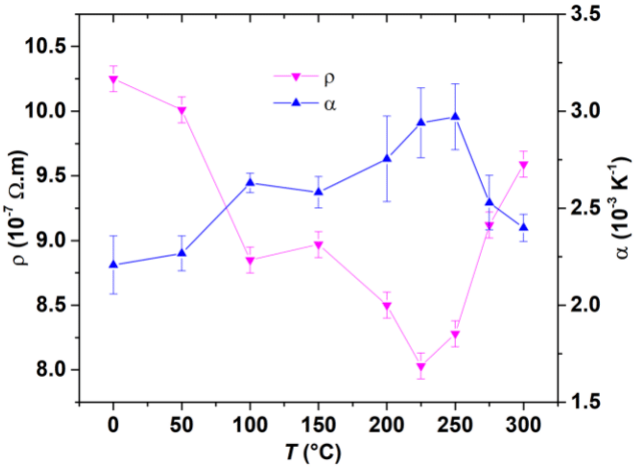

Figure 3: Determined values of α and ρ based on different *T* in the range from ≈ 105 °C to ≈ 295 °C at constant BV of 200 V.

Figure 3 shows that there is certain dependence of ρ and α parameters on temperature. Although, the XPS did not show different results for all samples, this could be probably influenced by certain amount of impurities in Ti thin films, as it is excellent getter material. Measured values of the ρ were in the range from $\approx 8.0 \cdot 10^{-7}$ Ω·m to $\approx 10.2 \cdot 10^{-7}$ Ω·m. It is obvious that values ρ and α dependent on each other. If the ρ is lower, the sample has also better value of α and on the contrary. We can define that the average value of ρ is ≈2× higher than the bulk material value, which is excellent for ≈ 80 nm thick layer. On the other side, the α was in the range from $\approx 2.3 \cdot 10^{-3}$ K^{-1} to $\approx 3.0 \cdot 10^{-3}$ K^{-1} which is reaching ≈ 71 % of bulk material value. This result is also good for such a thin film.

3. CONCLUSION

We presented a method to prepare the stress-free, pure [001] preferentially oriented Ti thin films with low ρ and good value of α deposited using the Kaufman ion-beam source. The experiments showed that BV and *T* have essential influence on crystallography, lattice parameters and residual stress of prepared Ti thin films.

The BV has significant influence on crystallography. All the samples have [001] orientation. We found that with increasing BV in the range from 200 V to 1200 V increases the presence of [100] towards to BV = 1200 V, where small contribution [101] plane is also present. The sample deposited at BV = 200 V shows only small presence of [100] plane along the [001]. We set constant ion-beam source settings for the next part of experiments where we changed the *T*.

We found that the *T* has essential influence on residual stress and obvious impact on crystallography. The compressive residual stress was reduced with increasing *T* from ≈ 150 °C towards the value of ≈ 295 °C where the tensile stress was reached. Samples deposited in the range of *T* from ≈ 155 °C to ≈ 273 °C show pure [001] orientation, while the sample deposited at ≈ 293 °C showed small contribution of [101] plane along the significant [001] plane. The stress-free sample was deposited at *T* ≈ 273 °C and had also the lowest FWHM of ≈ 0.27° and the highest diffraction peak. We determined the corresponding lattice parameters of this stress-free sample as $a_0 = (2.954 \pm 0.003)$ Å and $c_0 = (4.695 \pm 0.001)$ Å.

We measured the ρ and α electrical properties of all samples from second series. We obtained excellent results of electrical properties for ≈80 nm thick layer. The value of the ρ was in the range from $\approx 8.0 \cdot 10^{-7}$ Ω·m to $\approx 10.2 \cdot 10^{-7}$ Ω·m which is ≈ 2× higher than the bulk material value. The value of α was in the range from $\approx 2.3 \cdot 10^{-3}$ K^{-1} to $\approx 3.0 \cdot 10^{-3}$ K^{-1} reaching ≈ 71 % of bulk material value. These electrical parameters for stress-free sample with pure [001] orientation were $\rho = (9.2 \pm 0.1) \cdot 10^{-7}$ Ω·m and $\alpha = (2.6 \pm 0.2)$ K^{-1}.

The presented behavior and properties of Ti thin films especially the parameters of stress-free sample are attributed to deposition by the Kaufman ion-beam source at specific deposition conditions. These thin films are well suitable for MEMS applications. Furthermore, such a high quality properties are not achievable by the conventional magnetron sputtering technique.

ACKNOWLEDGEMENTS

We acknowledge the support of CEITEC Nano Research Infrastructure (ID LM2015041, MEYS CR, 2016–2019), CEITEC Brno University of Technology and Grant Agency of the Czech Republic under the contracts GA16-11140S and GACR 17-20716S. The work was also supported by Czech Ministry of Education, Youth and Sports of the Czech Republic under grant LO1401. For research, infrastructure of the SIX Center was used. Authors I. Gablech and J. Pekárek also acknowledge the foundation support FEKT/STI-J-17-4136.

REFERENCES

[1] CHAWLA, V., et al. Microstructural characterizations of magnetron sputtered Ti films on glass substrate. *Journal of Materials Processing Technology*, 2009, vol. 209, no. 7, pp. 3444-3451.

[2] CHEN, C.N., Fully quantitative characterization of CMOS-MEMS polysilicon/titanium thermopile infrared sensors. *Sensors and Actuators B-Chemical*, 2012, vol. 161, no. 1, pp. 892-900.

[3] DOLL, J.C., et al. Aluminum nitride on titanium for CMOS compatible piezoelectric transducers. *Journal of Micromechanics and Microengineering*, 2010, vol. 20, no. 2, pp. 8.

[4] LOPEZ, J.M., et al. Influence of oxygen on the morphological and structural properties of Ti thin films grown by ion beam-assisted deposition. *Thin Solid Films*, 2001, vol. 384, no. 1, pp. 69-75.

[5] TSUCHIYA, T., et al. Young's modulus, fracture strain, and tensile strength of sputtered titanium thin films. *Thin Solid Films*, 2005, vol. 484, no. 1-2, pp. 245-250.

[6] JACKSON, N., et al. Flexible-CMOS and biocompatible piezoelectric AlN material for MEMS applications. *Smart Materials and Structures*, 2013, vol. 22, no. 11, pp. 9.

[7] PEKÁREK, J., et al. Self-compensating method for bolometer–based IR focal plane arrays. *Sensors and Actuators A: Physical*, 2017, vol. 265, Supplement C, pp. 40-46.

[8] KHAN, Y., et al. Monitoring of Vital Signs with Flexible and Wearable Medical Devices. *Advanced Materials*, 2016, vol. 28, no. 22, pp. 4373-4395.

[9] KNISELY, K., et al. A MEMS AlN transducer array with flexible interconnections for use as a cochlear implant. *AIP Conference Proceedings*, 2015, vol. 1703, pp. 100004.

[10] URBAN, G., et al. Eurosensors 2015Fabrication, Simulation and Characterisation of MEMS Piezoelectric Vibration Energy Harvester for Low Frequency. *Procedia Engineering*, 2015, vol. 120, pp. 645-650.

[11] ASHRAF, M.W., et al. Micro Electromechanical Systems (MEMS) Based Microfluidic Devices for Biomedical Applications. *International Journal of Molecular Sciences*, 2011, vol. 12, no. 6, pp. 3648-3704.

[12] KERN, W., et al. *Handbook of Thin Film Deposition Processes and Techniques*. New York: William Andrew Publishing, 2001, pp. 30-35.

[13] CHANG, R.C., et al. Residual Stresses of Sputtering Titanium Thin Films at Various Substrate Temperatures. *Journal of Nanoscience and Nanotechnology*, 2010, vol. 10, no. 7, pp. 4562-4567.

[14] KHAN, M., et al. Residual strain and electrical resistivity dependence of molybdenum films on DC plasma magnetron sputtering conditions. *Materials Science in Semiconductor Processing*, 2014, vol. 27, pp. 343-351.

[15] SEO, H.-C., et al. Elastic buckling of AlN ribbons on elastomeric substrate. *Applied Physics Letters*, 2009, vol. 94, no. 9, pp. 092104.

[16] GABLECH, I., et al. Influence of Underlayer on Crystallography and Roughness of Aluminum Nitride Thin Film Reactively Sputtered by Ion-Beam Kaufman Source. In *Nanocon 2015: 7th International Conference on Nanomaterials - Research & Application.* Ostrava: TANGER, 2015, pp. 89-93.

[17] GABLECH, I., et al. Preparation of (001) preferentially oriented titanium thin films by ion-beam sputtering deposition on thermal silicon dioxide. *Journal of Materials Science*, 2016, vol. 51, no. 7, pp. 3329-3336.

[18] GABLECH, I., et al. Stress-free deposition of [001] preferentially oriented titanium thin film by Kaufman ion-beam source. *Thin Solid Films*, 2017, vol. 638, pp. 57-62.

[19] CATALOG THE KAUFMAN & ROBINSON INC. RFICP 40 ion optics supplement: Molybdenum Three-Grid Dished Focused 4-cm Diameter 45° Ellipse. 2013.

[20] HEDAIATMOFIDI, H., et al. Deposition of Titanium Layer on Steel Substrate Using PECVD Method: A Parametric Study. *Materials Sciences and Applications*, 2014, vol. 5, no. 3, pp. 140-148.

6 Influence of underlayer on aluminum nitride quality

6.1 Motivation of the article

Motivation for this article was based on previously studied literature where was mainly described the influence of underlayer on AlN growth. Since the Ti was chosen I wanted to compare and prove the influence of different underlayers such as (001) preferentially oriented Ti underlayer, (100) Si substrate and amorphous SiO_2 on (100) Si substrate.

Deposition of AlN is much complicated than deposition of other metals because it consists of aluminum and nitrogen which must be bind in good ratio. The deposition was provided by reactive sputtering using the same deposition source as before and 5N Al target. There are much more parameters than only ion-beam energy and deposition temperature which must be controlled and optimized. Therefore, I was working on the Ti layer optimization and simultaneously I started with simple experiments on influence of underlayer on AlN quality.

6.2 Conclusion on the article

This paper proves that underlayer has an important role and the underlayer for AlN must be selected carefully which was the main aim. The best results from the view of crystallography and roughness were observed on AlN deposited on Ti underlayer. This paper was basis for next complex manuscript about AlN preparation. These results were not taken account residual stress which is described later.

6.3 Contribution

I did all depositions and measurements. I also contributed to the analysis of the results and to the writing of the manuscript.

6.4 Article 4

The article **Influence of underlayer on crystallography and roughness of aluminum nitride thin film reactively sputtered by ion-beam Kaufman source** [56] was published in proceedings of the international WOS indexed conference **NANOCON 2015** in **October 2015.**

Influence of Underlayer on Crystallography and Roughness of Aluminum Nitride Thin Film Reactively Sputtered by Ion-Beam Kaufman Source

GABLECH Imrich[1,2*], SVATOŠ Vojtěch[1,2], PRÁŠEK Jan[1,2], HUBÁLEK Jaromír[1,2]

[1] Central European Institute of Technology, Brno University of Technology, Brno, Czech Republic, EU
[2] Brno University of Technology, Faculty of Electrical Engineering and Communication, Department of Microelectronics, Brno, Czech Republic, EU

**imrich.gablech@ceitec.vutbr.cz*

Abstract

This paper deals with deposition of aluminum nitride layer on different underlayers namely silicon (100), amorphous thermal silicon dioxide, and titanium (001). The aluminum nitride layer was deposited using 3-grid radio frequency inductive coupled plasma (RFICP) Kaufman ion-beam source which provides slow deposition rate with low energy of plasma ions. This possibility leads to high homogeneity and very smooth surface. Titanium layer was deposited by argon plasma at low energy of 200 eV to attain the highly oriented c-axis layer. The aluminum nitride was sputtered on substrate which was heated to 350 °C. The nitrogen plasma only at energy of 500 eV was used. It was observed the aluminum nitride deposited on thermal silicon dioxide has the highest root mean square of roughness (R_{RMS}) = 1.49 nm and the lowest intensity of X-ray diffraction in Bragg-Brentano focusing geometry (XRD–BB). The aluminum nitride deposited on silicon (100) shows higher intensity of XRD–BB and the lowest R_{RMS} = 0.48 nm. Although the R_{RMS} = 0.66 nm of aluminum nitride thin film deposited on titanium (001) underlayer was obtained, the highest intensity of XRD–BB was observed. Azimuthally averaged intensity of pole figures obtained using parallel beam setup represents the information about misorientation of individual crystallites. These analyses were performed for aluminum nitride layers deposited on titanium (001) film and silicon (100) wafer. Misorientation determined from full width at half maximum (FWHM) of the pole figures was of about 0.5° lower for aluminum nitride thin film deposited on titanium underlayer than one deposited directly on silicon substrate without silicon dioxide.

Keywords: Aluminum Nitride, Titanium, c-axis orientation, Kaufman ion-beam source, reactive sputtering, AFM, XRD

1. INTRODUCTION

Aluminum nitride (AlN) has attracted considerable huge attention as a piezoelectric layer in numerous MEMS devices such as actuators, sensors, and transducers [1,2]. The significant advantage of AlN film is its compatibility with CMOS technology [3]. Because the AlN is not ferroelectric material it does not require poling unlike the lead zirconate titanate (PZT) as another CMOS technology compatible piezoelectric material [4]. Aluminum nitride shows other extraordinary properties such as dielectric properties connected to wide band-gap, mechanical stiffness, high elasticity, high thermal conductivity, and low thermal expansion coefficient [5].

There have been published a number of papers dealing with the optimizing of its piezoelectric behavior. The characterization of piezoelectric material is important to be performed under the conditions of selected application [6]. For example the piezoelectric coefficient of aluminum nitride thin film is dependent on its surface roughness and grain size. Furthermore, the crucial parameter affecting AlN thin film properties and growth is a suitable underlayer [7]. In most microdevices, there are many materials which are suitable to be used as a bottom electrode for subsequent deposition of AlN film due to their hexagonal orientation for growth of wurtzite, e.g. Al (111), Pt (001), Ti (001), and Mo (110). The titanium electrode is also ideal because the lattice mismatch with aluminum nitride is comparable [5].

The conventional methods of AlN layer deposition are sputtering (e.g. radio frequency magnetron sputtering or ion-beam assisted deposition), metalorganic chemical vapor deposition (MOCVD), plasma enhanced chemical vapor deposition (PECVD), molecular beam epitaxy (MBE), and atomic layer deposition (ALD) [2,8].

In this paper, the aluminum nitride layer is deposited by ion-beam reactive sputtering which concludes to smoother layer than other conventional sputtering techniques. Three various possible underlayers for AlN thin film are investigated in terms of crystallographic orientation, average crystallite size, misorientation of individual crystallites, and roughness of layer surface.

2. EXPERIMENTAL

2.1. Deposition Processes

All depositions of AlN were performed on pieces of silicon wafer (20 x 20 mm) substrates (P-type with the (100) crystallographic plane parallel to surface and resistivity 6-12 Ω.cm) with different types of underlayer. AlN deposition was performed on silicon substrate with native oxide only, silicon substrate with 1 μm thick thermal silicon dioxide , and on titanium layer with (001) crystallographic plane parallel to the surface sputtered on silicon substrate (100) covered by 1 μm thick thermal silicon dioxide as mentioned below.

Before the sputtering deposition process, the silicon substrate with native oxide only was dipped in standard buffered oxide etchant (49% HF + 40% NH_4F in the 6:1 volume ratio) for 1 minute to remove native oxide. Substrates with thermal silicon dioxide were cleaned in the standard piranha solution (96% H_2SO_4 + 30% H_2O_2 in the 3:1 volume ratio) for 3 minutes, rinsed in deionized water and dried with compressed nitrogen.

The RFICP Kaufman ion-beam source with 3-grid focused ion optics was used for deposition. A titanium target with a purity of 99.995% and argon gas with a purity of 99.9996% were used for titanium deposition. Aluminum nitride was reactively sputtered by pure nitrogen plasma without presence of argon. The purity of nitrogen was 99.9999% and the purity of aluminum target was 99.995%. The sputtering chamber was pumped down to a pressure of $5 \cdot 10^{-9}$ mbar before start of deposition process.

2.2. Diagnostics methods

SmarLab (Rigaku) X-ray diffractometer (XRD) with a linear D/tex detector was employed to perform crystallography analysis in Bragg-Brentano focusing geometry. Pole figure analysis was performed with parallel beam setup. The surface topography and roughness (R_{RMS}) of deposited layers were determined using Atomic Force Microscopy (AFM) Dimension Icon (Bruker) in the ScanAsyst® mode.

3. RESULTS AND DISCUSSION

3.1. Titanium underlayer

Deposition of 100 nm thick titanium underlayer was performed on amorphous thermal silicon dioxide with very low energy of ions (200 eV), and low deposition rate of 0.04 Å/s. From X-ray diffractogram (Figure 1a) it is clear that only (001) preferential crystallographic orientation of the crystallites was obtained. Full width at half maximum (FWHM) of diffraction peak was 0.45°. Average crystallite size of 21 nm was calculated according to Scherrer equation. Smooth titanium surface topography of 0.55 R_{RMS} and its corresponding profile are depicted in Figure 1b and Figure 1c respectively.

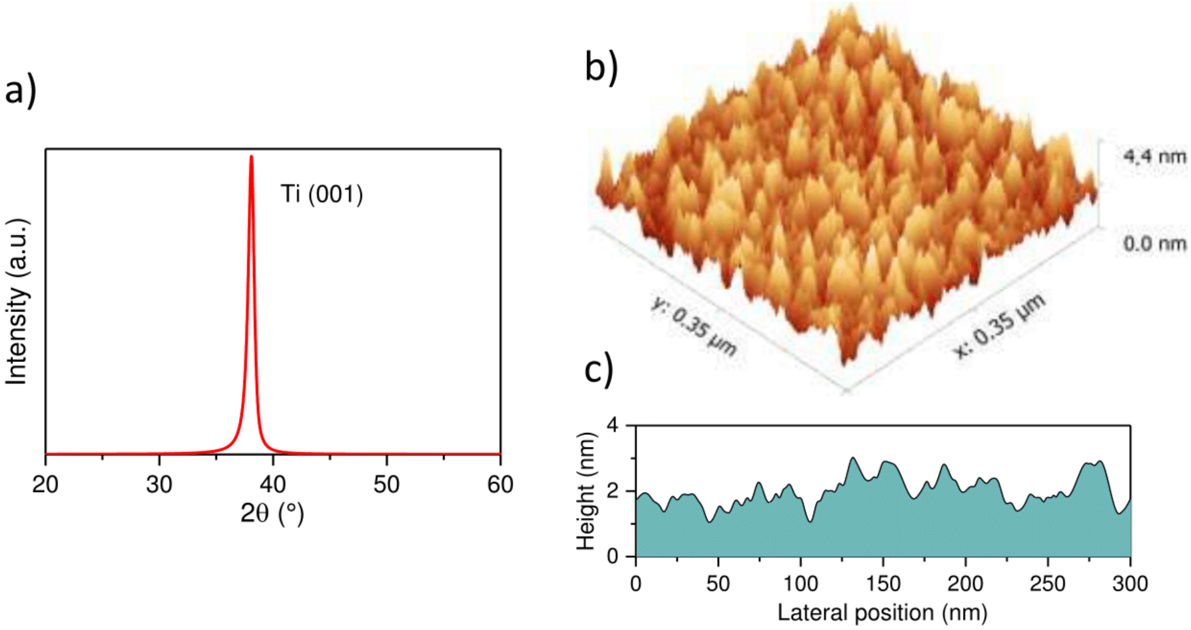

Fig. 1 XRD and AFM diagnostics of titanium thin film deposited by argon plasma low energy ions (200 eV); a) X-ray diffractogram showing titanium (001) preferential crystallographic orientation; b) surface topography of Ti layer deposited on thermal silicon dioxide; c) surface profile corresponding to the surface topography measurement shown in b).

As the high deposition temperature (up to 400 °C) of subsequent films is required the deposited titanium layer was exposed to 2 hours annealing peak process in vacuum chamber pumped down to $5{\cdot}10^{-7}$ mbar with heating and cooling rate of 5 °C/min up to 400 °C. X-ray diffractogram of annealed thin film (see Figure 2) confirms that the peak of (001) crystallographic plane is without any changes.

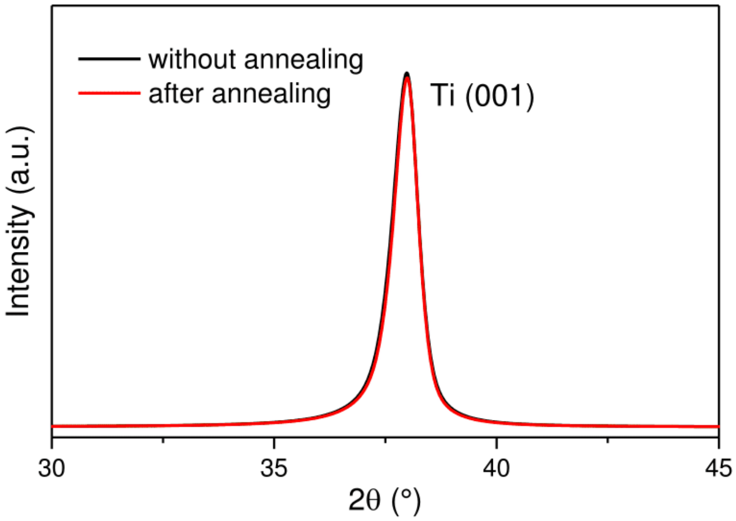

Fig. 2 X-ray diffractogram of titanium (001) before and after 2 hours annealing up to 400 °C.

3.2. Reactive sputtering of aluminum nitride

Aluminum nitride was deposited on three different underlayers with different crystallography: Si (100) with face-centered cubic lattice, the amorphous silicon dioxide and titanium (001) with hexagonal close-packed structure with cell parameters very similar to aluminum nitride. To ensure the same deposition conditions, the sputtering onto all three layers were done simultaneously in one process. Thickness of deposited AlN layer was 200 nm and deposition rate was 0.17 Å/s. During this process the substrate was heated up to 350 °C. Energy of bombarding nitrogen ions was set to be 500 eV. XRD and AFM analyses of this layer are shown in Figures 3a, 3b and 3c.

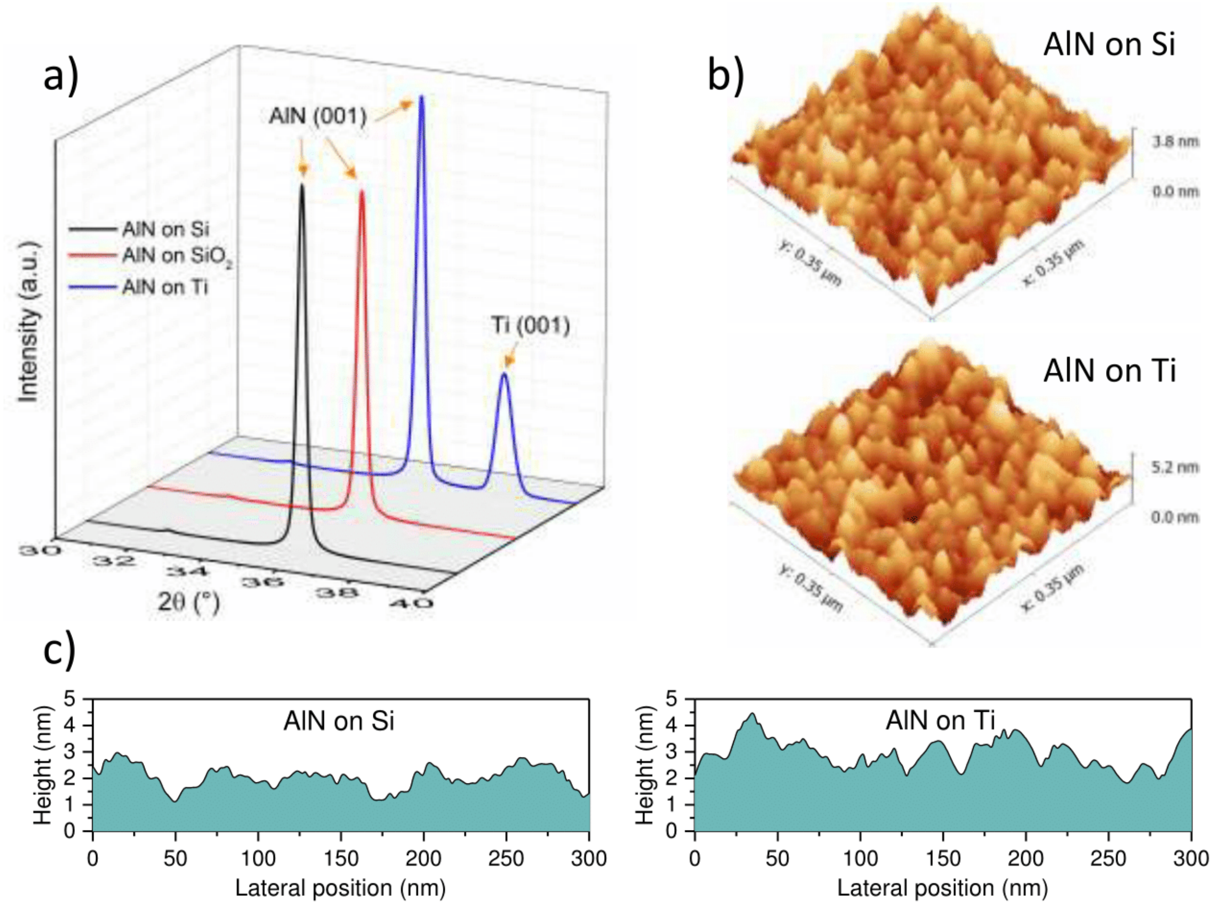

Fig. 3 XRD and AFM analyses of deposited AlN layers by pure nitrogen plasma with substrate heated to 350 °C; a) X-ray diffractograms of AlN thin film deposited on different underlayers showing only presence of (001) preferential crystallographic orientation; b) surface topography of AlN thin film layer deposited on Ti (001) underlayer and AlN thin film deposited directly on silicon wafer (100); c) surface profiles corresponding to the AFM surface topographies shown in b).

In Figure 3a, the highest diffraction peak of aluminum nitride layer (FWHM = 0.266°; crystallite size = 32.8 nm) deposited over titanium underlayer is evident. This layer has smooth surface with R_{RMS} = 0.66 nm (see Figure 3b and 3c). The lowest peak (see Figure 3a) and the highest R_{RMS} = 1.49 nm was achieved for aluminum nitride layer (FWHM = 0.262°; crystallite size = 33.3 nm) deposited on thermal amorphous silicon dioxide (see Figure 3b and 3c.). Aluminum nitride layer (FWHM = 0.252; crystallite size = 34.9 nm) deposited directly on polished silicon wafer (100) without native oxide has higher peak (see Figure 3a) than previously mentioned layer and the smoothest surface with R_{RMS} = 0.48 nm (see Figure 3b and 3c).

The pole figure orientation analysis of (001) crystallographic plane was performed for aluminum nitride on silicon and titanium underlayers to determine misorientation of individual crystallites. From the azimuthally averaged intensity of pole figure (see Figure 4), it is clear the misorientation of AlN crystallites on titanium underlayer is lower (FWHM = 4°) than on silicon (100) substrate without silicon dioxide (FWHM = 4.5°).

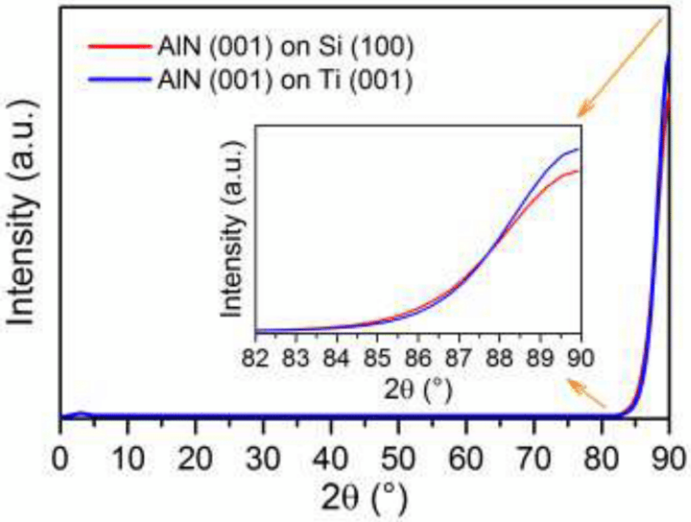

Fig 4. Azimuthally averaged intensity profiles extracted from pole figures for AlN (001) crystallographic plane deposited on Ti (001) underlayer and for AlN (001) crystallographic plane deposited directly on silicon wafer (100) without silicon dioxide.

CONCLUSION

In this paper, the influence of underlayer material on deposited aluminum nitride crystallography and roughness is described. In case of silicon dioxide underlayer, the lowest diffraction peak and the highest roughness of 1.49 nm was reached. Despite of deposition on the pure silicon wafer (100) the aluminum nitride thin film grows in c-axis direction. This layer has the lowest roughness of 0.48 nm and slightly higher intensity of diffraction peak than the layer deposited on silicon dioxide. Aluminum nitride layer deposited over titanium underlayer has the highest diffraction peak and negligibly higher roughness of 0.66 nm. On the other side, aluminum nitride layer deposited on titanium layer has according to the pole figure 0.5° smaller misorientation (FWHM = 4°) compared to the aluminum nitride layer deposited directly on pure silicon wafer (FWHM = 4.5°). Titanium underlayer proves to be excellent as bottom electrode due to its lattice parameters similar to aluminum nitride lattice which is obvious from azimuthally averaged intensity obtained from pole figure of (001) plane diffraction.

ACKNOWLEDGEMENTS

Research described in this paper was financed by the National Sustainability Program under grant LO1401. The work was also carried out with the support of the CEITEC Nano Core Facility under the CEITEC – open access project, ID number LM2011020, funded by the Ministry of Education, Youth and Sports of the Czech Republic under the activity „Projects of major infrastructures for research, development and innovations". For the research, infrastructure of the SIX Center was used.

REFERENCES

[1] POLLA, D. L. a FRANCIS, L. F. Processing and characterization of piezoelectric materials and integration into microelectromechanical systems. *Annual Review of Materials Science*, 1998, vol. 28, pp. 563-597. ISSN 0084-6600.

[2] SARAVANAN, S. et al. *Surface Micromachining Process for the Integration of AlN Piezoelectric Microstructures*. SAFE 2004, 7th Annual Workshop on Semiconductor Advances for Future Electronics. 2004. 9789073461437. Veldhoven, the Netherlands public.

[3] ABABNEH, A. et al. c-axis orientation and piezoelectric coefficients of AlN thin films sputter-deposited on titanium bottom electrodes. *Applied Surface Science*, 2012, vol. 259, pp. 59-65. ISSN 0169-4332.

[4] JACKSON, N. et al. Flexible-CMOS and biocompatible piezoelectric AlN material for MEMS applications. *Smart Materials and Structures*, 2013, vol. 22, no. 11. ISSN 0964-1726.

[5] DOLL, J. C. et al. Aluminum nitride on titanium for CMOS compatible piezoelectric transducers. *Journal of Micromechanics and Microengineering*, 2010, vol. 20, no. 2. ISSN 0960-1317.

[6] AL AHMAD, M. a PLANA, R. Piezoelectric Coefficients of Thin Film Aluminum Nitride Characterizations Using Capacitance Measurements. *Ieee Microwave and Wireless Components Letters*, 2009, vol. 19, no. 3, pp. 140-142. ISSN 1531-1309.

[7] IRIARTE, G. F. et al. Influence of substrate crystallography on the room temperature synthesis of AlN thin films by reactive sputtering. *Applied Surface Science*, 2011, vol. 257, no. 22, pp. 9306-9313. ISSN 0169-4332.

[8] FIGUEROA, U. et al. Production of AlN films: ion nitriding versus PVD coating. *Thin Solid Films*, 2004, vol. 469, pp. 295-303. ISSN 0040-6090.

7 Preparation of aluminum nitride piezoelectric layer

7.1 Motivation of the article

This article forms the main part of my research because high quality AlN is necessary for correct function of fabricated devices. AlN or AlN-based material is practically the only one material which can be prepared using PVD method and possess the utilization for applications where CMOS and biocompatibility are desirable. AlN is very modern material due to previously mentioned properties despite of its low value of d_{33} piezoelectric coefficient in comparison to other materials such as ZnO or PZT which are not compatible with CMOS technology. Fabrication of these materials often requires high temperatures and/or they are not compatible with a lot of instruments due to a risk of contamination.

In general, deposition parameters must be monitored and controlled because they have influence on several parameters such as the crystal orientation, misorientation of individual crystallites and average size of coherently diffracting domains which directly affect the value of d_{33} piezoelectric coefficient. On the other side, there are more important parameters such as residual stress, band-gap and surface roughness which are also important for functionality of fabricated device.

7.2 Conclusion on the article

This manuscript complexly describes preparation of AlN using dual RFICP Kaufman ion-beam source setup. Obtained results show influence of most significant parameters during deposition such as underlayer, ion-beam energy, deposition temperature, Ar : N_2 gas ratio in both ion-beam sources, pre- and *in situ* cleaning using secondary RFICP Kaufman ion-beam source. All these parameters were analyzed and it was described how to prepare high quality stress-free AlN for MEMS applications which is the most crucial part in this doctoral thesis. Furthermore, such prepared and optimized layer using PVD technique has higher quality in comparison to other layers mentioned in other literature. Fabricated diamond ring structure for optical display of stress is shown at the end of the manuscript. This suspended structure is ≈ 1 mm long and there is no evident buckling which proves the excellent quality of deposited AlN thin films.

7.3 Contribution

I deposited all thin films. I also did XRD measurements in Bragg-Brentano and Parallel beam setups and all AFM analyses. I measured d_{33} piezoelectric coefficient. I also did few ellipsometry measurements and scanning electron microscope (SEM) images and contributed to the writing of the manuscript.

7.4 Article 5

Article **Preparation of high-quality stress-free (001) aluminum nitride thin film using dual Kaufman ion-beam source setup** is under review in **Thin Solid Films** (2017 IF 1.939).

Elsevier Editorial System(tm) for Thin Solid Films
Manuscript Draft

Manuscript Number: TSF-D-18-01013

Title: Preparation of high-quality stress-free (001) aluminum nitride thin film using dual Kaufman ion-beam source setup

Article Type: Full Length Article

Section/Category: B. Surfaces, Interfaces, and Colloidal Behaviour

Keywords: Ion-beam sputtering deposition, Kaufman ion-beam source, aluminum nitride thin film, (001) preferential orientation, XRD, optical properties, ellipsometry, d33 piezoelectric coefficient

Corresponding Author: Mr. Imrich Gablech, Ing.

Corresponding Author's Institution: Brno University of Technology

First Author: Imrich Gablech, Ing.

Order of Authors: Imrich Gablech, Ing.; Vojtěch Svatoš; Ondřej Caha, Ph.D.; Adam Dubroka, Assoc. Prof.; Jan Pekárek, Ph.D.; Jaroslav Klempa; Pavel Neužil, Assoc. Prof.; Michael Schneider, Ph.D.; Tomáš Šikola, Prof.

Abstract: We proposed and demonstrated a preparation method of (001) preferentially oriented stress-free AlN piezoelectric thin films. The AlN thin films were deposited by the reactive sputtering technique at substrate temperatures up to 330 °C using a dual Kaufman ion-beam source setup. We deposited the AlN on Si (100), Si (111), amorphous SiO_2, and a (001) preferentially oriented Ti thin film and compared their crystallographic, optical, and piezoelectric properties. The AlN thin films deposited on the (001) preferentially oriented Ti thin films has the highest crystallographic quality. The stress-free AlN reached a high value of the piezoelectric coefficient $d_{33} = (7.33 \pm 0.08)$ $pC \cdot N^{-1}$. The properties of the AlN thin film prepared at such low temperatures are suitable for numerous microelectromechanical systems, piezoelectric sensors and actuators monolithically integrated with complementary metal-oxide-semiconductor signal processing circuits.

Suggested Reviewers: Jürgen Gerlach
Physical Department, Leibniz Institute of Surface Modification
juergen.gerlach@iom-leipzig.de
Nanostructures and thin film specialist.

Jarsolav Sobota
Institute of Scientific Instruments, The Czech Academy of Sciences
sobota@isibrno.cz
Specialist in thin film technology.

Jaap van den Berg
International Institute for Accelerator Applications, University of Huddersfield
j.vandenberg@hud.ac.uk
Professor of Ion Beam Physics.

Preparation of high-quality stress-free (001) aluminum nitride thin film using dual Kaufman ion-beam source setup

Imrich GABLECH[1,2*], Vojtěch SVATOŠ[1,2], Ondřej CAHA[3,4],
Adam DUBROKA[3,4], Jan PEKÁREK[1,2], Jaroslav KLEMPA[1,2],
Pavel NEUŽIL[1,2,5], Michael SCHNEIDER[6], Tomáš ŠIKOLA[1,7]

1 *Central European Institute of Technology, Brno University of Technology, Technická 3058/10, 61600 Brno, Czech Republic*

2 *Brno University of Technology, Faculty of Electrical Engineering and Communication, SIX Centre, Department of Microelectronics, Technická 3058/10, 61600 Brno, Czech Republic*

3 *Central European Institute of Technology, Masaryk University, Kamenice 753/5, 62500 Brno, Czech Republic*

4 *Masaryk University, Faculty of Science, Department of Condensed Matter Physics, Kotlářská 2, 60200 Brno, Czech Republic*

5 *Northwestern Polytechnical University, 127 West Youyi Road, Xi'an, Shaanxi, P.R. China*

6 *Department of Microsystems Technology, Vienna University of Technology, Floragasse 7, 1040 Vienna, Austria*

7 *Brno University of Technology, Institute of Physical Engineering, Technická 2896/2, 61669 Brno, Czech Republic*

*imrich.gablech@ceitec.vutbr.cz

Abstract

We proposed and demonstrated a preparation method of (001) preferentially oriented stress-free AlN piezoelectric thin films. The AlN thin films were deposited by the reactive sputtering technique at substrate temperatures up to 330 °C using a dual Kaufman ion-beam source setup. We deposited the AlN on Si (100), Si (111), amorphous SiO_2, and a (001) preferentially oriented Ti thin film and compared their crystallographic, optical, and piezoelectric properties. The AlN thin films deposited on the (001) preferentially oriented Ti thin films has the highest crystallographic quality. The stress-free AlN reached a high value of the piezoelectric coefficient $d_{33} = (7.33 \pm 0.08)\ \mathrm{pC \cdot N^{-1}}$. The properties of the AlN thin film prepared at such low temperatures are suitable for numerous microelectromechanical systems, piezoelectric sensors and actuators monolithically integrated with complementary metal-oxide-semiconductor signal processing circuits.

Keywords

Ion-beam sputtering deposition, Kaufman ion-beam source, aluminum nitride thin film, (001) preferential orientation, XRD, optical properties, ellipsometry, d_{33} piezoelectric coefficient

1. Introduction

Piezoelectric materials have a huge potential in numerous common applications. Lead zirconate titanate (PZT), quartz, lithium niobate, lithium tantalate, aluminum nitride (AlN), or zinc oxide (ZnO) is generally used [1-4]. They often have to be integrated with complementary metal-oxide-semiconductor (CMOS) devices. The crucial requirement for this technology is to deposit thin films at substrate temperatures below 450 °C using, for instance, techniques such as physical vapor deposition. AlN is a CMOS-compatible material, thus eliminating the contamination risk of the fabrication line compared with PZT and ZnO [5, 6]. AlN is also popular due to its bio-compatibility [7].

The AlN thin films have been already employed in various technical fields as an insulator and a passivation layer for thin film applications [8, 9], as energy harvesters [10, 11], mass sensors [12-15], acoustic sensors [16, 17], wave guides [18], optoelectronic devices [19, 20], tunable resonators [21], and many others. Excluding the piezoelectricity, there are some extraordinary properties of AlN thin films such as high thermal conductivity (320 $\mathrm{W \cdot mK^{-1}}$ at a temperature of 300 K), low thermal expansion coefficient at high temperatures, wide bandgap (6.2 eV), and high electric resistance (10^{13} $\Omega\cdot$cm), which results in a relatively high dielectric constant, mechanical stiffness, and high elasticity [22-24]. The AlN thin film is typically a wurtzite structured material and shows the major piezoelectric response along (001) direction, usually with the piezoelectric coefficient up to 6 $\mathrm{pC \cdot N^{-1}}$ [24, 25]. The piezoelectric coefficients of AlN are highly dependent on the crystal orientation and its misorientation, which is possible to modify at temperatures above 1000 °C [26, 27] after the deposition process is complete.

Numerous techniques of AlN deposition were previously employed. They can be sorted into two major groups. The first one uses a high deposition substrate temperature up to 1000 °C and the second one uses a lower substrate temperature. The first group contains deposition methods such as metalorganic chemical vapor deposition (MOCVD) [28-30], molecular beam epitaxy [31], and hydride vapor phase epitaxy [32]. The second one consists of methods such as reactive sputtering and evaporation, often assisted with ion-beam [33], pulsed laser deposition [34, 35], and plasma enhanced atomic layer deposition [36]. The piezoelectric properties and internal stress are sensitive to deposition process parameters [27].

In the presented study, we investigated AlN thin films with (001) preferential crystallographic orientation deposited on Si (100), Si (111), amorphous SiO_2, and a (001) preferentially oriented Ti thin film and compared their properties for various deposition conditions. All thin films presented in this report were deposited by a Kaufman ion-beam source (IBS) utilizing radio frequency inductively coupled plasma (RFICP) and, optionally, a secondary RFICP Kaufman IBS. We controlled the deposition substrate temperature in the range from 100 °C to 340 °C. We also varied the ion-beam current and its energy, which affected the kinetic energy of atoms of the sputtered material and deposition rate. We determined the material properties such as crystallographic parameters, residual stress, optical properties, and piezoelectric coefficient.

2. Experimental details

2.1. Aluminum nitride deposition process

We deposited 200 nm AlN thin films on square-shaped substrates with a size of 20 mm x 20 mm diced from silicon wafers with a diameter of 100 mm and thickness of 525 µm. The deposition was performed on four different Si wafers: two bare wafers Si (111) and Si (100), Si (100) wafer covered with an amorphous layer of SiO_2 with a thickness of 100 nm, and the same one covered with a layer of (001) preferentially oriented Ti [37, 38] with a thickness of 80 nm. All the substrates were pre-cleaned prior the actual deposition by Ar ion bombardment from the secondary RFICP Kaufman IBS with a 2-grid µ-dished collimated ion optics with a diameter of 40 mm. The pre-cleaning parameters were set as follows: ion-beam energy (BE) - 30 eV, ion-beam current (BC) - 15 mA, and sputter time - 180 s.

All thin films were deposited either by using the primary RFICP Kaufman IBS with a 3-grid dished focused ion optics (4 cm in diameter and with 45° ellipse pattern) only, or by concurrent using the primary and secondary IBS for the ion-beam assisted deposition (IBAD) described above (Fig. 1).

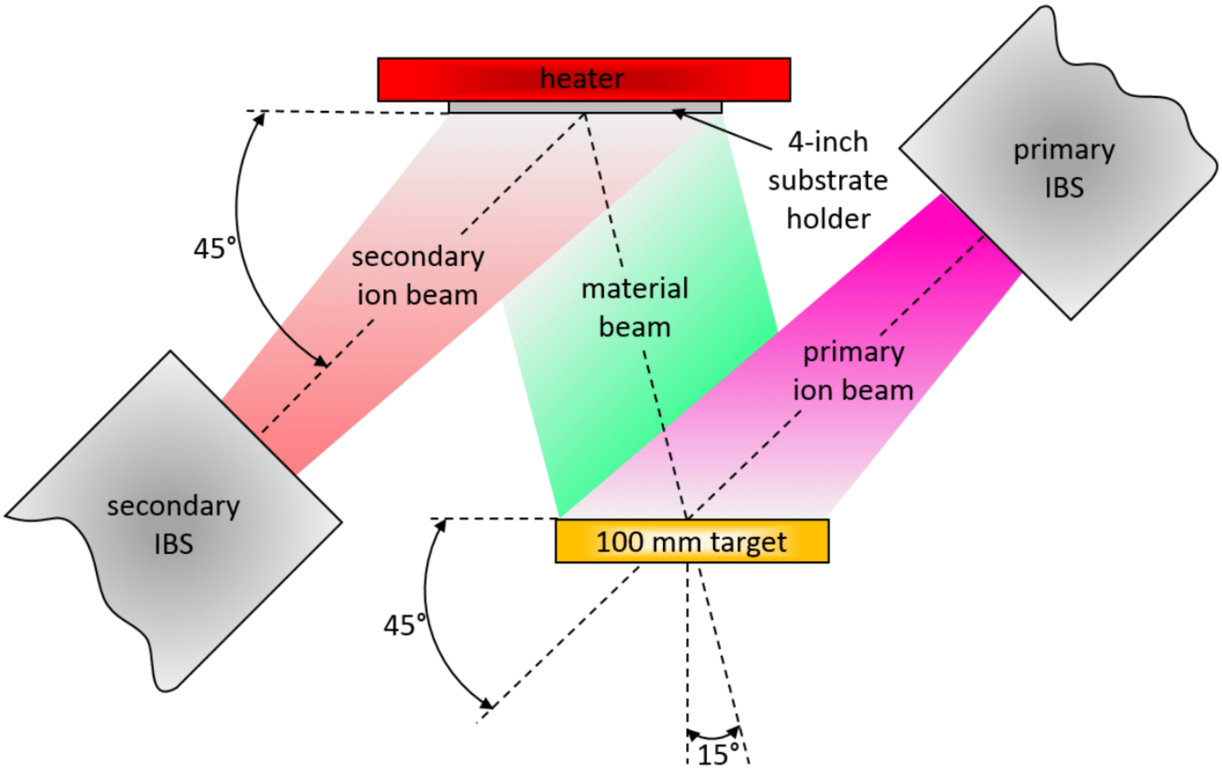

Fig. 1: Schematic of sputtering apparatus geometry with Kaufman ion-beam sources

We used an aluminum square-shaped target with a size of 100 mm x 100 mm and 5N purity for AlN deposition by Ar sputtering assisted with N_2 or Ar gas or their mixtures, both gases with 7N purity. The deposition parameters are listed in Tab. 1. Reduction of the ion-beam space charge was achieved by a KRI LFN 2000 charge neutralizer (KRI®). The sputtering chamber was evacuated to the base pressure of $5 \cdot 10^{-7}$ Pa by a turbomolecular pump with a pumping speed of $1200\ \mathrm{l \cdot s^{-1}}$ backed by a dry scroll vacuum pump. The process pressure was in the range from $8.5 \cdot 10^{-3}$ Pa to $1.5 \cdot 10^{-2}$ Pa. We monitored the AlN deposition rate and film thickness *in situ* using a quartz crystal sensor. Finally, the thickness was verified *ex situ* by ellipsometry and the average thickness was (195.9 ± 8.2) nm. We employed atomic force microscopy (AFM) using a Dimension Icon, Bruker, for surface roughness measurement. The surface roughness of all deposited AlN films was investigated in the ScanAsyst® – air measuring mode of AFM. The average surface roughness of all samples was (1.2 ± 0.3) nm with no evident dependence on the deposition parameters.

Tab. 1: Description of the deposition parameters

	Primary IBS				Secondary IBS				
Experiment series	BE (eV)	BC (mA)	Ar flow (sccm)	N_2 flow (sccm)	BE (eV)	BC (mA)	Ar flow (sccm)	N_2 flow (sccm)	*T* (ºC)
1	1200	65	0	8.0	IBS OFF				100 150 200 250 300
	1000	50		6.5					
	800	36		6.0					
	600	23		5.5					
	500	18		5.2					
	400	13		5.0					
2	400	13	0	5.0	20	6	10	0	330
							0	10	
					30	7	10	0	340
							0	10	
3	400	13	0	5.0	20	6	0	10	330
			1.5	3.5					
			2.5	2.5					
			3.5	1.5					
			5.0	0					

2.2. XRD methods

We characterized the deposited AlN thin films using four X-ray diffraction methods [37]. The first three methods were carried out by a Rigaku SmartLab system with a Cu X-ray tube containing a linear D/teX Ultra detector. The fourth method was conducted by a home-assembled diffractometer with a Cu X-ray tube, Bartels-type Ge 4×(220) monochromator, and scintillation detector.

The first method was based on the Bragg–Brentano (BB) geometry used to determine the lattice parameter of the planes parallel to the sample surface.

The second one, the grazing-incidence (GIXRD) method, was then used to measure the lattice parameter in the perpendicular direction to the sample surface. This in-plane measurement employed a parabolic multilayer mirror as a monochromator and parallel plate collimators with a divergence of 0.15º and 0.11º in the incident and scattered beam, respectively.

The third method was the rocking curve (RC) measurement in a standard parallel-beam (PB) setup using a 0.114° parallel slit analyzer. We fitted the measured data by the Rigaku PDXL2 software version 2.6.1.2.

The fourth method was used to extract the elastic stress σ_f of deposited AlN thin films. The stress was determined from the curvature difference of the Si (100) substrate before and after AlN deposition. The curvature radius of the sample was extracted from the Bragg angle dependence on the sample position. Its slope is inversely proportional to the curvature radius of crystallographic planes. The value of σ_f was calculated from the Stoney formula (Eq. 1) for Si (001)[39]:

$$\sigma_f t_f = \frac{h^2}{6} \cdot \frac{1}{s_{11} + s_{12}} \cdot \left(\frac{1}{R} - \frac{1}{R_0}\right), \tag{1}$$

where t_f is the layer thickness, h the substrate thickness, R_0 and R the initial and final substrate curvature radii, and s_{11} and s_{12} are the components of the silicon elastic compliance tensor. This method was conducted to determine the Si 004 diffraction peak position as a function of sample coordinates.

2.3. *Ellipsometry*

The optical properties were probed in the range from near infrared (0.6 eV) to ultraviolet (6.5 eV) energy by variable angle spectroscopy ellipsometry using a J.A. Woollam VASE ellipsometer equipped with a photomultiplier. The resolution of the spectrometer was set to 0.7 nm. We have collected the ellipsometric angles ψ and Δ and depolarization at angles of incidence 50º, 60º, 70º, and 80º. The results were then analyzed by the WVASE software version 3.2.

2.4. *Quasi-static measurement*

We determined the piezoelectric coefficient (d_{33}) using a system for quasi-static measurement while applying a force in the *c*-axis and measuring the generated charge between electrodes in the same direction. We used the PiezoMeter PM300 from Piezotest. The measurement was realized in a very low range mode for expected values in the range from 0 $\mathrm{pC{\cdot}N^{-1}}$ to 10 $\mathrm{pC{\cdot}N^{-1}}$ with an accuracy of ± 2%. The set parameters of force amplitude and test frequency amplitude were 0.25 N and 110 Hz, respectively.

3. Results and discussion

3.1. Crystallography

First, we investigated the influence of the primary IBS energy and substrate temperature on the crystallographic quality of AlN layers deposited on various substrates. Here, we used only nitrogen ions and the secondary IBS was off. We used XRD in the BB setup with the 2θ angle ranging from 30° to 60° to perform the phase analysis of all thin films deposited at various deposition temperatures, BEs, and substrates.

All thin films only exhibited a second-order 002 diffraction peak corresponding to the (001) crystallographic AlN plane. In the sample deposited on the Ti underlayer, the Ti (001) crystallographic plane was also detected. The AlN thin films different from those deposited on Si (100), Si (111), and SiO_2 at the BE above 1 keV and substrate temperatures below 150 ºC exhibited only the *c*-axis orientation. The thin films deposited on Si (100), Si (111), and SiO_2 at the BE above 1 keV and substrate temperature below 150 ºC did not have any preferential orientation. We also performed the RC measurement in the PB setup to determine average disorientation of individual crystallites.

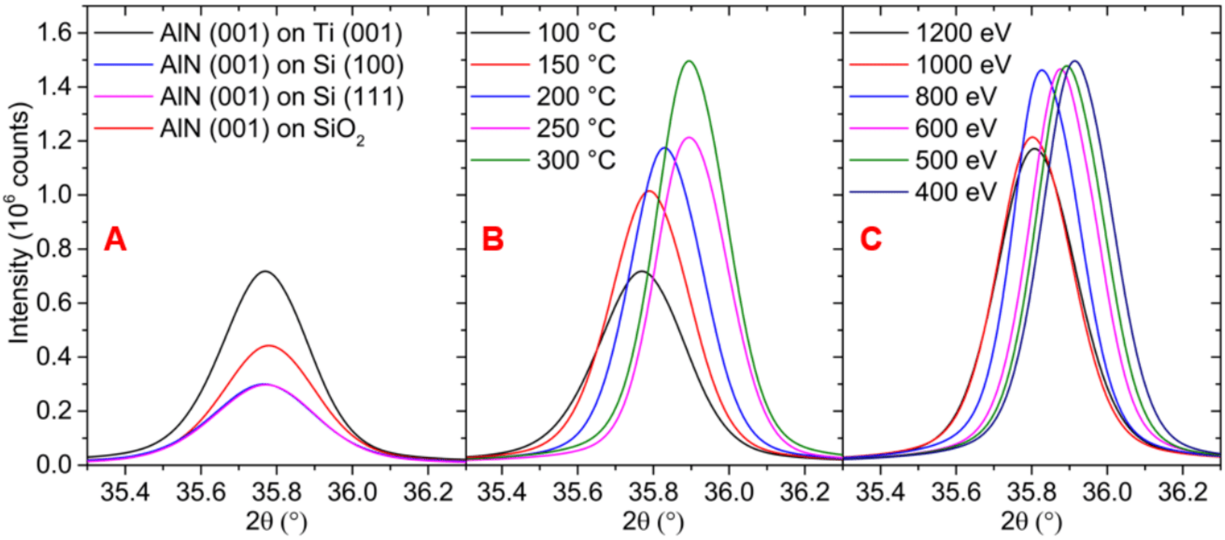

Fig. 2: X-ray diffractograms showing influence of various deposition parameters on AlN (with a thickness of 200 nm) 002 diffraction peak belonging to (001) plane: A) deposition on various surfaces with the constant BE 400 eV and substrate temperature 100 °C; B) depositions at

various substrate temperatures on the (001) preferentially oriented Ti thin film at the constant BE = 400 eV; C) depositions at various BEs and at substrate temperature of 300 °C for thin films grown on the (001) preferentially oriented Ti thin film

Fig. 2A shows the highest diffraction intensity of the AlN (001) appears for the AlN thin film deposited on the (001) preferentially oriented Ti thin film and it is also approx. 1.8× and 2.5× higher than that one related to this film deposited on the SiO_2 and bare silicon surfaces, respectively. The highest peak intensity from the film deposited on the (001) preferentially oriented Ti thin film is caused by the similarity of unstrained Ti crystal lattice parameters [37] to those of AlN [40].

Fig. 3A shows that the smallest BB-FWHM and RC-FWHM of the AlN (001) were achieved for the AlN thin film deposited on the (001) preferentially oriented Ti thin film, hence all further experiments discussed in this part are the thin films deposited on this film. Fig. 2B,C show the positive effect of lower BEs and higher substrate temperatures on the peak intensity and its shift toward a tabulated value of 36.06º [41, 42]. This phenomenon is described in the following section. Higher temperatures and BEs below 1000 eV have a positive influence on the BB-FWHM and RC-FWHM of the AlN (001) (Fig. 3B,C).

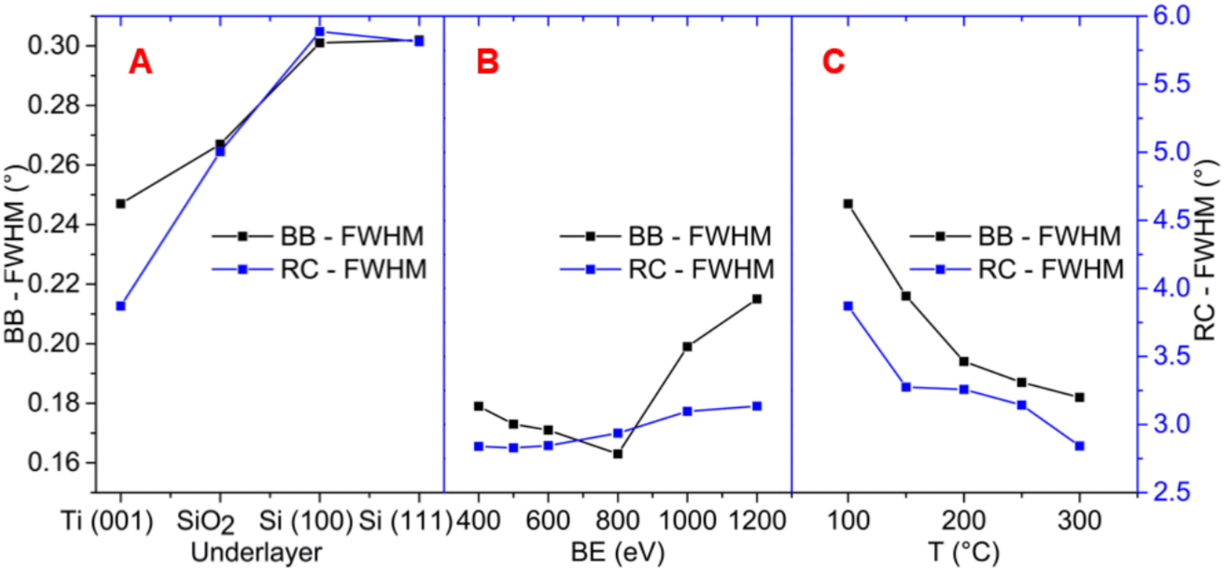

Fig. 3: Extracted data of BB – FWHM and RC – FWHM of the AlN (001) for previously mentioned samples: A) influence of the substrate surface for films deposited at the constant

BE = 400 eV and substrate temperature 100 °C; B) influence of BE for a constant substrate temperature of 300 °C grown on the (001) preferentially oriented Ti thin film; C) influence of different substrate temperatures in the range from 100 °C to 300 °C at the constant BE = 400 eV grown on the (001) preferentially oriented Ti thin film

We analyzed the previous results and then we set the deposition parameters as BE = 400 eV and temperature 300 °C. We also employed the secondary IBS and investigated the effect of related BE and type of the working gas (see Fig. 4).

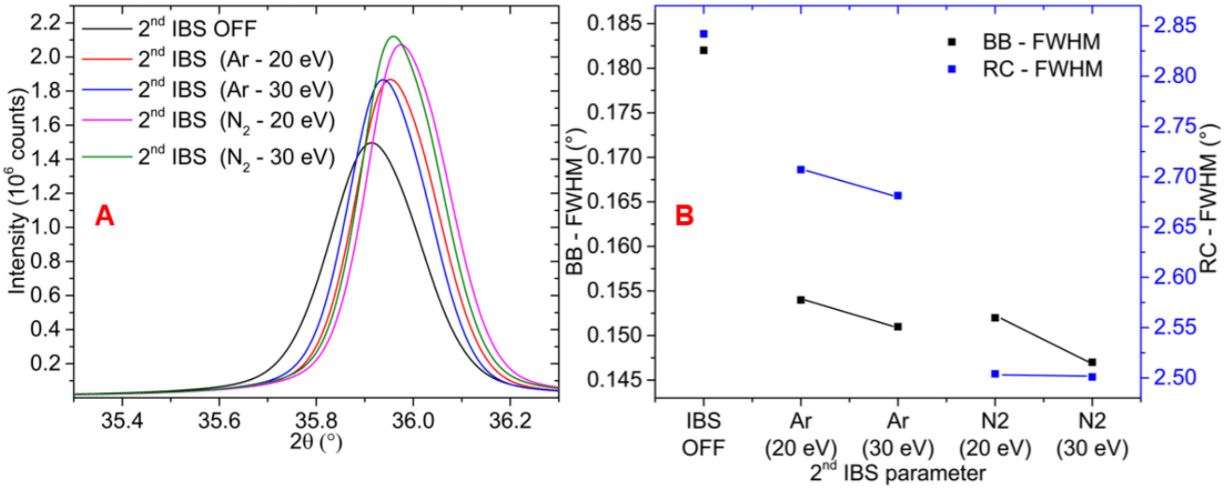

Fig. 4: A) X-ray diffractograms of AlN (001) showing the dependence on the secondary IBS parameters as BE = 20 eV or 30 eV and working gas either Ar or N_2 with a flow rate of 10 sccm; B) extracted data of BB – FWHM and RC – FWHM of the AlN (001) from the X-ray diffractogram and RC measurement showing the influence of the secondary IBS parameters

The ion-beam bombardment of the substrate from the secondary IBS had a positive influence on decreasing the BB-FWHM and the RC-FWHM of the AlN (001) (Fig. 4). There are two effects taking place during this AlN deposition. First, this bombardment at the BE below 100 eV reduced the tensile stress and caused compressive stress [43]. Second, the low energy (< 100 eV) ion-beam bombardment provided continuous cleaning of physisorbed impurities eliminating the compressive stress. We show that the bombardment at BE = 30 eV in comparison to the one at 20 eV shifts the AlN diffraction peak to the smaller values of the diffraction angle (Fig. 4A). The thin films deposited under assisting ion beams of BE = 30 eV resulted in the diffraction peaks of slightly higher intensities than of those related to the films deposited at BE = 20 eV. The deposition without the secondary IBS resulted in a diffraction peak shift to lower values of the diffraction angle.

Because the peak position differs from the optimal one by 0.4º to 0.6º, we decided to optimize the deposition parameters. The secondary IBS parameters such as BE and gas types were fixed to a value of 20 eV and pure N_2, respectively. Then we investigated the influence of the N_2:Ar ratio in the primary IBS (Tab. 1) leading to the optimal diffraction peak angle (Fig. 5).

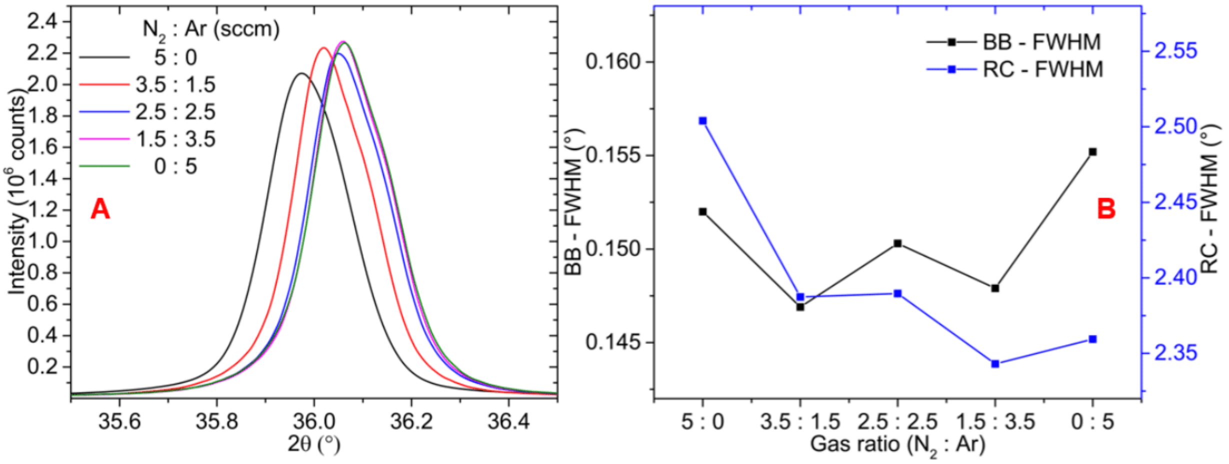

Fig. 5: Influence of the N_2:Ar ratio in the primary IBS: A) X-ray diffractogram of AlN (001); B) extracted data of BB – FWHM and RC – FWHM of the AlN (001) from the X-ray diffractogram and RC measurement

The N_2:Ar ratio causes a minimal change in the BB-FWHM of the AlN (001) in the order of 1/1000 and the RC-FWHM of the AlN (001) is marginally decreased for higher Ar concentration (Fig. 5B) while the diffraction peak shift is more pronounced (Fig. 5A). Higher Ar concentration during the deposition resulted in the change of stress values from compressive to tensile. We observed that the thin film deposited at the same N_2 and Ar flow rates, both of 2.5 sccm, resulted in a diffraction peak position of 36.06°, which is in good agreement with the tabulated value.

We also deposited 400 nm, 600 nm, 800 nm, and 1000 nm thick AlN layers with a preferential orientation of (001) to prove there is no peak shift related to the layer thickness (Fig. 6A). We observed both decreasing BB-FWHM and RC-FWHM of the AlN (001) with the increasing thickness of the thin films (Fig. 6B).

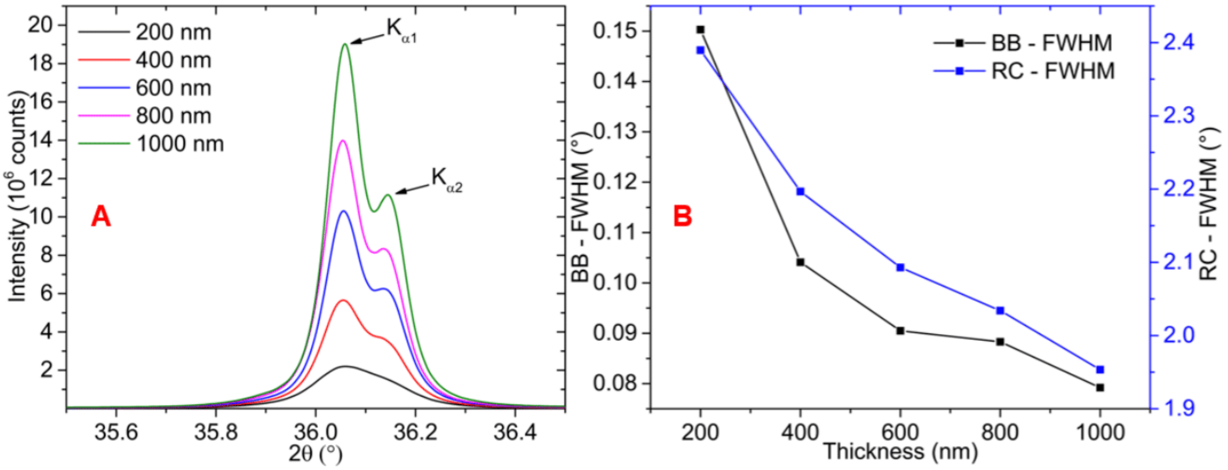

Fig. 6: A) X-ray diffractogram of AlN (001) showing the influence of the AlN thin film thickness on the peak position and its profile; B) extracted data of BB – FWHM and RC – FWHM of the AlN (001) from the X-ray diffractograms and RC measurement showing the influence of AlN thin film thickness

3.2. Stress characterization

Stress in thin films for MEMS applications is one of the most important parameters. The investigated AlN thin film was deposited on a Si (100) substrate and characterized by an XRD curvature measurement. We chose several samples from the previous experiments possessing different 2θ (BB) peak positions to demonstrate the dependence of the peak position on the residual stress (Fig. 7).

Fig. 7A shows the linear dependence of the 2θ (BB) position of the 002 diffraction peak corresponding to the *c* lattice parameter and 2θ (in-plane) position of the 110 diffraction peak for corresponding to the *a* lattice parameter on the residual stress. The residual stress can then be determined from the diffraction peak position. We found the 002 and 110 diffraction angles for the zero-stress thin film to be (36.059 ± 0.005)º and (59.327 ± 0.006)º, respectively. We used those values to calculate the lattice parameters using Bragg's law. We obtained c = (4.978 ± 0.001) Å and a = (3.113 ± 0.001) Å, where uncertainties in the brackets are given by fitting errors, which is in good agreement with the tabulated values a = 3.111 Å and c = 4.979 Å [41, 42]. We also found that the residual stress is independent on thin film thickness (Fig. 7B).

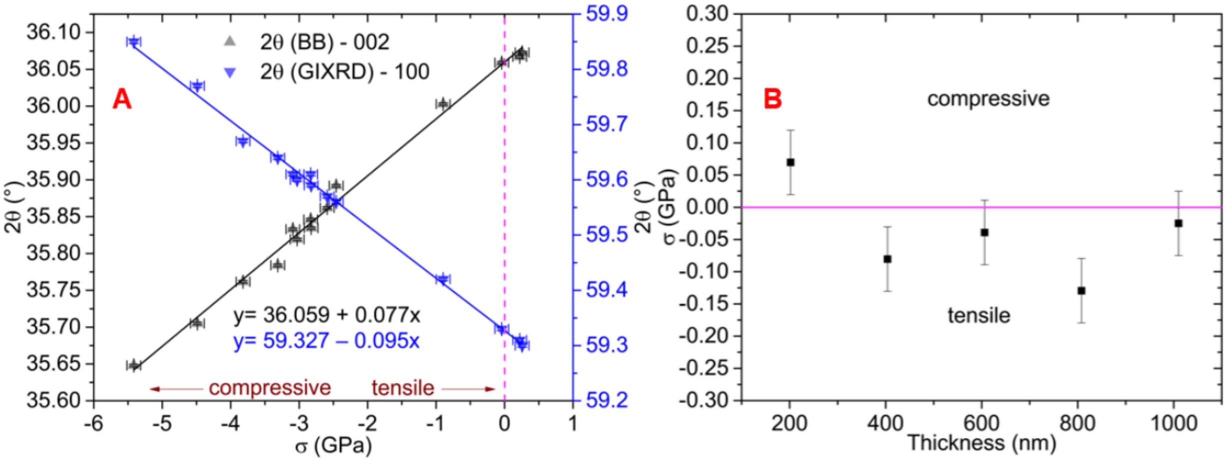

Fig. 7: A) 2θ (BB) position of the 002 diffraction peak corresponding to the c lattice parameter and 2θ (GIXRD) position of the 110 diffraction peak corresponding to the a lattice parameter as a function of the residual stress derived from the XRD curvature measurement; B) influence of the thin film thickness on the residual stress

Consequently, we fabricated a stress testing diamond ring structure [44] to prove there is no buckling of the deposited layer. The deposition parameters were set to achieve an AlN stress-free thin film with a thickness of 1000 nm on the Si (100) substrate. Fig. 8 shows the scanning electron microscopy (SEM) images of the fabricated structure with no evident buckling of the layer.

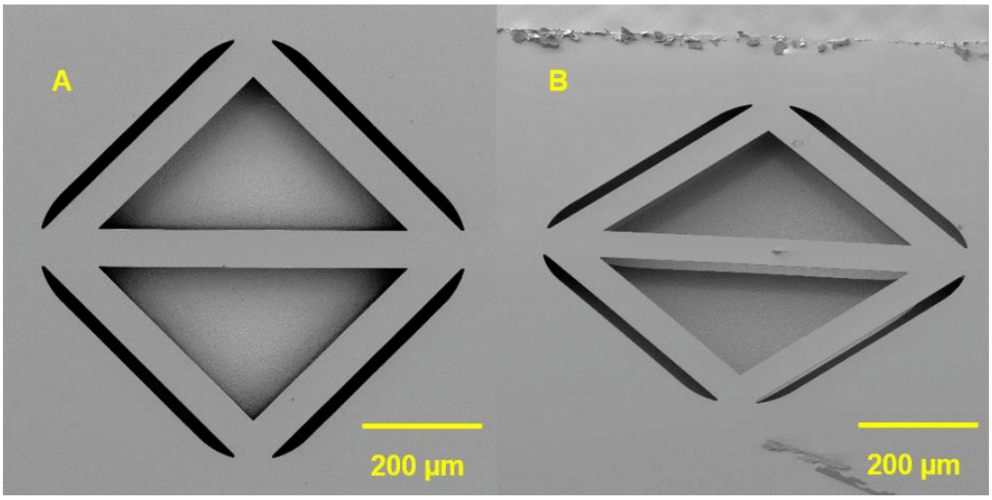

Fig. 8: SEM images of 1000 nm thick AlN diamond ring structure with no buckling: A) top view; B) tilted view at 45°

3.3. *The optical response*

The optical response of AlN thin films was investigated by ellipsometry for the wavelengths from 0.6 eV to 6.5 eV. Fig. 9A,B show an example of the spectra of the ellipsometric angles Ψ and Δ, respectively, obtained for the AlN layer deposited on Si (111) at various angles of incidence. The sharp structures in the spectra are fringes caused by interference in the AlN thin film that disappears above 6 eV where the interband absorption sets in. We analyzed the data with a model of coherent interferences in the AlN thin film on a substrate. The anisotropic properties of the AlN layer were taken into account with a uniaxial model with the ordinary and extraordinary axis oriented in- and out-of-plane, respectively. The dielectric functions in both axes were modeled with a set of Kramers–Kronig consistent oscillators. The spectra exhibit a weak intraband absorption that was modeled with a Gaussian oscillator centered at 6.5 eV. A small thickness inhomogeneity of 1% was taken into consideration. The surface and interface roughness were modeled with the effective medium approximation (Bruggeman model) [45]. The model spectra are displayed as solid lines in Fig. 9. The measured and modeled data are in good agreement for all angles of incidence.

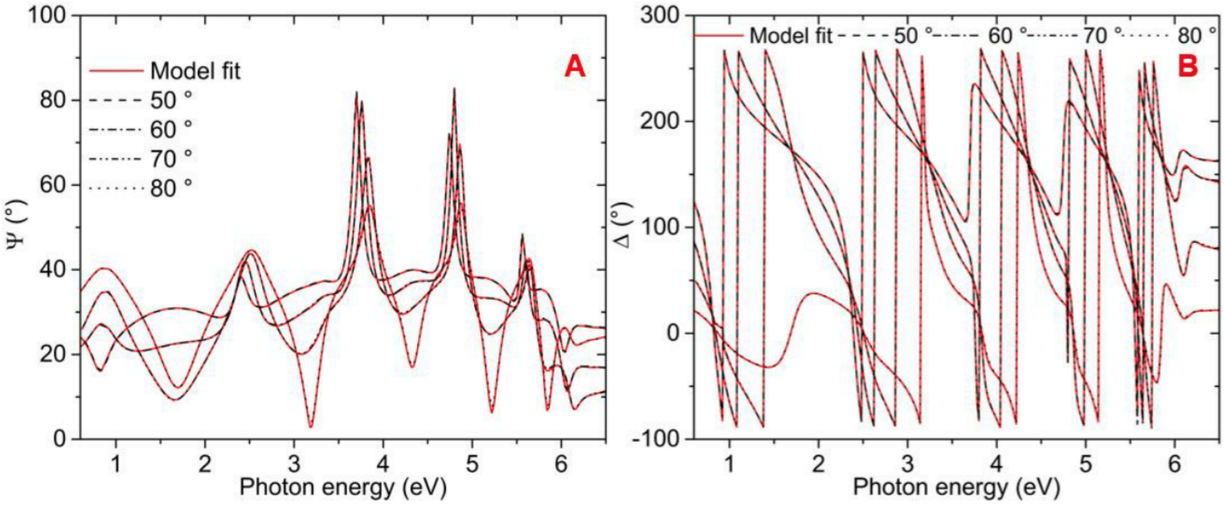

Fig. 9: Spectra of the ellipsometric angles A) ψ and B) Δ for the AlN (001) thin film deposited on Si (111) measured at angles of incidence 50°, 60°, 70°, and 80° (dashed lines represent the measured data and solid lines correspond to the model specified in the text)

Fig. 10A shows the real part of the dielectric function along the ordinary (black solid line) and the extraordinary (red solid line) axis, respectively, obtained for AlN grown on Si (111). The spectra display the well-known anisotropy [46]. The obtained values are in good agreement with the results reported earlier [47] being displayed as doted lines.

Fig. 10B displays the imaginary part of the ordinary dielectric function of AlN thin films deposited on all four substrates (solid lines). The extraordinary spectrum for the AlN (001) thin film deposited on Si (111) (dashed line) is shown for comparison as well. The strong absorption above 6 eV is due to the direct interband absorption that sets in 6.1 eV in the ordinary direction and at 5.8 eV in the extraordinary direction. These values are slightly lower compared with the values obtained on MOCVD grown samples [46]. Below the bandgap, the absorption does not drop to zero but down to 3.5 eV exhibits values significantly high above the sensitivity limits of the measurements (about 0.01). This intragap absorption is well known[48] and was attributed to Al interstitials [42]. Interestingly, this absorption is approx. 3× smaller in the thin film deposited on the substrate with the (001) preferentially oriented Ti thin film (black solid line) than in the thin films deposited on the other substrates. These results correlate well with the higher structural quality as seen in the X-ray data and can be interpreted as a result of smaller concentration of Al interstitials in AlN grown on the (001) preferentially oriented Ti thin film. Note that this intragap absorption is essentially absent in thin films grown by MOCVD [46].

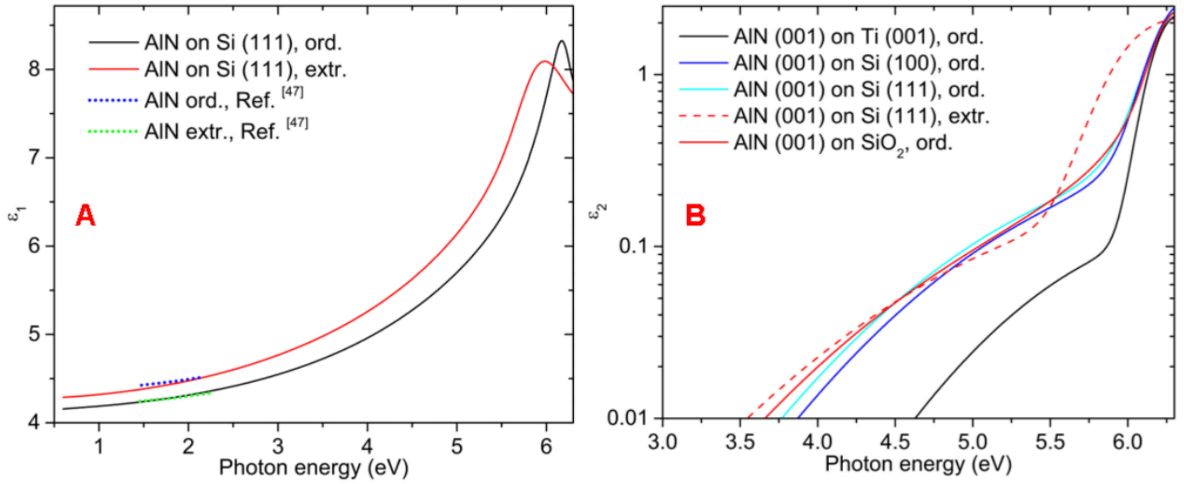

Fig. 10: A) Real and B) imaginary parts of the dielectric function obtained from the analysis of ellipsometry data: A) spectra along the ordinary (solid black line) and extraordinary (solid red line) direction of AlN deposited on Si (111) compared with data from Ref. [47] (dotted lines). B)

imaginary part of the ordinary dielectric function of AlN deposited on different substrates (solid lines) together with the extraordinary spectrum of AlN deposited on Si (111) (red dashed line)

3.4. Determination of d33 piezoelectric coefficient

We measured the d_{33} piezoelectric coefficient of seven chosen samples using the quasi-static method. All measured AlN thin films were deposited on the (001) preferentially oriented Ti thin films that also serve as a bottom electrode. The measured d_{33} values of thin films and a description of their deposition parameters are listed in Tab. 2.

Tab. 2: Measured d_{33} values of selected samples and their fabrication parameters

		Primary IBS			Secondary IBS						
Sample	d_{33} (pC·N^{-1})	BE (eV)	Ar flow (sccm)	N_2 flow (sccm)	BE (eV)	Ar flow (sccm)	N_2 flow (sccm)	T (ºC)	BB-FWHM (°)	RC-FWHM (°)	σ_f (GPa)
1	6.53 ± 0.13	1200	0	8.0	IBS OFF			100	0.68	8.2	7.0
2	6.78 ± 0.12	800	0	6.0	IBS OFF			250	0.21	3.2	5.4
3	6.95 ± 0.14	500	0	5.2	IBS OFF			200	0.19	3.2	3.8
4	7.11 ± 0.12	400	0	5.0	IBS OFF			250	0.19	3.1	2.6
5	7.32 ± 0.10	400	0	5.0	20	0	10	330	0.15	2.5	0.9
6	7.33 ± 0.08	400	2.5	2.5	20	0	10	330	0.15	2.4	0
7	7.33 ± 0.09	400	5.0	0	20	0	10	330	0.16	2.4	-0.2

All the samples have the (001) preferential orientation while the difference between these samples is in their value of RC-FWHM in the PB setup and residual stress. The first sample has the highest RC-FWHM of the AlN (001) in PB and has the lowest value of d_{33} in comparison with sample numbers 5, 6, and 7 with the lowest RC. The RC-FWHM of the last three samples is almost the same while the change of RC-FWHM between samples 5 and 7 is approx. 0.15°. The only difference between the samples is their residual stress. Although the difference in residual stress between samples 5 and 7 is 1.1 GPa, there is no evident influence of residual stress on the d_{33} values. We can see that the d_{33} values of all samples are high although their thin films were prepared under non-optimal deposition parameters. The best optimized layer with no residual stress (sample 6) has the highest obtained value of $d_{33} = (7.33 \pm 0.08)$ pC·N^{-1}, which is essential for the fabrication of MEMS.

Conclusions

We have presented a method suitable for the deposition of high-quality (001) preferentially oriented AlN thin films with a high value of the d_{33} piezoelectric coefficient for MEMS applications using primary and assisted Kaufman ion-beam sources. During the experiment, we controlled the operational parameters of these ion-beam sources and also substrate temperature via a built-in substrate heater.

The first part of the experiments showed that lower BE of the primary IBS and higher T have positive influence on all important parameters as BB-FWHM, RC-FWHM, and residual stress, which leads to a higher value of d_{33}. In the second part of the experiments, the secondary IBS was used for ion-beam bombardment of growing thin films by Ar or N_2 ions with BE of 20 eV and 30 eV, respectively. We found that the bombardment by N_2 ions at a lower BE value of 20 eV has a positive influence on reducing the compressive stress. In the last experiments, we changed only the gas ratio between Ar and N_2 in the primary IBS, which led to a change of compressive stress to tensile residual stress while the other parameters as BB-FWHM and RC-FWHM remained almost unchanged. These experiments provided complex information about the method for preparation of high-quality (001) preferentially oriented AlN thin films suitable for MEMS applications.

During these experiments, we obtained the linear dependence of c and a lattice parameters on the residual stress among a series of 14 samples. The dependence of the diffraction peak shift on the residual stress can be described by functions $y = 36.059 + 0.77x$ and $y = 59.327 - 0.95x$ for the 002 and 110 diffractions, respectively. These expressions give us the values of the unstrained lattice parameters c_0 and a_0 for $x = 0$. These values perfectly fit to the measured lattice parameters of the sample without residual stress which also has the best parameters from the whole set of experiments. This sample belongs to one of three samples with the highest d_{33}, such as (7.33 ± 0.08) pC·N^{-1}, and the best crystallographic parameters as the lowest values of BB-FWHM 0.15° and RC-FWHM 2.4° for a thin film thickness of 200 nm. We also investigated the optical properties of AlN thin films using ellipsometry. The obtained spectra exhibit a direct bandgap at

6.1 eV in the ordinary direction and at 5.8 eV in the extraordinary direction, which are values close to those previously published [46]. In addition, the spectra exhibit an intragap absorption due to Al interstitials. This absorption is the lowest in the AlN thin films deposited on the (001) preferentially oriented Ti thin films that correlate with the highest structural quality as seen from the XRD analysis. This is probably caused by the fact that both Ti and AlN thin films possess a hexagonal structure with similar lattice parameters.

Acknowledgements

We acknowledge the support of CEITEC Nano Research Infrastructure (ID LM2015041, MEYS CR, 2016–2019), CEITEC Brno University of Technology and Grant Agency of the Czech Republic under the contract GJ18-06498Y. Authors I. Gablech and J. Pekárek also acknowledge the foundation support FEKT/STI-J-17-4136. The infrastructure of the SIX Center of BUT and facility of Department of Microsystems Technology at TUW was utilized to conduct the experiments.

References

[1] D.M. Kim, C.B. Eom, V. Nagarajan, J. Ouyang, R. Ramesh, V. Vaithyanathan, D.G. Schlom, Thickness dependence of structural and piezoelectric properties of epitaxial Pb(Zr0.52Ti0.48)O-3 films on Si and SrTiO3 substrates, Appl. Phys. Lett., 88 (2006).

[2] M.H. Zhao, Z.L. Wang, S.X. Mao, Piezoelectric characterization of individual zinc oxide nanobelt probed by piezoresponse force microscope, Nano Lett., 4 (2004) 587-590.

[3] Y. Saigusa, 5 - Quartz-based piezoelectric materials A2 - Uchino, Kenji, Advanced Piezoelectric Materials, Woodhead Publishing2010, pp. 171-203.

[4] V.Y. Shur, 6 - Lithium niobate and lithium tantalate-based piezoelectric materials A2 - Uchino, Kenji, Advanced Piezoelectric Materials, Woodhead Publishing2010, pp. 204-238.

[5] J.C. Doll, B.C. Petzold, B. Ninan, R. Mullapudi, B.L. Pruitt, Aluminum nitride on titanium for CMOS compatible piezoelectric transducers, J. Micromech. Microeng., 20 (2010).

[6] M. Al Ahmad, R. Plana, Vertical displacement detection of an aluminum nitride piezoelectric thin film using capacitance measurements, Int. J. Microw. Wirel. Technol., 1 (2009) 5-9.

[7] N. Jackson, L. Keeney, A. Mathewson, Flexible-CMOS and biocompatible piezoelectric AlN material for MEMS applications, Smart Mater. Struct., 22 (2013).

[8] M.M. De Souza, S. Jejurikar, K.P. Adhi, Impact of aluminum nitride as an insulator on the performance of zinc oxide thin film transistors, Appl. Phys. Lett., 92 (2008).

[9] D. Kueck, P. Leber, A. Schmidt, G. Speranza, E. Kohn, AlN as passivation for surface channel FETs on H-terminated diamond, Diam. Relat. Mat., 19 (2010) 932-935.

[10] R. Elfrink, T.M. Kamel, M. Goedbloed, S. Matova, D. Hohlfeld, Y. van Andel, R. van Schaijk, Vibration energy harvesting with aluminum nitride-based piezoelectric devices, J. Micromech. Microeng., 19 (2009).

[11] A.B.A. Dow, A. Bittner, U. Schmid, N.P. Kherani, Design, fabrication and testing of a piezoelectric energy microgenerator, Microsyst Technol, 20 (2014) 1035-1040.

[12] P. Ivaldi, J. Abergel, M.H. Matheny, L.G. Villanueva, R.B. Karabalin, M.L. Roukes, P. Andreucci, S. Hentz, E. Defay, 50 nm thick AlN film-based piezoelectric cantilevers for gravimetric detection, J. Micromech. Microeng., 21 (2011).

[13] A. Heidari, Y.J. Yoon, M.I. Lee, L. Khine, M.K. Park, J.M.L. Tsai, A novel checker-patterned AlN MEMS resonator as gravimetric sensor, Sens. Actuator A-Phys., 189 (2013) 298-306.

[14] J. Xiong, X.L. Sun, P. Guo, D. Zheng, H.S. Gu, Analysis of resonance characteristics of solidly mounted resonator for mass sensing applications, Appl. Phys. A-Mater. Sci. Process., 116 (2014) 1573-1577.

[15] J. Toledo, V. Ruiz-Diez, G. Pfusterschmied, U. Schmid, J.L. Sanchez-Rojas, Flow-through sensor based on piezoelectric MEMS resonator for the in-line monitoring of wine fermentation, Sensor Actuat B-Chem, 254 (2018) 291-298.

[16] J. Jang, J. Lee, S. Woo, D.J. Sly, L.J. Campbell, J.H. Cho, S.J. O'Leary, M.H. Park, S. Han, J.W. Choi, J.H. Jang, H. Choi, A microelectromechanical system artificial basilar membrane based on a piezoelectric cantilever array and its characterization using an animal model, Sci Rep, 5 (2015).

[17] B.Z. Chen, F.T. Chu, X.Z. Liu, Y.R. Li, J. Rong, H.B. Jiang, AlN-based piezoelectric micromachined ultrasonic transducer for photoacoustic imaging, Appl. Phys. Lett., 103 (2013).

[18] Y.J. Chen, V. Krishnamurthy, Y.C. Lai, Y. Luo, Z.B. Hao, L. Wang, S.T. Ho, Fabrication of sub-200 nm AlN-GaN-AlN waveguide with cleaved end facet, J. Vac. Sci. Technol. B, 32 (2014).

[19] S. Zhao, A.T. Connie, M.H.T. Dastjerdi, X.H. Kong, Q. Wang, M. Djavid, S. Sadaf, X.D. Liu, I. Shih, H. Guo, Z. Mi, Aluminum nitride nanowire light emitting diodes: Breaking the fundamental bottleneck of deep ultraviolet light sources, Sci Rep, 5 (2015).

[20] W. Zheng, F. Huang, R.S. Zheng, H.L. Wu, Low-Dimensional Structure Vacuum-Ultraviolet-Sensitive (lambda < 200 nm) Photodetector with Fast-Response Speed Based on High-Quality AlN Micro/Nanowire, Adv Mater, 27 (2015) 3921.

[21] R.B. Karabalin, M.H. Matheny, X.L. Feng, E. Defay, G. Le Rhun, C. Marcoux, S. Hentz, P. Andreucci, M.L. Roukes, Piezoelectric nanoelectromechanical resonators based on aluminum nitride thin films, Appl. Phys. Lett., 95 (2009).

[22] S.C. Jain, M. Willander, J. Narayan, R.V. Overstraeten, III–nitrides: Growth, characterization, and properties, Journal of Applied Physics, 87 (2000) 965-1006.

[23] S.N. Ivanov, P.A. Popov, G.V. Egorov, A.A. Sidorov, B.I. Kornev, L.M. Zhukova, V.P. Ryabov, Thermophysical properties of aluminum nitride ceramic, Phys. Solid State, 39 (1997) 81-83.

[24] S. Trolier-McKinstry, P. Muralt, Thin film piezoelectrics for MEMS, J. Electroceram., 12 (2004) 7-17.

[25] E. Wistrela, M. Schneider, A. Bittner, U. Schmid, Impact of the substrate dependent polarity distribution in c-axis oriented AlN thin films on the etching behaviour and the piezoelectric properties, Microsyst Technol, 22 (2016) 1691-1700.

[26] K.S. Ramadan, D. Sameoto, S. Evoy, A review of piezoelectric polymers as functional materials for electromechanical transducers, Smart Mater. Struct., 23 (2014).

[27] M.A. Dubois, P. Muralt, Stress and piezoelectric properties of aluminum nitride thin films deposited onto metal electrodes by pulsed direct current reactive sputtering, Journal of Applied Physics, 89 (2001) 6389-6395.

[28] A. Kakanakova-Georgieva, D. Nilsson, E. Janzen, High-quality AlN layers grown by hot-wall MOCVD at reduced temperatures, J. Cryst. Growth, 338 (2012) 52-56.

[29] A.C. Jones, J. Auld, S.A. Rushworth, E.W. Williams, P.W. Haycock, C.C. Tang, G.W. Critchlow, The Deposition of Aluminum Nitride Thin-Films by Metal-Organic Cvd - an Alternative Precursor System, Adv Mater, 6 (1994) 229-231.

[30] Z. Chen, S. Newman, D. Brown, R. Chung, S. Keller, U.K. Mishra, S.P. Denbaars, S. Nakamura, High quality AlN grown on SiC by metal organic chemical vapor deposition, Appl. Phys. Lett., 93 (2008).

[31] M.A. Sanchez-Garcia, E. Calleja, E. Monroy, F.J. Sanchez, F. Calle, E. Munoz, R. Beresford, The effect of the III/V ratio and substrate temperature on the morphology and properties of GaN- and AlN-layers grown by molecular beam epitaxy on Si(111), J. Cryst. Growth, 183 (1998) 23-30.

[32] A. Volkova, V. Ivantsov, L. Leung, Hydride vapor phase epitaxy of high structural perfection thick AlN layers on off-axis 6H-SiC, J. Cryst. Growth, 314 (2011) 113-118.

[33] G.E. Stan, M. Botea, G.A. Boni, I. Pintilie, L. Pintilie, Electric and pyroelectric properties of AIN thin films deposited by reactive magnetron sputtering on Si substrate, Appl. Surf. Sci., 353 (2015) 1195-1202.

[34] W.L. Wang, W.J. Yang, Z.L. Liu, H.Y. Wang, L. Wen, G.Q. Li, Interfacial reaction control and its mechanism of AlN epitaxial films grown on Si(111) substrates by pulsed laser deposition, Sci Rep, 5 (2015).

[35] Z.P. Wang, A. Morimoto, T. Kawae, H. Ito, K. Masugata, Growth of preferentially-oriented AlN films on amorphous substrate by pulsed laser deposition, Phys. Lett. A, 375 (2011) 3007-3011.

[36] C. Ozgit, I. Donmez, M. Alevli, N. Biyikli, Self-limiting low-temperature growth of crystalline AlN thin films by plasma-enhanced atomic layer deposition, Thin Solid Films, 520 (2012) 2750-2755.

[37] I. Gablech, O. Caha, V. Svatoš, J. Pekárek, P. Neužil, T. Šikola, Stress-free deposition of [001] preferentially oriented titanium thin film by Kaufman ion-beam source, Thin Solid Films, 638 (2017) 57-62.

[38] I. Gablech, V. Svatos, O. Caha, M. Hrabovsky, J. Prasek, J. Hubalek, T. Sikola, Preparation of (001) preferentially oriented titanium thin films by ion-beam sputtering deposition on thermal silicon dioxide, J Mater Sci, 51 (2016) 3329-3336.

[39] G.C.A.M. Janssen, M.M. Abdalla, F. van Keulen, B.R. Pujada, B. van Venrooy, Celebrating the 100th anniversary of the Stoney equation for film stress: Developments from polycrystalline steel strips to single crystal silicon wafers, Thin Solid Films, 517 (2009) 1858-1867.

[40] PDF-2 database entry 00-025-1133, ICDD-JCPDS.

[41] O. Madelung, Semiconductors: Data Handbook, Springer Berlin Heidelberg2012.

[42] T.L. Tansley, R.J. Egan, Point-Defect Energies in the Nitrides of Aluminum, Gallium, and Indium, Phys Rev B, 45 (1992) 10942-10950.

[43] H.R. Kaufman, J.M.E. Harper, Ion-assist applications of broad-beam ion sources, P Soc Photo-Opt Ins, 5527 (2004) 50-68.

[44] K.C. Balram, D.A. Westly, M. Davanco, K.E. Grutter, Q. Li, T. Michels, C.H. Ray, L.Y. Yu, R.J. Kasica, C.B. Wallin, I.J. Gilbert, B.A. Bryce, G. Simelgor, J. Topolancik, N. Lobontiu, Y.X. Liu, P. Neuzil, V. Svatos, K.A. Dill, N.A. Bertrand, M.G. Metzler, G. Lopez, D.A. Czaplewski, L. Ocola, K.A. Srinivasan, S.M. Stavis, V.A. Aksyuk, J.A. Liddle, S. Krylov, B.R. Ilic, The Nanolithography Toolbox, J Res Natl Inst Stan, 121 (2016) 464-475.

[45] H. Fujiwara, Data Analysis Examples, Spectroscopic Ellipsometry, John Wiley & Sons, Ltd2007, pp. 249-310.

[46] G. Rossbach, M. Roppischer, P. Schley, G. Gobsch, C. Werner, C. Cobet, N. Esser, A. Dadgar, M. Wieneke, A. Krost, R. Goldhahn, Valence-band splitting and optical anisotropy of AlN, Phys Status Solidi B, 247 (2010) 1679-1682.

[47] A.R. Goni, F. Kaess, J.S. Reparaz, M.I. Alonso, M. Garriga, G. Callsen, M.R. Wagner, A. Hoffmann, Z. Sitar, Dependence on pressure of the refractive indices of wurtzite ZnO, GaN, and AlN, Phys Rev B, 90 (2014).

[48] H. Demiryont, L.R. Thompson, G.J. Collins, Optical-Properties of Aluminum Oxynitrides Deposited by Laser-Assisted Cvd, Appl Optics, 25 (1986) 1311-1318.

8 Fabrication of piezoelectric MEMS resonator with Hall Bar/FET structure

The device was fabricated using standard surface and bulk micromachining techniques. All materials and processes were compatible to CMOS technology. Fabrication of whole device consists of 10 lithography steps including 2D material shaping. The device was created on 535 μm thick 100 mm in diameter Si (100) wafer covered by 200 nm thick plasma-enhanced chemical vapor deposition (PECVD) low-stress (<0.3 GPa) SiO_2.

Ti (001) of 80 nm thickness was deposited in the first step. It combines the function of seed layer for AlN growth and bottom electrode of piezoelectric resonator. The next step was deposition of 1 μm thick piezoelectric AlN (001) layer. It was followed by deposition of 15 nm thick Ti (001) which serve as the protection of AlN to chemicals and oxidation and provides adhesion for top electrode material with higher elasticity. These deposition steps were followed by spin-coating of 3.5 μm thick positive photoresist (PR) AR-P 3540. Such a thickness was required for etching of 1 μm AlN due to poor selectivity to photoresist. The top Ti and AlN were etched in reactive-ion etching (RIE) machine using Cl_2 and BCl_3 plasma. The etching was stopped on bottom Ti layer using optical endpoint detection. This step formed the shape of piezoelectric resonator part (see **Figure 13**).

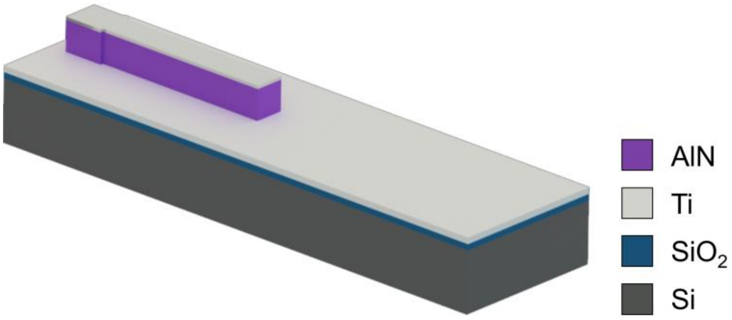

Figure 13: Shape of piezoelectric resonator.

The next fabrication step was forming of Ti (001) bottom piezoelectric resonator´s electrode and its leadout (see **Figure 14**). It was used PR AR-P 3540 with thickness of 1.4 μm. Then the Ti was etched in RIE tool using Cl_2 plasma. The etching was stopped on SiO_2 using optical endpoint detection.

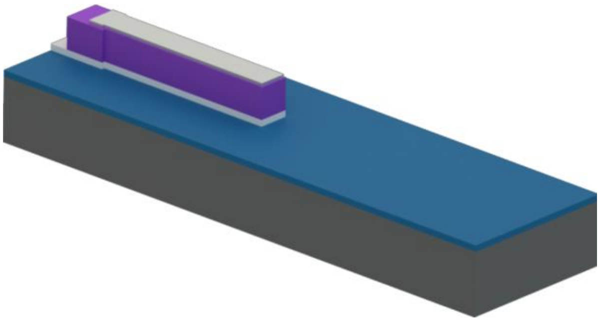

Figure 14: Shape of bottom electrode and its leadout of piezoelectric resonator.

The third step of device fabrication was conducted to deposition of 80 nm thick Al (111). It forms the top electrode and protects the uncovered Ti from bottom electrode to XeF$_2$ etching which takes a part in the last fabrication step. It also forms the gate electrode of Hall Bar/FET structure. Only the pattern of gate electrode was etched during this step. The rest Al is used as stop-layer for consecutive SiO$_2$ etching on Hall Bar/FET part. This Al stop-layer is not visible in following three figures to improve clarity of the model. The 1.4 μm thick PR AR-P 3540 was used. The etching of Al was done in the RIE machine using Cl$_2$ and BCl$_3$ plasma. The piezoelectric resonator (excluding the SiO$_2$ etching) is formed (see **Figure 15**) after this fabrication step.

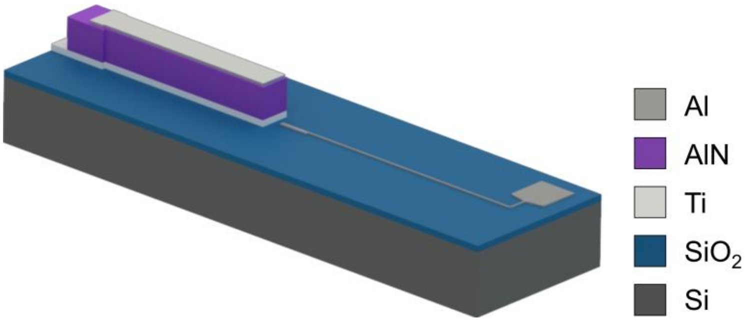

Figure 15: Shape of gate electrode of Hall Bar/FET stretchable part.

Two following fabrication steps are aimed at Hall Bar/FET structure creation. At first, low-stress SiO$_2$ was deposited to form gate oxide with thickness of 100 nm. It was followed by deposition of 50 nm thick Al (111) for source, drain and Hall bar electrode connections. The next lithography step was etching of Al covered by PR AR-P 3540 with thickness of 1.0 μm. The etching of Al was done using the same instrument and plasma as mentioned above. The fabricated electrode connections have width of 4.0 μm with spacing of 4.0 μm (see **Figure 16**).

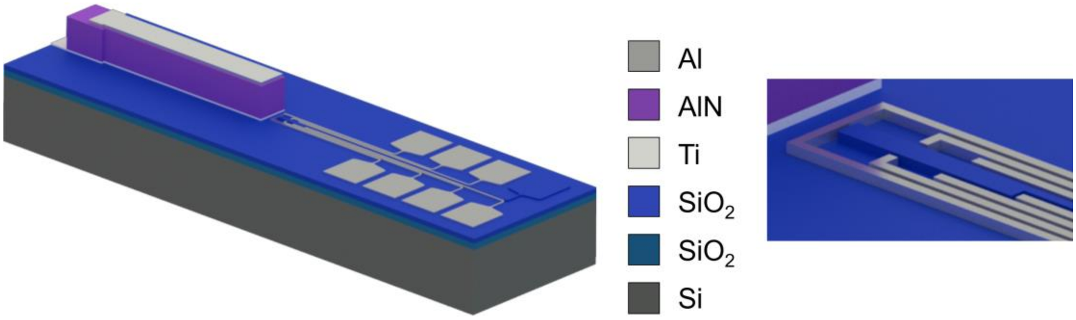

Figure 16: Shape of source, drain and Hall bar electrodes of stretchable part.

Next step was etching of SiO$_2$ gate. It was used the same PR with thickness of 1.4 μm. The SiO$_2$ was etched in RIE instrument using CHF$_3$, SF$_6$ and Ar plasma. The etching was stopped on the Al (see **Figure 17**). There was no endpoint detection which is not important since the Al and SiO$_2$ etching selectivity is very high.

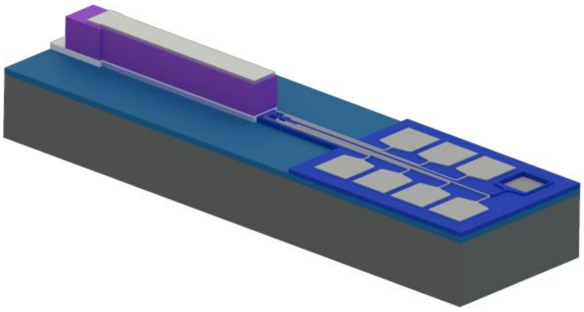

Figure 17: Shape of gate insulator layer.

The 80 nm thick Al (111) stop-layer is etched in this step to form top electrode and bottom electrode leadout protection (see **Figure 18**). This step also involves the fabrication of marks for wafer cutting/dicing. It was used the same PR with identical thickness as before. The Al was etched using the same RIE instrument with Cl and BCl_3 plasma.

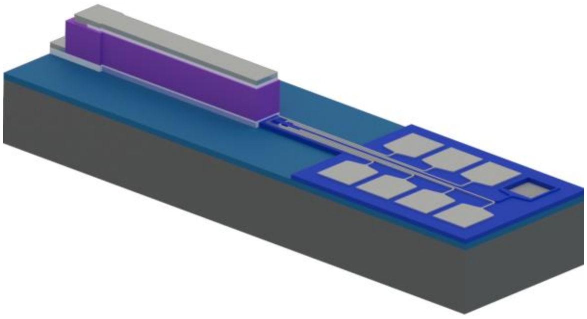

Figure 18: Shape of top electrode of piezoelectric resonator.

The whole structure of piezoelectric resonator with Hall Bar/FET structure is fabricated. The following steps are conducted to structure releasing and coating of pads with sufficient thickness which enables wire-bonding and the pads of Hall Bar/FET structure where 2D material is located.

The next fabrication step is 200 nm thick SiO_2 etching which reveals the Si for the last fabrication step in whole process (see **Figure 19**). The identical PR was used as before. The SiO_2 was etched in the same machine at the same conditions as mentioned above in this chapter.

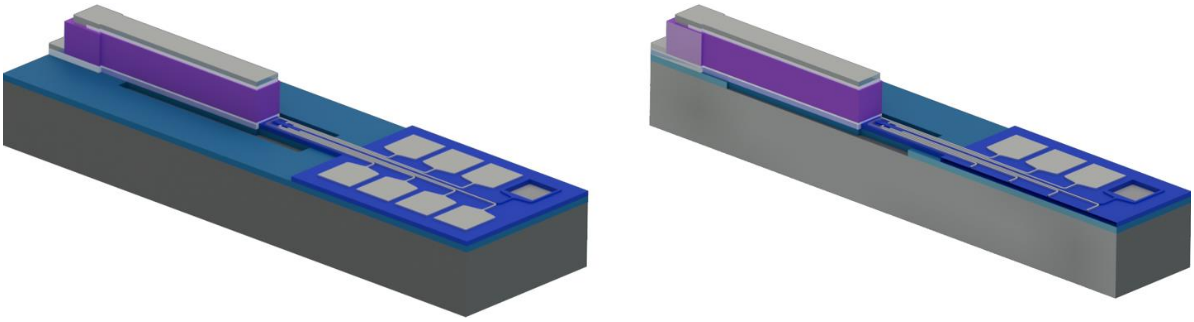

Figure 19: SiO_2 etching to open the underneath Si.

It was also important to make pads suitable for wire-bonding method of Al (see **Figure 20**).

The combination of 3.0 μm thick PR AR-BR 5460 and 1.4 μm PR AR-3540 was used to achieve positive lift-off. This technique must be used due to 700 nm Al deposition on pads which is not possible to etch on wafer with fabricated structure. The surface of Al was sputtered using Kaufman ion-beam source for a short time (<30 s) before 700 nm thick Al deposition to avoid bad contact due to Al surface oxidation.

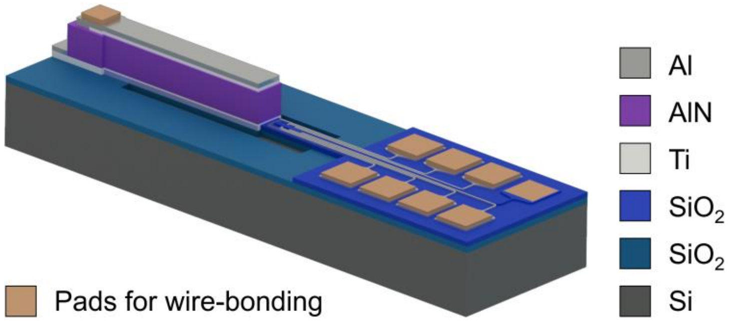

Figure 20: Creating of pads for wire-bonding.

It was important to make coating of Hall Bar/FET electrodes as the Al is not good material under graphene or other 2D materials. The Al suffers with surface oxidation which disallows forming of ohmic contact between electrode and 2D material. The same lift-off procedure was used in previous step. Only the sputtered material was Pt which can be exchanged with other materials suitable for ohmic contact guarantee (see **Figure 21**). All these materials must be compatible with XeF_2 etching which is done in the last fabrication step. The Au cannot be used due to the incompatibility with XeF_2 etching.

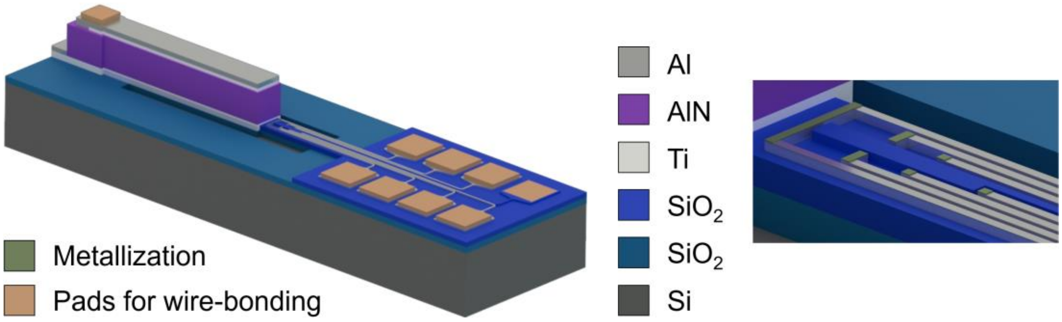

Figure 21: Metallization of source, drain and Hall Bar electrodes in position of electrical contact between electrodes and 2D material.

Last lithography is focused on graphene or another 2D material shaping (see **Figure 22**). These materials can be deposited using fishing technology, direct printing or drying of drops. Thin PR allowing to achieve more accurate resolution of pattern can be used in this step. It can be also used the standard PR AR-P 3540 with the thickness of 1 μm. The most important factor in this fabrication step is good adhesion between 2D material and substrate. The graphene or graphene oxide is then etched in O_2 plasma and the PR can be removed only by wet PR remover solution.

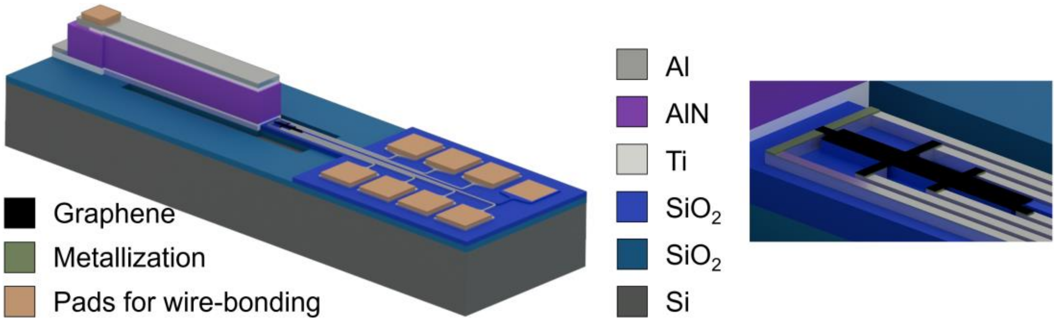

Figure 22: Shaping of graphene or another 2D material.

The last fabrication step is structure releasing using XeF_2 etching to remove underneath Si (see **Figure 23**). The Si etching is often done in mixture of XeF_2 and N_2. The ratio between XeF_2 and N_2 allows to control the etching speed and the presence of N_2 can improve the selectivity between Si and SiO_2 or SiN.

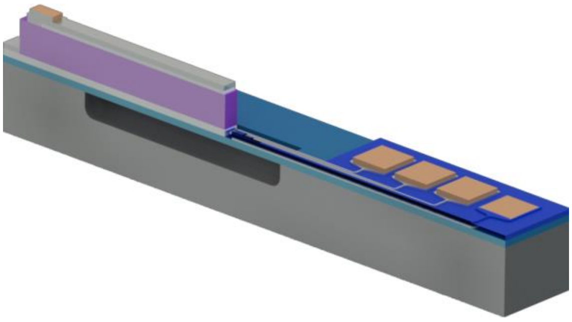

Figure 23: Releasing of piezoelectric resonator with Hall Bar/FET stretchable part using XeF_2 vapors.

9 Chip level packaging

The chip was fastened with a wax to the leadless carrier chip with 68 leadouts (LCC 68). LCC 68 was then placed in a printed circuit board (PCB) socket with SMA terminals (see **Figure 24**). Such mounted PCB was used for electrical and/or mechanical characterization of piezoelectric resonators.

The electrical interconnection of the structures was accomplished by wire-bonding using Au wire with diameter of 25 µm. The wire-bonding was utilized by thermosonic principle in which the substrate is subjected to pressure, temperature, and ultrasound, thereby ensuring that the wire is connected to the contact surface.

Firstly, a bond was formed on the top electrode on the chip and then on the LCC 68 pad. A very small pressure on the top electrode has to be chosen, because of the very thin layers, to avoid mechanical damage through AlN interlayer and thus shorten the electrodes. The compressive force for the first bond was chosen to 200 µN with ultrasound for 1 s. For the second bond, the compressive force was 350 µN with ultrasound for 250 ms.

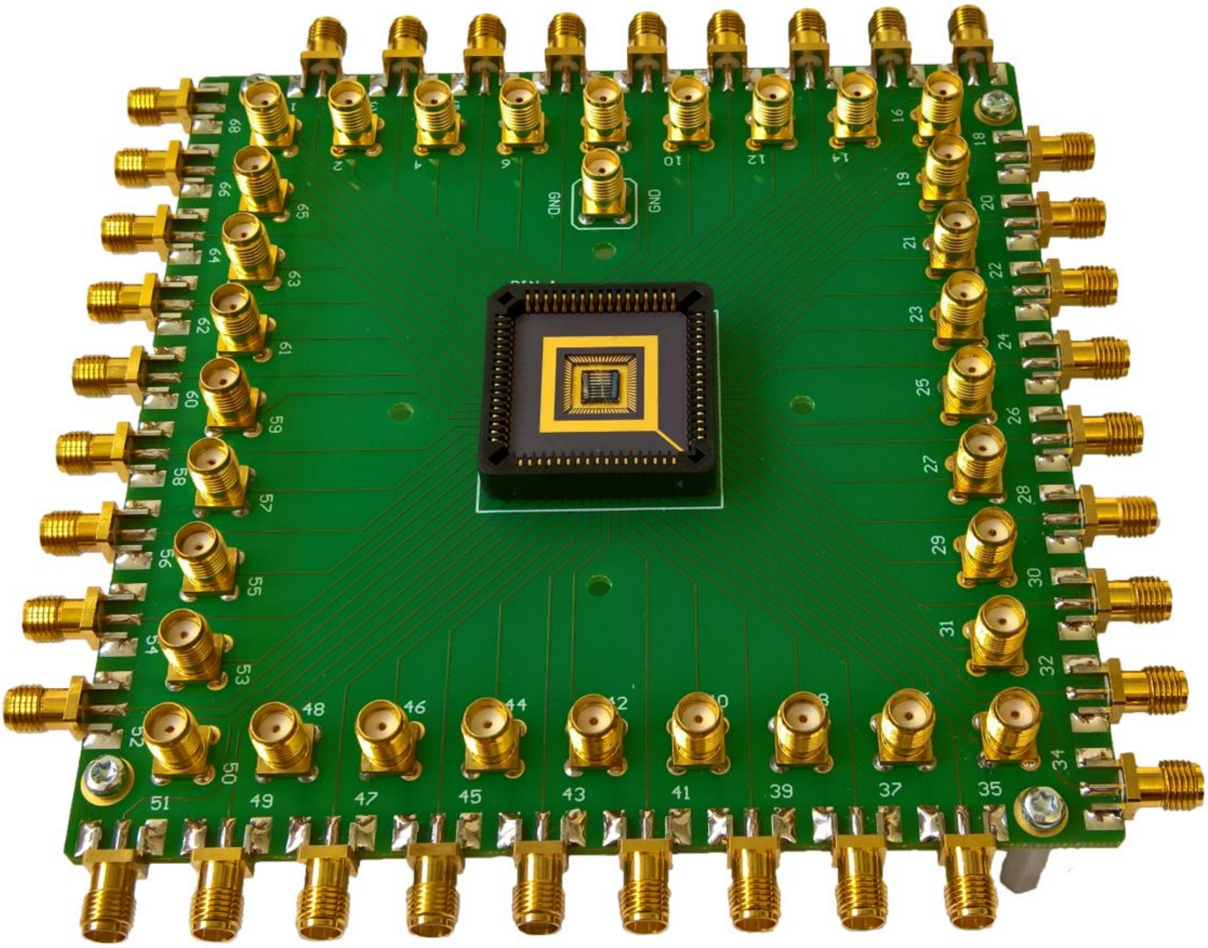

Figure 24: Fabricated chip with piezoelectric resonators with Hall Bar/FET structure mounted into the LCC 68 package placed in the PCB socket with SMA terminals for electromechanical characterization.

10 Verification of piezoelectric resonator model and function

Simple piezoelectric resonator was simulated and fabricated in this part. It was designed as one-clamped cantilever beam. The main aim was to compare the modelling using finite element method (FEM) and real fabricated structure. All physical simulations were done in ANSYS® Workbench 19.1. which uses FEM. The simulation software was also equipped with MEMS and piezoelectric add-on which is important for harmonic analyses.

The simple resonator (see **Figure 25**) which was fabricated and compared to FEM simulation consist of 5 layers: 200 nm SiO_2 / 80 nm Ti / 800 nm AlN / 15 nm Ti / 50 nm Al. The length (l) and width (w) which were used for comparison between fabricated resonator and simulation was 500 µm and 50 µm, respectively.

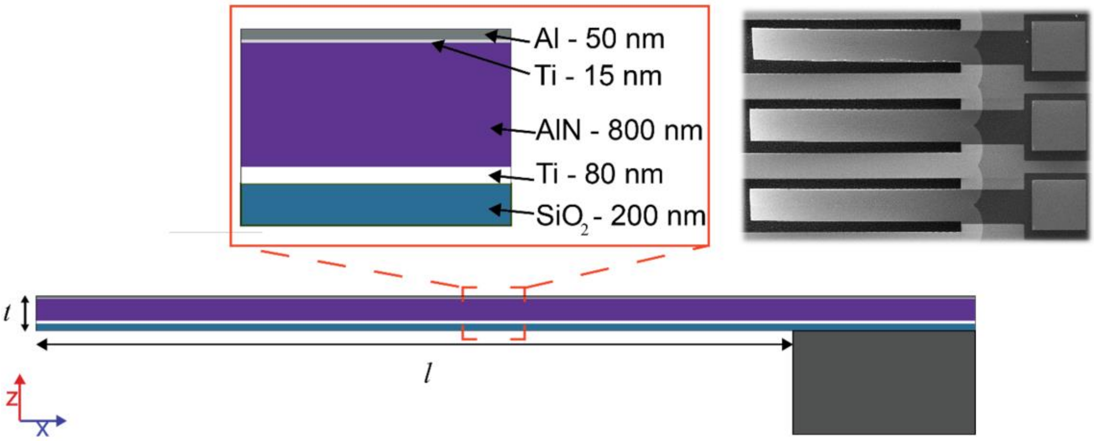

Figure 25: Scheme and SEM image of fabricated and simulated simple piezoelectric resonator.

10.1 FEM analyses

Firstly, the modal simulation was done. This simulation was used to find resonant modes without applied electrical or mechanical force. The one-clamped beam with above mentioned dimensions has the first resonant frequency (f_r) of 5361 Hz (see **Figure 26**). The resonator is fixed on the right side. The face was fixed as displacement with 0 value in all axes.

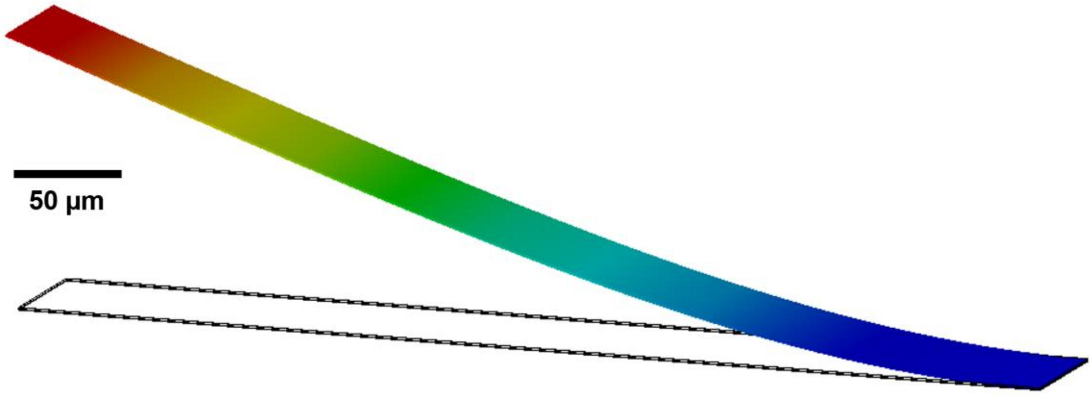

Figure 26: One-clamped beam piezoelectric resonator with first natural frequency of 5361 Hz.

Resonance frequencies (f_n) can be also described mathematically [57]. Consider a one-clamped beam with certain number of layers N for constant l with corresponding thickness (h_i), density (ρ_i) and Young´s modulus of elasticity (E) of each layer. The f_n can be described with following equation:

$$f_n = \frac{(\lambda_n)^2}{2\pi l^2}\sqrt{\frac{\int_h E(z-z_0)^2 dz}{\sum_{i=1}^{N}(h_i\rho_i)}},$$

where λ_n is very accurate simplified coefficient of modal parameter for one-clamped cantilever and z_0 is the position of neutral axis. On the other side, this equation cannot be used for more complicated structures. Therefore, the FEM simulations take a part as major analytic solution of multilayered piezoelectric resonators with more sophisticated design.

This simulation was also expanded on more dimensions such as w (see **Figure 27A**) and l (see **Figure 27B**) of piezoelectric resonators. These results are shown for the f_r. This analysis is useful for design and fabrication of structures with requested resonance frequencies.

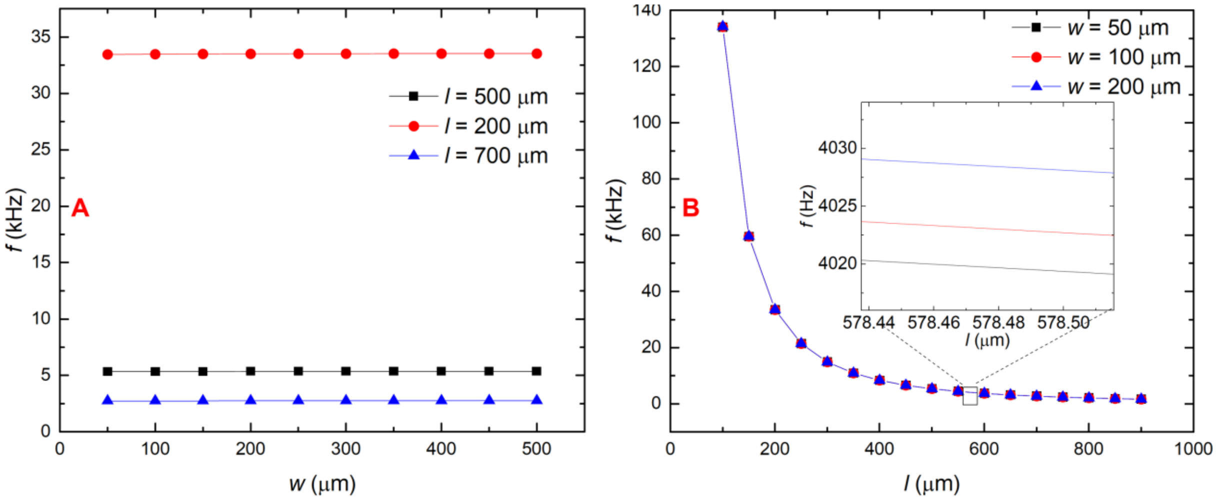

Figure 27: Dependency of the f_r on resonator dimensions:
A) Different w; B) Different l.

Performed simulations showed the expected dependency of resonance frequency on dimensions which corresponds with previously mentioned equation. It is obvious that the l of resonator has significant influence on value of f_r.

The next important is harmonic analysis which reveals the information about response of structure on harmonically applied load. The voltage with value of 1 V was applied across electrodes of piezoelectric resonator. The analysis was performed for frequency range from 1 Hz to 0.2 MHz. **Figure 28** shows the displacement in z-axis (D_z) at the loose end of cantilever.

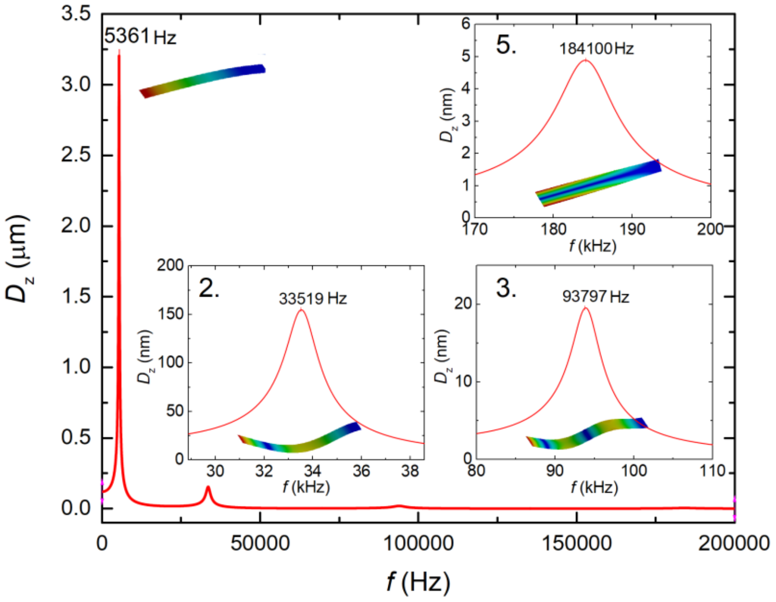

Figure 28: Displacement (at the loose end of beam) dependence on frequency of applied voltage of 1 V in range from 1 Hz to 0.2 MHz.

The FEM analyses show that displacement in resonance mode is higher than out of resonance frequency. This phenomenon is important for resonators aimed at strain inducing because the strain is a few orders higher then out of resonance. The strain results are described in chapter 17.

10.2 Characterization

This section compares simulated and measured parameters. Attention is paid to the measurement of resonator parameters using the LCR meter and the vibrometric method [58]. The Keysight E4990A impedance analyzer was used for the measurement. However, this method was not very appropriate due to the small excitation voltage to measure the first resonant frequency.

Therefore, an external mechanical excitation was used employing vibrometric measurements. Card generator NI-PXI 6259 generated signal (sine wave or white noise) which changed into vibrations in vibration exciter BK4809. This measurement was possible to perform only up to 10 kHz due to the limitation of the test socket and vibration exciter BK4809. On the other side, such a range is suitable for the measurement of f_r. The generated signal was changed to the vibrations which were measured on the socket housing by the PDV-100 laser vibrometer. The laser vibrometer measured the speed of the mechanical movement with a sensitivity of 200 mV·(mm·s^{-1})$^{-1}$. Output electrical signal from vibrometer was measured with card NI-6259. The generated charge on the resonator electrodes was measured at the same time. Its value was measured as the electric voltage via the IEPE100 electric charge amplifier. The LabVIEW application then used both spectral analyzes to calculate the ratio of the resonator signal and the signal from the vibrometer for each frequency (Q_1, Q_2) (see **Figure 29**).

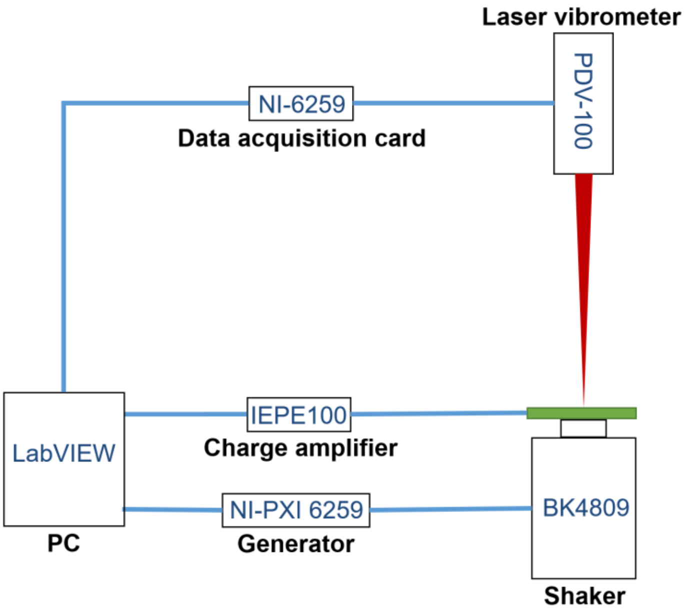

Figure 29: Schematic of vibrometric measurement.

The socket was initially loaded with white noise in the range from 1 kHz to 10 kHz to find the f_r. Q_1 and phase (φ) changes are depicted in **Figure 30**. The resonance peak was detected over time but suppressed by the surrounding environment. Since the resonator dimensions were several orders of magnitude smaller in comparison to the laser beam track, the exact resonator deflection value could not be measured. It would be necessary to focus the laser beam spot directly at the end of the resonator for exact determination of deflection in *z*-axis.

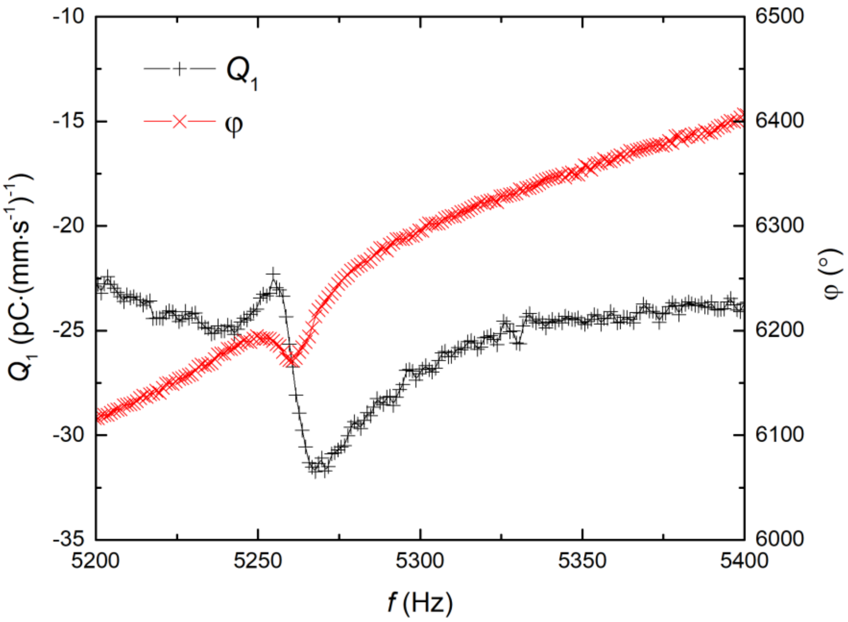

Figure 30: Frequency response for resonator with dimensions (50 × 500) μm excited by white noise.

The piezoelectric resonator was then excited by sine wave signal (see **Figure 31**) after the f_r was found. This measurement confirms the values obtained in previous analysis with white noise. Both types of measurements show the same f_r = 5263 Hz.

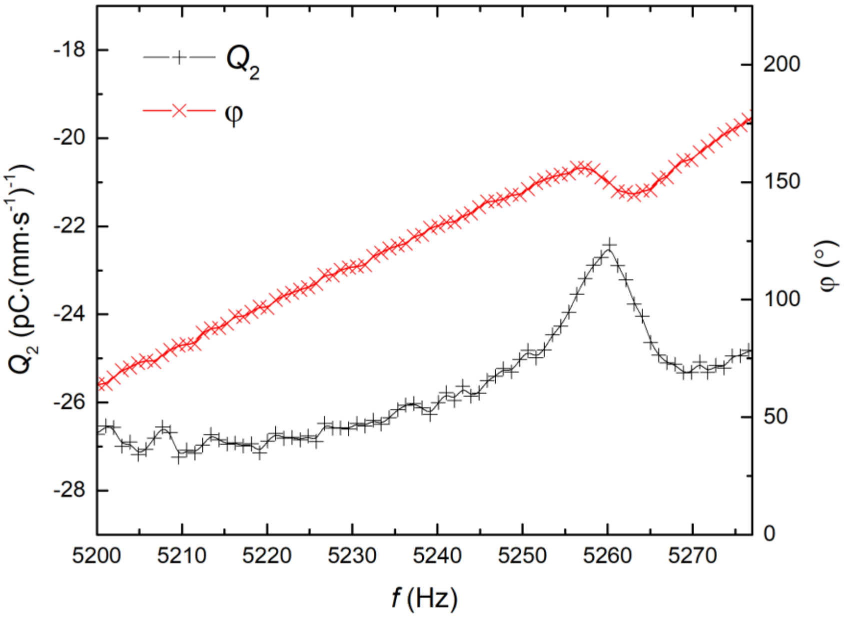

Figure 31: Dependence of the signal transmission on the frequency for a resonator of dimensions (50 × 500) μm with sine wave excitation.

Signal spectra from 30 kHz to 9 MHz were measured using the impedance analyzer Keysight E4990A. The similar structures described in literature [58] show the sharp resonance peaks with high value of quality factor (Q_f) in RLC measurement usually at units of MHz due to their dimensions. The resistance measurement of such resonator is shown in the **Figure 32** which confirms the literature results. The most significant change in resistance lies at the frequency of 4.23 MHz. The calculated value of Q_f was ≈ 4550.

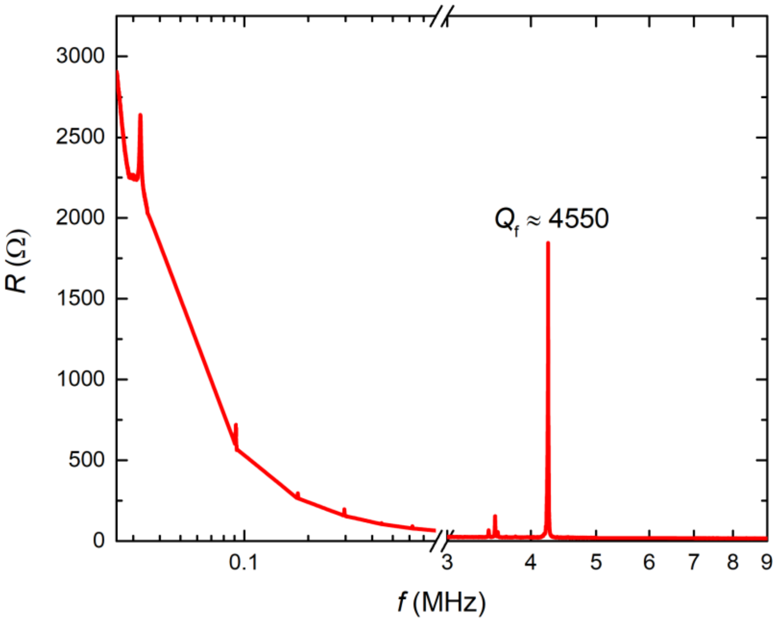

Figure 32: Dependence of resonator resistance with dimensioins of (50 × 500) μm on frequency.

The obtained values of resonance frequency by simulation (f_s) and measurements (f_m) are shown in **Table 1**. The calculated deviation of the measured values from the simulation is less than

≈ 3 % for all resonant frequencies. This simulation of model can be considered as reality corresponding, taking into account the number of parameters that may not be exactly determined. The values entered into the simulation such as thickness of each individual layer, interfaces formed during depositions and mechanical properties of individual materials, are almost impossible to determine with high precision. The third, sixth, and some higher resonant frequencies were not detected because of their toroidal movement or very low change of parameters.

Table 1: Comparison of measured and simulated values for resonator size (50 × 500) for detected resonant frequencies.

Resonance mode	**1.**	**2.**	**4.**	**5.**	**7.**	**…**	**42.**	**43.**
f_m [kHz]	5.26	32.11	91.21	178.33	295.72	…	3430	4230
f_s [kHz]	5.36	33.08	93.17	182.49	302.38	…	3530	4360

Such precision and definition of model including the previously determined properties (such as stress-free layers and known value of d_{33} etc.) is sufficient for modeling of more complex structures fabricated using the same materials and their processing.

10.3 Experimental resonator functionality verification

The resonators were mechanically powered by the sine wave at the certain frequencies including the f_r using the loudspeaker. This simple method should demonstrate the functionality of piezoelectric resonator and prove the eventual possibility of further using as audio filter bank which is often used in cochlear implant. The Keysight DSOX2014A oscilloscope was used to monitor the reaction of piezoelectric cantilever on loudspeaker. This reaction accompanied by generating of charge was measured as output voltage (V) since the piezoelectric resonator behaves in principle like an energy harvester. **Figure 33** shows the dependency of generated voltage on the intensity of the excitation sound. The value of the output peak to peak voltage (V_{PP}) corresponding to sound acoustic intensity of 74 dB was ≈ 998 µV.

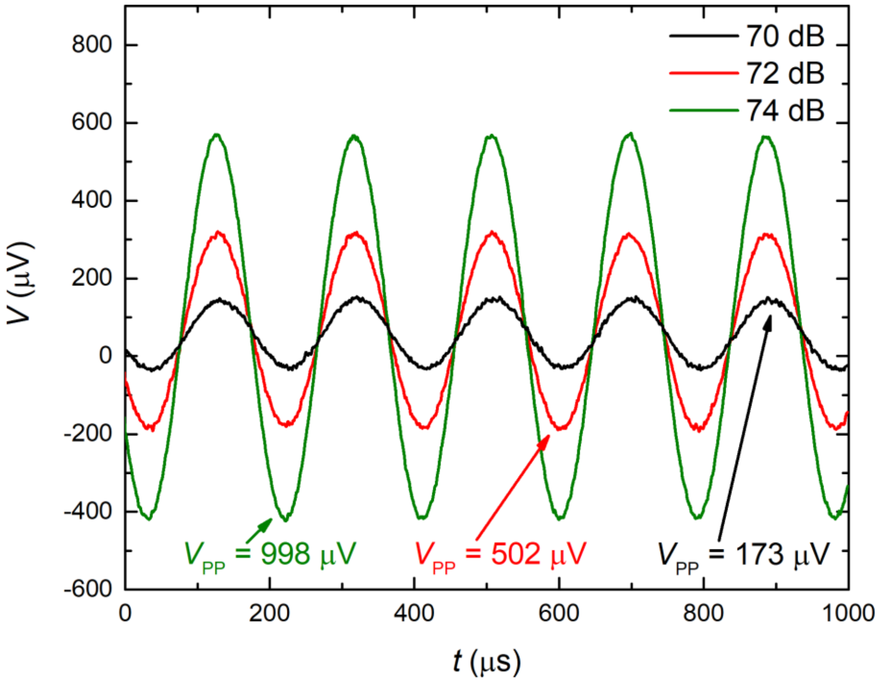

Figure 33: Voltage measured on piezoelectric cantilever beam resonator electrodes with dimensions of (500 × 50) μm at f_r = 5263 Hz with different values of sound acoustic intensity generated by loudspeaker.

The resonator was also excited with non-resonance frequency to compare the magnitude of output voltage on resonators electrodes. **Figure 34** shows that the output voltage at non-resonance frequencies of 5000 Hz and 5600 Hz is ≈ 30 % lower than the output voltage at resonance frequency of 5263 Hz when the sound acoustic intensity was constant.

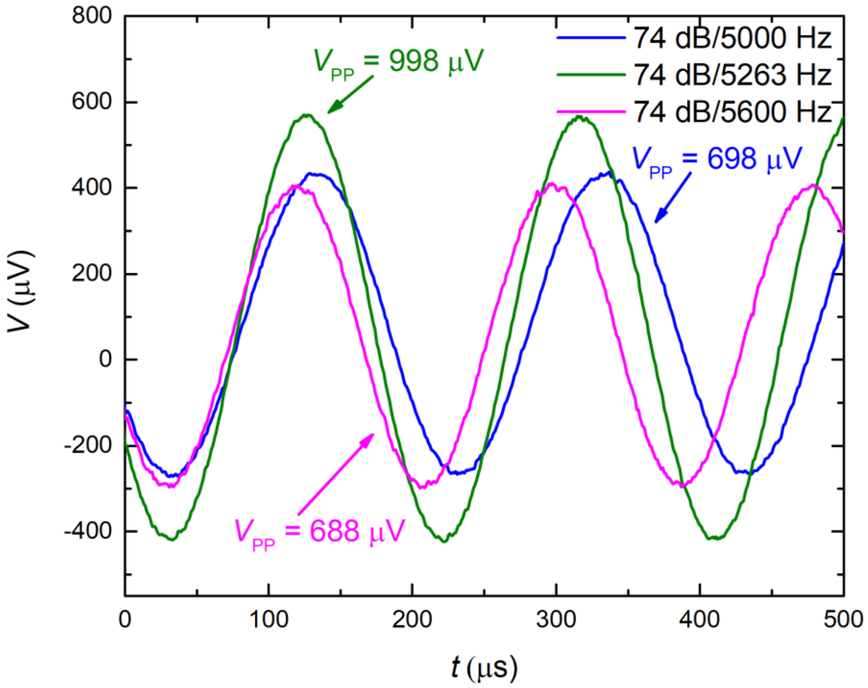

Figure 34: Voltage measured on resonator electrodes with dimensions of (500 × 50) μm at the non-resonance frequencies of 5000 Hz and 5600 Hz in comparison to voltage measured at f_r of 5263 Hz with constant sound acoustic intensity of 74 dB generated by loudspeaker.

Such results promise the possible utilization e.g. for cochlear implants in combination with sophisticated read-out circuits [59]. This simple fabrication technology allows to make the field of piezoelectric resonators with different dimensions on one chip. This possibility is important for coverage of whole spectrum of audibility.

11 Possible resonator functionalization

11.1 Motivation of the article

This article has its own motivation, but I was invited as contributor because there were few critical microfabrication steps and I also have experiences in metals detection in solution using standard electrochemistry methods such as cyclic voltammetry. The main aim of this manuscript was to increase the active surface area with nanostructures. Fabricated nanostructure has ≈ 1440× larger surface area than standard thin film. There are a lot of toxic metals which presence must be detected in very short time because they are dangerous even in ppb or ppm concentrations.

Fabrication of these structures has a few similarities to fabrication of piezoelectric resonators. This device contains the standardly used metal and dielectric materials which must be shaped. It was important to decide how to fabricate this structure. The major factors are the dimensions and etching chemistry compatibility of all materials. The etching of gold is also problematic mainly if it is on thin layer of some material which must be preserved undamaged after the gold is removed.

11.2 Conclusion on the article

I did single mask lithography process where the wet etching is not possible due to small dimensions and the underetching must be eliminated. The only one possible way how to etch materials was to use ion-milling method using Kaufman ion-beam source because gold is not possible to etch using RIE method. Therefore, it was important to stop the etching when the underlayer is revealed. The mass spectrometer was used for this purpose which helped me to stop etching in the right time. This technology can be alternatively used during piezoelectric resonator fabrication.

Final structure of this device can be modified by gold functionalization. This structure in combination with piezoelectric resonator can be used as gravimetric sensor. For example, thiol-based crosslinker could be used for biomolecules (such as proteins) adsorption and their subsequent detection.

11.3 Contribution

I did all lithography and microfabrication steps and SEM images. I also helped to solve a few issues of voltammetry measurements.

11.4 Article 6

Article **Nanostructured Gold Microelectrode Array for Ultrasensitive Detection of Heavy Metal Contamination** [60] was published in **Analytical Chemistry** (2017 IF 6.042) in **January 2018.**

analytical chemistry
Article
Cite This: Anal. Chem. 2018, 90, 1161−1167
pubs.acs.org/ac

Nanostructured Gold Microelectrode Array for Ultrasensitive Detection of Heavy Metal Contamination

Pavel Podešva,[†] Imrich Gablech,[‡] and Pavel Neužil*,[†,‡]

[†]Northwestern Polytechnical University, School of Mechanical Engineering, Department of Microsystem Engineering, 127 West Youyi Road, Xi'an, Shaanxi 710072, P. R. China

[‡]Central European Institute of Technology, Brno University of Technology (BUT), Purkyňova 656/123, 612 00 Brno, Czech Republic

Supporting Information

ABSTRACT: Availability of potable water is a problem especially in developing countries as their water sources are often contaminated biologically as well as by heavy metals. Electrochemical methods are suitable for field application to monitor heavy metal contents. Noble metal electrodes with large surface areas are the subject of intensive development as they can yield an improved signal-to-noise ratio, enhanced sensitivity, and lower limits of detection (LOD). Here, we present a nanostructured Au microelectrode array subsequently modified by selective electrodeposition in lithographically defined circles within a partially cross-linked gelatin layer. This method increased its surface area by a factor of ≈1440 in comparison with an original lithography-based prepared array. The Au surface properties can be tailored by a degree of gelatin layer cross-linking. We used this array for an ultrasensitive detection of the As^{3+} ions content by stripping voltammetry achieving LOD of ≈0.0212 parts per billion (signal-to-noise ratio = 3.3), 470× below the content limit recommended by the World Health Organization for potable water. These nanostructured arrays were used to detect ions of other metals such as Cr, Cd, Hg, Cu, and Sb. In combination with a portable electrochemical device, we can envision an ultrasensitive heavy metal detection system for field application to monitor heavy metal contamination.

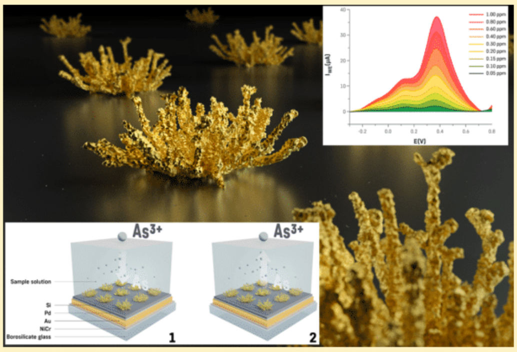

We present an array of microfabricated electrodes which are subsequently modified to 3D microstructure by electrochemical deposition, showing greatly enhanced surface area and, thus, sensitivity for electrochemical detection. Availability of potable water is a key problem in number of developing countries as their water sources are contaminated with biological or metal ion pollutants. The biological contamination can be eliminated in a rather simple way but the key problems are metal ion pollutants such as As, Cr, Cd, Hg, Pb, and Zn.[1,2] Also developed countries water sources often suffer from metal ion pollutants presence. One of the most severe pollutant is highly toxic arsenic. Its total ions (As^{3+} and As^{5+}) content in drinking water is limited below level of 10 μg L^{-1} (10 ppb) by World Health Organization (WHO) guidelines.[3−5]

Common analytical methods to monitor As ion level contamination can be split into two groups: spectral and electrochemical. Spectroscopic methods such as hydride generation coupled with atomic absorption and emission spectrometry or inductively coupled plasma with mass spectrometry have detection limits well below the recommended level and are especially suitable for centralized routine analysis of water and mineralized solid samples such as soils or tissues.[4,6]

One of the most commonly used electrochemical methods to detect metal contamination is anodic stripping (linear or differential) voltammetry[6] with detection limits comparable to classical spectrometric methods.[7] The instruments are relatively simple and can be miniaturized for field measurements and point of detection for waste and drinking water monitoring.

Anodic stripping voltammetry (ASV) is a powerful method used to detect traces of heavy metals in environmental, clinical, and industrial samples. The system is based on a three-electrode configuration, electrically grounded working electrode (WE), reference electrode (RE), and an auxiliary (counter) electrode (AUX). The ASV consists of two steps: preconcentration (PR) and stripping (ST). The extensive duration of the PR step at the reduction potential of selected metals results in a significant amount of this metal being deposited at the WE surface from a relatively low concentration in the tested sample. Then, the applied potential is scanned to a higher level, and preconcentrated metals at the WE surface are oxidized back to their cationic forms at their specific potentials, resulting in an electrical current (I_{WE}) with peak amplitude ($I_{WE\ (Peak)}$)

Received: September 12, 2017
Accepted: December 1, 2017
Published: December 1, 2017

DOI: 10.1021/acs.analchem.7b03725
Anal. Chem. 2018, 90, 1161−1167

corresponding to the amount of predeposited metal and proportional to the concentration of analyte in the sample.

$$\text{PR step:}\quad M^{n+} + ne^- \rightarrow M^0$$

$$\text{ST step:}\quad M^0 \rightarrow M^{n+} + ne^-$$

This method provides a sensitive, qualitative, and quantitative detection of metals.[8]

Stripping voltammetry with Hg-based WEs has been frequently used with high reproducibility and sensitivity for heavy metal detection. However, there is a growing demand for Hg-free sensors and instruments. Silver suffers from signal interference with water electrolysis.[9] WEs made of Au provide a more sensitive response to As oxidation than other WE materials. Gold also has higher oxygen overpotential than Pt, thus, Au was found to be a superior material for WEs.[7,10,11] Numerous configurations of Au electrodes have been used previously, such as discs, rotating discs, polycrystalline Au electrodes, Au microelectrodes, and microelectrode arrays as well as various nanostructured films serving as a working electrode surface.

Nanostructured materials exhibit different and, in many cases, superior properties compared with bulk material. Electrodes with nanostructured surfaces induce specific interactions with the analyte, which may sometimes induce lowering of the required overvoltage for the process to occur and, consequently, even lead to higher and sharper current peaks at less extreme potentials.[12]

Nanostructured materials have typically 2×−1000× larger surface area than planar materials of the same size and are formed by oriented and controlled or random morphology. Such enhanced surface areas allow chemical sensing and, particularly in electrochemistry, improved sensitivity and detection limits. The increased surface area allows the immobilization of greater amounts of reagent or analyte on the surface without changing the overall electrode dimensions. This leads to larger currents, as Faradaic current usually scales linearly with electrode area and significantly larger electrode area can yield better signal-to-noise (SNR) ratios, enhanced sensitivity, and lower detection limits.[12,13]

Nanostructured surface area electrodes are the subject of intensive development and have been fabricated using a number of different approaches.[13−15] These approaches can be divided into two main groups: (1) Top-down techniques are based on disassembling the main bulk material as by etching, dealloying, laser ablation, or lithographic patterning. (2) Bottom-up techniques build the structure from the base, as through electrodeposition, to grow various types of dendritic structures. These methods use hard templates such as alumina, zeolites, porous materials, self-assembled spherical particles, and soft templates like H_2 bubble formation, surfactants, liquid crystals, or polymers. Another subgroup of bottom-up techniques are various self-assembly methods using metal nano- and microparticles of various shapes and using a number of assembling strategies.[12,16,17]

Arsenic is a metalloid with specific electrical resistance of ≈333 nΩ m at 20 °C, ≈15× higher than the one of Au. The WE surface becomes saturated with the As during the PR step once the deposited As^0 exceeds the formation of a monolayer. Then, the monolayer starts to limit the electron transfer, suppressing the deposition rate of As from the solution. This results in a nonlinear relationship between As concentration and the stripping current peak.[18]

Preconcentration efficiency is influenced by applied voltage, rising from 0 V to −0.4 V; however, for more negative potentials, PR efficiency decreases again due to H_2 generation, which effectively blocks the electrode surface and decreases the current. It was reported that PR potential of −0.25 V or −0.5 V yields ≈50% efficiency of PR at −0.4 V.[19] In the past, the PR efficiency and prevention of electrode saturation was increased by the codeposition of As with Cu, forming a conductive intermetallic phase.[20,21]

Total As ion concentration is the sum of electrochemically active As^{3+} and electrochemically inactive As^{5+}. In the first step, the As^{3+} concentration is determined. Then the As^{5+} is reduced into As^{3+}, which is again quantified. The reduction can be conducted either electrochemically or by various compounds compatible with stripping voltammetry such as ascorbic acid,[21] sodium sulfite,[22] or α-cysteine.[23,24] This has to be performed in an acidic environment, such as HCl, HNO_3, or $HClO_4$ so that As^{5+} can be reduced to As^{3+} and stabilized in the trivalent cationic form. Stripping peak (method sensitivity) rises with decreasing pH, although at $pH < 1$, method sensitivity decreases due to the low overpotential of Au to the H_2 and supporting electrolyte with concentration of 1 M acid is typically selected in ASV protocols as a good compromise. During ASV, the elimination of dissolved oxygen is necessary to prevent the As stripping signal from decreasing with time.[25] This can be done by bubbling an inert gas through the sample solution, such as N_2 or Ar or chemically by adding hydrazine hydrochloride to the solution as a stabilizing agent for the elimination of dissolved O_2.[24]

The limit of detection (LOD) of As^{3+} performed by ASV has greatly improved through method developments over the past 50 years from parts per billion (ppb) to the subppb level. Thus, far, the lowest LOD reported is ≈0.0096 ppb using carbon WE modified by Au nanoparticles and a linear sweep stripping voltammetry (LSV) method with ≈180 s PR time (t_p).[7]

■ EXPERIMENTAL SECTION

List of Used Chemicals. Gelatin (bovine, alkaline, B type, 260 bloom). Arsenic analytical standards with weight concentration of 1 g L^{-1}, n-hexane, glutaraldehyde, 1H,1H,2H,2H-perfluoro decyltriethoxysilane (FAS-17), gold(III) chloride, sodium carbonate, potassium ferrocyanide, trypsin, potassium hydroxide, cysteine, all analytical grade. Nitric and sulfuric acids were of ultrapure grade. Water used for all experiments was deionized with specific resistance > 18.0 MΩ cm at temperature of 25 °C.

List of Used Instrumentation. We used a dip coater, electrodeposition and all electrochemical measurements were conducted using DY2116B potentiostat (Digy-ivy Inc.) in three electrode arrangement with Pt wire counter electrode (CE) and reference electrode (RE) Ag/AgCl/KCl with concentration of 3 M and scanning electron microscope Mira 3 (Tescan a.s., Czech Republic).

Nanostructured Au Arrays Fabrication. We fabricated the devices at glass substrate (wafers) with a diameter of ≈100 mm (see Figure 1). First the wafers were covered with sputtered sandwich layer of NiCr, Au, Pd, and Si with thicknesses of ≈50 nm, ≈200 nm, ≈20 nm, and ≈200 nm, respectively. The Pd was used as an adhesion layer for Si.[26] Then we performed optical lithography and then patterned the sandwich metal by Ar ion-based ion milling. We stopped the etching at the Au layer using secondary ion mass spectroscopy-based end point detection. Subsequently we diced the wafers

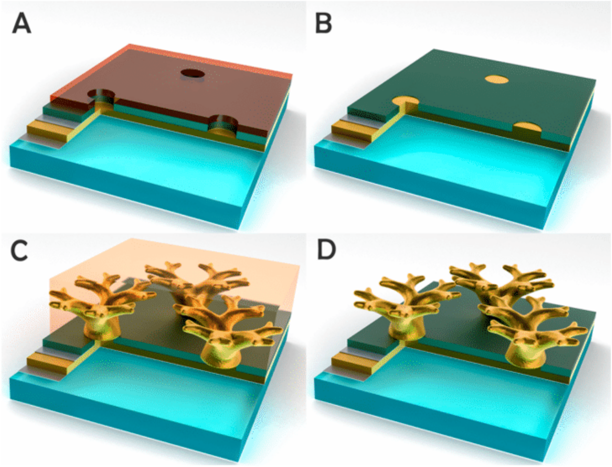

Figure 1. (A) NiCr/Au/Pd/Si sandwich structure on a glass wafer with photolithographically opened circular windows and ion-milling-etched Si and Pd layers stopping at the Au layer. (B) Chip after wafer dicing, Au electroplating, and photoresist removal. (C) Gelatin deposition by dip-coating and nanostructured Au formation. (D) Final array of nanostructured Au after gelatin removal and cleaning. (3D model of nanostructured Au downloaded from Linden, S. v. d. Binary Roots, https://grabcad.com/library/binary-roots (2012), which we would like to acknowledge here).

into individual chips with dimensions of (≈10 × ≈20) mm using a diamond blade dicing saw and then removed the photoresist layer. We washed the substrate with water followed by ethanol. Surface was then cleaned by O_2 plasma for ≈300 s using a power of ≈100 W, followed by FAS-17 coating by the chemical vapor deposition (CVD) method. The FAS-17 formed a hydrophobic layer at the Si preventing Au electrodeposition within Si covered areas.

Next we increased the Au layer thickness in opened circles of the array by ≈200 nm by electroplating using $KAu(CN)_2$ Au plating solution[27,28] for ≈10 min at potential of ≈−0.7 V at Ag/AgCl/KCl RE. The electrodeposited Au covered sidewall of Pd layer avoiding its subsequent interfering with electrochemical measurements.

The chips were then treated by O_2 plasma for ≈25 s using power of ≈100 W to make surface hydrophilic without removal of FAS-17 from pores. The chips were dip-coated with a gelatin layer using ≈12% weight to volume water solution maintained at ≈40 °C with lifting speed of ≈75 mm min^{-1}. Thickness of gelatin layer in the dry state was (3.28 ± 0.11) μm (mean ± standard deviation).

Next the gelatin layer was cross-linked by ≈0.05% glutaraldehyde solution for ≈12 h at ≈4 °C, and then the glutaraldehyde was removed by washing in water. We optimized the degree of gelatin cross-linking by changing reaction time in the glutaraldehyde bath to achieve the maximum surface area of nanostructured Au.[14] The chip was immersed into a ferrocyanide gold plating solution for ≈1 min. It caused the gelatin to swell and gets saturated with the solution. The nanostructures Au was then deposited using constant potential of ≈−1.8 V at RE for ≈2400 s. The mean value of i_{WE} was ≈84.9 μA corresponding to current density of ≈103 mA cm^{-2}. The total electric charge was ≈0.204 C corresponding to ≈415.8 μg of deposited nanostructured Au. Once the electrodeposition of Au was completed, the gelatin

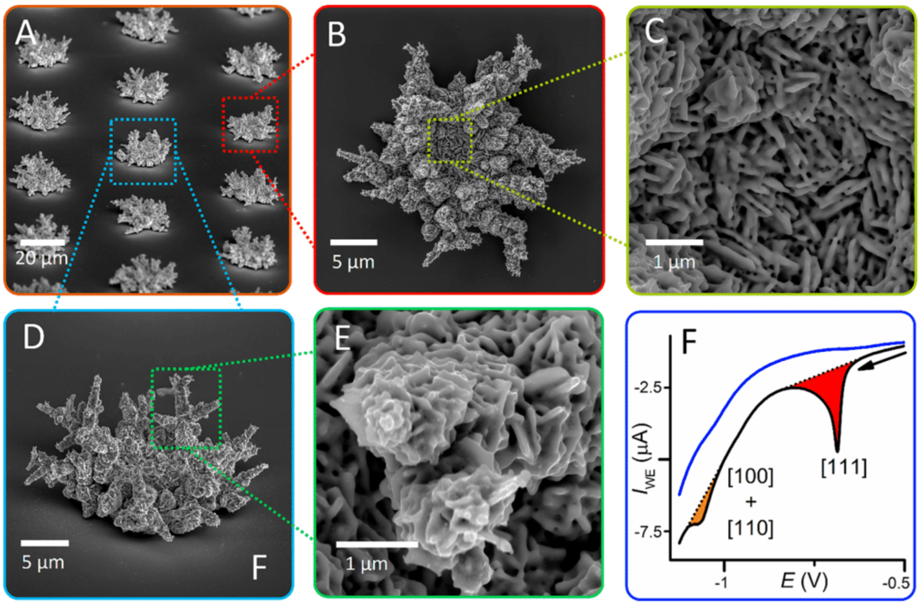

Figure 2. Micrographs of an array of nanostructured Au microelectrodes. (A) Overview of nanostructured clusters array showing shape variability. (B) Detailed top view of a single nanostructured Au cluster showing flat central part and branching outer region. (C) Detail of the cluster central part with tabular crystals structure. (D) Side overview of nanostructured Au cluster showing that peripheral structure part is not in contact with substrate and growing upward. (E) Detail of the branch with individual Au leaf-like structures resembling *Araucaria araucana* leaves arrangement. (F) Reductive desorption of cysteine. The nanostructured Au electrode was immersed in ≈10 mM solution of cysteine for ≈15 min at ambient temperature and then rinsed with water. Subsequently, we performed CV in 0.5 M KOH with set scan rate (v) of 50 mV s^{-1} in the range between ≈0 V and ≈− 1.2 V at the Ag/AgCl RE and monitored the cysteine desorption (black curve). The peak area (red) corresponding to Au with domain of [111] is ≈4.35× larger than the peak area (orange) corresponding to Au with domain of [110] combined with the one of [100]. The blue curve represents the third cycle.

DOI: 10.1021/acs.analchem.7b03725
Anal. Chem. 2018, 90, 1161−1167

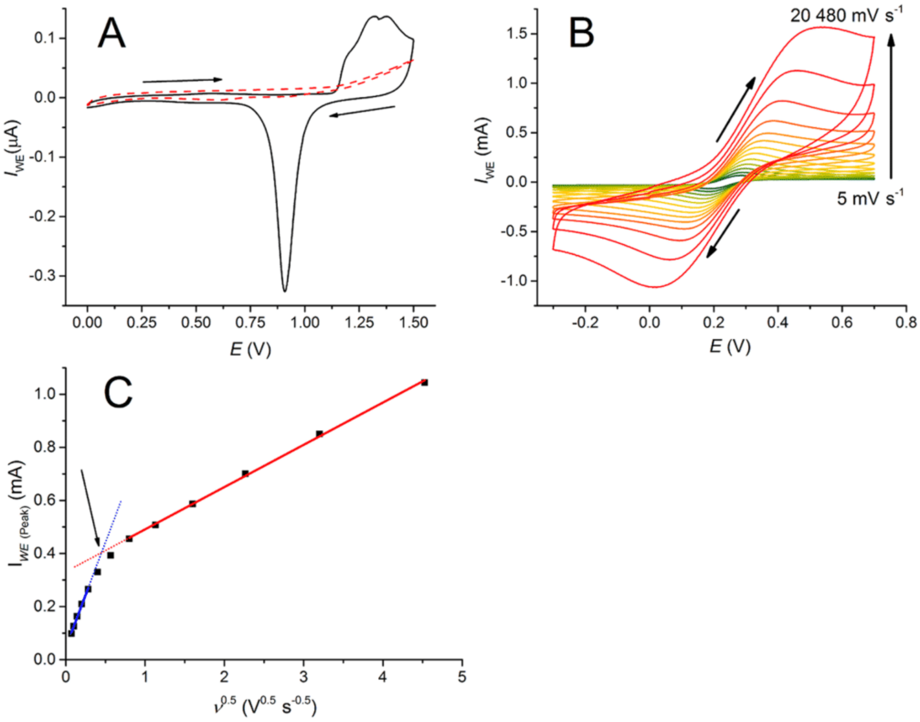

Figure 3. (A) Cyclic voltammogram in 0.5 M H_2SO_4 using a set scan rate of 100 mV s^{-1} of nanostructured microelectrode array (black line) and microelectrode array without nanostructure (red line). The electroactive area of nanostructured Au microelectrode array was calculated to be ≈110.87 mm^2, representing an approximate 1440-fold enlargement compared with the area of the flat Au microelectrode. (B) CV of nanostructured microelectrode array in Fe^{2+}/Fe^{3+}solution with concentration of ≈10 mM with ν (5, 10, 20, 40, 80, 160, 320, 640, 1 280, 2 560, 5 120, 10 240, and 20 480) mV s^{-1}. (C) Plot of $Fe^{3+}I_{WE(Peak)}$ vs $\sqrt{\nu}$. We found that the plot has two linear regions for ν 5−80 mV s^{-1} (lower ν) and 640−20 480 mV s^{-1} (higher ν) (mean ± standard deviation), respectively, with the transition nonlinear region in between those two. Amplitudes of s were (790 ± 32.6) μA V$^{0.5}$ s$^{-0.5}$ and (159 ± 2.57) μA V$^{0.5}$ s$^{-0.5}$ for lower and higher ν, respectively, with a crossing of linear regressions at ≈204 mV s^{-1}. The amplitudes A measured using the Fe^{2+}/Fe^{3+} redox system and determined by the Randles−Sevcik equation, equal 10.95 ± 0.45 mm^2 and 2.21 ± 0.04 mm^2 (mean ± standard deviation) for lower and higher ν, respectively, representing an approximate 132-fold and 26.8-fold increase of electroactive area compared with the planar electrode area.

was decomposed with ≈0.5% trypsine solution for ≈48 h at temperature of ≈40 °C and all its traces removed using ≈5% KOH solution also at temperature of ≈40 °C.

Au Surface Activation. Prior to the As^{3+} electrochemical experiments, the nanostructured Au electrodes were first cleaned to remove adsorbed organic traces by using a mixture of three parts NH_3 solution (≈25% by weight of NH_3) and one part of aqueous H_2O_2 (≈30%) for ≈5 min at ambient temperature followed by rinsing with deionized water and drying with N_2. Subsequently, the electrode surface was activated by CV in ≈0.5 M H_2SO_4 solution at a set ν of 100 mV s^{-1} between potentials ≈−200 mV and ≈1500 mV at the Ag/AgCl/KCl RE until a stable voltammogram was observed, which typically required 40−60 cycles.[19] Once the activation process was completed, the electrode was rinsed with water, dried with N_2, and immediately used.

We used ≈0.01 M HNO_3 solution as the supporting electrolyte for all As ion determination experiments. Each sample was first purged by N_2 for ≈10 min prior to analysis and the electrochemical cell with a volume of ≈100 mL was permanently stirred and capped by N_2 to avoid contamination with O_2.

■ RESULTS AND DISCUSSION

We used the software "Nanolithography Toolbox" to design electrodes comprising an array of circles in hexagonal configuration with diameters of 5 μm, pitch of 50 μm, and covering an area of 3 mm × 3 mm.[29] The combined geometric area of all circles was ≈8.24 × 10^{-2} mm^2.

The devices were fabricated using process described above in the Nanostructured Au Arrays Fabrication section. Then we first determined the morphology and homogeneity of the deposited Au (Figure 2A−E) using a scanning electron microscope (SEM). This nanostructured material had hierarchical configuration with its main body resembling a tree trunk growing from lithographically defined circular areas. Then, the main trunk divided into individual branches with each exhibiting further forking. All these structures were formed by interconnected Au leaves with a thickness of ≈100 nm and with pore diameters ranging from ≈50 to 300 nm, greatly enhancing the total nanostructured Au surface area and are significantly different from dendritic structures obtained by other methods[30] (Figure 2D,E). The nanostructured Au had an obvious enlargement of surface area with respect to the original Au circle.

Nanostructured Au surfaces consist of three main crystallographic orientations, Au[111], Au[100], and Au[110], with each exhibiting different binding strengths toward an attached thiol group of the self-assembled monolayer (SAM). A method to determine crystallographic orientation is based on desorption of short-chain thiol molecules, such as cysteine or mercaptopropionic acid, during cyclic voltammetry (CV).

DOI: 10.1021/acs.analchem.7b03725
Anal. Chem. 2018, 90, 1161−1167

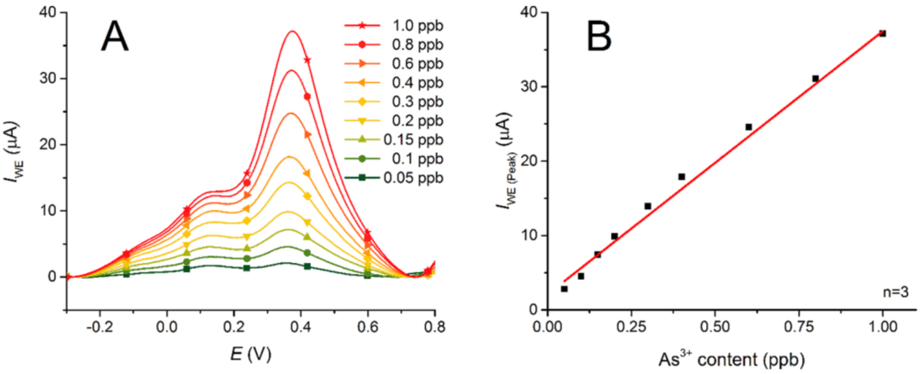

Figure 4. Determination of LOD for nanostructured gold microelectrode array by standard addition and calibration curve for the same. (A) Arsenic ion concentrations from ≈0.05 ppb to ≈1 ppb were measured at v 20 V s^{-1} and determined from $I_{we(Peak)}$. Because of complex shape of peaks, we did not use peak area readings. (B) From the calibration curve for the As^{3+} concentration range from ≈0.05 ppb to ≈1 ppb, we found the LOD value of ≈0.0212 ppb and LOQ ≈ 0.0643 ppb.

Reductive desorption of a cysteine SAM during CV exhibits three distinguished peaks at −700 mV, − 1000 mV, and −1100 mV at the Ag/AgCl/KCl RE for Au surfaces with orientations of Au[111], Au[100], and Au[110], respectively. The ratios between peak current amplitudes reflect the ratios of the crystallographic domains. These results have been reported.[31−33] We used this method to characterize different surface Au crystallographic domains in the nanostructured Au (Figure 2F). We estimated that the ratio of surface Au[111] domain to the sum of surface area with the Au[100] and Au[110] domains was ≈4.35:1.

We then determined the total electrochemically accessible (active) area (A) using a method based on charge transfer amplitude during the electrochemical reduction of the gold oxide monolayer in ≈0.5 M H_2SO_4 solution according to the equation:

$$A = \frac{Q_d}{S} \cdot v \tag{1}$$

where Q_d is the charge density required to reduce the gold oxide, S is the area of the cathodic peak, and v is the set scan rate (Figure 3A).[34] We found that A was ≈110.87 mm^2, an ≈1440-fold increase compared with the original ≈0.0824 mm^2 array area.

We then determined A again using CV measurements of ≈10 mM Fe^{2+}/Fe^{3+} in ≈100 mM KCl supporting electrolyte at different v (Figure 3B) as per the Randles−Sevcik equation:[35]

$$I_{WE(peak)} = 0.4463nFAC\left(\frac{nFvD}{RT}\right)^{0.5},$$

$$s = \frac{dI_{WE(peak)}}{d\sqrt{v}} = 0.4463nFAC\left(\frac{nFD}{RT}\right)^{0.5}$$

and

$$A = \frac{s}{268\,600n^{3/2}D^{1/2}C} \tag{2}$$

where s is defined as $dI_{WE(peak)}/d\sqrt{v}$, n is the number of electrons transferred in the redox event, F is the Faraday constant, D is the diffusion coefficient of Fe^{2+} ions, C is the concentration (analyte activity), R is the universal gas constant, and T is the thermodynamic temperature. We found that the nanostructured Au array exhibits two distinguished regions with different amplitudes of A_1 = (10.95 ± 0.45) mm^2 and A_2 = (2.21 ± 0.04) mm^2 (mean ± standard deviation) for lower and higher v, respectively, representing an approximate 132-fold and ≈26.8-fold increase of A (Figure 3C).

There is a significant difference of ≈50 and ≈10 times between A values determined by these two methods. The first method is based on the removal of a surface Au oxide monolayer; thus, the method detects on practically the entire electrode surface. The first method is also influenced by experimental conditions such oxidation potential, scanning rate, and time at the oxidation potential.[36] The second method depends on the diffusion from the solution; thus, only peripheral parts of the Au structure are still active with increasing amplitude of v while the internal parts of the structure operate in a locally depleted solution.

The test sequence consisted of a cleaning step (CS) with potential ≈400 mV for ≈30 s and PR was performed at potential ≈−400 mV for ≈300 s. We performed a series of tests to construct a calibration curve with As^{3+} concentrations in the range of ≈0.05 ppb to ≈1 ppb to determine the system LOD (Figure 4A).

LOD is defined as 3.3 × SD/S, where SD is the standard deviation and S is the slope of calibration curve. The limit of quantification (LOQ) is then defined as ≈10 × SD/S.[37] We determined the LOD value to be ≈0.0212 ppb and LOQ ≈ 0.0643 ppb (Figure 4B).

We also constructed a calibration curve for As^{3+} concentration in the range of ≈0.125−5 ppb and found LOD ≈ 0.0423 ppb and LOQ ≈ 0.128 ppb (Supporting Information). We then tested the linear response region of the nanostructured electrode array to increase t_p duration using the concentration of As^{3+} in a solution of ≈5 ppb and determined the maximum value of t_p ≈ 800 s, where further increases of t_p start to deviate from linear behavior (Figure S2 in the Supporting Information). After optimization, we found v of ≈10 V s^{-1} as a good compromise between $I_{WE(peak)}$ and its broadening. The method of data extraction is described in Supporting Information.

■ CONCLUSION

We developed a process to create an array of islands of nanostructured Au on a glass substrate. These islands were defined by UV lithography and nanostructured Au was formed by selective electrodeposition of Au in a gelatin matrix. This nanostructured Au had the surface area approximate 1440×

greater than the original one. The surface of nanostructured Au consisted of ≈81% electrically active surface area of Au with crystallographic orientation [111]. The properties of such structures can be modified further by changing the lithography design, such as the shape, size, or pitch of islands or by processing parameters, such as degree of gelatin cross-linking, electrodeposition potential, or time.

We used this nanostructured Au array to determine As^{3+} concentration in water using the LSV method. We achieved one of the best LOD values reported thus far (≈ 0.0212 ppb with ≈300 s predeposition time in an electrochemical cell with volume of ≈100 mL.[7,10,23] Further improvement of the LOD could be achieved in ≈1 M HCl electrolyte, which is recommended for the best deposition efficiency in the detection of As^{3+} ions.[9]

The LSV measurement using nanostructured Au array had good repeatability, thus this material is suitable for the long-term monitoring of As^{3+} or other heavy metal ion contamination in drinking or wastewater. We can foresee its integration with a simple instrumentation tool as a key part of a portable system for environmental monitoring[38] and also possibly biosensing.[39]

■ ASSOCIATED CONTENT

Ⓢ Supporting Information

The Supporting Information is available free of charge on the ACS Publications website at DOI: 10.1021/acs.analchem.7b03725.

Calibration curve for range 0.125−5 ppm As^{3+}, linearity of I_{WE} vs E with t_p as parameter, and method of data extraction (PDF)

■ AUTHOR INFORMATION

Corresponding Author

*Phone: +86 150 9133 1869. E-mail: pavel.neuzil@nwpu.edu.cn, pavel.neuzil@gmail.com.

ORCID

Pavel Podešva: 0000-0001-7083-6522
Pavel Neužil: 0000-0001-9040-281X

Notes

The authors declare no competing financial interest.

■ ACKNOWLEDGMENTS

This work was financially supported by 1000 Foreign Expert Plan of P.R. China, Award Number G2016QR0001, and partially supported by the Ministry of Education, Youth and Sports of the Czech Republic under the Project CEITEC 2020 (Grant LQ1601) and by the OP VVV CEITEC Nano+ CZ.02.1.01/0.0/0.0/16_013/0001728 Project as well as by GACR Project Numbers 17-20716S and 16-11140S. We also acknowledge the support of CEITEC Nano Research Infrastructure ID LM2015041, MEYS CR, 2016−2019.

■ REFERENCES

(1) Schwarzenbach, R. P.; Egli, T.; Hofstetter, T. B.; Gunten, U. v.; Wehrli, B. *Annu. Rev. Environ. Resour.* **2010**, *35*, 109−136.
(2) Nriagu, J. O.; Pacyna, J. M. *Nature* **1988**, *333*, 134−139.
(3) Department of Health and Human Services, Public Health Service. *Toxicological Profile for Arsenic: Agency for Toxic Substances and Disease Registry (ATSDR)*, 2007; https://www.atsdr.cdc.gov/toxprofiles/tp2.pdf.
(4) World Health Organization. *Guidelines for drinking-water quality*, 4th ed.; 2011, http://apps.who.int/iris/bitstream/10665/44584/1/9789241548151_eng.pdf.
(5) Smedley, P. L.; Kinniburgh, D. G. *Appl. Geochem.* **2002**, *17*, 517−568.
(6) Wong, C. H. A.; Pumera, M. *RSC Adv.* **2012**, *2*, 6068−6072.
(7) Dai, X.; Nekrassova, O.; Hyde, M. E.; Compton, R. G. *Anal. Chem.* **2004**, *76*, 5924−5929.
(8) Kaplin, A. A. *Zh. Anal. Khim.* **1973**, *28*, 2192−2196.
(9) Forsberg, G.; O'Laughlin, J. W.; Megargle, R. G.; Koirtyihann, S. *Anal. Chem.* **1975**, *47*, 1586−1592.
(10) Jena, B. K.; Raj, C. R. *Anal. Chem.* **2008**, *80*, 4836−4844.
(11) March, G.; Nguyen, T. D.; Piro, B. *Biosensors* **2015**, *5*, 241−275.
(12) Seeber, R.; Terzi, F.; Zanardi, C. *Functional Materials in Amperometric Sensing: Polymeric, Inorganic, and Nanocomposite Materials for Modified Electrodes*; Springer-Verlag: Berlin, Heidelberg, Germany, 2014.
(13) Collinson, M. M. *ISRN Anal. Chem.* **2013**, *2013*, 692484.
(14) Juřík, T.; Podešva, P.; Farka, Z.; Kovář, D.; Skládal, P.; Foret, F. *Electrochim. Acta* **2016**, *188*, 277−285.
(15) Zhang, Y.; Chu, W.; Foroushani, A.; Wang, H.; Li, D.; Liu, J.; Barrow, C.; Wang, X.; Yang, W. *Materials* **2014**, *7*, 5169−5201.
(16) Kassing, R.; Petkov, P.; Kulisch, W.; Popov, C. *Functional Properties of Nanostructured Materials*; Springer: Dordrecht, The Netherlands, 2006.
(17) Koch, C. C. *Nanostructured Materials: Processing, Properties and Applications*, 2nd ed.; William Andrew: Norwich, NY, 2006.
(18) Davis, P. H.; Dulude, G. R.; Griffin, R. M.; Matson, W. R.; Zink, E. W. *Anal. Chem.* **1978**, *50*, 137−143.
(19) Feeney, R.; Kounaves, S. *Anal. Chem.* **2000**, *72*, 2222−2228.
(20) Adeloju, S.; Young, T.; Jagner, D.; Batley, G. *Anal. Chim. Acta* **1999**, *381*, 207−213.
(21) Barra, C. M.; dos Santos, M. M. C. *Electroanalysis* **2001**, *13*, 1098−1104.
(22) Mrzljak, R. I.; Bond, A. M.; Cardwell, T. J.; Cattrall, R. W.; Newman, O.; Champion, B.; Hey, J. *Analyst* **1994**, *119*, 1051−1055.
(23) Mardegan, A.; Scopece, P.; Lamberti, F.; Meneghetti, M.; Moretto, L. M.; Ugo, P. *Electroanalysis* **2012**, *24*, 798−806.
(24) Švancara, I.; Vytřas, K.; Bobrowski, A.; Kalcher, K. *Talanta* **2002**, *58*, 45−55.
(25) Franke, J. P.; De Zeeuw, R. A. *Pharm. Weekbl.* **1981**, *3*, 1042−1047.
(26) Lambrechts, M.; Sansen, W. *Biosensors: Microelectrochemical Devices*; CRC Press: Boca Raton, FL, 1992.
(27) Panda, H. *Handbook on Electroplating with Manufacture of Electrochemicals*; Asia Pacific Business Press Inc.: Delhi, India, 2017.
(28) Schlesinger, M.; Paunovic, M. *Modern Electroplating*, 5th ed.; John Wiley & Sons: Hoboken, NJ, 2010.
(29) Balram, K. C.; Westly, D. A.; Davanco, M.; Grutter, K. E.; Li, Q.; Michels, T.; Ray, C. H.; Yu, L.; Kasica, R.; Wallin, C. B. *J. Res. Natl. Inst. Stand.* **2016**, *121*, 464−475.
(30) Lin, T.-H.; Lin, C.-W.; Liu, H.-H.; Sheu, J.-T.; Hung, W.-H. *Chem. Commun.* **2011**, *47*, 2044−2046.
(31) Arihara, K.; Ariga, T.; Takashima, N.; Arihara, K.; Okajima, T.; Kitamura, F.; Tokuda, K.; Ohsaka, T. *Phys. Chem. Chem. Phys.* **2003**, *5*, 3758−3761.
(32) El-Deab, M. S. *Electrochim. Acta* **2009**, *54*, 3720−3725.
(33) El-Deab, M. S.; Arihara, K.; Ohsaka, T. *J. Electrochem. Soc.* **2004**, *151*, E213−E218.
(34) Trasatti, S.; Petrii, O. A. *J. Electroanal. Chem.* **1992**, *327*, 353−376.
(35) Kissinger, P. T.; Heineman, W. R. *J. Chem. Educ.* **1983**, *60*, 702−706.
(36) Sukeri, A.; Saravia, L. P. H.; Bertotti, M. *Phys. Chem. Chem. Phys.* **2015**, *17*, 28510−28514.
(37) Miller, J. N.; Miller, J. C. *Statistics and Chemometrics for Analytical Chemistry*, 5th ed.; Pearson Education Ltd.: Harlow, Essex, U.K., 2005.

(38) Neuzil, P.; Campos, C. D. M.; Wong, C. C.; Soon, J. B. W.; Reboud, J.; Manz, A. *Lab Chip* **2014**, *14*, 2168−2176.

(39) Pumera, M.; Sanchez, S.; Ichinose, I.; Tang, J. *Sens. Actuators, B* **2007**, *123*, 1195−1205.

DOI: 10.1021/acs.analchem.7b03725
Anal. Chem. 2018, 90, 1161−1167

12 Resonator compatible microfluidics

12.1 Motivation of the article

This work was created as the idea of buried channel for flow of liquids in Si. Such a closed channel can be integrated on piezoelectric resonator and device can be used in vacuum which also improves the sensitivity in case of gravimetric sensor. The dimensions of such channels can vary from units to thousands of micrometers which perfectly fits the size of MEMS piezoelectric resonators.

There are a lot of possibilities how to make buried channels but none of them is compatible with technology for piezoelectric resonator fabrication. In many cases are used non-Si substrates or some materials and etching methods which cannot be combined with before fabricated structure on wafer. The very often problem is etching selectivity and risk of machine contamination with some materials.

12.2 Conclusion on the article

I found the way how to fabricate buried microfluidic channels in Si substrate using only single mask lithography. It eliminates possible issues which rapidly increases with number of photolithography steps. All fabrication technology was realized using CMOS compatible materials, surface and bulk microfabrication methods. The channel is formed using parylene which is biocompatible material. Therefore, this buried channel could be also used for living cells examination. In combination with MEMS piezoelectric resonator it allows to detect some phenomena in cells which are accompanied with the change of temperature or weight.

I also invented a method how to cleave a flexible material such as parylene at ambient temperature during this manuscript preparation. The sample was dipped in liquid nitrogen for a few seconds and immediately after the sample was pulled out it was possible to break it. This method was very useful for preparation of samples for SEM.

12.3 Contribution

I did all fabrications steps except the femtosecond laser photo ablation. I also performed the external tubing connection and I did SEM images and liquid nitrogen channel cryo-cleaving. I also contributed to the analysis of the results and to the writing of the manuscript.

12.4 Article 7

Article **Fabrication of buried microfluidic channels with observation windows using femtosecond laser photo ablation and parylene-C coating** [61] was accepted and will be published in **Microfluidics and Nanofluidics** (2017 IF 2.384) in **Q4/2018.**

Fabrication of buried microfluidic channels with observation windows using femtosecond laser photoablation and parylene-C coating

Imrich GABLECH[1], Jakub SOMER[1], Zdenka FOHLEROVÁ[1], Vojtěch SVATOŠ[1], Jan PEKÁREK[1], Stanislav KURDÍK[1], Jianguo FENG[2], Peter FECKO[1], Pavel PODEŠVA[2], and Pavel NEUŽIL[2*]

1 *Central European Institute of Technology, Brno University of Technology, Purkyňova 123, 613 00 Brno, Czech Republic*

2 *Northwestern Polytechnical University, 127 West Youyi Road, Xi'an, Shaanxi, 710072, P.R. China*

*pavel.neuzil@npwu.edu.cn

Abstract

We developed an advanced method for fabricating microfluidic structures comprising channels and inputs/outputs buried within a silicon wafer based on single level lithography. We etched trenches into a silicon substrate, covered these trenches with parylene-C, and selectively opened their bottoms using femtosecond laser photoablation, forming channels and inputs/outputs by isotropic etching of silicon by xenon difluoride vapors. We subsequently sealed the channels with a second parylene-C layer. Unlike in previously published works, this entire process is conducted at ambient temperature to allow for integration with complementary metal oxide semiconductor devices for smart readout electronics. We also demonstrated a method of chip cryo-cleaving with parylene presence that allows for monitoring of the process development. We also created an observation window for *in situ* visualization inside the opaque silicon substrate by forming a hole in the parylene layer at the silicon backside and with local silicon removal by xenon difluoride vapor etching. We verified the microfluidic chip performance by forming a segmented flow of a fluorescein solution in an oil stream. This proposed technique provides opportunities for forming simple microfluidic systems with buried channels at ambient temperature.

Introduction

Microfluidic technologies began to expand rapidly after Manz's group demonstrated a miniaturized chip that performed capillary electrophoresis[1] and, later, a flow-through polymerase chain reaction system[2]. Those chips were made using technology based on a double glass substrate. Researchers used fabrication steps known from conventional microelectromechanical systems (MEMS) technology with the addition of deep glass etching with HF/HCl solution[3] using an Au/Cr mask and glass–glass bonding process.[4] As these processes are rather complicated, there has been a lot of interest in creating microfluidic chips by using a Si substrate instead of glass to create channels/chambers and then seal the glass cover with anodic bonding. This reliable bonding technique is known for its use in pressure sensors and other MEMS devices.[5] The Si or glass patterning and subsequent bonding are relatively expensive, especially considering the need for a cleanroom facility and equipment. Scientists are, understandably, looking for simpler and cheaper methods to produce microfluidic devices to fulfill the required parameters.[6] Plastics such as polydimethylsiloxane (PDMS), acrylic, and polycarbonate have become popular materials for fabricating microfluidic devices. Computer numerical control is used for low-volume production, whereas microinjection molding, imprinting,[7] and hot embossing[8] are used for large-scale production.[9] PDMS is especially popular as it allows for the rapid prototyping of microfluidic devices without requiring a great investment in cleanroom technology. The drawback of PDMS is its porosity and rather high cost, which prevent this material from being utilized for commercial microfluidic products. Nevertheless, PDMS has been successfully used in microfluidic applications such as label-free separation and sorting,[10] barcoding and sequencing using droplet generation,[11] particle channel diffusion,[13] hydrodynamic stretching of single cells,[14] the investigation of bacteria physiology,[15-16] and in a quantitative study of antibiotic diffusion through lipid membranes.[12]

Unfortunately, as with most other techniques making microfluidic devices, creating a channel with a circular cross-section that allows a well-defined liquid flow is rather challenging. There are also electrochemical microfluidic devices currently in large-scale production that are made from plastic and metal layers and utilize laser-based patterning.[10] Microfluidic channels are also prepared by a femtosecond laser direct-writing method on glass, which requires post-annealing above 1000 °C.[11] Femtosecond laser direct writing is also used to make non-buried channels in SiC substrates.[12] Microfluidics with paper subtrate[13] and virtual microfluidics systems containing fluid walls[14] are also popular.

Silicon substrates for microfluidic devices have their merits, as the planar technology employed for integrated circuits and MEMS production was developed around them. The advantage of silicon as a mechanical material is its well-known technology, enabling vertical or lateral etching with an etch rate of 4–5 $\mu m \cdot min^{-1}$, and its excellent selectivity to other materials, allowing for the production of complex shapes. Silicon is also resistant to temperatures well in excess of 1000 °C; an insulating layer of SiO_2 can be produced by thermal oxidation of silicon. It also has excellent thermal conductivity and high value of Young's modulus. Silicon oxidation is an important step that covers the channel sidewalls and bottom with SiO_2 and, subsequently, modifies its surface for the chosen purpose. Microfluidic channels are often etched into silicon substrate and capped with anodically bonded glass specifically developed for this purpose to match the silicon thermal expansion coefficient. This technique is well developed but, by default, produces channels with a non-circular cross-section profile. Glass–glass microfluidic systems also do not produce circular channels; moreover, the choice of etching processes for glass is very limited compared with those for silicon.

Is there a way to simplify the Si-based technology, such as using only a single substrate without capping with a second one? A technique called "buried channel technology" (BCT) has been demonstrated[15] using different methods. Researchers etched a trench in a Si substrate using deep reactive ion etching (DRIE) and coated the trench with a suitable material. This material was then selectively removed at the trench bottom using reactive ion etching. The Si at the bottom of the trench was dry etched by SF6 plasma, wet etched electrochemically in HF solution, or chemically etched in HF/HNO3 or KOH solution. The Si substrate can also be etched by XeF_2 vapors. The sidewall passivation was then removed and the trench filled with SiO_2 or Si_3N_4 prepared by a low-pressure chemical vapor deposition (LPCVD) technique. The substrate was subsequently placed into KOH solution, releasing the tubes. Built-in tensile stress in the stoichiometric LPCVD Si_3N_4 layer limits its thickness to ≈ 300 nm, as thicker layers develop cracks. The thin film filling the trenches requires them to be made with a maximum thickness between 0.5 and 0.6 μm; this tiny trench width limits the etched depth. Another option is to use low-stress Si_xN_y, wherein the layer can be significantly thicker (up to a few micrometers[16]), which relaxes the fabrication process window rule. The BCT technique was further improved[17] by replacing the LPCVD layer with parylene,[18] which makes the entire technique much more robust, as there is no risk in depositing a parylene layer with a thickness of 0.1–50 μm. In addition, parylene is an optically transparent material. Researchers etched trenches in Si substrates and then deposited a layer of parylene. This layer coated the sidewalls and filled the channel to the top, thus sealing it to form a buried tube. The BCT was further improved[19] by making the process compatible with complementary metal oxide semiconductor (CMOS) technology with complex microfluidic structures.[20] All these techniques require pinhole-free protection of sidewalls and highly isotropic etching without damaging the edges at the top, which is a rather complicated task.

Silicon itself is a great material for device fabrication, as its technology is well established and the material itself, commonly used with a crystallographic orientation of (100), has high value of Young's modulus at ≈ 179 GPa, making it a mechanically stable material. It also has thermal conductivity of ≈ 130 $W \cdot m^{-1} \cdot K^{-1}$, an exceptionally high value for nonmetallic materials, making silicon microfluidics suitable for applications requiring heating, cooling, or forming a temperature gradient. Unfortunately, silicon is not transparent in the visible spectrum. SiO_2, glass, PDMS, and cyclic olefin copolymers are transparent materials commonly used to fabricate microfluidics devices. However, making buried microchannels with round cross-sections, such as those made by BCT, is a complicated if not impossible task with these materials.

Here, we show a single level lithography BCT based on a combination of DRIE of Si, trench conformal coating with optically transparent parylene, femtosecond laser photoablation of the center of the trench bottom, parylene deposition, and Si etching by XeF_2. This simple yet robust method for creating buried microfluidics by opening the bottom of a parylene-coated channel paves the way for the development of complex microfluidic systems.

Experimental

Design considerations

Our goal was to fabricate a buried channel using a simple procedure. There are a few layout parameters linked to the channel diameter, and each is discussed below.

We wanted to employ two Si etching processes: DRIE and vapor etching by XeF_2. The DRIE etch rate is related to the opening dimension at the lithography mask. Different sizes are etched with different etch rates, resulting in a "lag" effect that researchers sometimes take advantage of.[21] XeF_2 etching is a diffusion-limited process, and the etch rate through smaller openings in the mask is significantly slower than through larger holes. The different opening sizes during DRIE would subsequently cause an uneven channel diameter, which we decided to avoid; instead, we followed the rule of identical linewidth, resulting in a consistent channel diameter.

XeF_2 etching is a strictly isotropic process in which the vertical etching and lateral undercutting are practically identical, resulting in a semicircular shape. The targeted diameter of the channel was ≈ 250 µm (radius of ≈ 125 µm) and required the removal of ≈ 125 µm of silicon in the vertical direction. This defined a minimum etch depth of more than ≈ 125 µm; therefore, we set the targeted etch depth to 200 µm to provide a 60% safety margin.

The aspect ratio between the linewidth and etched depth during the DRIE process is 1:20 or greater; we chose a linewidth of 20 µm, which results in a non-challenging aspect ratio of 1:10. The etched trench is wide enough to accommodate the laser spot for the subsequent photoablation process. Finally, the trench has to be completely closed with a layer of parylene. If the trench width is 20 µm, then it requires the deposition of 10 µm of parylene, again a non-challenging process step. In this case, we deposited parylene with a thickness of 30 µm to ensure the sealing of the trench. This thickness does not practically affect the channel transparency.

Because the inlets/outlets should have a diameter of ≈ 1 mm, there is an apparent conflict, as the chosen linewidth for the entire design is 20 µm. We used a similar technique as before,[18] forming overlapping circular channels in the area of inlets/outlets, with three concentric donuts with set diameters of 200 µm, 600 µm, and 1000 µm. The set distance between those lines is 180 µm (radius 2 – radius 1 – linewidth), which is less than the targeted etching of 250 µm (125 µm × 2). A design with these parameters would result in completely undercut structures at inlets/outlets, resulting in a hole with a diameter of ≈ 1020 µm, whereas the buried channel has the desired diameter of ≈ 250 µm. The subsequent parylene deposition, with a thickness of ≈ 30 µm sealing the trenches, cannot close the inlet/outlet holes. Overall, the maximum size of the channel is limited by the wafer thickness and the minimum size by spot size of the laser for photoablation.

Finally, the channels can be designed with practically any shape, either straight or less regular, e.g., serpentine. The only design rule we would have to follow is the minimum distance between channels given by their diameter. If this rule is not followed, then the channels would merge with each other, which is the desired result in the inlet/outlet regions.

Taking advantage of the lag effect, the process could also be semi-three-dimensional, with areas with shallower channels and smaller diameter and deeper channels with larger diameter. We wanted to avoid this, as it would cause a problem with laser focusing during the photoablation process.

Chip design

The microfluidic device layout was designed using Nanolithography Toolbox,[22] a Java script-based software. We chose a simple microfluidic device with three inlets and a single outlet connected by a channel with a length of ≈ 25 mm and a double T-junction originally designed for capillary electrophoresis (Figure 1). The script file was converted into a graphic database system II file format and transferred via direct-writer laser system onto a soda lime glass mask.

Figure 1 Layout of a microfluidic chip with a channel, double T-junction, four inlets/outlets, and alignment marks for laser photoablation and for observation. Inlets are labeled with numbers 1, 2, and 3 while the outlet is number 4. Black arrows point to the two alignment marks for laser photoablation, and blue arrows point to the two alignment marks for microscope alignment.

Fabrication

The microchannel fabrication was conducted using the Si (100) wafer with diameter and thickness of ≈ 100 mm and ≈ 535 µm, respectively. We performed standard lithography using positive photoresist (PR) AZ 9260 with thickness of ≈ 10 µm (Figure 2A). After the PR was spun on the wafer, it was baked at ≈ 110 °C for ≈ 165 s. Contact lithography was then performed with ultraviolet light exposure of ≈ 1600 $\mathrm{mJ \cdot cm^{-2}}$, split into three individual doses (Figure 2B). The exposed PR was developed using a KOH-based developer for ≈ 300 s. We then etched the exposed Si using DRIE (known as the Bosch process[23]) by performing loops consisting of etching and passivation steps with durations of 5 s and 2 s, respectively. The etching was performed with SF_6 gas set with a pressure of ≈ 4 Pa, radio frequency (RF) plasma power of 1800 W, and SF_6 flow rate of $\approx 3.3 \cdot 10^{-6}\ \mathrm{m^3 \cdot s^{-1}}$. The passivation step with C_4F_8 gas with a pressure of ≈ 3.3 Pa was conducted with plasma RF power of 1500 W and C_4F_8 gas flow rate of $\approx 3.0 \cdot 10^{-6}\ \mathrm{m^3 \cdot s^{-1}}$. We used 310 loops to etch the Si substrate to a depth of ≈ 217 µm (Figure 2C). We removed the PR using N-methyl-2-pyrrolidione solution at ≈ 80 °C for ≈ 600 s. The wafer was exposed to O_2 plasma with power of ≈ 300 W for ≈ 180 s at a pressure of ≈ 6 Pa to complete the PR removal (Figure 2D). Subsequently, we deposited parylene with a thickness of ≈ 1.5 µm using a chemical vapor deposition technique. Parylene provides an excellent conformal coating (Figure 2E). The pressure in the chamber during parylene deposition was maintained at ≈ 1.6 Pa to ensure uniformity of the parylene layer across the entire sample.

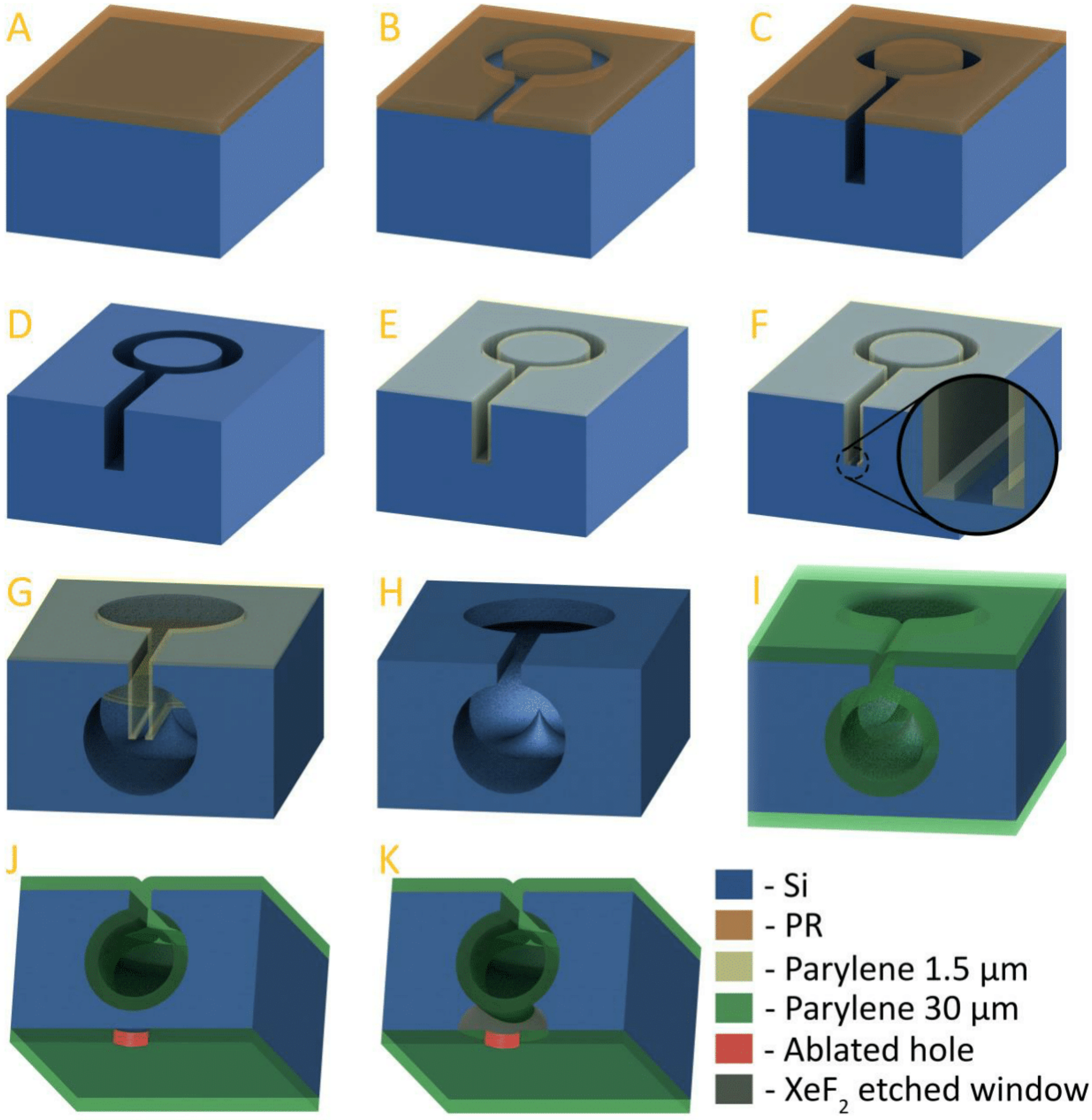

Figure 2 Wafer fabrication process steps: (A) PR coating; (B) patterned PR after exposure and development; (C) DRIE of silicon substrate; (D) PR stripping; (E) first deposition parylene; (F) photoablation of parylene at the trench bottom (inset shows details); (G) Si isotropic etching using XeF_2 *vapor to form the channel; (H) parylene removal using* O_2 *plasma; (I) second parylene deposition for channel sealing; (J) backside parylene removing; and (K) etching a backside hole by* XeF_2 *for an observation inside the channel.*

The crucial fabrication step was photoablation of the parylene at the bottom of the trenches using the femtosecond micromachining laser (Light Conversion, model PHAROS PH1-06, Yb:KGW lasing medium) with principal wavelength of ≈ 515 nm. The laser generated ultrashort pulses with duration of ≈ 300 fs with maximum amplitude of pulse energy of ≈ 200 µJ. The laser was focused into the bottom of the trenches using an aspherical lens with focal length of ≈ 40 mm, forming a laser spot size with diameter of ≈ 9.0 µm (Figure 2F). Because of locally generated heat, photoablation of the parylene layer was performed with no microcracks or shockwave-induced damage to the sidewalls.

Next, we exposed the wafer to the XeF_2 vapors to achieve isotropic etching of the Si at the trench bottom where the parylene layer had been removed by the laser photoablation (Figure 2G). This Si etching formed a channel with a nearly perfect circular cross-section profile. The parylene layer was then removed by an O_2 plasma etching step with power of ≈ 300 W and duration of ≈ 1 h (Figure 2H) at O_2 pressure of ≈ 6 Pa. We then deposited a second layer of parylene with a thickness of ≈ 30 µm to seal the channels (Figure 2I). The deposition parameters were the same as before.

After the structure was finished, we formed a hole in the parylene layer at the chip backside with the femtosecond laser as before (Figure 2J) and exposed the silicon substrate there to XeF_2 vapor (Figure 2K). This formed a hole at the chip backside, allowing optical access to monitor the channel.

We checked the most critical fabrication steps with scanning electron microscopy (SEM), starting with the cross-sections of the channel area after DRIE (Figure 3A). The next image shows the channel after the first parylene layer is completely removed by O_2 plasma (Figure 3B). Making a cross-section of a chip covered with parylene is tricky because, unlike silicon, parylene is not brittle at room temperature, meaning it cannot be cleaved. We scratched the parylene-covered microfluidic chip with a diamond scriber as usual and placed the chip into liquid nitrogen to cool it to a temperature of ≈ −195 °C, making the parylene brittle. We then took the chip out, placed it on a wooden support, and cleaved it to show the channel after sealing the trench with parylene (Figure 3C).

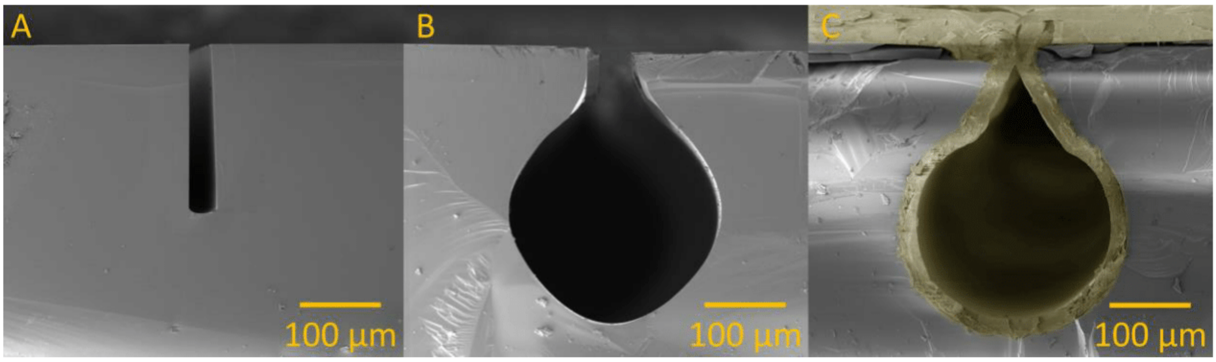

Figure 3 SEM cross-section images of fabricated microfluidic chip: (A) after DRIE and resist stripping; (B) after photoablation process, silicon etching by XeF_2 vapor, and parylene removal; and (C) after channel sealing with a second layer of parylene (false yellow colors increase the contrast for parylene).

Results and discussion

We designed and fabricated a device with a nearly round channel cross-section. The most desirable cross-section of any pipe used for fluid transport is circular, as there are no singularities or imperfections in the flow along the pipe wall. Here, ≈ 87.5% of the cross-section of the etched channel in silicon was circular (Figure 3B). There was an area next to the originally etched trench with rounded corners probably caused by slightly lower adhesion of the parylene to the silicon sidewalls of the etched trench; thus the undercutting of silicon there. Once the parylene was deposited, the channel was circular with a relatively small area with a "V" shape (Figure 3C).

We demonstrated operation of this microfluidic device by generating a segmented flow inside the microfluidic system using the double T-junction (Figure 4A). Because the parylene provides a hydrophobic surface, a segmented flow of water-based fluorescence was formed in a stream of mineral oil. We used this segmented flow system for convenience, as we perform quite a few experiments with this emulsion, especially for polymerase chain reactions. The chip was connected to three syringe pumps: inlet number 1 with fluorescein solution with concentration of $\approx 40\ \mu\mathrm{mol{\cdot}L^{-1}}$ and inlets 2 and 3 with mineral oil. The center and one side inlet were connected to pumps with oil, while the second side inlet was connected to a pump with fluorescein. All pumps were set to a pumping rate of $1\ \mu\mathrm{L{\cdot}min^{-1}}$. The chip was placed under an optical microscope (Figure 4B), with the XeF_2-etched cavity positioned under the objective lens with magnification of 10× and numerical aperture (N.A.) of 0.25.

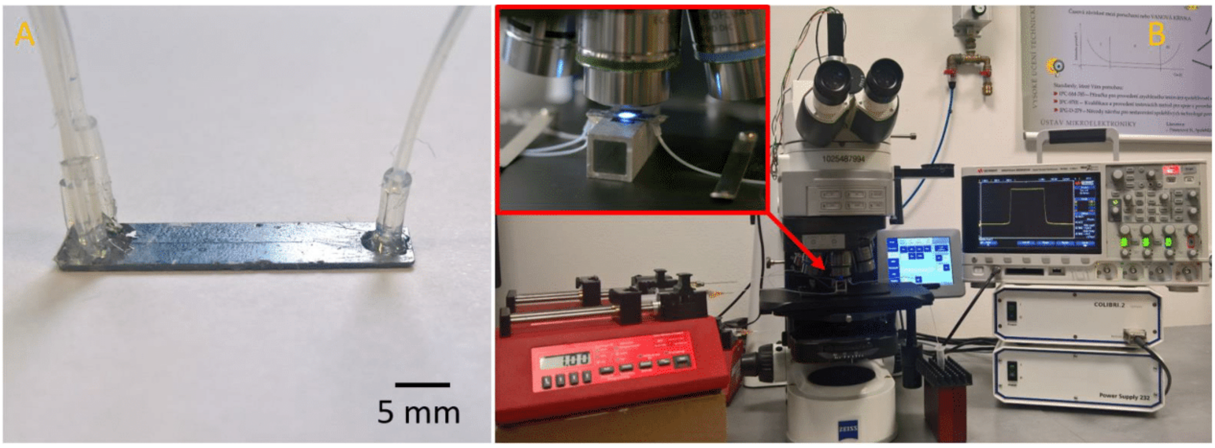

Figure 4 (A) Fabricated chip with tubing connection; (B) testing setup for microfluidics system.

This visualization allowed us to monitor the flow inside the buried channel inside the opaque Si substrate without obstruction. We also captured the backside view of the channel using SEM (Figure 5A), which is supported by the optical image (Figure 5B).

We used a light-emitting diode (LED) with principal wavelength of ≈ 470 nm to illuminate the channel. We observed the emitted light in the range between ≈ 500 nm and ≈ 550 nm with a CMOS camera and then, to monitor the fluorescence amplitude, with a photomultiplier tube (PMT), both methods with a fluorescein isothiocyanate fluorescence filter set.

The intensity of the fluorescent image was rather low; thus, the CMOS camera required a relatively long integration time of a few seconds, resulting in a blurred image. Therefore, we used an LED power supply with external control by a transistor–transistor logic-level signal. We set the exposure time on the camera to trigger a single light pulse with full brightness and duration of ≈ 5 ms. This system is similar to a photographic flash or a stroboscope that “freezes” the segmented flow image (Figure 5B). The captured image showed a dynamic contact angle inside the microfluidic channel. The shape of the fluorescein plug was typical for moderately hydrophobic surfaces.[24]

We then replaced the CMOS camera with a PMT and used an objective lens with magnification of 20× and N.A. of 0.22. The internal microscope aperture was set to minimum to limit the illuminated spot inside the channel. The PMT gain was set to the minimum value by setting the external voltage power supply to 0.5 V, as the fluorescein provided a rather high amplitude signal. The PMT output signal was recorded by an oscilloscope (Figure 5C).

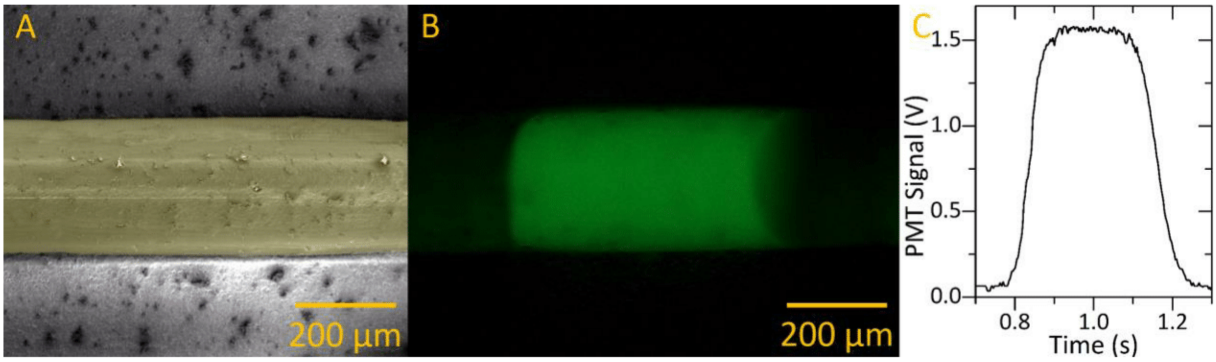

Figure 5 (A) SEM image of channel from backside view using false yellow-colored parylene for contrast improvement. (B) Optical image of the fluorescein plug in the oil inside the microfluidic channel. The plug has a non-symmetrical shape typical for moderately hydrophobic surfaces. (C) Amplitude of fluorescence as a function of time monitoring the segmented flow inside the microfluidic chip. The rising and falling edges have different shapes, demonstrating the non-symmetry of the plug caused by the moderately hydrophobic parylene coating inside the channel.

The signal corresponded to the previous work of a fluorescein/oil-segmented flow inside channels coated with moderately hydrophobic material. This simple experiment demonstrated that the microfluidic chip was successfully fabricated, and we were able to form a segmented flow inside the chip.

Conclusion

We demonstrated a method to create a buried microfluidic channel with all processes conducted at ambient temperature.

The process is robust, as the opening in the channel bottom does not interfere with the sidewalls' protective parylene layer, unlike other techniques in which the sidewalls' thin SiO_2 layer is attacked by XeF_2 during Si etching. The technique of opening the bottom of a coated channel is unique and, along with subsequent isotropic silicon etching and parylene deposition, paves the way to utilize this simple method to make BCT chips at ambient temperature. We also introduced a new technique of chip cryo-cleaving at room temperature to obtain a cross-section of a chip covered with non-brittle material with hydrophobic surface properties.

We used this microfluidic device to demonstrate the feasibility of fabrication by forming a segmented flow inside the buried channel. For visualization, we opened a tiny spot at the chip backside and removed Si from that area. The etched hole allowed us to see inside the channel even though the channel was originally buried inside the opaque Si substrate.

Acknowledgments

We acknowledge the support of CEITEC Nano Research Infrastructure (ID LM2015041, MEYS CR, 2016–2019), CEITEC Brno University of Technology, and Grant Agency of the Czech Republic under the contracts GA16-11140S. Authors I. Gablech, J. Somer, and J. Pekárek also acknowledge the foundation support FEKT/STI-J-17-4136. We would also like to acknowledge F. Urban for valuable discussion as well as providing access to the femtosecond laser, and J. Klempa for help with device fabrication.

References

1 Harrison, D. J., Manz, A., Fan, Z. H., Ludi, H. & Widmer, H. M. Capillary electrophoresis and sample injection systems integrated on a planar glass chip. *Anal. Chem.* **64**, 1926-1932, (1992).

2 Kopp, M. U., de Mello, A. J. & Manz, A. Chemical amplification: Continuous-flow PCR on a chip. *Science* **280**, 1046-1048, (1998).

3 Iliescu, C., Jing, J., Tay, F. E. H., Miao, J. M. & Sun, T. T. Characterization of masking layers for deep wet etching of glass in an improved HF/HCl solution. *J. Coat. Technol.* **198**, 314-318, (2005).

4 Iliescu, C., Taylor, H., Avram, M., Miao, J. M. & Franssila, S. A practical guide for the fabrication of microfluidic devices using glass and silicon. *Biomicrofluidics* **6**, 16505-16505, (2012).

5 Petersen, K. E. Silicon as a mechanical material. *Proc. IEEE* **70**, 420-457, (1982).

6 Faustino, V., Catarino, S. O., Lima, R. & Minas, G. Biomedical microfluidic devices by using low-cost fabrication techniques: A review. *J. Biomech.* **49**, 2280-2292, (2016).

7 Martynova, L. *et al.* Fabrication of Plastic Microfluid Channels by Imprinting Methods. *Anal. Chem.* **69**, 4783-4789, (1997).

8 Velten, T., Schuck, H., Haberer, W. & Bauerfeld, F. Investigations on reel-to-reel hot embossing. *Int. J. Adv. Manuf. Tech.* **47**, 73-80, (2010).

9 Becker, H. & Gartner, C. Polymer microfabrication methods for microfluidic analytical applications. *Electrophoresis* **21**, 12-26, (2000).

10 Ramchandani, N. & Heptulla, R. A. New technologies for diabetes: a review of the present and the future. *Int. J. Pediatr. Endocrinol.* **2012**, 28-28, (2012).

11 Liu, C. N. *et al.* Compact 3D Microfluidic Channel Structures Embedded in Glass Fabricated by Femtosecond Laser Direct Writing. *J. Laser Micro. Nanoen.* **8**, 170-174, (2013).

12 Huang, Y. G., Wu, X. D., Liu, H. W. & Jiang, H. R. Fabrication of through-wafer 3D microfluidics in silicon carbide using femtosecond laser. *J. Micromech. Microeng.* **27**, (2017).

13 Xia, Y. Y., Si, J. & Li, Z. Y. Fabrication techniques for microfluidic paper-based analytical devices and their applications for biological testing: A review. *Biosens. Bioelectron.* **77**, 774-789, (2016).

14 Walsh, E. J. *et al.* Microfluidics with fluid walls. *Nat. Commun.* **8**, (2017).

15 Ilic, B., Czaplewski, D., Zalalutdinov, M., Schmidt, B. & Craighead, H. G. Fabrication of flexible polymer tubes for micro and nanofluidic applications. *J. Vac. Sci. Technol. B* **20**, 2459-2465, (2002).

16 Iliescu, F. S., Teo, J. C. M., Vrtacnik, D., Taylor, H. & Iliescu, C. Cell therapy using an array of ultrathin hollow microneedles. *Microsystem Technologies*, (2017).

17 Boer, M. J. d. *et al.* Micromachining of buried micro channels in silicon. *J. Microelectromech. Syst.* **9**, 94-103, (2000).

18 Soon, J. B. W. *et al.* in *microTAS 2010.* 608-610 (2010).

19 Fekete, Z., Pongracz, A., Furjes, P. & Battistig, G. Improved process flow for buried channel fabrication in silicon. *Microsyst. Technol.* **18**, 353-358, (2012).

20 Zellner, P., Renaghan, L. & Agah, M. in *Transducers 2009.* 192-195 (2009).

21 Feng, J., Fohlerová, Z., Liu, X., Chang, H. & Neužil, P. Microfluidic device based on deep reactive ion etching process and its lag effect for single cell capture and extraction. *Sens. Actuators B Chem.* **269**, 288-292, (2018).

22 Balram, K. C. *et al.* The Nanolithography Toolbox. *J. Res. Natl. Inst. Stand.* **121**, 464-475, (2016).

23 Larmer, F., Schilp, A., Funk, K. & Offenberg, M. in *IEEE International MEMS '99 Conference.* 211-216 (1999).

24 Castro, E. R. *et al.* Determination of dynamic contact angles within microfluidic devices. *Microfluid. Nanofluidics* **22**, 51, (2018).

13 Device with similar fabrication process

13.1 Motivation of the article

Article is focused on modified MEMS IR microbolometer fabrication. This device is utilized with CNTs which make it original in the field of IR bolometer and can be used for real-time IR imaging. The novelty of this device is controlled growth of CNTs directly on the membrane. Growth is completely CMOS compatible because the rest of the substrate is kept at ambient temperature. There is no problem which could be caused by CNTs growth, because it is local process and mainly it is the last step in whole fabrication process. There is absolutely no heat or contamination risk to other materials or instruments used for fabrication.

Additionally, this device has many similar fabrication steps to MEMS piezoelectric resonator. Firstly, it uses the Ti as resistor which is used for temperature measurement and also for CNTs growth. Microbolometer contains a lot of same materials and involve totally of 7 lithography steps which is similar to fabrication of piezoelectric resonators where are 10 lithography steps. The next similarity is using of XeF_2 to etch underneath Si to release the structure. And the last similarity is that the bottom layer of suspended membrane is PECVD SiO_2.

13.2 Conclusion on the article

This work completely describes the fabrication and characterization of IR MEMS microbolometer and brings a lot of innovations to fabrication process of piezoelectric resonators due to process similarity. The next is Ti loading with high temperature which proves the Ti endurance. Other important aspect was the membrane releasing using XeF_2 vapor which is identical to fabrication of piezoelectric resonators. The last important is the local growth of CNTs on the membrane. This process could be simply integrated into piezoelectric fabrication. All the materials and processes are compatible so it would only request one more lithography step.

13.3 Contribution

I did some XeF_2 etching for membrane releasing. I also performed optimization of local CVD growth of CNTs. Additionally, I did SEM images for manuscript. I also contributed to the analysis of the results and to the writing of the manuscript.

13.4 Article 8

Article **In situ observation of carbon nanotube layer growth on microbolometers with substrates at ambient temperature** [62] was published in **Journal of Applied Physics** (2017 IF 2.176) in **March 2018.**

JOURNAL OF APPLIED PHYSICS **123**, 114503 (2018)

In situ observation of carbon nanotube layer growth on microbolometers with substrates at ambient temperature

Vojtěch Svatoš,[1] Imrich Gablech,[1] B. Robert Ilic,[2] Jan Pekárek,[1] and Pavel Neužil[1,3]
[1]*Brno University of Technology, Technická 3058/10, 616 00 Brno, Czech Republic*
[2]*Center for Nanoscale Science and Technology, National Institute of Standards and Technology, Gaithersburg, Maryland 20899, USA*
[3]*Northwestern Polytechnical University, 127 West Youyi Road, Xi'an, Shaanxi, People's Republic of China*

(Received 20 November 2017; accepted 1 March 2018; published online 20 March 2018)

Carbon nanotubes (CNTs) have near unity infrared (IR) absorption efficiency, making them extremely attractive for IR imaging devices. Since CNT growth occurs at elevated temperatures, the integration of CNTs with IR imaging devices is challenging and has not yet been achieved. Here, we show a strategy for implementing CNTs as IR absorbers using differential heating of thermally isolated microbolometer membranes in a C_2H_2 environment. During the process, CNTs were catalytically grown on the surface of a locally heated membrane, while the substrate was maintained at an ambient temperature. CNT growth was monitored *in situ* in real time using optical microscopy. During growth, we measured the intensity of light emission and the reflected light from the heated microbolometer. Our measurements of bolometer performance show that the CNT layer on the surface of the microbolometer membrane increases the IR response by a factor of (2.3 ± 0.1) (mean ± one standard deviation of the least-squares fit parameters). This work opens the door to integrating near unity IR absorption, CNT-based, IR absorbers with hybrid complementary metal-oxide-semiconductor focal plane array architectures. *Published by AIP Publishing.*
https://doi.org/10.1063/1.5016465

INTRODUCTION

Infrared (IR) imaging in the wavelength range from 8 μm to 14 μm, also known as thermal imaging, has found widespread applications spanning disparate fields of engineering and life and physical sciences. Room-temperature and cooled thermal imagers have been used in preventive maintenance, night vision, medical imaging, security, and space applications.[1] Heat sensing, uncooled microbolometers[2] in the form of focal plane arrays (FPAs) represent a class of integrated, two-dimensional ensemble thermal detector arrays with multiplexed readout. In contrast to cryogenically cooled devices, uncooled IR microbolometers have numerous advantages including higher reliability, reduced power consumption and smaller physical dimensions. Modern microbolometer devices, operating at room temperature, are based on thermally isolated membrane architectures with integrated temperature sensors. The incident radiation, absorbed as heat, increases the temperature of the microbolometer membrane. The temperature change (ΔT_{IR}), proportional to the power of incident radiation (P_{IR}), is given by

$$\Delta T_{IR} = \frac{P_{IR}}{G}, \tag{1}$$

where G is the thermal conductance of the microbolometer.

The FPA imagers are mass produced using Si-based complementary metal-oxide-semiconductor (CMOS) architectures. The imager consists of an array of pixels, with each pixel connected to a read-out integrated circuit. The microbolometer pixels are created using microelectromechanical system (MEMS) technology. The microbolometer membranes are typically made from various CMOS-compatible materials such as silicon dioxide (SiO_2), silicon nitride, amorphous Si and SiGe. Mid-IR absorption (η), in the range of interest from 8 μm to 14 μm of these materials, depends on the film thickness and composition. For instance, η for SiO_2 with a thickness of ≈0.6 μm ranges from ≈35% (Ref. 3) to ≈48%.[4] The key challenge is then to maximize η, while using a CMOS compatible process. Several developed strategies to increase η suffer from a significant increase in processing costs and complexity.

The first reported IR absorbing carbon nanotube (CNT) layer was implemented on the surface of a pyroelectric detector[5] sparking an interest in CNTs as an electromagnetic radiation absorber.[6,7] Controlled placement of vertically aligned CNT layers requires growth in a chemical vapor deposition (CVD) reactor at elevated temperatures above 550 °C,[8] using lithographically patterned catalytic materials.[9] The highest temperature that CMOS devices can withstand is typically below 475 °C. This value represents the eutectic temperature of the commonly used Al-Si contacts in CMOS chips. Modern CMOS devices with titanium silicide, tantalum nitride, nickel silicide[10] and other barrier materials between aluminum and silicon can be heated to higher temperatures. Nevertheless, exposing the CMOS chips to a temperature of 550 °C required for CNT growth is undesirable, thereby making the CNT growth on the surface of CMOS chips a major integration challenge. Shulaker *et al.*[11] showed a complex, thermal release tape process for transferring CNTs from one substrate to another. This method is not suitable for mechanically suspended devices such as MEMS-based microbolometer FPAs.

Here, we demonstrate a spatially localized Joule heating technique, warming up only the bolometer membrane, for

Fe-based catalytic CNT growth on the surface of the bolometer membrane, while the rest of the substrate remains at room temperature. This method enables the integration of a highly efficient, IR-absorbing CNT layer into existing monolithic CMOS FPA imagers.

RESULTS AND DISCUSSION

Microbolometer design and fabrication

Using the Nanolithography Toolbox,[12] we designed 40 μm × 40 μm microbolometer membranes[4] using a fabrication flow outlined in Fig. 1. Microbolometers, with an embedded Ti resistive temperature detector (RTD) and a Fe layer for catalytic CNT growth, were fabricated using conventional Si bulk-micromachining techniques. Prior to membrane release, we measured the RTD resistance and the temperature coefficient of resistance (α) using a probe station with a heated wafer chuck. The corresponding measured ambient temperature resistance (R_0) and α values were (7.726 ± 0.250) kΩ and (0.53 ± 0.01) m K^{-1}, both representing the measured mean ± standard deviation, respectively. The experimental procedure and uncertainties are described in the supplementary material section 1. Membranes were then released by removing the underlying Si using XeF$_2$ vapors. Subsequently, CNT growth was carried out on individual chips.

Microbolometer characterization

Following membrane release, microbolometer chips were mounted onto a leadless chip carrier with 68 pads and electrically connected with gold wires using wire-bonding. Packaged bolometer devices were then placed into a vacuum chamber with a Ge window. Using a method described by Gu *et al.*,[13] at a pressure of ≈7.7 × 10^{-4} Pa and an applied voltage amplitude (V_b) of ≈0.6 V with known values of R_0 and α, we determined the thermal capacitance (H), G and the thermal time constant ($\tau = H/G$). Our measurements over three sets of bolometer devices show $H = (3.113 \pm 0.009)$ nJ·K^{-1}, $G = (160.9 \pm 2.7)$ nW·K^{-1} and $\tau = (19.35 \pm 0.34)$ ms (mean ± standard deviation). The experimental procedure and uncertainties are described in the supplementary material section 2. At a constant pressure of ≤5 Pa and ambient temperature of ≈25 °C, the convective heat transfer and

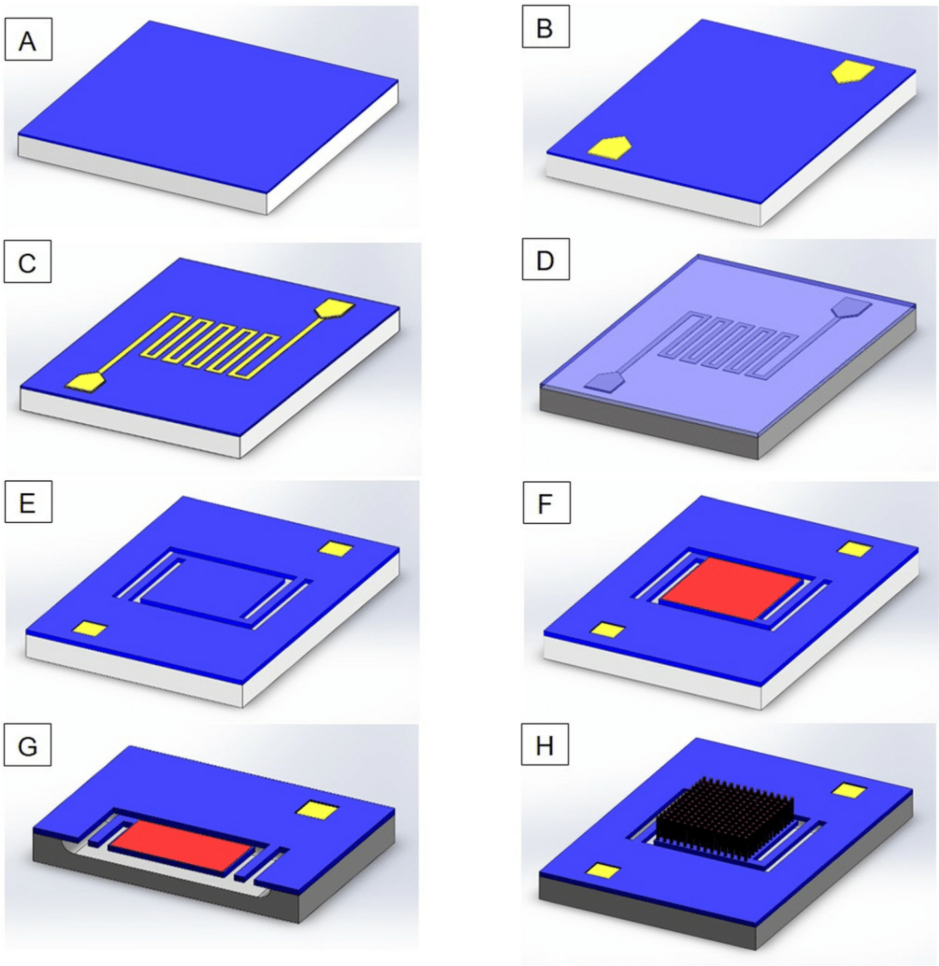

FIG. 1. Fabrication process flow of the MEMS based microbolometer. (a) Deposition of ≈0.25 μm plasma enhanced CVD (PECVD) SiO$_2$ on the Si substrate. (b) Lithographic definition of ≈0.9 μm thick Al bond pads. (c) ≈30 nm sputter deposited Ti temperature sensor definition using optical lithography and reactive ion etching. (d) Deposition of ≈0.25 μm PECVD SiO$_2$ for the protection of metal layers. (e) SiO$_2$ patterning to create access to bonding pads and etch holes for the microbolometer membrane release. (f) Deposition of the catalytic Fe layer using a photoresist lift-off process. (g) Cross-section of a microbolometer chip following microbolometer membrane release using XeF$_2$ vapors. (h) Catalytic CNT growth on the surface of the membrane.

radiation loss are negligible and consequently, G is solely determined by the thermal conduction of the microbolometer legs (P_C).[14] Once the microbolometer membrane warms up by the dissipated Joule heat (P_J), the radiation heat loss (P_R), based on the Stefan-Boltzmann law, cannot be neglected. The amplitude of P_J, distributed between P_R and P_C, is given by

$$P_J = P_R + P_C = A\cdot\varepsilon\cdot\sigma\cdot T^4 + G\cdot\Delta T, \tag{2}$$

where $A = 2\cdot a^2$ is the top and bottom areas of the square microbolometer membrane of length a, ε is the emissivity of the microbolometer membrane, σ is the Stefan-Boltzmann constant, T is the thermodynamic temperature, and ΔT is the temperature difference between the microbolometer membrane and the substrate chip. We measured the bolometer response to a square wave pulse[13] over a range of V_b values [Fig. S4(a) in supplementary material section 3]. In the vicinity of $V_b = 0$, where self-heating effects are neglected, our calculations show $G = (180.4 \pm 1.2)$ nW·K^{-1}, $H = (3.602 \pm 0.024)$ nJ·K^{-1} and $\tau = (19.96 \pm 0.02)$ ms (all are mean ± fitting error). Here and below, the fitting error corresponds to one standard deviation of the least-squares fit parameters. The values are in good agreement with the ones determined at $V_b \approx 0.6$ V. Collectively, these data show that self-heating plays a minor role in the bolometer performance.

Monitoring of CNT growth

The packaged bolometer devices were then placed into a vacuum chamber equipped with a glass window, tubes for gas and vacuum connections, and an electrical feedthrough, as schematically shown in Fig. 2(a). The chamber was then placed under an optical microscope equipped with ≈9 mm working distance, 50× objective with a numerical aperture (NA) of 0.55. The ≈7 mm distance between the bolometer membrane and the glass window allowed for high-resolution, *in situ* observation of the subsequent CNT growth processes. Thermal conditioning of the catalytic layer was accomplished by heating the microbolometer using $P_J \approx 200\,\mu$W in the 5% H_2 + 95% N_2 forming gas (FG) environment for ≈15 min. To determine the Joule heat threshold required for growth, we increased P_J until the onset of CNT growth. Further increase in P_J revealed an upper limit of 750 μW above which the bolometer membrane was physically damaged from the excessive power dissipation. To circumvent the membrane damage, P_J was set to 650 μW. Using a closed-loop feedback configuration, P_J was maintained by the controlling voltage V_{BOL}, while measuring the current I_{BOL} through the microbolometer resistor. During CNT growth, we maintained a chamber pressure of ≈5 Pa by adjusting the partial pressures of individual gases at ≈1.5 Pa and ≈3.5 Pa for FG and C_2H_2, respectively. Under the above conditions, the CNT thickness was controlled by growth time. Following CNT growth, surface passivation was not carried out. Figures 2(b) and 2(c) show optical micrographs of the microbolometer membrane before and after growth, at ≈65% of the field of view, respectively. A typical microbolometer membrane with grown CNTs is shown in Figs. 3(a) and 3(b). A video [Fig. 2(d)] (Multimedia view) shows real time CNT growth on the surface of the bolometer membrane.

We used finite element modelling (FEM) to show the temperature distribution within the thermally isolated membrane and the surrounding substrate. For the computation, we considered a silicon volume of 160 μm × 180 μm × 75 μm with a suspended bolometer membrane and materials of dimensions resembling the fabricated devices. We used 20-node thermal solid elements for the Si substrate and 10-node tetrahedral thermal solid elements for Ti and SiO_2 layers. The initial boundary condition for the Si substrate was set to 25 °C. Directly following this, we applied a voltage of 0.8 V between the ends of the two Ti metal traces. The FEM results [Figs. 3(c) and 3(d)] show heat concentration within the

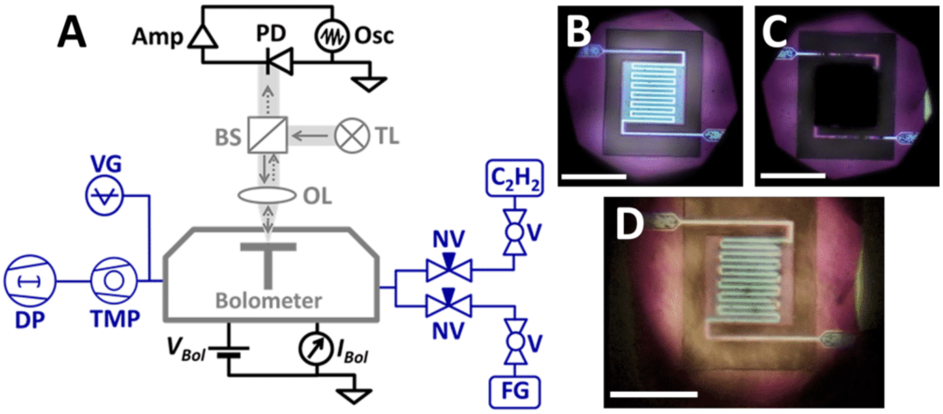

FIG. 2. (a) Schematic illustration of the experimental setup. The microbolometer was placed into a vacuum chamber with an inlet for gas delivery and a pumping port. Gas flow was controlled by needle valves (NV). Chamber evacuation was accomplished using a combination of a turbo molecular pump (TMP) with a backing dry vacuum pump (DP). Using an optical microscope with a 50× objective lens (OL), the optical window flange allowed for real-time monitoring of the CNT growth process. Reflectance measurements during CNT growth were accomplished using a tungsten lamp (TL) in conjunction with a beam splitter (BS) to illuminate the microbolometer membrane. Emission and reflection during CNT growth were measured using a silicon photodiode (PD). The I_p was converted to a voltage using a current preamplifier (Amp) that was monitored using an oscilloscope (Osc). The P_J amplitude dissipated in the microbolometer membrane was set using a closed-loop feedback system by controlling the amplitude of V_{BOL} while measuring I_{BOL} and keeping the P_J at a predetermined value. Optical micrographs of a microbolometer (b) before and (c) after the CNT growth. The scale bars in (b), (c) and (d) represent a length of ≈40 μm. (d) A video showing the real-time CNT growth at the bolometer membrane captured with a microscope equipped with a 50× objective lens. Multimedia view: https://doi.org/10.1063/1.5016465.1

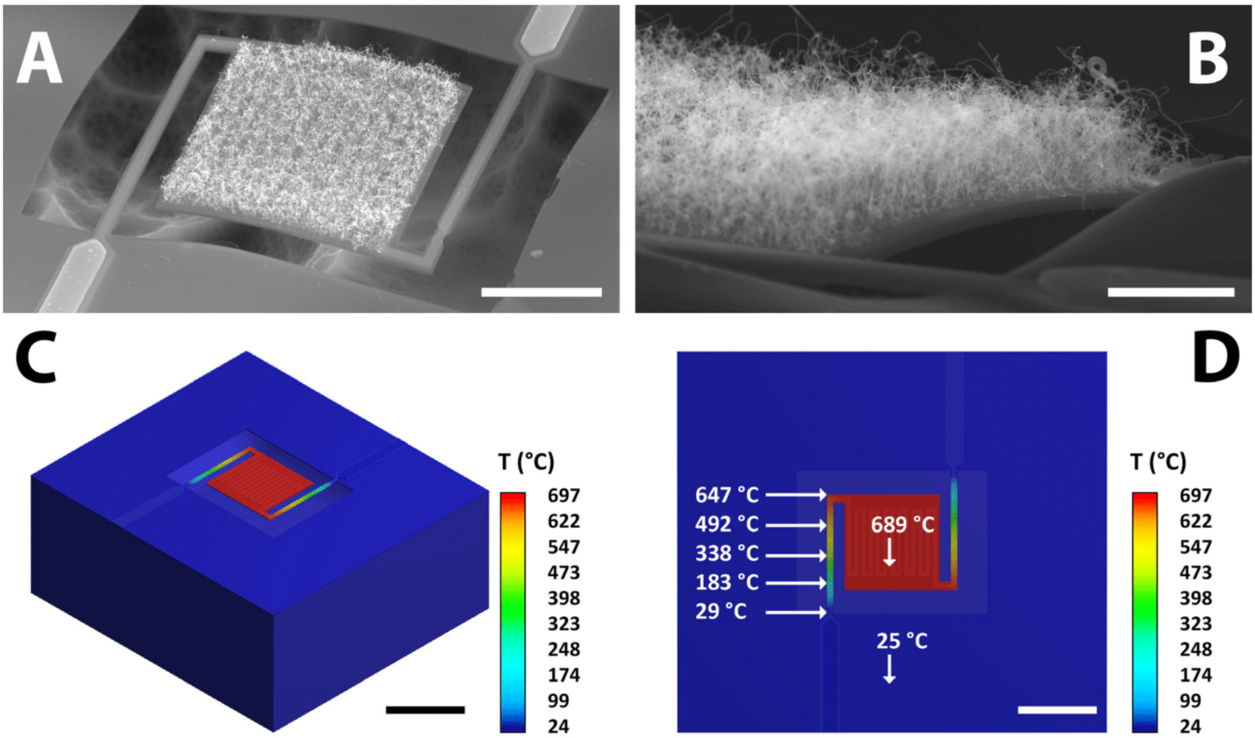

FIG. 3. Scanning electron micrographs of a fabricated microbolometer showing (a) a thermally isolated, undercut microbolometer membrane following CNT layer growth. (b) Zoomed-in view of the CNTs near the membrane edge. The scale bars in (a) and (b) represent the lengths of ≈20 μm and ≈5 μm, respectively. FEM analysis with (c) perspective and (d) top-down views of the temperature distribution within the structure. The heat is localized within the suspended, membrane region with the surrounding Si substrate at 25 °C. The scale bars in (c) and (d) represent lengths of ≈40 μm. The annotations in (D) represent temperatures at various locations, denoted by the corresponding arrows, along the structure.

suspended membrane with the substrate at approximately room temperature.

The measured photocurrent (I_p) from the silicon photodiode during the CNT growth was related to the emitted radiation from the heated membrane [Fig. 4(a), supplementary material section 5]. During the measurements, the microscope light source was turned off. I_p was converted into a voltage (V_p) using a current preamplifier with an active low-pass filter. The amplitude of V_p was monitored using an oscilloscope. I_p as a function of time (t) during the growth phase, initiating at $t \approx 112$ s, can be approximated by a first order exponential decay in combination with a linear decay

$$I_p = I_0 + I_1 \cdot e^{-\frac{t-t_0}{\tau_e}} + I_2 \cdot t, \tag{3}$$

where I_0 is the steady state photocurrent offset, I_1 is the maximum photocurrent, t_0 is the time at the onset of amplitude decay [≈112 s in Fig. 4(a)], τ_e is the emission time constant, and I_2 is the coefficient of linear I_p decay. Our measurements show values of $\tau_e = (34.91 \pm 1.26)$ s and $I_2 = (-15.94 \pm 2.02)$ fA·s^{-1}, both values are mean ± one standard deviation measured from 3 devices [Fig. 4(a)]. The uncertainties are calculated from the functional fitting error using Eq. (3). Details of the measurement results are in the supplementary material section 4. The value of τ_e can serve as a guide to minimize the CNT growth time with a saturated absorbance value.

Since the amplitude of I_p is proportional to P_J, the exponential decay of the I_p as a function of t can be derived from Eq. (2), while accounting for the geometric change of the radiation emitting area during CNT growth. The G value of a microbolometer is determined by the cross-sectional areas, length and thermal conductivity of the two microbolometer legs. Since the CNT layer was grown from the lithographically defined catalyst spanning the square shaped microbolometer membrane with an area of A [see Figs. 1(g) and 1(h)], the value of G remains constant during CNT growth.

During the growth, since P_J was held constant at ≈650 μW, the terms A and G in Eq. (2) can be also considered as constant. Consequently, the CNT layer on the surface of the membrane increased ε and decreased T. With increasing ε, the membrane emits radiation in all directions thereby lowering the temperature. Consequently, the power emitted per unit area of the microbolometer membrane decreases (supplementary material section 5). Measured resistance during the CNT growth allowed a qualitative determination of the microbolometer temperature change ΔT

$$R_b = \frac{V_{BOL}}{I_{BOL}}; \quad R_b = R_0(1 + \alpha \cdot \Delta T); \quad \text{and} \\ \Delta T = \frac{1}{\alpha}\left(\frac{V_{BOL}^2}{P_J \cdot R_0} - 1\right), \tag{4}$$

where R_0 and α are the corresponding ambient resistance at $T \approx 298$ K and the temperature coefficient of resistance of the temperature sensor, respectively. The ΔT amplitude dropped once P_J reached an amplitude of ≈650 μW at the onset of CNT growth.

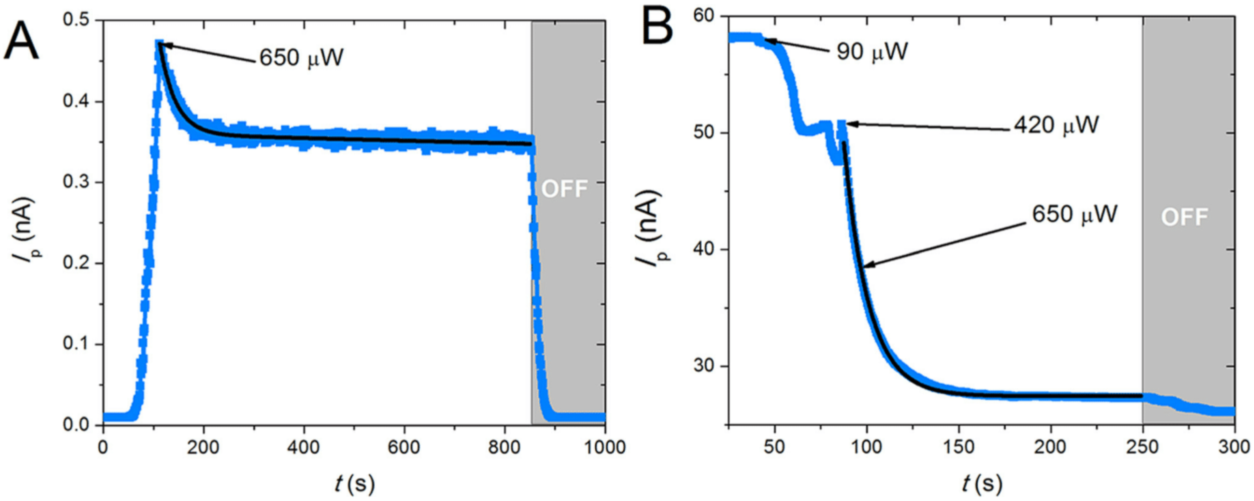

FIG. 4. (a) Typical optical emission from the microbolometer membrane as a function of t during CNT growth. P_J was gradually increased at a rate of $\approx 8\,\mu W \cdot s^{-1}$ up to 650 μW. At $t \approx 53$ s, we observed light emission from the membrane. CNT growth, initiating at $t \approx 112$ s with $P_J \approx 650\,\mu W$, increased the microbolometer emissivity and thereby lowered the microbolometer membrane temperature. At $t \approx 850$ s, heating was switched off ($P_J = 0$) and the CNT growth ceased. Directly following this, the light emission quickly decayed to zero. We determined the value of τ_e using Eq. (3) as (32.03 ± 0.82) s (mean ± fitting error). The solid line represents a first-order exponential decay functional fit. (b) Under similar conditions, we measured the optical reflection from the microbolometer. At $t \approx 40$ s, an increase from a steady state of $P_J \approx 90\,\mu W$ caused the membrane reflectivity to drop. The CNT growth initiated at $t \approx 86.5$ s with $P_J \approx 420\,\mu W$. The newly grown CNT layer lowered the membrane reflection with a time constant $\tau_r = (13.44 \pm 0.07)$ s (mean ± fitting error). The maximum $P_J \approx 650\,\mu W$ occurred at $t \approx 96$ s. At $t \approx 250$ s, the heating was switched off, following which the reflection amplitude changed marginally. The solid line represents a first-order exponential decay functional fit.

Above, we assumed a negligible emission contribution from the membrane sidewalls and considered the source of emission solely from A. However, during CNT growth, the total surface area as a function of the CNT layer thickness (t_c) increases by a factor of $4 \cdot a \cdot t_c$ (supplementary material section 6), while the sidewall emission increases with t_c. This increase is not negligible and consequently, results in a decrease of I_p at a rate of (−15.70 ± 1.38) fA$\cdot$s^{-1} (mean ± fitting error) [Fig. 4(a)].

Using a ≈ 100 W tungsten lamp, we illuminated the bolometer membrane and measured the reflectance during CNT growth [Fig. 4(b) and supplementary material section 7]. The dynamics of the reflection-based experiment differed from the emissivity measurement. Once the CNT growth is initiated at $P_J \approx 420\,\mu W$, the amplitude of light reflected from the membrane decreased following an exponential decay of the first order with time constant $\tau_r = (13.44 \pm 0.07)$ s (mean ± one standard deviation from 3 devices). The faster τ_r, in comparison with τ_e, shows that the related reflection from the membrane in the visible spectrum of electromagnetic radiation is sensitive to small changes in surface properties, whereas a much thicker layer of CNTs is required to cause significant changes to τ_e.[6]

Inserting the parameters obtained from the above microbolometer characterization into Eq. (2) allowed us to calculate the amplitude of P_J as a function temperature, without the CNT layer and for various CNT thickness values of up to 30 μm [Fig. 5(a)]. In our calculations, we used $\varepsilon_{SiO2} = 0.48$ and $\varepsilon_{CNT} = 1$ for the emissivity of membranes without[4] and with[11,15] CNTs, respectively. Furthermore, the area of the CNT membrane was $A = 2 \cdot a^2 + 4 \cdot a \cdot t_c$ (see supplementary material section 6). The results in Fig. 5(a) show that the P_J amplitude required to heat up the bolometer membrane without and with the CNT layer to the same value of T increases with increasing thickness of the CNT layer.

We then calculated the power of emitted radiation $P_{ER} = b \cdot \varepsilon \cdot \sigma \cdot T^4$ from a 1 μm^2 area (b) of the bolometer membrane without CNTs and for various CNT layer thicknesses. Figure 5(b) shows a significant emission dependence with respect to the CNT layer thickness.

Experimental data in Fig. 6 show that membranes with CNTs are cooler and emit ≈0.23 of the power emitted by membranes without CNTs. Our results further show that the CNT layers increased the value of thermal capacitance H by a factor ≈5, to (14.83 ± 0.53) nJ$\cdot$K^{-1} (mean ± standard deviation, 3 measurements).

CNT layer performance

We placed the bolometer, connected in a balanced Wheatstone bridge configuration, into a vacuum chamber and evaluated the P_{IR} response. The amplitude of P_{IR} was controlled by the distance (D) between the black body at $T \approx 673.15$ K and the bolometer from $D \approx$ (59.5, 74.5, 89.5, 104.5, and 119.5) mm. The P_{IR} was estimated using the equation[4]

$$P_{IR} = a^2 \cdot \varepsilon_{bb} \cdot \tau_F \cdot M \left[\frac{\left(\frac{d}{2}\right)^2}{D^2 + \left(\frac{d}{2}\right)^2} \right], \tag{5}$$

where ε_{bb} is the emission of the black body with an amplitude of ≈0.95 (manufacturer's datasheet value), τ_F is the average experimentally determined transmittance of the Ge window with a value of $\tau_F \approx 0.76$, M is the integrated radiant exitance of the black body (supplementary material section 8)

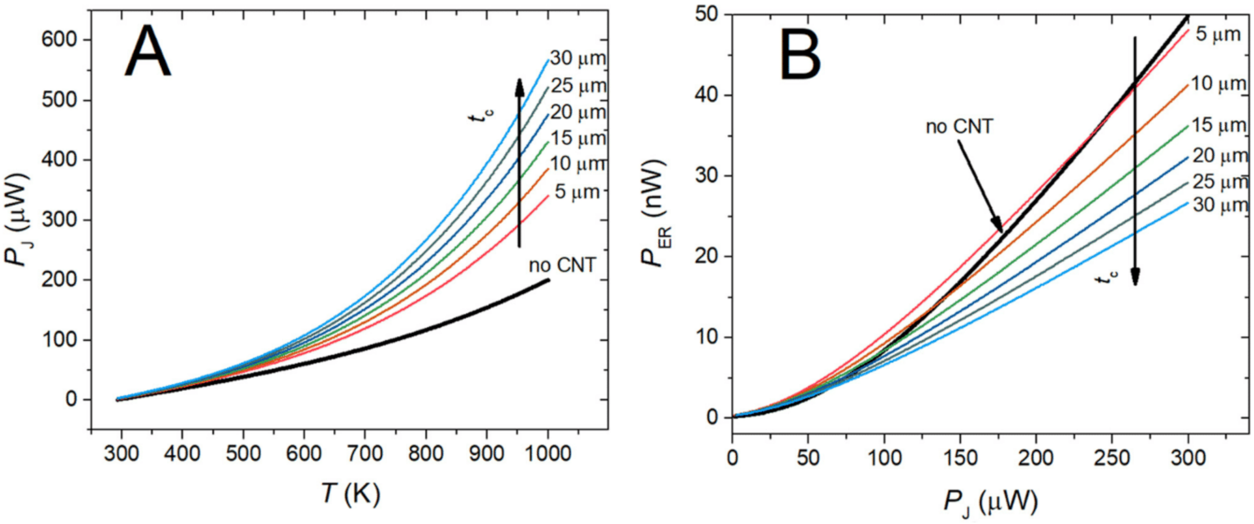

FIG. 5. (a) Calculated values of dissipated Joule heat P_J as a function of T for microbolometers without CNTs (thick black line) and for various CNT thickness values. The CNT membranes require a larger P_J to remain at a distinct T. (b) Calculated values of P_{ER} as a function of P_J for microbolometers without CNTs (thick black line) and for various t_c values.

according to Planck's radiation law with an amplitude of $\approx 2588\,\mathrm{W{\cdot}m^{-2}}$ and $d \approx 10.5\,\mathrm{mm}$ is the diameter of the black body radiation source. The value of τ_F was determined by a ratio of an output signal of a commercial microbolometer based IR camera with and without the Ge window. The microbolometer responsivity to IR radiation ($\Re_{IR}$) is defined as

$$\Re_{IR} = \frac{\Delta V_{out}}{P_{IR}}. \tag{6}$$

Our results show that by adding the CNT absorbing layer, the $\Re_{IR}$ increased by a factor of (2.3 ± 0.1) (mean ± fitting error) (Fig. 7).

CONCLUSIONS

Our work presented here for the first time demonstrates CNT growth on the surface of suspended microbolometer membranes while keeping the device substrate at room temperature. By taking advantage of the thermally isolated nature of the released microbolometer membrane, the developed CMOS fabrication compatible method allows for the integration of IR absorbing CNTs with a variety of active device architectures including FPAs. Our results show ≈2.3-fold IR responsivity increase with grown CNT absorbers and reached a $\Re_{IR}$ of $(16.35 \pm 0.48)\ \mathrm{kV{\cdot}W^{-1}}$. Furthermore, the IR absorption near unity is determined solely by the CNT

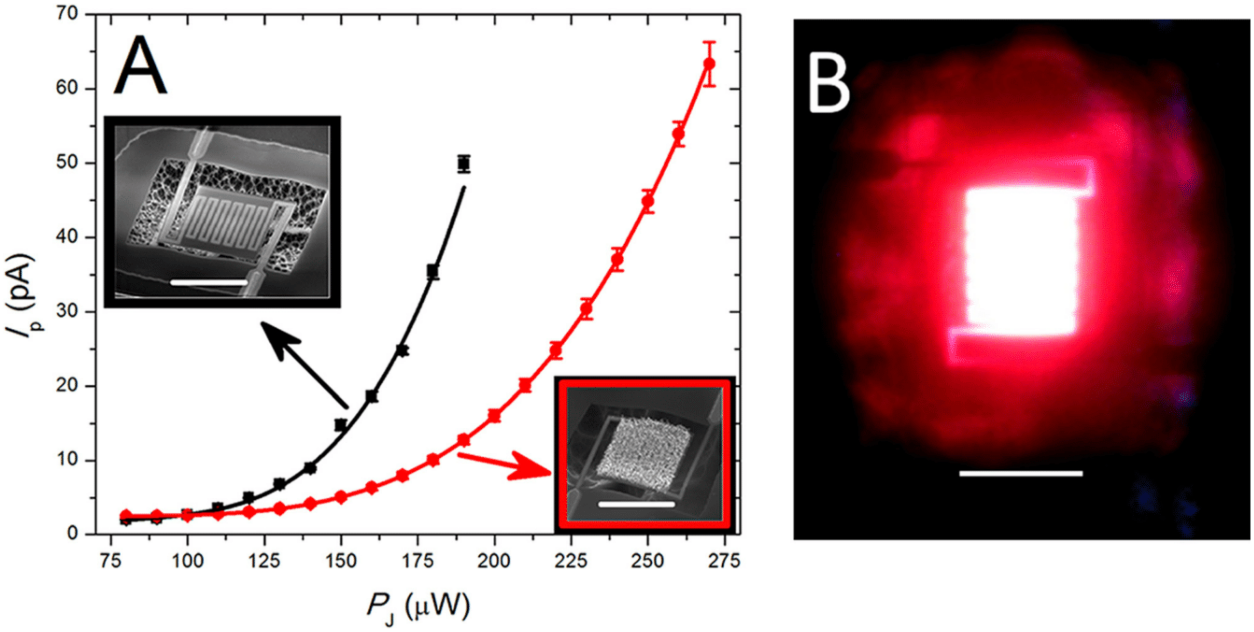

FIG. 6. (a) Measured light emission amplitude from bare (black squares) and CNT covered (red circles) microbolometer membrane as a function of dissipated P_J. The two insets are scanning electron micrographs of microbolometers with and without the CNT layer. Scale bars represent 40 μm. Solid lines represent a 4th order polynomial curve fitting with the cubic coefficient set to zero. The radiation power amplitude of the microbolometer with the CNT is ≈0.23 of the one without. Filled in markers are average values and vertical bars represent one standard deviation resulting from repeated measurements across a device. (b) Optical micrograph showing light emission from the membrane at $P_J \approx 650\ \mu\mathrm{W}$. The scale bar represents 40 μm.

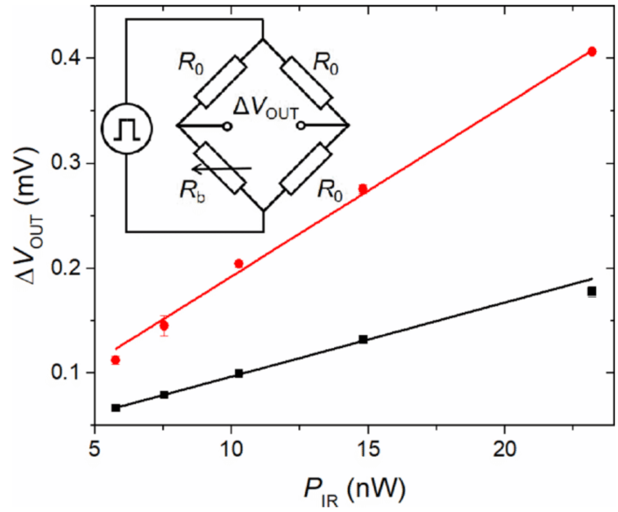

FIG. 7. Wheatstone bridge output voltage change ΔV_{OUT} as a function of incident P_{IR} for microbolometers with (red circles) and without (black squares) a CNT layer. The amplitude of P_{IR} was calculated from the black body bolometer distance as per Eq. (5) and supplementary material section 8. The bridge was biased with a square wave pulse of amplitude ≈0.6 V and duration ≈200 ms. The ΔV_{OUT} amplitude was captured at $t \approx 200$ ms. Using linear regression, the microbolometer $\Re_{IR}$ with and without CNTs is (16.35 ± 0.48) kV·W^{-1} and (7.08 ± 0.24) kV·W^{-1}, both (mean ± standard deviation, across 3 measurements), respectively. Filled-in markers are average values and vertical bars represent one standard deviation resulting from repeated measurements across three devices. Overall, with CNTs, $\Re_{IR}$ increases by a factor of (2.3 ± 0.1) (mean ± fitting error).

layer, regardless of the membrane material and thickness, the cavity and the underlying IR reflector. The promising growth technique of highly absorbing CNT layers using spatially localized heating on the surface of suspended membranes opens opportunities for complex integration of these absorbing layers for efficient IR imaging and FPA emission applications.

SUPPLEMENTARY MATERIAL

See supplementary material for microbolometer resistance and temperature coefficient of resistance measurement, evaluation of microbolometer thermal parameters, microbolometer response to varying V_b, details of emission measurement during CNT growth, resistance measurement during CNT growth, emission measurement from the microbolometer with CNTs, reflection measurement from bolometer membrane during CNT growth, and calculation of blackbody radiant exitance.

ACKNOWLEDGMENTS

V. Svatoš, I. Gablech, J. Pekárek, and P. Neužil acknowledge the financial support by the Ministry of the Interior of the Czech Republic under VI20152019043 project. We also acknowledge the support of CEITEC Nano Research Infrastructure (ID LM2015041, MEYS CR, 2016–2019) and the SIX Center of Brno University of Technology, where measurements were conducted. The authors would also like to acknowledge great help from Mr. Jaroslav Klempa for performing the FEM of temperature distribution in the bolometer and the staff of the Center for Nanoscale Science and Technology facility at the National Institute of Standards and Technology, Gaithersburg, USA, where these devices were fabricated.

[1] A. Rogalski, Infrared Phys. Technol. **54**, 136 (2011).
[2] K. C. Liddiard, Infrared Phys. **24**, 57 (1984).
[3] P. Neuzil, Y. Liu, H. H. Feng, and W. J. Zeng, IEEE Electron Device Lett. **26**, 320 (2005).
[4] T. Mei, P. Neuzil, G. Karunasiri, and W. Zeng, Appl. Phys. Lett. **80**, 2183 (2002).
[5] J. H. Lehman, C. Engtrakul, T. Gennett, and A. C. Dillon, Appl. Opt. **44**, 483 (2005).
[6] Z.-P. Yang, L. Ci, J. A. Bur, S.-Y. Lin, and P. M. Ajayan, Nano Lett. **8**, 446 (2008).
[7] J. Lehman, A. Sanders, L. Hanssen, B. Wilthan, J. Zeng, and C. Jensen, Nano Lett. **10**, 3261 (2010).
[8] M. Meyyappan, D. Lance, C. Alan, and H. David, Plasma Sources Sci. Technol. **12**, 205 (2003).
[9] S. M. Huang, L. M. Dai, and A. W. H. Mau, Adv. Mater. **14**, 1140 (2002).
[10] S.-L. Zhang and M. Östling, Crit. Rev. Solid State Mater. Sci. **28**, 1 (2003).
[11] M. M. Shulaker, G. Hills, N. Patil, H. Wei, H.-Y. Chen, H. S. P.Wong, and S. Mitra, Nature **501**, 526 (2013).
[12] K. C. Balram, D. A. Westly, M. Davanco, K. Grutter, Q. Li, T. Michels, C. H. Ray, L. Yu, R. Kasica, C. B. Wallin, I. Gilbert, B. A. Bryce, G. Simelgor, J. Topolancik, N. Lobontiu, Y. Liu, P. Neuzil, V. Svatos, K. A. Dill, N. A. Bertrand, M. Metzler, G. Lopez, D. A. Czaplewski, L. Ocola, K. Srinivasan, S. Stavis, V. Aksyuk, J. A. Liddle, S. Krylov, and B. R. Ilic, J. Res. Natl. Inst. Stand. **121**, 464 (2016).
[13] X. Gu, G. Karunasiri, G. Chen, U. Sridhar, and B. Xu, Appl. Phys. Lett. **72**, 1881 (1998).
[14] X. He, G. Karunasiri, T. Mei, W. J. Zeng, P. Neuzil, and U. Sridhar, IEEE Electron Device Lett. **21**, 233 (2000).
[15] K. Mizuno, J. Ishii, H. Kishida, Y. Hayamizu, S. Yasuda, D. N. Futaba, M. Yumura, and K. Hata, Proc. Natl. Acad. Sci. U.S.A. **106**, 6044 (2009).

14 Ultra-low resistance change measurement using lock-in amplifier

14.1 Motivation of the article

This article is focused on description of electrical measuring method of microbolometer using lock-in amplifier in combination with pre-amplifier. This method should be suitable for precise and quick measurement allowing precise determination of the microbolometer parameters and also the temperature determination of objects which is function of absorbed irradiated power.

This method uses the balanced Wheatstone bridge and allows to determine very low changes in microbolometer resistance. This setup can also be used to determine resistance changes in other materials. In this case, such method will be used on measurement of resistance changes in 2D materials.

14.2 Conclusion on the article

This manuscript describes the using of measurement method for resistance changes determination. It allows to measure very low changes of resistance with high precision. Such advantage will be useful for measurement of 2D materials due to expectation of very low changes in electrical parameters when the strain will be lower than ≈ 0.5 %. This setup also offers the measurement on locked resonance frequency and phase which will improve the determination of 2D material parameters in time.

14.3 Contribution

I participated on all measurements and on developing of measurement setup. I also participated on few steps of microbolometer fabrication process. The optimized Ti was also used for fabrication of this device. I also contributed to the analysis of the results and to the writing of the manuscript.

14.4 Article 9

Article **Precise determination of thermal parameters of a microbolometer** [63] was published in **Infrared Physics & Technology** (2017 IF 1.851) in **September 2018.**

Infrared Physics and Technology 93 (2018) 286–290

Contents lists available at ScienceDirect

Infrared Physics & Technology

journal homepage: www.elsevier.com/locate/infrared

Regular article

Precise determination of thermal parameters of a microbolometer

Vojtěch Svatoš[a,b], Imrich Gablech[a,b], Jan Pekárek[a,b], Jaroslav Klempa[a,b], Pavel Neužil[a,b,c,*]

[a] Central European Institute of Technology, Brno University of Technology, Purkyňova 123, 61200 Brno, Czech Republic
[b] Brno University of Technology, Faculty of Electrical Engineering and Communication, SIX Centre, Department of Microelectronics, Technická 3058/10, 61600 Brno, Czech Republic
[c] Northwestern Polytechnical University, 127 West Youyi Road, Xi'an, Shaanxi, PR China

ARTICLE INFO

Keywords:
Microbolometer
MEMS
Thermal parameters
Lock-in amplifier
IR response

ABSTRACT

Determination of microbolometer thermal properties such as thermal capacitance, conductance, time constant, and IR responsivity is of the utmost importance as they directly influence microbolometer performance. Here we show a technique to measure them by using a minimized self-heating effect, thus leading to their precise determination via measurements based on an AC-biased Wheatstone bridge containing a microbolometer. The bridge outputs were subtracted from each other by a differential voltage preamplifier with its output processed by a lock-in amplifier. The lock-in amplifier output as a function of the amplitude of AC bias provided an amplitude of microbolometer thermal conductivity. A microbolometer temperature response to pulse irradiation of its membrane provided the value of its thermal time constant and, thus, its thermal capacitance. Finally, we also extracted microbolometer responsivity using a blackbody IR source. The method was experimentally verified using a micromachined bolometer, which showed excellent agreement with the analytical solution.

1. Introduction

Midrange infrared (IR) with a wavelength range from ($\approx$8 to $\approx$14) µm has a wide range of applications such as security and commercial uses. Among security applications, IR surveillance can help firefighters look for people in dense smoke or to identify fire hot spots to extinguish. IR devices can also help police identify cars recently arrived in a parking area. Typical commercial applications are as an aid for driving in poor visibility, looking for hot spots in an electrical power distribution system, finding heat leakages from buildings to conserve energy, precise tumor identification during surgery, and many others. The development of midrange IR detectors dates back to 1947 with the invention of a pneumatic IR detector, called the “Golay cell [1]”. In 1984 [2], and following an improvement in 1986 [3], a new concept of a microbolometer as part of a microelectromechanical system (MEMS) device was introduced. This allowed the integration of an array of microbolometers with read-out integrated circuits into a focal plane array, i.e., a true IR imager. The microbolometer, operating in a vacuum, consists of an IR-absorbing thermally isolated membrane integrated with an embedded temperature sensor. Most commonly, the resistive temperature detector (RTD) is made of metal such as Ti [2], phase transition materials such as VO_x [4], or semiconductors such as amorphous Si [5]. Their resistance amplitude R changes with temperature change ΔT as per the equation

$$R = R_0(1 + \alpha\cdot\Delta T) \tag{1}$$

where R_0 is sensor resistance at ambient temperature T_0 and α is its temperature coefficient of resistance. Microbolometer membrane ΔT expressed as change of sensor resistance change (ΔR) is:

$$\Delta R = R - R_0 = R_0\cdot\alpha\cdot\Delta T \tag{2}$$

The ΔT value is linearly proportional to the amplitude of absorbed IR radiation (P_{IR}) and inverse to the value of the microbolometer thermal conductance (G) [6], making the G amplitude the parameter of utmost importance

$$\Delta T = \frac{P_{IR}}{G} \tag{3}$$

Other important parameters are thermal capacitance (H) and the thermal time constant (τ), which determine the rate of the microbolometer response as

$$\tau = \frac{H}{G} \tag{4}$$

Thus, all three parameters G, H, and τ have to be determined to optimize the microbolometer performance.

A well-established technique to determine specific heat and thermal conductivity of thin film materials and structures based on 3ω method were proposed earlier [7,8]. The structures were thermally modulated

---

* Corresponding author at: Northwestern Polytechnical University, 127 West Youyi Road, Xi'an, Shaanxi, PR China.
E-mail address: pavel.neuzil@nwpu.edu.cn (P. Neužil).

https://doi.org/10.1016/j.infrared.2018.07.037
Received 10 May 2018; Received in revised form 30 July 2018; Accepted 30 July 2018

making this method especially suitable for thin film materials, less for slow MEMS devices such as IR microbolometers. A single measurement-based method to determine parameters G, H, and τ was proposed and demonstrated by biasing an unbalanced Wheatstone bridge, including a microbolometer with an RTD sensor made of Ti, by a single voltage pulse with a bias amplitude (V_B) with time period $\ll\tau$ at a pressure of $\approx 7.7 \times 10^{-4}$ Pa [9]. The microbolometer behavior is governed by a differential heat balance equation

$$H\frac{d\Delta T}{dt} + G\cdot\Delta T = P_J - P_R = \frac{V_B^2}{4R_0} - P_R, \tag{5}$$

where $P_J = \frac{V_B^2}{4R_0}$ is dissipated joule heat in the microbolometer resistor with an actual value of R_0. At a constant pressure of ≤ 5 Pa, heat convection due to energy transfer by the movement of gas molecules surrounding the membrane and radiation losses P_R at ambient temperature of 25 °C are also negligible [10]. The Eq. (5) with neglected amplitude of P_R can be solved as

$$\Delta T = \frac{V_B^2}{4G\cdot R_0}\left[1 - \exp\left(-\frac{t}{\tau}\right)\right], \tag{6}$$

where t is time. The researchers expressed the Wheatstone bridge output in simplified form as function of time [9]

$$\Delta V = \frac{\alpha\cdot V_B^3}{16G\cdot R_0}\left[1 - \exp\left(-\frac{t}{\tau}\right)\right] \tag{7}$$

With knowledge of V_B, R_0 and α of ≈ 1 V, ≈ 3.9 kΩ, and $\approx 0.0025\ \mathrm{K}^{-1}$, respectively, researchers extracted the value of G from Eq. (7) at steady-state and the value of H from the pulse response slope for $t = 0$ s. The thermal time constant was calculated using Eq. (4). The proposed method was simple; however, during the measurement the P_J amplitude was ≈ 64.1 μW causing the microbolometer membrane with calculated G value of $\approx 7.8 \times 10^{-7}\ \mathrm{W\,K^{-1}}$ warming by the excessive value of $\Delta T \approx 82.2$ K affecting the R_0 value, which was considered to be constant. The modulated amplitude of R_0 value due to ΔT resulted in a measurement error as Eq. (7) assumes R_0 to be constant. Lowering the V_B amplitude does lower the error due to smaller variation of R amplitude, but the measurement precision suffered due to the low output voltage of the system and signal-to-noise ratio (SNR) because the system response is linearly proportional to the amplitude of V_B.

In addition, at ambient temperature, the radiation determined by the Stefan–Boltzmann law can no longer be neglected. The amplitude of P_J is then split between power loss due to thermal conduction (P_C) and amplitude of P_R:

$$P_J = P_C + P_R = G\cdot\Delta T + A\cdot\varepsilon\cdot\sigma\cdot T^4 \tag{8}$$

where $A = 2a^2$ is the total area of a microbolometer membrane with square shape and side length of a with neglecting its sidewalls area, ε is the emissivity of the microbolometer membrane material, σ is the Stefan–Boltzmann constant with value of $\sigma \approx 5.6704 \times 10^{-8}\ \mathrm{W\,m^{-2}\,K^{-4}}$, and T is the thermodynamic temperature. This situation becomes even worse once the microbolometer membrane is heated up by $\Delta T \approx 82.2$ K as the P_R amplitude increases by a factor of ≈ 2.7.

A method to determine all thermal parameters, such as G, H, and τ, based on a short voltage pulse with duration of ≈ 60 μs was proposed [11]. This technique allowed employment of V_B with amplitude up to ≈ 5 V, resulting in an improved SNR. Due to short pulse duration, the self-heating effect was negligible as it resulted in minimal influence by variation of R. Modern microbolometers use two [12,13] or three-level membrane configurations or carbon nanotubes as IR-sensitive materials [14] and their responses to the P_J are more complicated. Therefore the short pulse technique [11] cannot be utilized and the long pulse method [9] does not provide results with sufficient precision.

Here we show a technique of precise determination of G, H, and τ of an AC-powered Wheatstone bridge containing a microbolometer device with the bridge output signal processed by lock-in amplification technique. The colossal SNR of a lock-in amplifier allowed us to perform the microbolometer testing using a V_B value as low as ≈ 10 mV root mean square (RMS). This low amplitude of V_B resulted in P_J of ≈ 26 nW, leading to marginal microbolometer membrane temperature increase of ≈ 59 mK and allowing precise determination of the value of G with P_R having a minimized effect on the measurement. The value of τ was then extracted by observing the transient response of the microbolometer output to modulated external power supply and calculated H using Eq. (4) as $H = \tau\ G$.

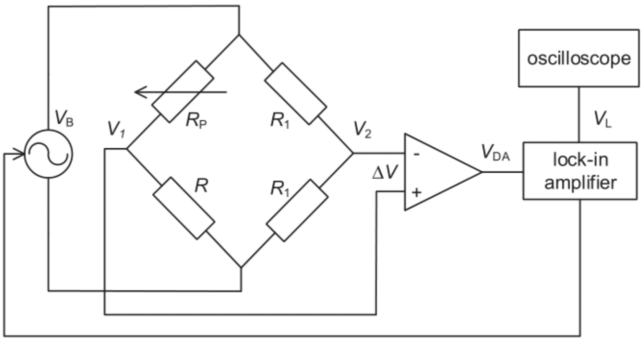

Fig. 1. Schematic of the system used for microbolometer testing. The microbolometer was connected into a Wheatstone bridge powered by an AC signal supplied by a lock-in amplifier. The balancing resistor R_P represents two potentiometers with maximum resistance value of 20 kΩ and 100 Ω, respectively, each with 20 turns for fine-tuning of the bridge balance. The R_1 represents two resistors with the fixed value of 20 kΩ and R stands for microbolometer resistance. The voltage difference of the bridge outputs was amplified by a differential voltage preamplifier with gain B set to 1000, its output voltage processed by a lock-in amplifier, and its output recorded by an oscilloscope.

2. Results and discussion

2.1. Theory and analytical solution

Let us consider the microbolometer connected to a Wheatstone bridge powered by an AC voltage with an amplitude of V_B RMS with its outputs processed by a differential amplifier with a gain factor of B and its output signal processed by a lock-in amplifier with gain of S (Fig. 1). The lock-in amplifier output voltage (V_L) can be expressed as function of ΔT and V_B (see Supplementary S1 for derivation of the equation) as

$$V_L = 10\frac{\left[\frac{R_0(1+\alpha\Delta T)}{R_0(1+\alpha\Delta T)+R_0} - \frac{1}{2}\right]V_B\cdot B}{S} \tag{9}$$

defining transfer function of entire system. For small values of ΔT the value of $\alpha\Delta T \ll 1$ the Eq. (9) can be simplified as

$$V_L = 10\frac{\alpha\Delta T\cdot}{4\cdot S}V_B\cdot B \tag{10}$$

The bridge was power by an AC voltage frequency ≫ than the one corresponding to the τ of the microbolometer. As the microbolometer membrane cannot be modulated by the AC, the total P_J can be considered as $P_J = \frac{V_B^2}{4\cdot R_0}$ warming up the membrane by $\Delta T = \frac{P_J - P_R}{G}$. Assuming the microbolometer membrane had the size of (25 × 25) μm² and ε of 0.48 (as per Ref. [15]), the amplitude of P_R at T_0 would be ≈ 251 nW. This P_R would cause the microbolometer membrane with G value of 180.4 nW K⁻¹ (in Ref. [16]) to increase its membrane temperature only by ≈ 1.39 K. Nevertheless, as the ΔT during the microbolometer measurement is minimal, the P_R does not significantly change; thus, Eq. (8) can be simplified to $G = P_C/\Delta T$ as the P_R only causes an offset of the ΔV. We can then express V_L as function of G (Supplementary S1) as

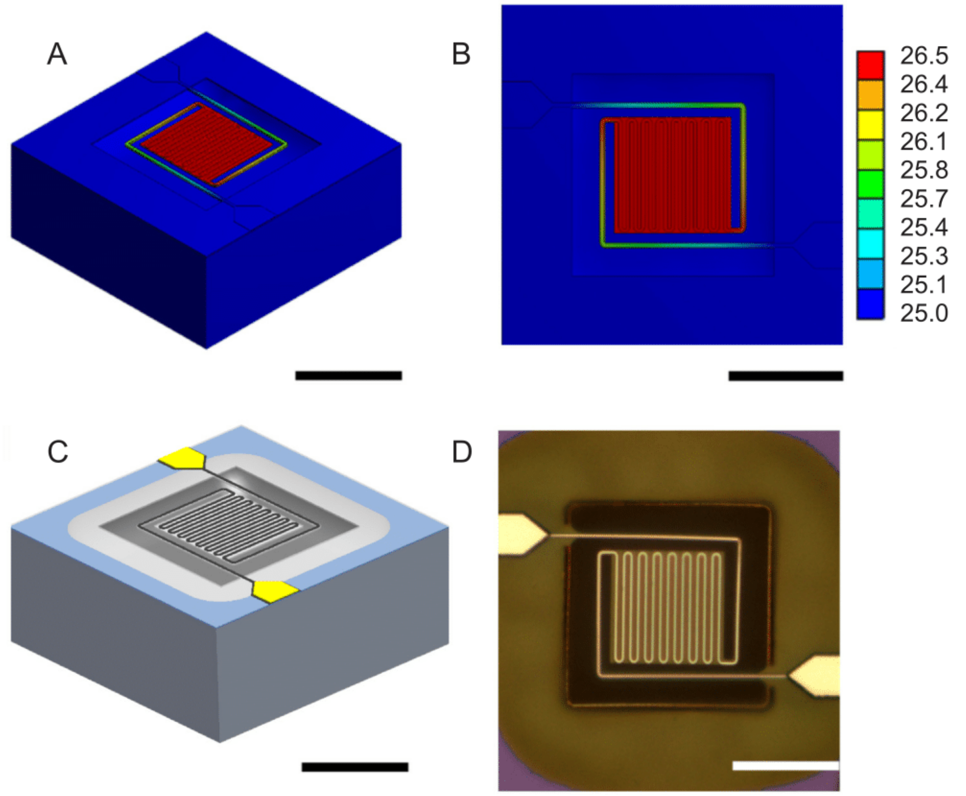

Fig. 2. Finite element modeling of the microbolometer membrane temperature using an AC-powered microbolometer with 100 mV RMS with (A) isometric and (B) top view. The temperature values are depicted in units of °C. First, we created the 3D model according to the actual device to be fabricated. The metal trace made of titanium with thickness of 80 nm and width of 0.8 µm was sandwiched between two layers of SiO_2 with same thickness of 0.25 µm. The microbolometer legs had width of 1.2 µm and length of 62 µm, and the membrane had size of $(25 \times 25)\,mm^2$. The silicon substrate had size of $(160 \times 180)\,\mu m^2$ and thickness of 75 µm (for simulation purpose only). The membrane was undercut by 25 µm both vertically and laterally. We set the temperature at the chip bottom to a fixed value of 25 °C. The electro-thermal simulation was performed for $V_B = 100$ mV RMS, showing the temperature distribution and the minimal temperature increase of ≈1.5 °C. (C) 3D model of microbolometer structure and (D) optical micrographs of an actual fabricated microbolometer. The bar represent length of 25 µm.

$$V_L = 10 \frac{\alpha \cdot V_B^3 \cdot B}{16 \cdot S \cdot G \cdot R_0} \tag{11}$$

2.2. Microbolometer design and fabrication

With an assumption of a microbolometer membrane with size of $(25 \times 25)\,\mu m^2$, its legs made of SiO_2 and with width, thickness, and length of 1.2 µm, 0.424 µm, and 62 µm, respectively, we calculated the predicted microbolometer parameters G, H, and τ using the analytical model described in Supplementary S2 as $G = 57.8\,nW\,K^{-1}$, $H = 0.55\,nJ\,K^{-1}$, and $\tau = 9.6\,ms$. We also performed an electro-thermal simulation for the model using the identical dimension for V_B of 100 mV RMS. The resulted temperature distribution of the final element modeling is shown in Fig. 2A and B and the temperature increase is estimated to be ≈1.5 °C.

The actual device layout was generated by a script-based Nanolithography Toolbox [16]. The chip with microbolometers was fabricated using Ti RTDs [17,18] embedded in a SiO_2 layer using the conventional Si bulk-micromachining techniques shown earlier [14]. Once the fabrication was almost completed and with the membrane still firmly attached to the substrate, we measured the R_0 and α values using a probe station with a temperature-controlled wafer holder (Supplementary Section 1 in Ref. [14]). The corresponding measured values of R_0 and α were ≈9.58 kΩ and $\approx 0.0023\,K^{-1}$, respectively. The wafer was then diced into individual chips by a diamond blade dicing saw and individual chips were exposed to vapors of XeF_2 until the membranes were completely released as schematically shown by three dimensional drawing (Fig. 2C) and fabricated device in the microphotograph in Fig. 2D. The chips were mounted onto a leadless chip carrier with 68 pads and electrically connected with Al wires using an ultrasonic wire-bonding. The packaged microbolometer devices were subsequently placed into a vacuum chamber with either glass or a Ge window and evacuated to pressure of 4.3×10^{-2} Pa, well below the limiting pressure of 5 Pa, thus eliminating the thermal convection as well as thermal conduction of the surrounding environment [10].

2.3. Measurement and discussion

The microbolometer with parameters described in previous paragraph was then connected into a Wheatstone bridge as per Fig. 1 and balanced by two adjustable resistors, one with maximum resistance of ≈20 kΩ for a rough balance of the bridge and a second one with maximum resistance of ≈100 Ω for bridge fine-tuning: both were types with 20 turns. The bridge was powered by a sine wave generator with an adjustable amplitude of V_B RMS provided by a lock-in amplifier. Both bridge outputs were connected to two inputs of a differential voltage preamplifier with gain set to 1000. We also activated an internal band pass filter set to 10 dB/decade with low and high cut-off frequencies set to 300 Hz and 3 kHz, respectively, to further improve the SNR. The ΔV signal was processed by a lock-in amplifier with S value set to 0.1 V. We numerically determined the Eq. (9) as function of V_B and ΔT (Supplementary S3):

$$V_L = 57.44 \cdot \Delta T \cdot V_B \tag{12}$$

We measured an amplitude of the V_L as a function of the V_B in a set range from 10 mV RMS to 100 mV RMS with a set step of 10 mV RMS. This experiment was repeated three times and we plotted the V_L as a function of V_B (Fig. 3) and performed the curve-fitting using a polynomial function of third order with first and second coefficients set to zero based on Eq. (11) as

$$V_L = A_3 \cdot V_B^3 + A_0, \tag{13}$$

with $A_3 = 10 \frac{B \cdot \alpha}{16 \cdot S \cdot G \cdot R_0}$ and A_0 is the bridge offset due to its imbalance, which is always presented. The A_3 fitting coefficient had value of $(3633.1 \pm 4.7)\,V^{-2}$, resulting in a G value of $(41.23 \pm 0.05)\,nW\,K^{-1}$, both (mean ± fitting error).

A vacuum chamber equipped with a glass window was placed under an optical microscope with an objective lens magnification of 50× and numerical aperture of 0.55. We then monitored the Wheatstone bridge response once the microbolometer was exposed to the blue light with principal wavelength of 470 nm from the microscope. Even though the

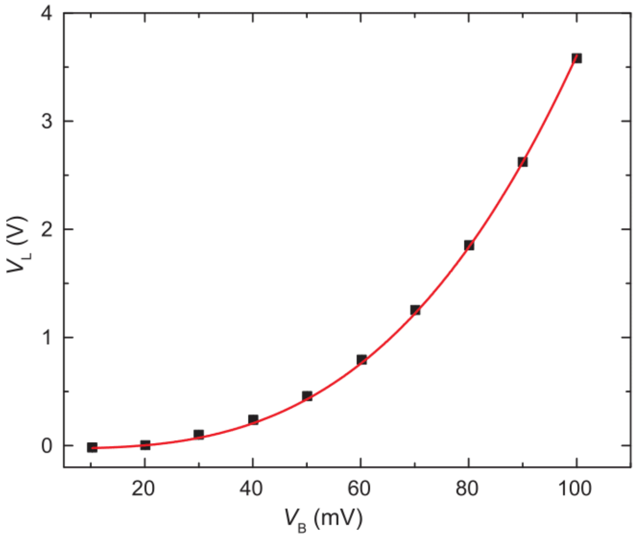

Fig. 3. Microbolometer response at the lock-in amplifier output as a function of V_B RMS, measured three times (black squares). We performed a function curve fit (red line) using polynomial function of third order $V_L = A_0 + A_1 \cdot V_B + A_2 \cdot V_B^2 + A_3 \cdot V_B^3$ setting values of linear and parabolic coefficient A_1 an A_2 to zero. The fitting value of $A_3 = (3633.0 \pm 4.7)\,\mathrm{V}^{-2}$ (mean ± fitting error) resulted in a G value of $(41.23 \pm 0.05)\,\mathrm{nW\,K^{-1}}$. The nearly perfect fitting R^2 value of 0.99999 suggests that the fitting model is correct.

microbolometer membrane absorption at the light emitting diode (LED) wavelength is rather limited, the heating the microbolometer by a LED with V_B set to 0.1 V caused the change of V_L (ΔV_L) of (783.31 ± 0.65) mV (mean ± standard deviation). We applied Eq. (12) and we found corresponding ΔT value as (136.47 ± 0.11) mK (mean ± standard deviation). As we already determined value of G to be $(41.23 \pm 0.05)\,\mathrm{nW\,K^{-1}}$ (mean ± fitting error), we can now calculate dissipated power in the membrane due incident light from a blue LED as ≈5.63 nW.

We performed the experiment of detecting the amplitude of ΔV_L with blue light off and on with different value of V_B value from 20 mV RMS to 100 mV RMS with a step of 20 mV (Fig. 4). We did the curve-fitting using an exponential function of first-order to the ΔV_L signal

$$\Delta V_L = V_{L2} + (V_{L1} - V_{L2}) \cdot e^{-\frac{t-t_0}{\tau}} \tag{14}$$

where V_{L1} and V_{L2} are the lock-in amplifier output voltages without and with irradiation by an LED, respectively and t_0 is time when the light was switched on. The value of τ was determined as $\tau = (15.46 \pm 0.56)$ ms (mean ± standard deviation from 30 measurements) and, with modified Eq. (4) ($H = \tau \cdot G$), we also calculated the value of $H = (0.637 \pm 0.34)\,\mathrm{nJ\,K^{-1}}$, (mean ± standard deviation) and as predicted due to small amplitude of ΔT the value of V_B had no influence on the τ amplitude.

We also used this measurement to determine the system power resolution. The V_L amplitude with V_B = 100 mV RMS had a value of (783.31 ± 0.65) mV (mean ± standard deviation) and the sensitivity can be defined as 3 × standard deviation value, which is 1.95 mV. With the system transfer function of $\approx 57.44\,\mathrm{V\,V^{-1}\,K^{-1}}$ (Supplementary Section 3) and G value of $(41.23 \pm 0.05)\,\mathrm{nW\,K^{-1}}$, both (mean ± fitting error), the 1.95 mV of 3 × standard deviation corresponded to the ΔT value of ≈340 μK resulting in system power resolution (ΔP) of ≈14 pW. This ΔP value could be further lowered by increase of the lock-in amplifier sensitivity, which would require thermal shield of the its vacuum chamber to suppress its temperature fluctuation.

Finally, we replaced the glass window of the vacuum chamber with a window made of Ge and exposed the microbolometer to IR radiation from a blackbody with an aperture d of ≈10.5 mm and temperature set to 200 °C, 300 °C, and 400 °C, respectively. The Wheatstone bridge was biased with V_B set to 50 mV RMS warming up the microbolometer membrane only by ≈160 mK. We monitored the ΔV_L amplitude while the microbolometer was irradiated by a blackbody with different set temperatures and distances (D). The distance was modulated by the number (n) of spacers with identical thickness w of ≈15.2 mm placed between the chamber and the blackbody from $n = 1$ to $n = 8$, which varied the distance change from $D = D_0$ to $D = D_0 + n\,w$. D_0 is minimal distance between the blackbody and the microbolometer membrane and estimated to be ≈30 mm (Fig. 5A). We calculated the amplitude of incident IR power radiation absorbed by the microbolometer membrane as was done previously [14]:

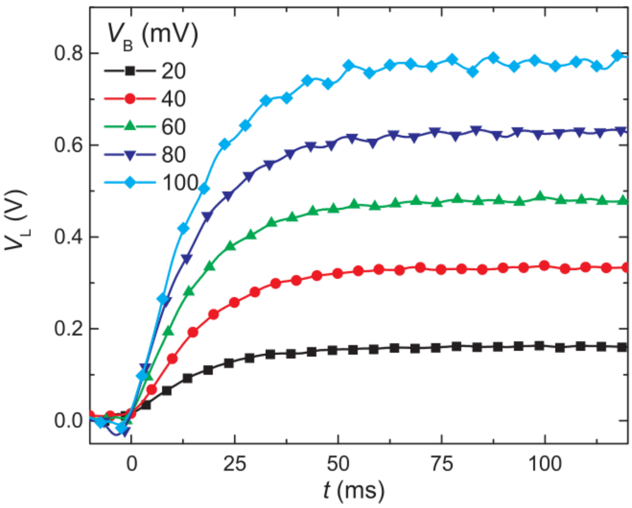

Fig. 4. Microbolometer response at the lock-in amplifier output V_L as a function of time with microbolometer on/off illuminated by a LED dissipated power in the microbolometer of ≈5.63 nW. We set the V_B amplitude as (20, 40, 60, 80, and 100) mV RMS marked by black squares, red circles, green up triangles, dark-blue down triangles, and light-blue rotated squares, respectively. We performed function curve-fitting using Eq. (12) and extracted value of $\tau = (15.46 \pm 0.56)$ ms (mean ± standard deviation from 30 measurements), exhibiting no influence of V_B on the τ value in the entire range of used V_B values. (For interpretation of the references to colour in this figure legend, the reader is referred to the web version of this article.)

$$P_{IR} = a^2 \cdot \varepsilon_{bb} \cdot \tau_F \cdot M \left[\frac{\left(\frac{d}{2}\right)^2}{D^2 + \left(\frac{d}{2}\right)^2} \right] \tag{15}$$

where ε_{bb} is the emission of blackbody radiation (≈0.95 as per manufacturer's datasheet), τ_F is the average experimentally determined transmittance of the Ge window ($\tau_F \approx 0.95$), and M is the integrated radiant excitance of the blackbody according to Planck's radiation law ($\approx 2588\,\mathrm{W\,m^{-2}}$) [15]. We plotted the microbolometer system response as a function of the number of spacers of the function of P_{IR} (Fig. 5B) and the linear curve-fitting slope

$$\Re_{IR} = \frac{\Delta V_L}{P_{IR}} \tag{16}$$

which provided us with system responsivity $\Re_{IR}$ of $(5.55 \pm 0.38)\,\mathrm{MV\,W^{-1}}$, $(7.42 \pm 0.21)\,\mathrm{MV\,W^{-1}}$, and $(7.94 \pm 0.11)\,\mathrm{MV\,W^{-1}}$ for blackbody temperatures of 200 °C, 300 °C, and 400 °C, respectively, all (mean ± fitting error).

3. Conclusion

We demonstrated a method to extract thermal parameters such as G, H, and τ as well as $\Re_{IR}$ from the microbolometer using the lock-in amplification technique. The proposed method is applicable with a

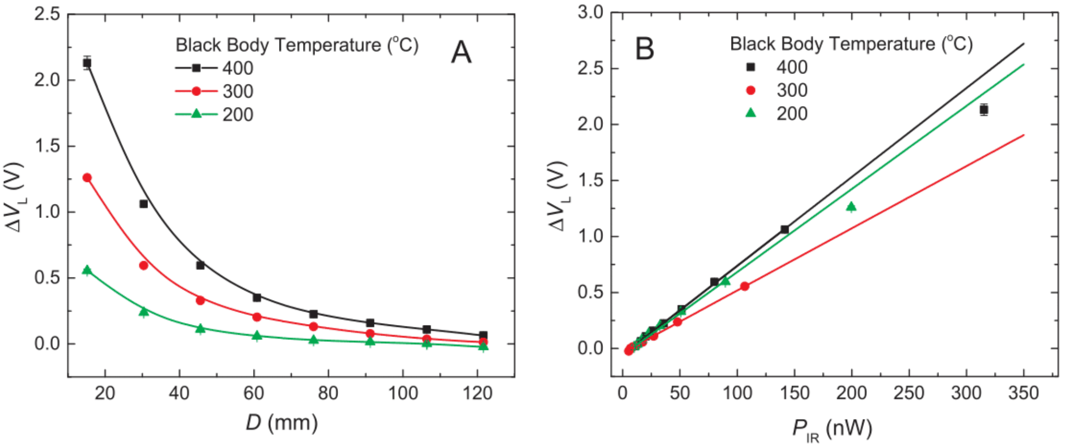

Fig. 5. Microbolometer response to the IR radiation (A) as a function of the distance with black body temperature as parameter. (B) Microbolometer response at the lock-in amplifier output as a function of incident IR radiation power.

biasing microbolometer with small voltage that causes negligible warming of its membranes during the measurement. This suppresses the self-heating effect and loses due to radiation change during the measurement and, thus, provides a precise value of the *G* parameter. With intentionally increased power dissipated in the microbolometer membrane by a step function, the transient analysis of the system output provided the τ value as well as *H*. Finally, the microbolometer response to irradiation with IR from a black body source provided the IR responsivity in a range from $(5.55 \pm 0.38)\,\mathrm{MV\,W^{-1}}$, $(7.42 \pm 0.21)\,\mathrm{MV\,W^{-1}}$ to $(7.94 \pm 0.11)\,\mathrm{MV\,W^{-1}}$. This measurement demonstrated that the proposed method is suitable for applications where extreme sensitivity is required. We also determined the system having an excellent power resolution of $\approx 14\,\mathrm{pW}$. This could be increased further by lock-in amplifier setting, making this one of the most sensitive calorimeters.

Acknowledgment

Authors would like to acknowledge financial support of GACR Project Number 17-20716S, support of Czech Ministry of Education under grant LO1401, technical support of Nano+, Centrum SIX, as well as help from staff at the Center for Nanoscale Science and Technology of NIST, Gaithersburg, MD, USA. Finally, the authors are also grateful to Pavel Podešva for his help with graphical design.

Conflict of interest

Authors declare no conflict of interested related to the submitted manuscript.

Appendix A. Supplementary material

Supplementary data associated with this article can be found, in the online version, at https://doi.org/10.1016/j.infrared.2018.07.037.

References

[1] M.J.E. Golay, A pneumatic infra-red detector, Rev. Sci. Ins. 18 (1947) 357–362.
[2] K.C. Liddiard, Thin-film resistance bolometer IR detectors, Infrared Phys. 24 (1984) 57–64.
[3] K.C. Liddiard, Thin-film resistance bolometer IR detectors .2, Infrared Phys. 26 (1986) 43–49.
[4] B. Cole, R. Horning, B. Johnson, K. Nguyen, P.W. Kruse, M.C. Foote, High performance infrared detector arrays using thin film microstructures, in: Proceedings of 1994 IEEE International Symposium on Applications of Ferroelectrics, 1994, pp. 653–656.
[5] A.J. Syllaios, T.R. Schimert, R.W. Gooch, W.L. McCardel, B.A. Ritchey, J.H. Tregilgas, Amorphous silicon microbolometer technology, MRS Proc. 609 (2011) A14–14.
[6] P.W. Kruse, Chapter 2 principles of uncooled infrared focal plane arrays, in: P.W. Kruse, D.D. Skatrud (Eds.), Semiconductors and Semimetals, Elsevier, 1997, pp. 17–42.
[7] L. Lu, W. Yi, D.L. Zhang, 3 Omega method for specific heat and thermal conductivity measurements, Rev. Sci. Ins. 72 (2001) 2996–3003.
[8] T. Yamane, N. Nagai, S. Katayama, M. Todoki, Measurement of thermal conductivity of silicon dioxide thin films using a 3 omega method, J. Appl. Phys. 91 (2002) 9772–9776.
[9] X. Gu, G. Karunasiri, G. Chen, U. Sridhar, B. Xu, Determination of thermal parameters of microbolometers using a single electrical measurement, Appl. Phys. Lett. 72 (1998) 1881–1883.
[10] X. He, G. Karunasiri, T. Mei, W.J. Zeng, P. Neuzil, U. Sridhar, Performance of microbolometer focal plane arrays under varying pressure, IEEE Electron Device Lett. 21 (2000) 233–235.
[11] P. Neuzil, T. Mei, Evaluation of thermal parameters of bolometer devices, Appl. Phys. Lett. 80 (2002) 1838–1840.
[12] D.F. Murphy, A. Kennedy, M. Ray, R. Wyles, J. Wyles, J.F. Asbrock, C. Hewitt, D.V. Lue, T. Sessler, J.S. Anderson, D. Bradley, R. Chin, H. Gonzales, C.L. Pere, T. Kostrzewa, Resolution and sensitivity improvements for VOx microbolometer FPAs, in: AeroSense 2003, SPIE, 2003, pp. 12.
[13] L. Hyung-Kew, Y. Jun-Bo, Y. Euisik, J. Sang-Baek, Y. Yoon-Joong, L. Wook, K. Sang-Gook, A high fill-factor infrared bolometer using micromachined multilevel electrothermal structures, IEEE Trans. Electron Devices 46 (1999) 1489–1491.
[14] V. Svatoš, I. Gablech, B.R. Ilic, J. Pekárek, P. Neužil, In situ observation of carbon nanotube layer growth on microbolometers with substrates at ambient temperature, J. Appl. Phys. 123 (2018) 114503.
[15] T. Mei, P. Neuzil, G. Karunasiri, W. Zeng, Approach to measure thermal efficiency of bolometer sensors, Appl. Phys. Lett. 80 (2002) 2183–2185.
[16] K.C. Balram, D.A. Westly, M. Davanco, K. Grutter, Q. Li, T. Michels, C.H. Ray, L. Yu, R. Kasica, C.B. Wallin, I. Gilbert, B.A. Bryce, G. Simelgor, J. Topolancik, N. Lobontiu, Y. Liu, P. Neuzil, V. Svatos, K.A. Dill, N.A. Bertrand, M. Metzler, G. Lopez, D.A. Czaplewski, L. Ocola, K. Srinivasan, S. Stavis, V. Aksyuk, J.A. Liddle, S. Krylov, B.R. Ilic, The nanolithography toolbox, J. Res. Natl. Inst. Stand. 121 (2016) 464–475.
[17] I. Gablech, V. Svatoš, O. Caha, M. Hrabovský, J. Prášek, J. Hubálek, T. Šikola, Preparation of (001) preferentially oriented titanium thin films by ion-beam sputtering deposition on thermal silicon dioxide, J. Mater. Sci. 51 (2016) 3329–3336.
[18] I. Gablech, O. Caha, V. Svatoš, J. Pekárek, P. Neužil, T. Šikola, Stress-free deposition of [001] preferentially oriented titanium thin film by Kaufman ion-beam source, Thin Solid Films 638 (2017) 57–62.

15 Review of possible future 2D functional materials

15.1 Motivation of the article

Motivation of this article was to examine the other 2D materials than graphene. Few problems with graphene occurred during the fabrication process of MEMS piezoelectric resonator with Hall Bar/FET structure. The main problems were the poor quality of CVD-prepared graphene and its transfer with consequent shaping.

Further, the graphene is relatively well described in many publications and there is not much space for others. As this work is mainly based on fabrication of MEMS piezoelectric resonator with Hall Bar/FET structure for modulation of graphene monolayer properties, this structure should be alternatively useful for examination of other 2D materials. These new materials offer space for publications about fundamental and applied research.

15.2 Conclusion on the article

The possibilities of use of new 2D materials such as arsenene, antimonene, germanene, silicene and phosporene are summarized in this work. There are not much experimental papers describing their behavior due to their novelty. These manuscripts were mostly based on theoretical modelling. This review clearly states the possibilities of future practical applications for these materials. Next important is the broadening knowledge in field of 2D materials. The main insight is that these materials can be utilized for various applications thanks to their properties, just as graphene. It can be advantageous for using these 2D materials on piezoelectric structures and FETs, for instance gas sensors.

15.3 Contribution

This is principally group work where we summarized the knowledge about new 2D materials. Each author added his expertise of every mentioned material. I also contributed to the writing of the manuscript.

15.4 Article 10

Article **Monoelemental 2D Materials-based Field Effect Transistors for Sensing and Biosensing: Phosphorene, Antimonene, Arsenene, Silicene, and Germanene go beyond Graphene** [64] was published in **TrAC- Trends in Analytical Chemistry** (2017 IF 7.034) in **August 2018.**

Trends in Analytical Chemistry 105 (2018) 251–262

Contents lists available at ScienceDirect

Trends in Analytical Chemistry

journal homepage: www.elsevier.com/locate/trac

Monoelemental 2D materials-based field effect transistors for sensing and biosensing: Phosphorene, antimonene, arsenene, silicene, and germanene go beyond graphene

Imrich Gablech [a, b], Jan Pekárek [a, b], Jaroslav Klempa [a, b], Vojtěch Svatoš [a, b],
Ali Sajedi-Moghaddam [a], Pavel Neužil [c, **], Martin Pumera [a, d, *]

[a] Central European Institute of Technology, Brno University of Technology, Purkyňova 123, CZ-61200 Brno, Czech Republic
[b] Brno University of Technology, Faculty of Electrical Engineering and Communication, Department of Microelectronics, Technická 3058/10, CZ-61600 Brno, Czech Republic
[c] Northwestern Polytechnical University, 127 West Youyi Road, Xi'an, Shaanxi, PR China
[d] Division of Chemistry & Biological Chemistry, School of Physical Mathematical Science, Nanyang Technological University, Singapore 637371, Singapore

ARTICLE INFO

Article history:
Available online 25 May 2018

Keywords:
Antimonene
Arsenene
Phosphorene
Silicene
Germanene
Graphene
FET
Sensing

ABSTRACT

Graphene has been of immense interest for its interesting electronic properties, such as being a zero-band gap semiconductor. However, to be able to usefully employ graphene for electronics and electronic-transduction system sensors and biosensors, one needs to open this band gap. This proofs to be challenging on reproducible, scalable way. There are other 2D monoelemental materials that exhibit useful band gap and which can be used for field effect transistor- (FET-) based sensing and biosensing. Here we discuss trends in the development of FET-based sensors utilizing 2D phosphorene, arsenene, antimonene, silicene, and germanene.

1. Introduction

In the past two years, there has been great interest in 2D monoelemental materials beyond graphene, such Group IVA silicene and germanene and Group VA phosphorene, arsenene, and antimonene (Fig. 1). While graphene, which is a single sheet of graphite (see IUPAC definition from 1995 [1]), has received enormous interest over the past 14 years, its utilization for some applications, such as field effect transistors (FETs), is limited as it does not show any band gap. Such a band gap needs to be engineered by modification of the graphene. Other layered systems and their 2D layered counterparts, such as transition metal dichalcogenides (typical example is MoS_2) and transition metal oxides, have been investigated in recent years as they show a sizable band gap. One can find a large variety of layered materials comprising two, three, or more elements. Here, we wish to focus on materials that are layered but monoelemental. The number of monoelemental layered materials is limited and includes layered forms of phosphorus (called "black phosphorus" and known from 1916 [2] and rediscovered in 2017 [3]), arsenic, antimony, and bismuth [4]. Unlike graphene, these materials are semiconductors (that is, materials with an energy band gap) when exfoliated to a single layer and are, therefore, immensely useful for the construction of FETs.

Group VA materials include phosphorus, arsenic, antimony, and bismuth. These materials have either (A) rhombohedral structure or (B) orthorhombic structure (see Fig. 2). Note that two layers of atoms are chemically bonded in an "armchair" or "boat" configuration to create one sheet (thus, the sheet is not atomically thin as in the case of graphene, but naturally two-atoms-thick and with no double bond between the sheets). Note that layers of black phosphorus are held together by rather weak van der Waals forces while layers of As, Sb, and Bi are held by stronger chemical bonds.

Layered and 2D materials based in Group IVA, germanene [6], and silicene [7] are 2D analogs of graphene; however, the atoms are

---

* Corresponding author. Division of Chemistry & Biological Chemistry, School of Physical Mathematical Science, Nanyang Technological University, Singapore 637371, Singapore.
** Corresponding author.
E-mail addresses: pavel.neuzil@npwu.cn (P. Neužil), pumera.research@gmail.com (M. Pumera).

https://doi.org/10.1016/j.trac.2018.05.008
0165-9936/

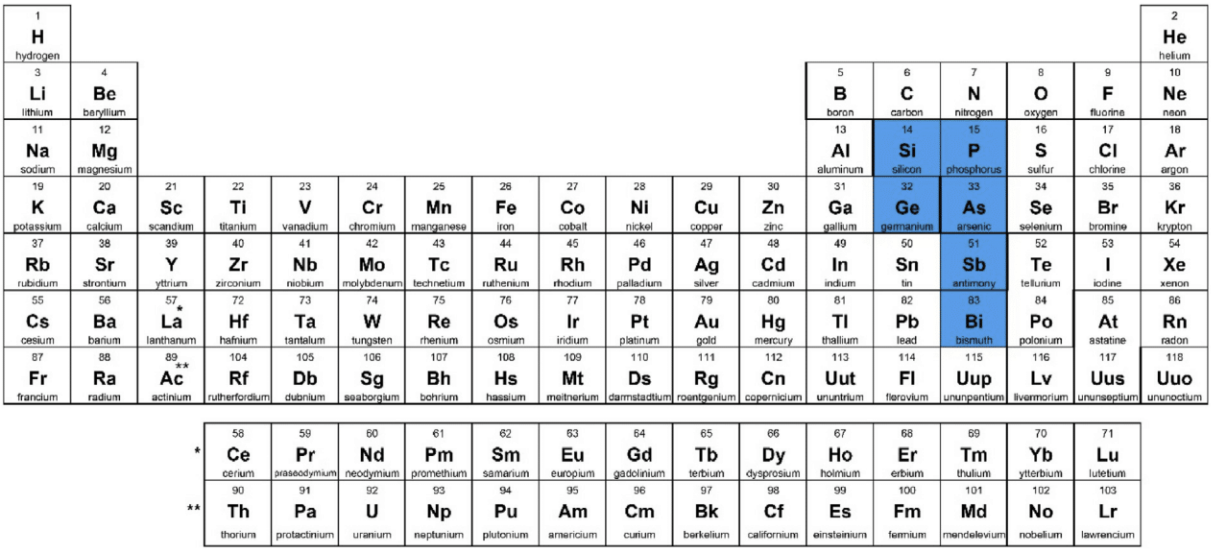

1 H hydrogen																	2 He helium
3 Li lithium	4 Be baryllium											5 B boron	6 C carbon	7 N nitrogen	8 O oxygen	9 F fluorine	10 Ne neon
11 Na sodium	12 Mg magnesium											13 Al aluminum	14 Si silicon	15 P phosphorus	16 S sulfur	17 Cl chlorine	18 Ar argon
19 K potassium	20 Ca calcium	21 Sc scandium	22 Ti titanium	23 V vanadium	24 Cr chromium	25 Mn manganese	26 Fe iron	27 Co cobalt	28 Ni nickel	29 Cu copper	30 Zn zinc	31 Ga gallium	32 Ge germanium	33 As arsenic	34 Se selenium	35 Br bromine	36 Kr krypton
37 Rb rubidium	38 Sr strontium	39 Y yttrium	40 Zr zirconium	41 Nb niobium	42 Mo molybdenum	43 Tc technetium	44 Ru ruthenium	45 Rh rhodium	46 Pd palladium	47 Ag silver	48 Cd cadmium	49 In indium	50 Sn tin	51 Sb antimony	52 Te tellurium	53 I iodine	54 Xe xenon
55 Cs cesium	56 Ba barium	57 * La lanthanum	72 Hf hafnium	73 Ta tantalum	74 W tungsten	75 Re rhenium	76 Os osmium	77 Ir iridium	78 Pt platinum	79 Au gold	80 Hg mercury	81 Tl thallium	82 Pb lead	83 Bi bismuth	84 Po polonium	85 At astatine	86 Rn radon
87 Fr francium	88 Ra radium	89 ** Ac actinium	104 Rf rutherfordium	105 Db dubnium	106 Sg seaborgium	107 Bh bohrium	108 Hs hassium	109 Mt meitnerium	110 Ds darmstadtium	111 Rg roentgenium	112 Cn copernicium	113 Uut ununtrium	114 Fl flerovium	115 Uup ununpentium	116 Lv livermorium	117 Uus ununseptium	118 Uuo ununoctium
		*	58 Ce cerium	59 Pr praseodymium	60 Nd neodymium	61 Pm promethium	62 Sm samarium	63 Eu europium	64 Gd gadolinium	65 Tb terbium	66 Dy dysprosium	67 Ho holmium	68 Er erbium	69 Tm thulium	70 Yb ytterbium	71 Lu lutetium	
		**	90 Th thorium	91 Pa protactinium	92 U uranium	93 Np neptunium	94 Pu plutonium	95 Am americium	96 Cm curium	97 Bk berkelium	98 Cf californium	99 Es einsteinium	100 Fm fermium	101 Md mendelevium	102 No nobelium	103 Lr lawrencium	

Fig. 1. Periodic table with elements of interest marked in blue.

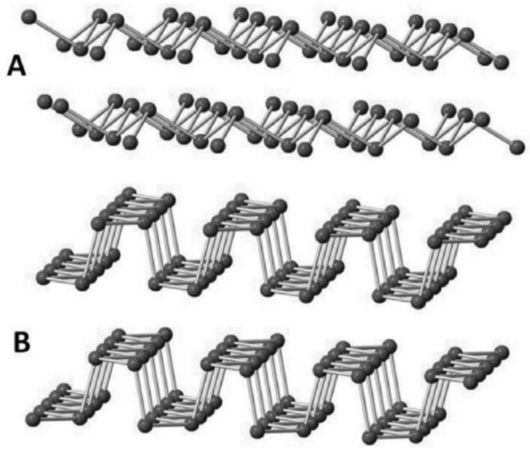

Fig. 2. Structures of rhombohedral layered (black) phosphorus, arsenic, antimony, and bismuth (A) and orthorhombic layered arsenic and (black) phosphorus (B). Reprinted from Ref. [4].

not aligned in a perfect plane such as in graphene [5]. The structures of germanene and silicene are shown in Fig. 3.

The FET principle was proposed as early as 1926 [8] and practically demonstrated more than 30 years ago [9]. This paved the way to create the modern metal oxide semiconductor FET (MOSFET) in complementary configuration (CMOS) based on silicon technology, which has become the default technology used nowadays in practically all electronic devices. The basic FET is a four-terminal structure (Fig. 4A) consisting of a gate, source, drain, and a substrate. The device can operate in three different modes [10]: subthreshold, linear [Equation (1)] and saturated [Equation (2)], depending on the voltages connected to the terminals (here we assume that the source and the substrate are connected):

$$I_D = \frac{\boldsymbol{\mu_n} \cdot C_d}{2} \cdot \frac{W}{L} \cdot \left[\left(V_{GS} - \mathbf{V_T} - \frac{V_{DS}}{2}\right) \cdot V_{DS}\right] \mathit{for}\ V_{GS} \geq V_T\ \mathit{and}\ V_{DS} \ll V_{GS} - V_T \qquad (1)$$

or

$$I_D = \frac{\boldsymbol{\mu_n} \cdot C_d}{2M} \cdot \frac{W}{L} \cdot (V_{GS} - \mathbf{V_T})^2\ \mathit{for}\ V_{GS} \geq V_T\ \mathit{and}\ V_{DS} \geq V_{GS} - V_T, \qquad (2)$$

where I_d is drain current, V_{GS} is gate-source voltage, V_T is threshold voltage, μ_n is electron mobility in the substrate and with a value of 1400 $cm^2 \cdot V^{-1} \cdot s^{-1}$ for silicon at 25°C, C_d is dielectric capacitance per unit area of the gate material, W and L are width and length of the transistor, respectively, V_{DS} is the drain-source voltage, and M is a function of substrate doping concentration and gate dielectric properties (Fig. 4A). Normally, the device operates in any of two active regions: either linear or saturated. The I_d amplitude can be affected electrically by V_{GS} or V_{DS} as well as by modulation of V_T, μ_n, and C_d. The last three items are constant in CMOS devices as they are encapsulated by light opaque materials. On the other hand, the FET sensors operate differently as the gate is in contact with an analyte. Then, the values of either V_T, μ_n, or C_d are modulated by the analyte and affect the I_D amplitude, which is measured and provides information regarding the analyte.

The gate dielectric material is electrically insulated; thus, ideally, the steady-state direct electrical current (DC) flowing through the gate dielectric can be considered to have a value of $I_G = 0$ A. That makes the FET a transducer affecting the I_d by an induced electric field without loading the gate voltage source. It can be considered also as a high-to-low impedance converter. Soon after the MOSFET introduction, researchers started to investigate if the FET principle can be also used for sensing applications and several FET clones were proposed and tested.

A family of chemical and biochemical sensors based on V_T modulation starting with pH-detecting ion-sensitive FETs (ISFETs) [11] (Fig. 4B) is currently used also to detect other ions, such as Na^+, K^+, Ca^{2+}, Cl^-, and the ISFET clone, called “enzyme FET” (ENFET) for glucose, urea, and cholesterol. Originally, H_2 gas-sensing FETs were introduced with the gate made from an ultrathin Pd layer that allows H_2 to diffuse at an elevated temperature of 150°C through the Pd layer to the Pd–insulator interface to affect the device threshold voltage [12]. The device operation was extended to sensing other gases such as CO, H_2S, and NH_3.

The utility of 2D materials for FET-based devices was investigated more than decade ago for graphene [13,14] by studying the electric field effect in this 2D material. It was found that its μ_n has an

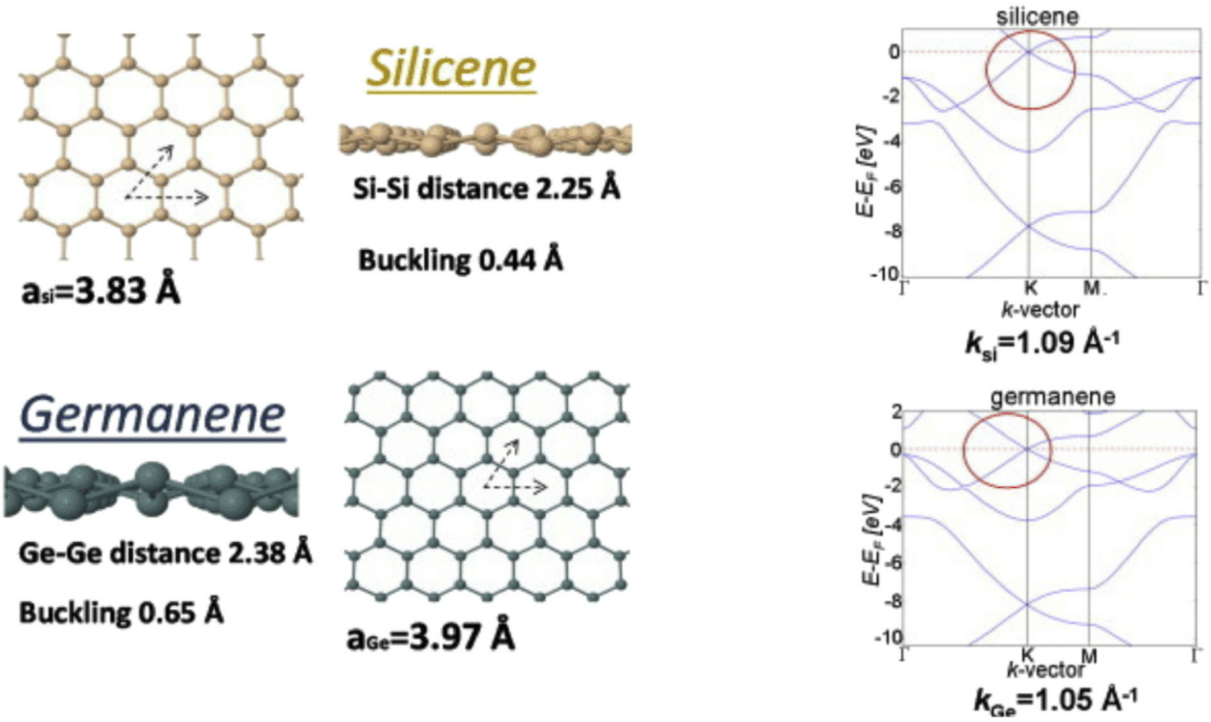

Fig. 3. Structures of silicene and germanene. Reprinted with permission from Ref. [5].

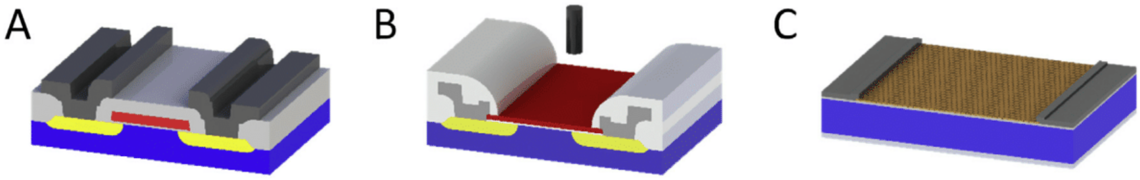

Fig. 4. (A) A MOSFET (ISFET) and (C) graphene FET. Blue and yellow colors represent silicon substrate with both types of doping, n and p, respectively or vice versa, light gray color represents SiO_2, (A) red polycrystalline silicon layer for the MOSFET gate or (B) ISFET gate materials such as Si_3N_4, and (C) brown graphene.

exceptionally high value of 15,000 $cm^2 \cdot V^{-1} \cdot s^{-1}$, which is more than 10× higher than the one of Si. As per Eqs. (1) and (2), 10× higher amplitude of μ_n causes 10 times greater I_D with the same change of V_T and C_D. Since then, graphene has been extensively studied, including graphene-based FETs for various sensing applications [15] as the I_D value can be affected by modulating the μ_n either mechanically by stretching the 2D material or by chemically modifying its properties. The first can be used for mechanical sensing and the second for chemical or biochemical sensing.

There are two types of graphene-based FETs: those with a top-gate as well as the back-gate and those with a back gate only [16]. The first one is easier to control as modulating the electric field in the 2D material is simple; however, its fabrication is more complicated. In addition, the FET with 2D material sandwiched between two dielectrics is not very suitable for any chemical or biochemical sensing application as there is no direct access to the 2D material unless the top dielectric layer is extremely thin. The device with the back gate only has an advantage of 2D material direct exposure by the environment making its response fast but also more difficult to control [16]. To construct FET-based sensing devices, the presence of an energy band gap is important as the material properties are strongly dependent on it. The conductivity of the material is determined by the electrons with enough energy to be excited across the energy band gap. This feature can be modulated by the presence of an analyte at the FET surface as this will affect the energy band gap and, thus, its conductivity. Higher mobility also allows more sensitive measurement as per Eqs. (1) and (2).

We overview key theoretical studies and applications of 2D materials as the main parts of FET-based sensors for sensing of gases, small molecules, and biomolecules (see Table 1).

2. 2D materials for FET sensors and biosensors

2.1. Phosphorene

Kou et al. [21] performed first-principle calculations to study the interaction of phosphorene with physisorbed small molecules such

Table 1
Summarized properties of antimonene, arsenene, phosphorene, silicone, and germanene.

Material	Energy band gap (eV)	Carrier mobility ($cm^2 \cdot V^{-1} \cdot s^{-1}$)
Antimonene	1–1.5	10–100 or 500–1200 [17]
Arsenene	2.5	10–100 or 500–1200 [17]
Phosphorene	1.5	260 [18]
Silicene	0.002–0.5	100 (measured) 2.57 × 10^5 (calculated) [19]
Germanene	<0.05	6 × 10^5 (calculated) [20]

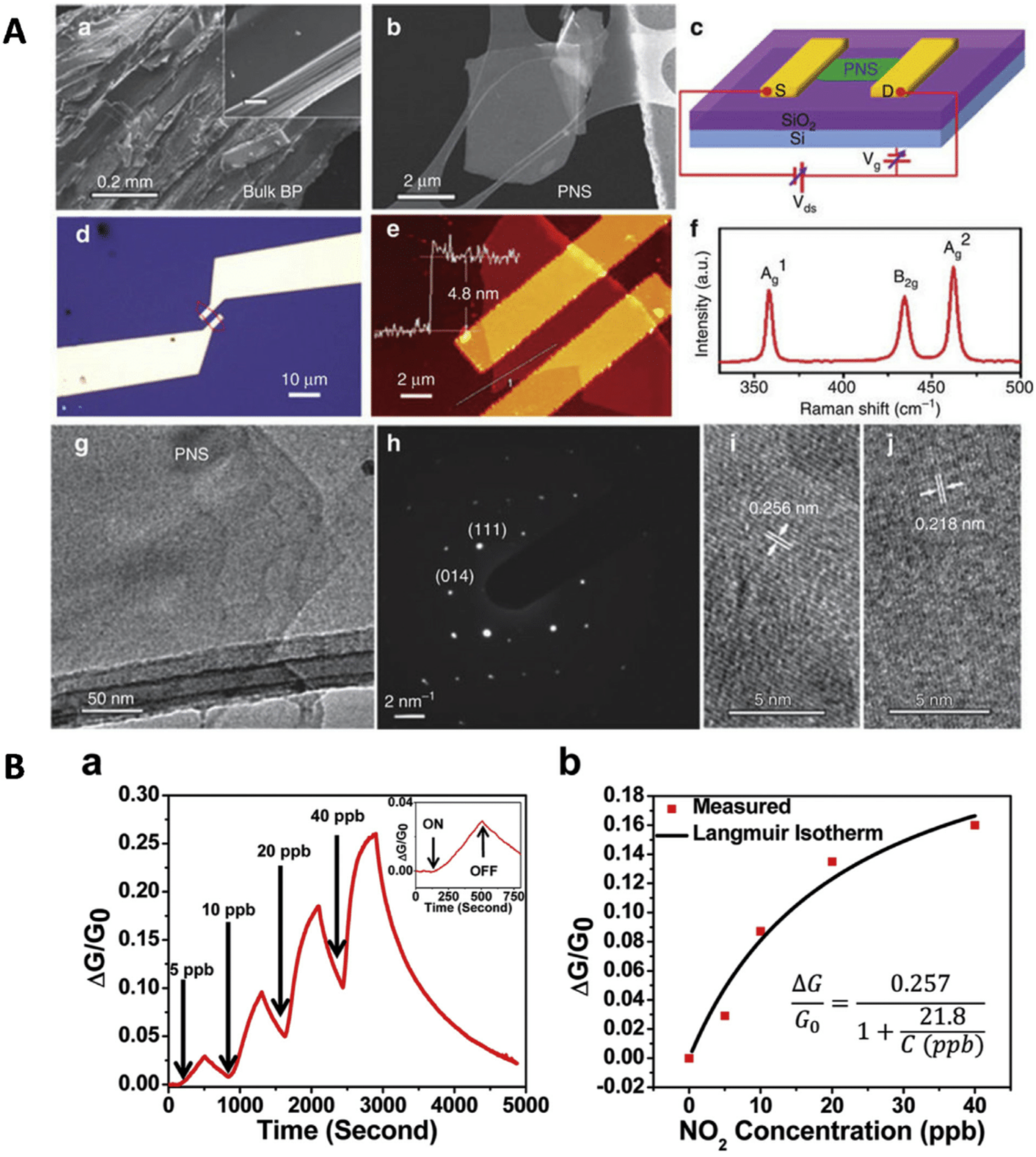

Fig. 5. Black phosphorus (BP) FET for gas sensing (A): (a) scanning electron microscopy (SEM) image of bulk BP. The inset is a magnified image showing the layered structure; scale bar, 10 μm; (b) SEM image of exfoliated PNS; (c) schematic of an FET device based on the PNS and the circuit for electrical and sensing measurements; (d, e) optical microscopy and AFM images of the PNS sensor device showing that the PNS electrically bridges the gold electrodes. The profile in (e) indicates the PNS has a thickness of 4.8 nm; (f) Raman spectrum of PNS; and (g, h, i, j) TEM image, selected area electron diffraction (SAED) pattern, and high-resolution TEM (HRTEM) images of PNS. The two HRTEM images (i, j) demonstrate two representative lattice spacings of PNS. (B) NO_2 gas sensing performance of multilayer BP FET: (a) relative conductance change ($\Delta G/G_0$) vs. time in seconds for a multilayer BP sensor showing sensitivity to NO_2 concentrations (5–40 ppb). Inset shows a zoomed-in image of a 5 ppb NO_2 exposure response with identification of points in time where the NO_2 gas is switched on and off and (b) $\Delta G/G_0$ plotted vs. NO_2 concentration applied to the BP FET showing an agreement between the measured values (red squares) and the fitted Langmuir isotherm. The equation in the bottom right is the fitted Langmuir isotherm.

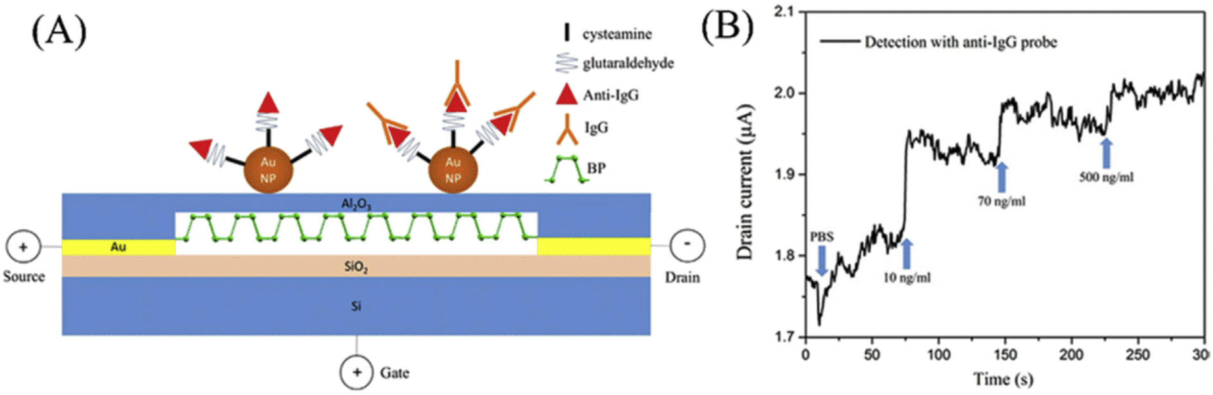

Fig. 6. (A) Cross sectional schematic illustration of the BP-based FET biosensor. (B) Dynamic response of the biosensor to different concentrations of IgG. Reproduced from Ref. [26].

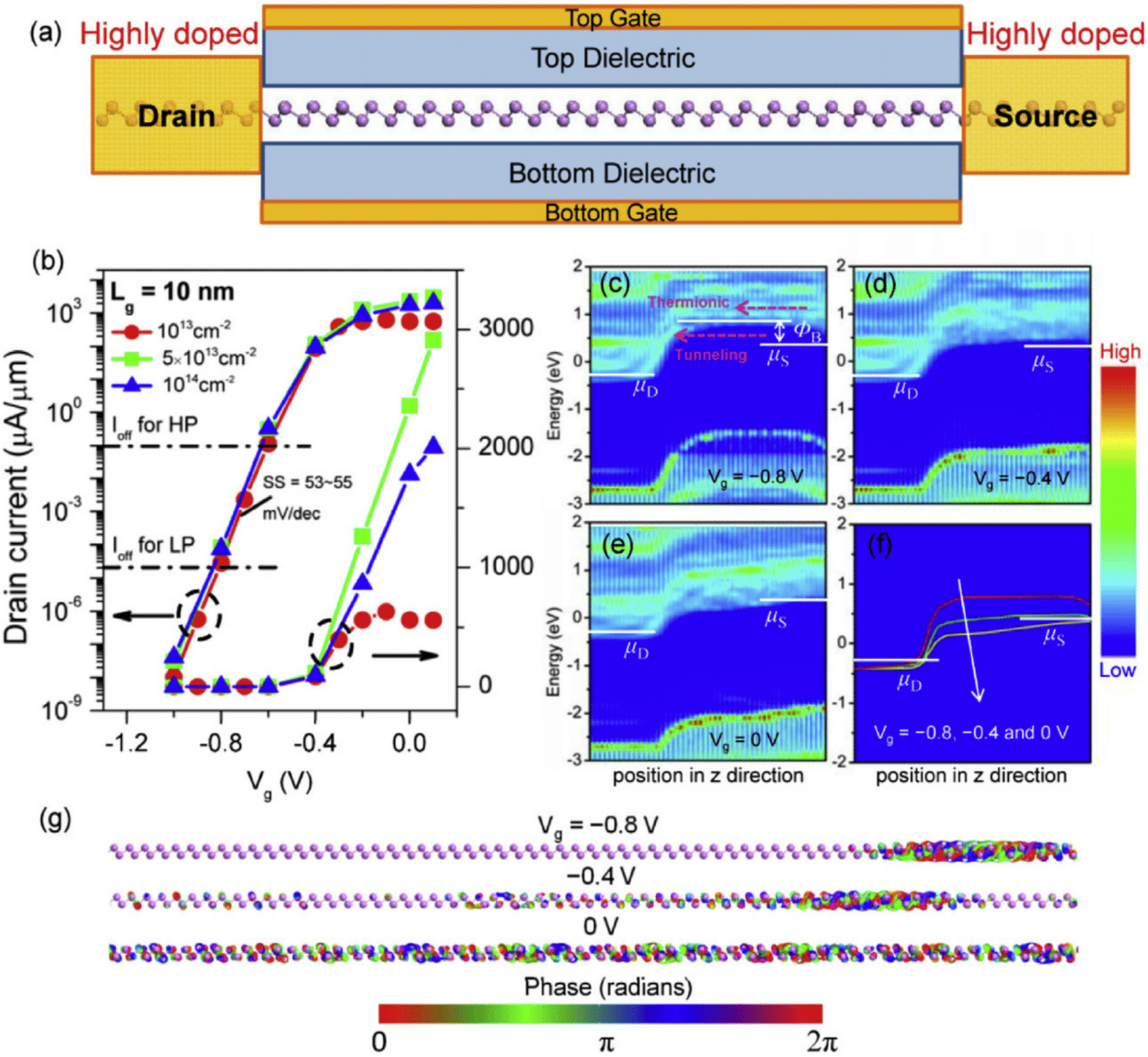

Fig. 7. ML arsenene DG MOSFET with $L_g = 10$ nm: (a) schematic of an arsenene DG MOSFET without UL structures; (b) transfer characteristics for different source and drain electron doping concentrations (N_e) on log (left-hand axis) and linear scales (right-hand axis). Position-resolved LDOS in the channel region at V_g = (c) −0.8, (d) −0.4, and (e) 0 V for $N_e = 5 \times 10^{13}$ cm^{-2}. The responding conduction band profiles along the channel are given in (f). The white solid line represents the Fermi level at the source or drain. Illustrated in (c) as an example, red dashed arrows represent the thermionic and tunneling electron transports, and Φ_B is the effective barrier height; and (g) transmission eigenstates at $E = V_{ds}/2$ and k = (1/3, 0) for V_g = −0.8, −0.4, and 0 V, respectively. The isovalue is 0.2 au. Reproduced from Ref. [27].

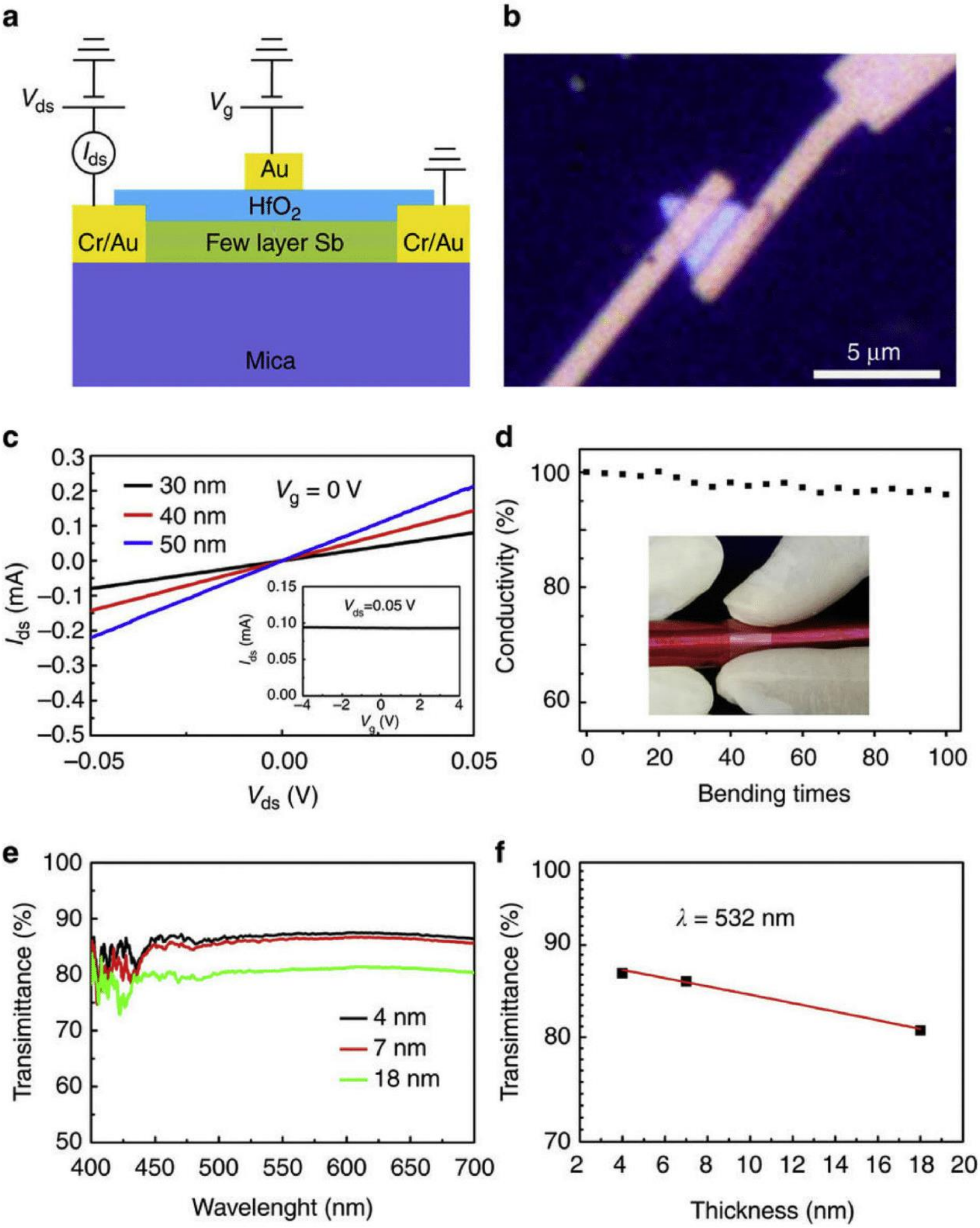

Fig. 8. Flexible transparent conductivity of antimonene polygons: (a) schematic illustration of top-gated antimonene thin film transistors; (b) optical image of a typical device fabricated on a triangular antimonene sheet; (c) I_{ds}–V_{ds} characteristics of three tested devices acquired at $V_g = 0$ V. Inset: I_{ds}–V_g curve of the 30-nm thick antimonene device acquired at 0.05 V bias voltage; (d) electrical conductivity of the tested device after bending. Inset: Photograph of bended antimonene devices on mica substrate; (e) transmittance spectra of three typical antimonene polygons of 4, 7, and 18 nm thicknesses, respectively; and (f) transmittance of antimonene polygons versus sample thickness. Reproduced from Ref. [29].

as CO, H_2, NH_3, NO_X, O_2, and H_2O. They investigated energetics, charge transfer, and magnetic moment on the basis of dispersion-corrected density functional theory (DFT). The authors concluded that CO, H_2, NH_3, and H_2O molecules behave as weak donors, whereas O_2 and NO_2 behave as strong acceptors. NO_2 molecules also have the strongest interaction with the material [22].

The experimental study reported by Cui et al. [23] proved the theoretical calculations. The phosphorene nanosheets (PNS) devices can still detect contents of NO_2 molecules below than 100 parts per billion (ppb) due to significant change of the hole concentration in the PNS while its carrier mobility is negligible (Fig. 5A). The sensitivity of black phosphorus FET to NO_2 was further improved to the ppb levels for NO_2 (Fig. 5B) [24]. Black phosphorus is sensitive to water in general; this has been utilized for water vapor sensing by FET based on electrochemically exfoliated FET [25].

The ultrathin BP layers are subject of oxidation, thereby hindering its performance [3]. Recently, a solution to this problem was demonstrated by Chen and co-workers who reported a mechanically exfoliated BP biosensor passivated by a very thin film of Al_2O_3 in order to detect human immunoglobulin G (IgG) through anti-human IgG-conjugated gold nanoparticles [26]. The IgG detection was accomplished by measuring changes in source-drain current upon the antibody–antigen binding interactions (Fig. 6A). The BP biosensor demonstrated a limit of detection (LOD) of 10 $ng \cdot mL^{-1}$ and fast response time on the order of seconds (Fig. 6B).

2.2. Arsenene

Wang et al. [27] performed the first investigation of the many-body effect, carrier mobility and, performance of monolayer arsenene (Fig. 7). The carrier mobility in arsenene 10 nm FET was estimated to be 21 $cm^2 \cdot V^{-1} \cdot s^{-1}$ for electrons and 66 $cm^2 \cdot V^{-1} \cdot s^{-1}$ for holes, respectively.

Liu et al. [28] performed the first-principle calculation to determine the adsorption of CO, CO_2, N_2, NH_3, NO, and NO_2 molecules on pristine arsenene. The interaction between these gas molecules and the arsenene monolayer is intermediate between the physisorbed and chemisorbed states. The authors predicted a significant modification of density of states near the Fermi level caused by the adsorption of NO and NO_2 molecules, and this adsorption also leads to a magnetic moment of 1 μB. The theoretical basis shows the great potential of an arsenene monolayer for gas detection using electrical and magnetic methods.

2.3. Antimonene

Ji et al. [29] synthesized high-quality, few-layer antimonene polygons on mica substrate through van der Waals epitaxy (Fig. 8). Their electrical characterizations demonstrate that the synthesized antimonene polygons have good electrical conductivity on the order of 10^4 $S \cdot m^{-1}$. HRTEM microscopy and Raman spectroscopy also revealed that the obtained antimonene polygons are consistent

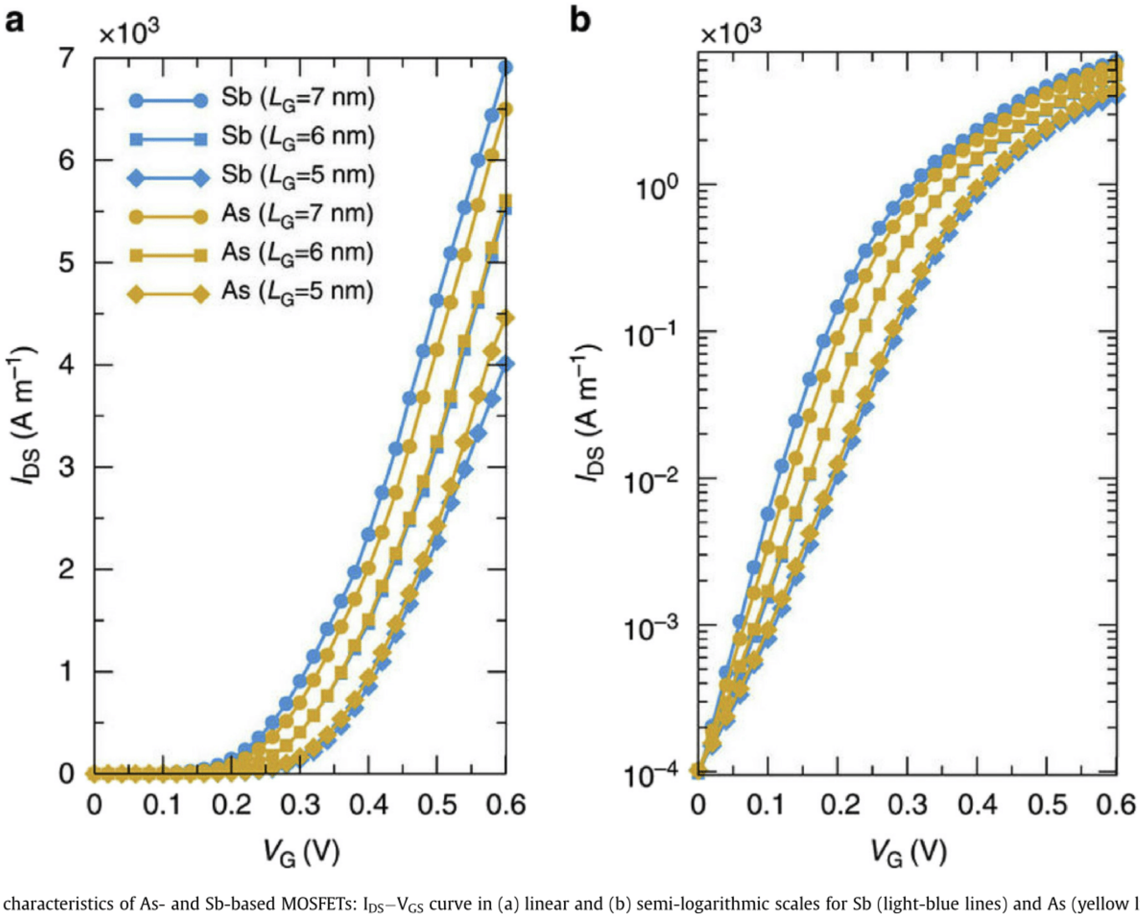

Fig. 9. Transfer characteristics of As- and Sb-based MOSFETs: I_{DS}–V_{GS} curve in (a) linear and (b) semi-logarithmic scales for Sb (light-blue lines) and As (yellow lines) transistors with $L_G = 7$ nm, $V_{DS} = 0.6$ V, and $t_{ox} = 0.5$ nm (circles), $L_G = 6$ nm, $V_{DS} = 0.57$ V, and $t_{ox} = 0.45$ nm (squares) and $L_G = 5$ nm, $V_{DS} = 0.54$ V, and $t_{ox} = 0.42$ nm (diamonds). Reproduced from Ref. [30].

with the atomic structure of the most stable allotrope of monolayer antimonene. Optical microscopy, AFM, Raman spectroscopy, and XPS also proved the good stability of antimonene polygons when exposed in air. Pizzi et al. [30] provided a comprehensive analysis of 2D FET transistors based on arsenene and antimonene (Fig. 9). They showed that these materials are promising for high-performance devices for digital applications. Due to the channel lengths below 10 nm and the atomic thickness of the exploited 2D materials, short channel effects are suppressed and tunneling starts to play a major role.

The pristine antimonene was evaluated as a high-performance gas sensor based on its gas-adsorption behaviors [31]. It was reported that the polluted gas adsorbates (NH_3, SO_2, NO, and NO_2) showed a stronger affinity toward antimonene with considerable absorption energies and elevated charge transfers while the atmospheric gas molecules (N_2, CO_2, O_2, and H_2O) bind weakly. The monolayered antimonene seems a promising sensing material for pollutant gas gases detection due to the susceptibility of its electronic properties induced by the absorbed molecules. The antimonene was predicted as the most suitable candidate for acetone sensors due to sensitivity and high selectivity [32].

2.4. Silicene

The silicene band gap can be opened without degrading its carrier mobility, which is ideal for the fabrication of high-performance FET devices. Tao et al. [33] performed measurements of silicene FET at room temperature. His results (Fig. 10) on silicene prepared by encapsulated delamination with native electrodes show carrier mobility of ~100 $cm^2 \cdot V^{-1} \cdot s^{-1}$.

Prasongkit et al. [34] estimated silicene sensitivity and selectivity on detection of NO, NO_2, NH_3, and CO gases using DFT and the no-equilibrium Green's function method. They revealed strong sensitivity of pristine silicene for NO and NO_2 but unusable for CO and NH_3 detection. Doping of silicene with B or N atoms resulted to enhanced binding energy (Fig. 11A) and charge transfer (Fig. 11B), which positively affected the sensitivity. Silicene-based devices are predicted to be very selective and sensitive gas sensors.

2.5. Germanene

Madhushankar et al. [35] synthesized and experimentally studied the electronic properties of germanene FET (Fig. 12A).

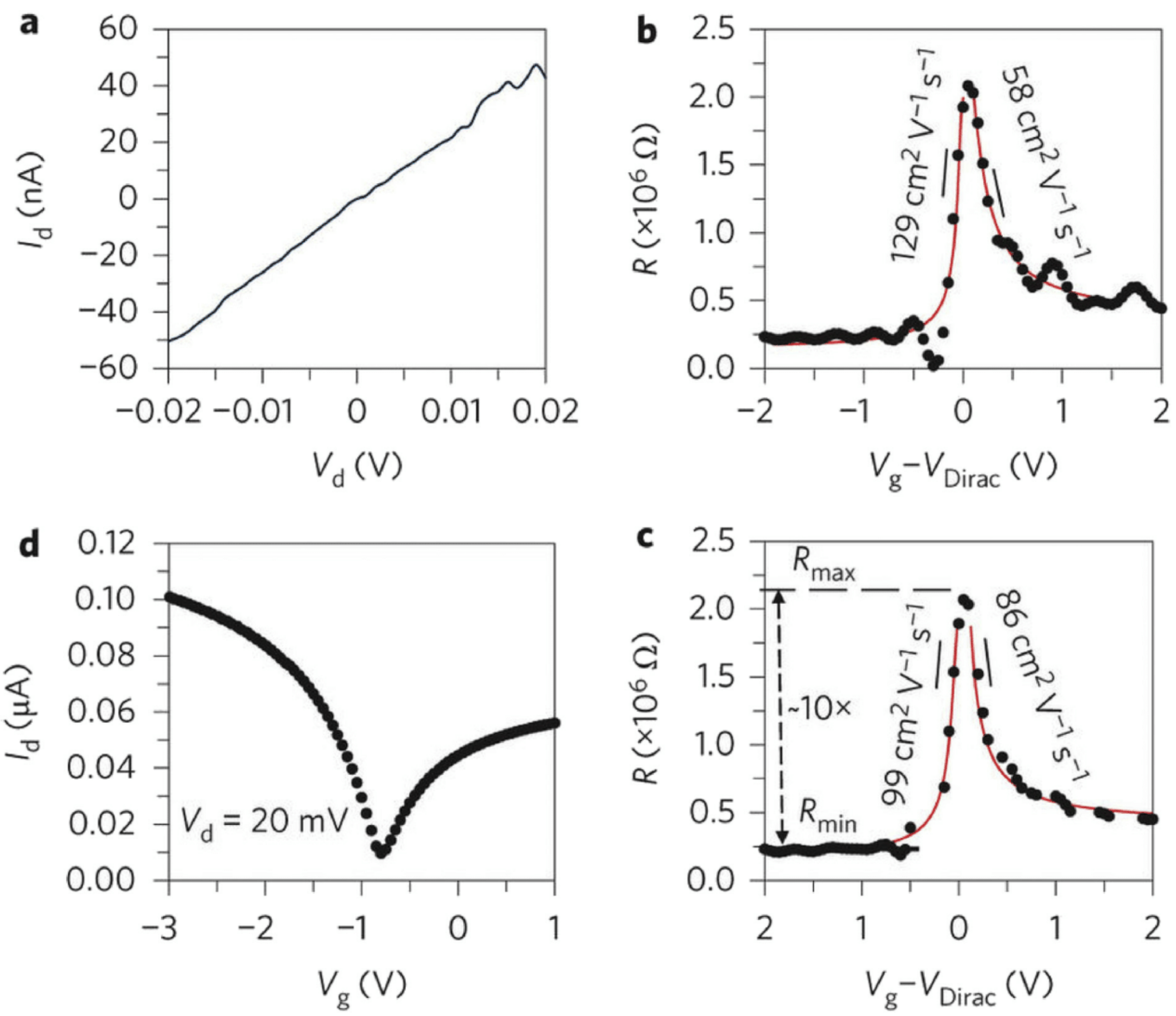

Fig. 10. (a) Low-field linear I_d vs. V_d response at $V_g = 0$. (b, c) R vs. (V_g−V_{dirac}) of silicene devices 1 and 2, respectively. Measured transfer characteristics (dots) are in good agreement with a widely used ambipolar diffusive transport model (line), which yields extracted low-field hole and electron carrier mobilities of 129 and 99 $cm^2 \cdot V^{-1} \cdot s^{-1}$ and 58 and 86 $cm^2 \cdot V^{-1} \cdot s^{-1}$ in devices 1 and 2, respectively, with similar residual carrier concentration of ~3–7 × 10^9 cm^{-2}, more than an order of magnitude lower than in graphene transistors. (d) I_d vs. V_g curve of silicene device 2 displays ambipolar electron–hole symmetry expected from silicene. In B–D, both devices are from the same mixed-phase silicene sample with channel length of 1.8 μm and width of 230 nm, and fixed V_d = 20 mV for the measurements. Reproduced from Ref. [33].

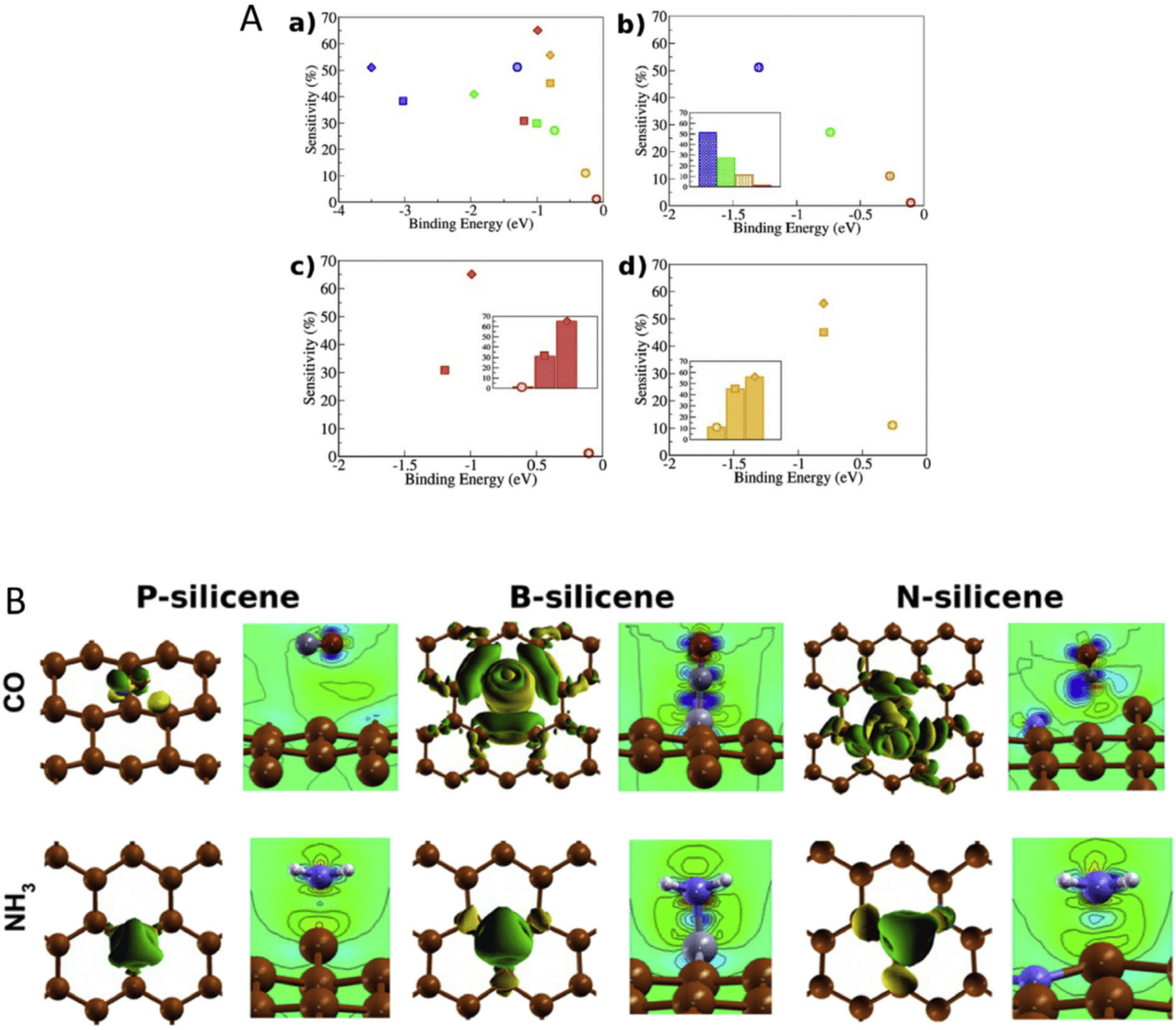

Fig. 11. Silicene sensitivity estimation for gas sensing (A): (a) sensitivity versus binding energy for NO (green), NO_2 (blue), NH_3 (orange), and CO (red) gas molecules on P-silicene (circle), B-silicene (square) and N-silicene (diamond) devices, respectively; (b) the four gas species on P-silicene (the inset shows the sensitivity comparison for P-silicene); (c) CO on three devices; and (d) NH_3 on three devices. The insets of parts (c) and (d) are the sensitivity comparison for one gas on the three different devices. (B) Charge density difference for CO (upper) and NH_3 (lower panel) on P-, B-, and N-silicene devices for each type of nanosensor. Isosurfaces are plotted for isovalues of 0.0004 (0.002) e × $bohr^{-3}$ for CO (NH_3) alongside contour plots. For the isosurface plots, the green color represents negative charge density difference while yellow corresponds to a positive change in charge density. Reproduced from Ref. [34].

Authors performed initial electrical characterization at room temperature in the linear regime (Fig. 12B). Their germanene devices demonstrated transport in both electron- and hole-doped regimes with on/off current ratio of up to 10^5 (10^4) and carrier mobilities of 150 $cm^2 \cdot V^{-1} \cdot s^{-1}$ (70 $cm^2 \cdot V^{-1} \cdot s^{-1}$) at room temperature.

Gupta et al. [36] used a first-principles DFT calculation to show the possibility of the germanene monolayer for toxic gas detection. Theoretical prediction showed that molecules of NH_3, NO_2, and SO_2 are physisorbed on germanene. Based on these results (Fig. 13A), the NO_2 has the strongest interaction with the hexagonal armchair germanene monolayer (273.72 meV). The NO_2 molecule has also much higher values of the charge transfer (Fig. 13B) than other investigated gases, which results in the highest stability and sensitivity for this molecule. Reported results indicate the germanene monolayer has a huge potential as a miniaturized sensor for detecting NO_2 gas.

3. Conclusions

The many potential applications of ultrathin 2D materials in sensing and biosensing FETS have taken the chemistry and physics fields by storm. There has been intensive research on the utilization of graphene for FET sensors, and more recently by 2D transition metal dichalcogenides (TMD, for an example MoS_2, WS_2, $MoSe_2$ and others) for FET based sensors. While the band-gap of TMD depends not only on their composition but also on phase purity, which is in many cases challenging to control, this is not a main issue for mono-elemental materials, such 2D phosphorene, arsenene, antimonene and group IVA materials, such as silicene and germanene. Therefore it is not surprising that the utilization of 2D Group VA materials, such as phosphorene, arsenene, antimonene, and Group IVA materials, such as silicene and germanene, for FET sensors, is in rapid development. We have shown here only selected examples

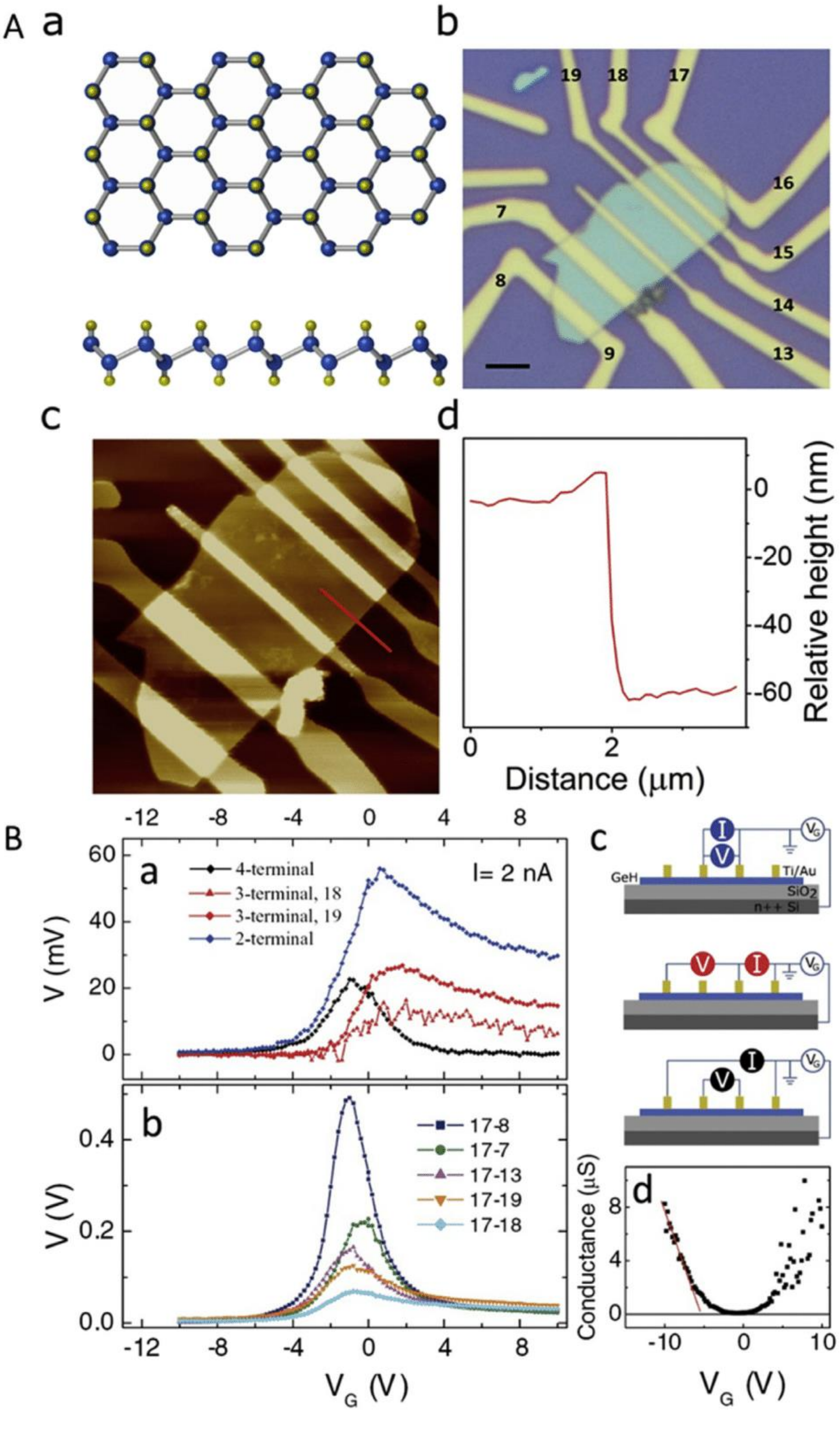

Fig. 12. Germanene as FET (A): (a) schematic representation of a germanene monolayer (top and side views) with Ge atoms (blue) at the corners of hexagons and H atoms (yellow) bonded to Ge; (b) optical image of the germanene flake-based device on top of a Si/SiO$_2$ substrate with Ti/Au electrodes (scale bar is 3 μm); (d) AFM image of the germanene transistor; and (d) height profile is plotted along the red line as shown in panel (c) giving the flake thickness to be 60 nm. (B) (a) Measured signal V plotted for 2-terminal (blue), 3-terminal (red), and 4-terminal (black) configurations as a function of the gate voltage. The 3-terminal measurements were performed using both contacts 18 (triangles) and 19 (diamonds). The applied constant current between source and drain was 2 nA, and the measurements were performed at room temperature; (b) 2-terminal measurements as a function of V$_G$ performed using different distances between the contacts while keeping the same source contact. The resistance values at the curve maxima scale approximately with the channel length (for the sample geometry, see Fig. 12A(b)). $I = 2$ nA; (c) 2-, 3-, and 4-terminal measurement configurations allow the contact and channel-related resistances to be extracted separately; and (d) room temperature conductance calculated from the 4-terminal measurement shown in panel (a). The red line represents a linear fit resulting in a mobility of ~30 cm^2·V^{-1}·s^{-1}. Reproduced from Ref. [35].

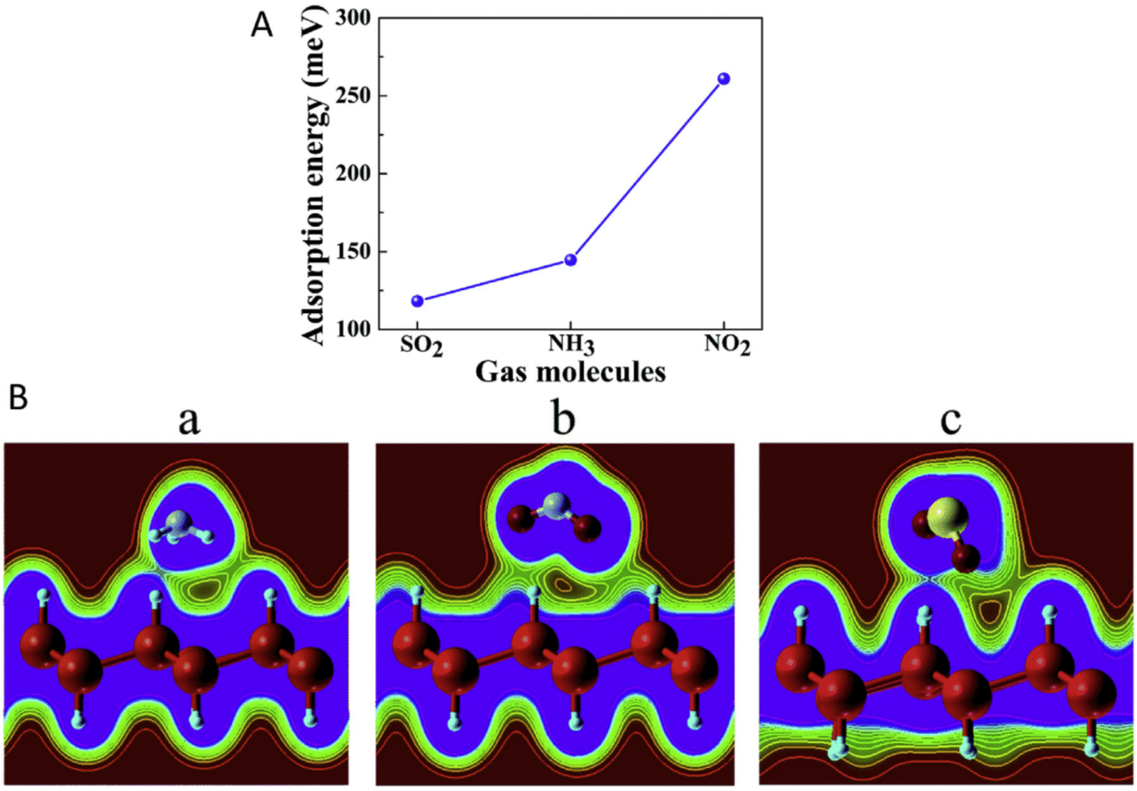

Fig. 13. (A) Adsorption energies (meV) of NH_3, SO_2, and NO_2 gas molecules on the hexagonal armchair (3 × 3 × 1) germanene monolayer of lowest energy (E-type) configuration. (B) Charge density difference plots for (a) NH_3 (b) NO_2, and (c) SO_2 gas molecules interacting with the top surface of the hexagonal armchair 3 × 3 × 1 germanene monolayers of E-type configurations.

describing trends in this area with applications in the field of analytical chemistry.

Acknowledgement

We acknowledge the support of Grant Agency of the Czech Republic under the contract GJ18-06498Y and support of the Ministry of Education, Youth and Sports of the Czech Republic under the project OP VVV CEITEC Nano+ (CZ.02.1.01/0.0/0.0/16_013/0001728). Authors I. Gablech and J. Pekárek also acknowledge the foundation support FEKT/STI-J-17-4136. M.P. thanks A*Star grant (No. SERC A1783c0005), Singapore.

References

[1] E. Fitzer, K.H. Kochling, H.P. Boehm, H. Marsh, Recommended terminology for the description of carbon as a solid – (IUPAC recommendations 1995), Pure Appl. Chem. 67 (1995) 473–506.
[2] P.W. Bridgman, Further note on black phosphorus, J. Am. Chem. Soc. 38 (1916) 609–612.
[3] R. Gusmao, Z. Sofer, M. Pumera, Black phosphorus rediscovered: from bulk material to monolayers, Angew. Chem. Int. Ed. 56 (2017) 8052–8072.
[4] M. Pumera, Z. Sofer, 2D monoelemental arsenene, antimonene, and bismuthene: beyond black phosphorus, Adv. Mater. 29 (2017).
[5] A. Dimoulas, Silicene and germanene: silicon and germanium in the "flatland", Microelectron. Eng. 131 (2015) 68–78.
[6] E. Golias, E. Xenogiannopoulou, D. Tsoutsou, P. Tsipas, S.A. Giamini, A. Dimoulas, Surface electronic bands of submonolayer Ge on Ag(111), Phys. Rev. B 88 (2013).
[7] P. Vogt, P. De Padova, C. Quaresima, J. Avila, E. Frantzeskakis, M.C. Asensio, A. Resta, B. Ealet, G. Le Lay, Silicene: compelling experimental evidence for graphenelike two-dimensional silicon, Phys. Rev. Lett. 108 (2012).
[8] L.J. Edgar, in: U. Grant (Editor), Device for Controlling Electric Current, Lilienfeld Julius Edgar USA, 1928.
[9] D. Kahng, in: U.P. Office (Editor), Electric field controlled semiconductor device, Bell Telephone Laboratories, Inc., N.Y. USA, US, 1963.
[10] S.M. Sze, K.K. Ng, MOSFETs, Physics of Semiconductor Devices, John Wiley & Sons, Inc., 2006, pp. 293–373.
[11] P. Bergveld, Development of an ion-sensitive solid-state device for neurophysiological measurements, IEEE Trans. Biomed. Eng. 17 (1970) 70–71.
[12] K.I. Lundstrom, M.S. Shivaraman, C.M. Svensson, Hydrogen-sensitive Pd-Gate Mos-transistor, J. Appl. Phys. 46 (1975) 3876–3881.
[13] A.K. Geim, K.S. Novoselov, The rise of graphene, Nat. Mater. 6 (2007) 183–191.
[14] K.S. Novoselov, A.K. Geim, S.V. Morozov, D. Jiang, Y. Zhang, S.V. Dubonos, I.V. Grigorieva, A.A. Firsov, Electric field effect in atomically thin carbon films, Science 306 (2004) 666–669.
[15] B.B. Zhan, C. Li, J. Yang, G. Jenkins, W. Huang, X.C. Dong, Graphene field-effect transistor and its application for electronic sensing, Small 10 (2014) 4042–4065.
[16] F. Schwierz, Graphene transistors, Nat. Nanotechnol. 5 (2010) 487–496.
[17] Y. Wang, Y. Ding, Electronic structure and carrier mobilities of arsenene and antimonene nanoribbons: a first-principle study, Nanoscale Res. Lett. 10 (2015) 1–10.
[18] H. Liu, A.T. Neal, Z. Zhu, Z. Luo, X.F. Xu, D. Tomanek, P.D. Ye, Phosphorene: an unexplored 2D semiconductor with a high hole mobility, ACS Nano 8 (2014) 4033–4041.
[19] J. Zhao, H. Liu, Z. Yu, R. Quhe, S. Zhou, Y. Wang, C.C. Liu, H. Zhong, N. Han, J. Lu, Y. Yao, K. Wu, Rise of silicene: a competitive 2D material, Prog. Mater. Sci. 83 (2016) 24–151.
[20] X.-S. Ye, Z.-G. Shao, H. Zhao, L. Yang, C.-L. Wang, Intrinsic carrier mobility of germanene is larger than graphene's: first-principle calculations, RSC Adv. 4 (2014) 21216–21220.
[21] L.Z. Kou, T. Frauenheim, C.F. Chen, Phosphorene as a superior gas sensor: selective adsorption and distinct I-V response, J. Phys. Chem. Lett. 5 (2014) 2675–2681.
[22] Y.Q. Cai, Q.Q. Ke, G. Zhang, Y.W. Zhang, Energetics, charge transfer, and magnetism of small molecules physisorbed on phosphorene, J. Phys. Chem. C 119 (2015) 3102–3110.
[23] S.M. Cui, H.H. Pu, S.A. Wells, Z.H. Wen, S. Mao, J.B. Chang, M.C. Hersam, J.H. Chen, Ultrahigh sensitivity and layer-dependent sensing performance of phosphorene-based gas sensors, Nat. Commun. 6 (2015).
[24] A.N. Abbas, B. Liu, L. Chen, Y. Ma, S. Cong, N. Aroonyadet, M. Koepf, T. Nilges, C. Zhou, Black phosphorus gas sensors, ACS Nano 9 (2015) 5618–5624.
[25] M.B. Erande, M.S. Pawar, D.J. Late, Humidity sensing and photodetection behavior of electrochemically exfoliated atomically thin-layered black phosphorus nanosheets, ACS Appl. Mater. Interfaces 8 (2016) 11548–11556.
[26] Y.T. Chen, R. Ren, H.H. Pu, J.B. Chang, S. Mao, J.H. Chen, Field-effect transistor biosensors with two-dimensional black phosphorus nanosheets, Biosens. Bioelectron. 89 (2017) 505–510.

[27] Y.Y. Wang, P. Huang, M. Ye, R. Quhe, Y.Y. Pan, H. Zhang, H.X. Zhong, J.J. Shi, J. Lu, Many-body effect, carrier mobility, and device performance of hexagonal arsenene and antimonene, Chem. Mater. 29 (2017) 2191–2201.

[28] C. Liu, C.S. Liu, X.H. Yan, Arsenene as a promising candidate for NO and NO_2 sensor: a first-principles study, Phys. Lett. 381 (2017) 1092–1096.

[29] J.P. Ji, X.F. Song, J.Z. Liu, Z. Yan, C.X. Huo, S.L. Zhang, M. Su, L. Liao, W.H. Wang, Z.H. Ni, Y.F. Hao, H.B. Zeng, Two-dimensional antimonene single crystals grown by van der Waals epitaxy, Nat. Commun. 7 (2016).

[30] G. Pizzi, M. Gibertini, E. Dib, N. Marzari, G. Iannaccone, G. Fiori, Performance of arsenene and antimonene double-gate MOSFETs from first principles, Nat. Commun. 7 (2016).

[31] R.S. Meng, M. Cai, J.K. Jiang, Q.H. Liang, X. Sun, Q. Yang, C.J. Tan, X.P. Chen, First principles investigation of small molecules adsorption on antimonene, IEEE Electron. Device Lett. 38 (2017) 134–137.

[32] D.W. Wang, A.J. Yang, J.F. Chu, P.L. Lv, L. Yang, X.H. Wang, M.Z. Rong, Antimonene: A Promising Candidate for Acetone Sensors with High Selectivity and Sensitivity, IEEE SENSORS, 2017, pp. 1–3.

[33] L. Tao, E. Cinquanta, D. Chiappe, C. Grazianetti, M. Fanciulli, M. Dubey, A. Molle, D. Akinwande, Silicene field-effect transistors operating at room temperature, Nat. Nanotechnol. 10 (2015) 227–231.

[34] J. Prasongkit, R.G. Amorim, S. Chakraborty, R. Ahuja, R.H. Scheicher, V. Amornkitbamrung, Highly sensitive and selective gas detection based on silicene, J. Phys. Chem. C 119 (2015) 16934–16940.

[35] B.N. Madhushankar, A. Kaverzin, T. Giousis, G. Potsi, D. Gournis, P. Rudolf, G.R. Blake, C.H. van der Wal, B.J. van Wees, Electronic properties of germanane field-effect transistors, 2D Mater. 4 (2017).

[36] S.K. Gupta, D. Singh, K. Rajput, Y. Sonvane, Germanene: a new electronic gas sensing material, RSC Adv. 6 (2016) 102264–102271.

16 FET structure for 2D material characterization

Deposition and shaping of graphene is very time consuming and it is not a main aim of this doctoral thesis, thus planar electrodes for characterization of 2D material were fabricated. These NiCr/Au structures were made on conductive Si (100) substrate covered with 30 nm thick thermal SiO_2 (see **Figure 35**). Thin SiO_2 film with low dielectric strength did not allow to regulate the gate voltage. Distances between electrodes were (0.5, 1.0, 2.0 and 5.0) µm. Lithography of such small structures were realized in National Institute of Standards and Technologies (Gaithersburg - USA), using step and repeat camera with resolution of 280 nm.

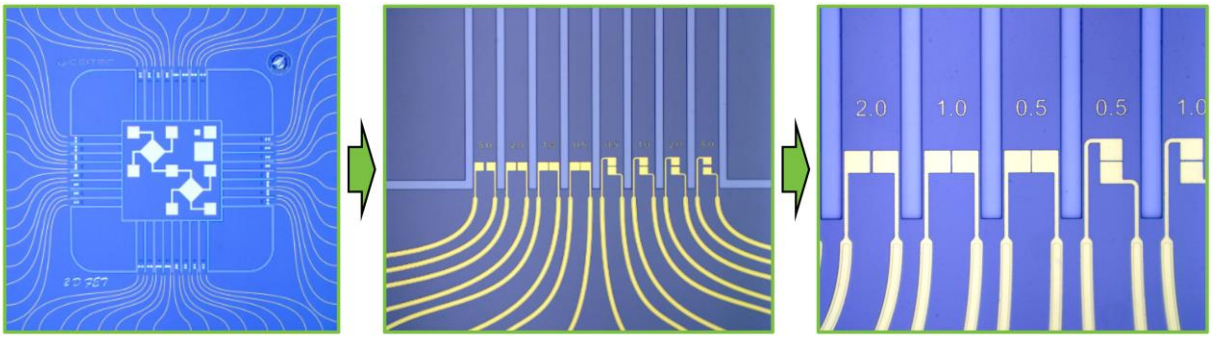

Figure 35: Fabricated chip for 2D materials electrical characterization.

Graphene oxide with concentration of $1\ \mathrm{mg{\cdot}ml^{-1}}$ was drop-coated from water suspension. Samples were dried from ambient room temperature to ≈ 60 °C for 15 min with step of $2\ \mathrm{{}^{\circ}C{\cdot}min^{-1}}$. Process had to be realized with moderate changes of temperature to protect graphene oxide flakes from vaporized water. Subsequent annealing at pressure of $\approx 8{\cdot}10^{-5}$ Pa and temperature of ≈ 120 °C during 6 hours at vacuum furnace improved the behavior of electrical contact between graphene oxide and electrodes. Graphene oxide flake does not have to always be positioned between electrodes, thus SEM analysis was provided (see **Figure 36**).

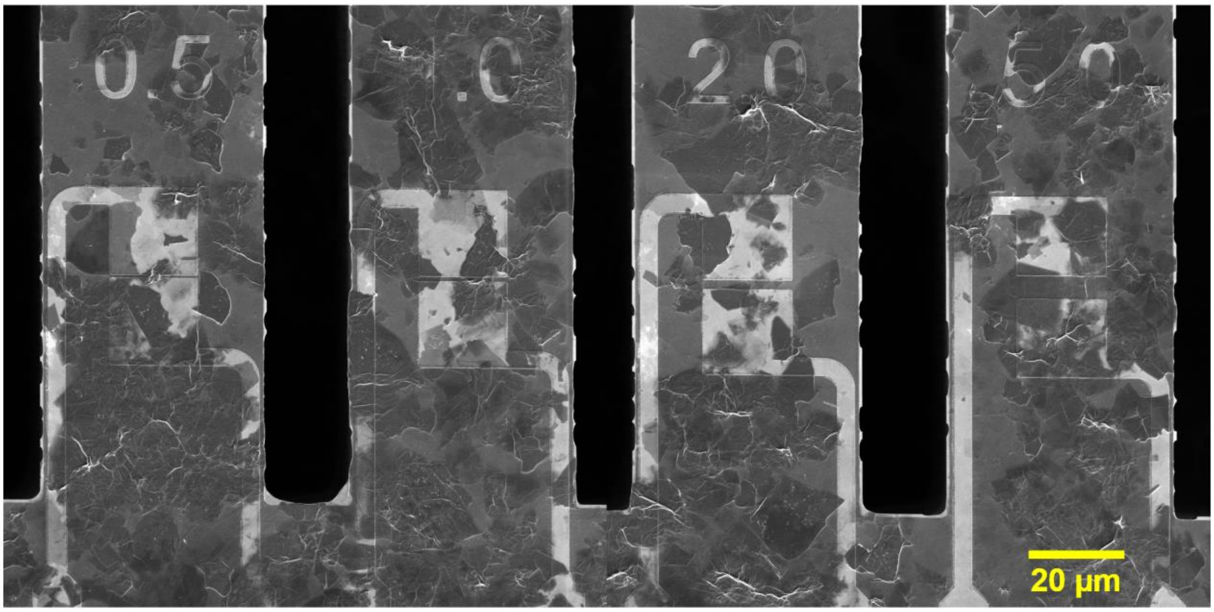

Figure 36: SEM image of graphene oxide flakes on chip.

Graphene oxide electrical characterization was realized as current measurement (I_M) on Cascade MPS150 probe station using Keithley 4200-SCS parameter analyzer for voltage (V_B) range from −1 to +1 V. This method examined the possibility of deposition from suspension as one of the potential variants despite its inaccuracy. Samples can be purified with O_2 plasma which removes impurities and etch graphene oxide, thus samples can be repeatedly used. Final resistivity of graphene is dependent on the distance between electrodes which can be from tenths to hundreds of micrometers. Graph shows nonlinear curves which point to Schottky contact between graphene oxide and electrodes (see **Figure 37**). Electrical contact can be further improved by annealing or choosing of another electrode material. This fact will be used for future optimization of sophisticated piezoelectric resonator with Hall Bar/FET structure for utilization of 2D materials.

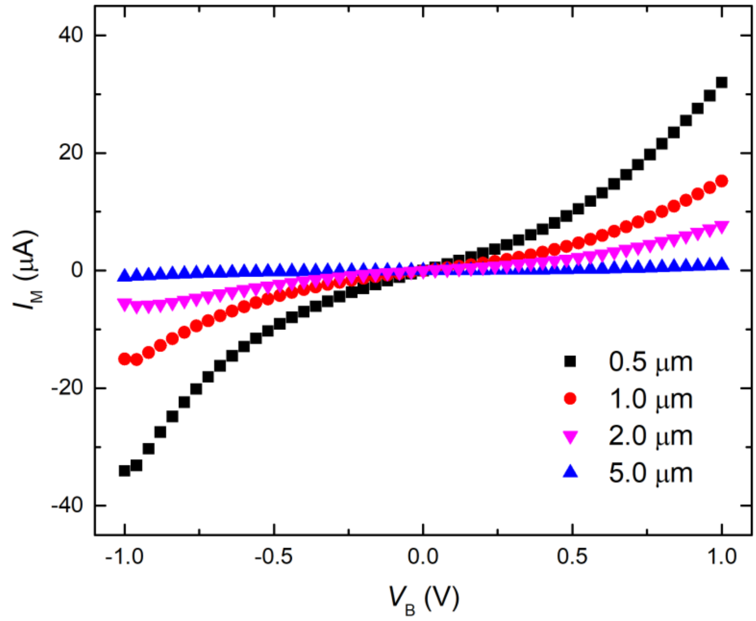

Figure 37: Current voltage curves of graphene oxide flakes drop-coated on electrodes with various gaps of (0.5, 1.0, 2.0 and 5.0) μm.

17 Structure for strain inducing

17.1 Motivation of the article

Motivation of this article was to summarize progress in last 4 years of my PhD study as final result. It led to fabrication and simulation of final structure suitable for strain inducing. This article shows how strain can be induced in MEMS structure using piezoelectric resonator. The structure can be utilized with many other 2D materials than graphene, as they have been described in my review article (see chapter 15).

17.2 Conclusion on the article

It summarizes the possible strain values based on simulations. It also shows the fabricated MEMS device consisting of 10 lithography steps which was greatly challenging. The shown model can be further optimized. It will be realized in GAČR project of me and my supervisor which started in January 2018. We will focus on geometry of whole structure which can improve the maximal induced value of strain over 2 %. These simulations are described below this article in addition simulations results section. We will also do the electrical characterization after the 2D materials will be placed and eventually shaped on top of Hall Bar/FET structure. Development and fabrication of this structure is very expensive and time consuming. Structures will be fully optimized using FEM analyses before the new chip generation allowing higher strain values, will be prepared. The 2D material such as graphene, arsenene, antimonene, silicene, and germanene will be characterized on these new structures. The testing will involve detection of gases and FET characterization.

17.3 Contribution

I did each fabrication steps of whole device. I also did SEM images and FEM simulations with support of Jaroslav Klempa. I also contributed to the analysis of the results and to the writing of the manuscript.

17.4 Article 11

The Article **A new method for 2D materials properties modulation by controlled induced mechanical strain** [65] was accepted in **Eurosensors** international conference in **August 2018**. This article will be then submitted in **Sensors** impacted journal which is possible output of conference paper.

proceedings

Proceeding

A new method for 2D materials properties modulation by controlled induced mechanical strain

Imrich Gablech [1], Jan Pekárek [1,*], Jaroslav Klempa [1], Petr Vyroubal [1], Vojtěch Svatoš [1], and Pavel Neužil [2,†]

[1] Brno University of Technology, Technická 3058/10, 612 00 Brno, Czech Republic
[2] Northwestern Polytechnical University, 127 West Youyi Road, Xi'an, Shaanxi, 710072, P.R. China
* Correspondence: pekarek@vutbr.cz; Tel.: +420-541-146-192
† Correspondence: pavel.neuzil@gmail.com; Tel.: +420-541-146-194

Presented at the **Eurosensors 2018 Conference**, Graz, Austria, September 9–12, 2018.
Received: date; Accepted: date; Published: date

Abstract: This paper proposes a new method for characterization of 2D materials under the precisely specified conditions. It is achieved by integration of a 2D material as a field effect transistors structures with a piezoelectric resonator. Properties of the 2D material can be mechanically adjusted by the resonator. It results in the independent and precise control of an amplitude of induced mechanical strain, its modulating frequency, which all influence the 2D material properties. The electrical field required to measure 2D material field effect transistors will not be affected by the vibrations, thus giving us a chance to perform the precise measurement of the electrical properties of the 2D material. This approach has a great potential for measuring and monitoring cells, enzymes, nucleic acids, deoxyribonucleic acid and ribonucleic acid. It can be also used for measurement of toxic, combustive or waste gases.

Keywords: 2D materials; induced strain; piezoelectric resonator; FET structure;

---

1. Introduction

In the past two years, there has been great interest in 2D monoelemental materials beyond graphene, such as group IVA elements: silicene and germanene and group VA elemets:phosphorene, arsenene, and antimonene[1]. The utilization of 2D materials for field effect transistor (FET) based devices was investigated more than decade ago for graphene by studying the electric field effect in this 2D material. Since then, graphene has been extensively studied, including graphene-based FETs for various sensing applications. The drain current value through FET structure can be affected by modulating the electron mobility in the substrate either mechanically by stretching the 2D material or chemically by modifying its properties. The first can be used for mechanical sensing and the second for chemical or biochemical sensing.

Here we propose a new method for characterization of 2D materials under well-defined conditions. The fundamental concept is based on the integration of 2D material as Hall bar/FET structures with the piezoelectric resonator. The Hall bar/FET structures are used to measure modulated 2D material electrical properties as a function of induced strain and/or electric field (Figure 1A). The FET allows to modulate the concentration of charge carriers by the gate voltage. The entire structure is fabricated on a Si (100) wafer substrate using planar technology.

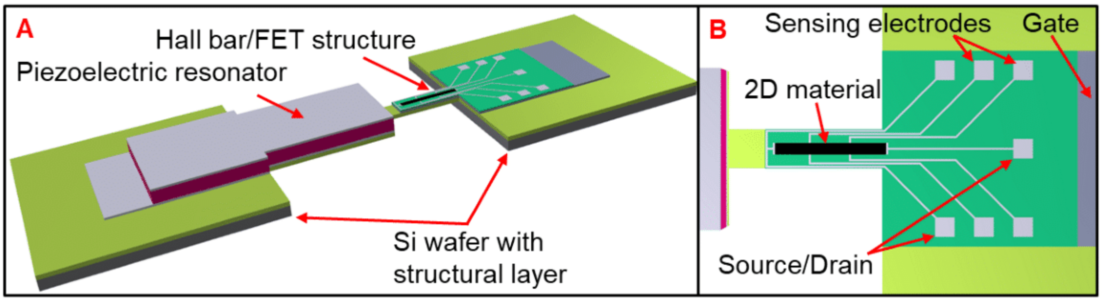

Figure 1. Proof of concept and principle of proposed structure (not to scale): A) MEMS piezoelectric resonator mechanically linked to stretching Hall bar/FET structure; B) The detail of stretching part with 2D material using Hall Bar/FET structure for electric measurements of 2D material properties.

Our unique structure gives us an opportunity to control and to decouple the mechanical and the electrical phenomena. Mechanical oscillations of the 2D material are induced by an independent AC bias applied at the piezoelectric resonator without affecting the gate voltage of the FET in contrary to previously published work[2]. We are able to measure the electrical Hall bar/FET properties separately with the induced strain as a parameter. This decoupling significantly increases the measurement precision. It allows application of a small gate voltage at the FET to modulate the Fermi level simultaneously with a high voltage at the resonator to optimize the conditions. This approach could be applied on different structure designs containing a number of piezoelectric resonators linked mechanically to the Hall bar/FET structures in different directions. It will allow us to induce uniaxial or biaxial strain in 2D material and to determine its influence on 2D material properties and its utilization as a sensor.

2. Numerical model of piezoelectric resonator

We performed a structural finite element method (FEM) analyses of a single clamped SiO_2/Ti/AlN/Ti/Al piezoelectric resonator linked mechanically to a single clamped stretching device representing graphene Hall Bar/FET structure made of SiO_2/Al/SiO_2/Ti/Pt. The appropriate properties of material were set for each part of the model. We used the SOLID226 element (20-node brick) for numerical discretization (Figure 2 supporting piezoelectric analysis.

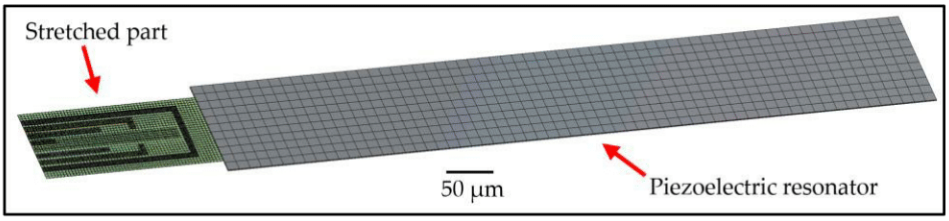

Figure 2. The meshed model of single clamped piezoelectric resonator linked mechanically to single clamped stretching device representing 2D material Hall Bar/FET structure.

The coupled solution of the electrostatic and structural solver was realized via the piezoelectric matrix $[e]$:

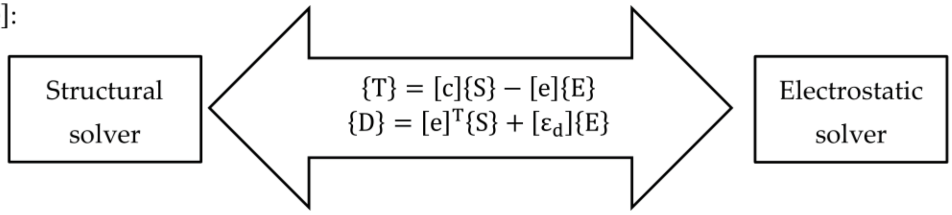

$$\{T\} = [c]\{S\} - [e]\{E\}$$
$$\{D\} = [e]^T\{S\} + [\varepsilon_d]\{E\}$$

where $\{T\}$ is the stress vector, $[c]$ is the elastic stiffness matrix, $\{S\}$ is the elastic strain vector, $[e]$ is the piezoelectric matrix, $\{E\}$ is the electric field intensity vector, $\{D\}$ is the electric flux density vector, and $[\varepsilon_d]$ is the dielectric permittivity matrix.

Firstly, we performed modal analysis determining eigenfrequencies of the entire system. These results served as input for boundary conditions of piezoelectric harmonic analysis. The actual values of deformation, induced strain and maximal stress were determined in harmonic analysis.

3. Results and discussion

Modal analysis was used to determine the natural frequencies and mode shapes of a structure. The natural frequencies and mode shapes are important parameters in the design of a structure for dynamic load conditions. In order to achieve the good convergence of the ANSYS solver, a numerical damping of 0.005 was used[3].

FEM structural analysis (Figure 3) shows the influence of resonator bending on induced strain (ε) into the stretched part which is linked mechanically to the resonator part. The size of resonator part was 600 µm × 100 µm and the size of stretched part was 100 µm × 75 µm. The harmonic analysis was performed in range from 0 to 200 kHz and four resonant modes (Figure 3) were found. The 3rd and 6th resonance modes from the modal analysis did not show any response due to different bending mode (torsional).

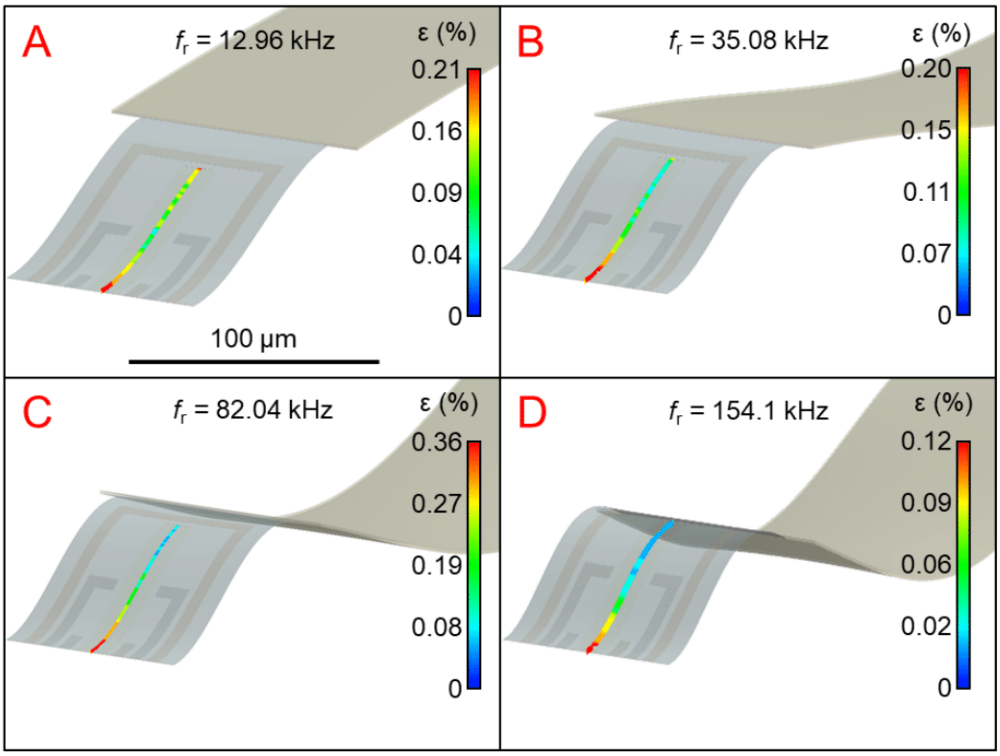

Figure 3. The strain distribution in 2D material placed on the single clamped stretching part. The stretching part is linked mechanically to the single clamped piezoelectric resonator: A) 1st mode at frequency of 12.96 kHz; B) 2nd mode at frequency of 35.08 kHz; C) 4th mode at frequency of 82.04 kHz; D) 5th mode at frequency of 154.1 kHz. The black scale bar is the same for all figures.

We simulated the strain distribution as a function of AC bias voltage up to 20 V applied to electrodes of the piezoelectric resonators. We obtained the maximum value of the induced strain ≈0.36% in dynamic mode for a path placed as the 2D material (Figure 3C). The induced strain was relatively lower than that achieved by other researchers[2, 4]. On the other hand, the induced strain can be modulated by tuning the resonator frequency. The strain value can be further increased by changing the dimensions and shapes of resonators. Longer and narrower part of resonator together with the shorter stretching part increases rapidly the maximum induced strain in 2D material.

The simulated structures were fabricated (Figure 4) and will be tested in the future with new 2D materials.

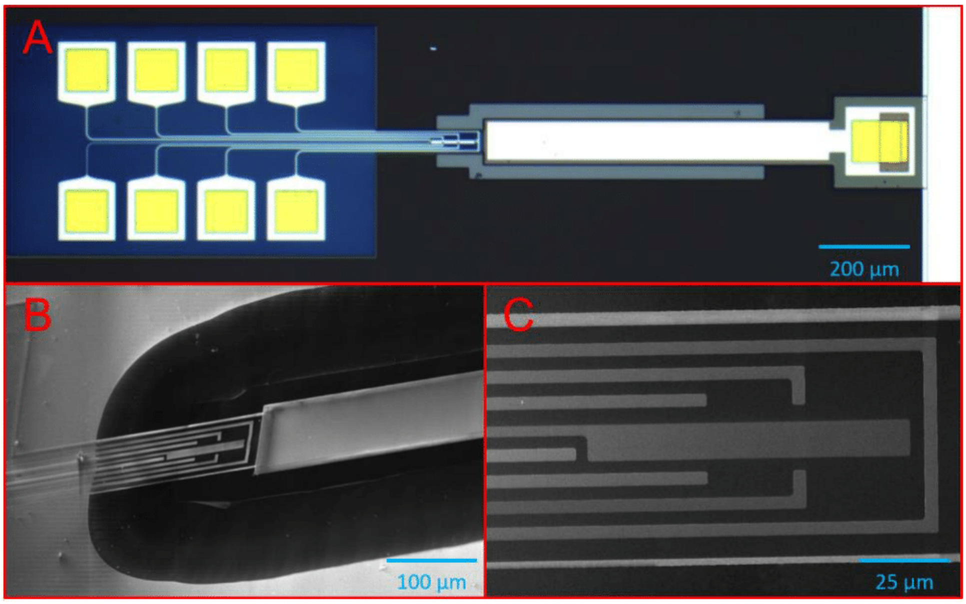

Figure 4. Fabricated structure for 2D material characterization: A) An optical image of entire structure; B) scanning electron microscope analysis of released resonator; C) the detail of stretched part with electrodes.

4. Conclusion

This paper proposed the idea of modulating the properties of 2D material monolayer. We simulated structures for the 2D material characterization. It will be possible to precisely control the induced strain for any 2D material. We obtained value of induced strain of 0.36% for frequency of 82.04 kHz. This can be modified by changing the dimensions of the resonator and the stretched part. The simulated structures were fabricated using the standard planar technology processes and will be used for 2D material characterization.

Acknowledgments: We acknowledge the support of the Grant Agency of the Czech Republic under the contract GJ18-06498Y, the support of the Ministry of Education, Youth and Sports of the Czech Republic under NPU I programme (projects No. LO1210 and LO1401), and the support of BUT no. FEKT/STI-J-17-4136. This research work has been carried out in the Centre for Research and Utilization of Renewable Energy (CVVOZE) and in the SIX Center of BUT.

Conflicts of Interest: The authors declare no conflict of interest. The founding sponsors had no role in the design of the study; in the collection, analyses, or interpretation of data; in the writing of the manuscript, and in the decision to publish the results.

References

1. Gablech, I.; Pekárek, J.; Klempa, J.; Svatoš, V.; Sajedi-Moghaddam, A.; Neužil, P.; Pumera, M., Monoelemental 2D materials-based field effect transistors for sensing and biosensing: Phosphorene, antimonene, arsenene, silicene, and germanene go beyond graphene. *TrAC Trends in Analytical Chemistry* **2018,** *105*, 251-262.
2. Dong, J.; Liu, S.; Fu, Y.; Wang, Q., Investigation of strain-induced modulation on electronic properties of graphene field effect transistor. *Physics Letters A* **2017,** *381* (4), 292-297.
3. Putnik, M.; Cardanobile, S.; Nagel, C.; Degenfeld-Schonburg, P.; Mehner, J., Simulation and modelling of the drive mode nonlinearity in MEMS-gyroscopes. *Procedia Engineer* **2016,** *168*, 950-953.
4. Choi, S.-M.; Jhi, S.-H.; Son, Y.-W., Controlling Energy Gap of Bilayer Graphene by Strain. *Nano Letters* **2010,** *10* (9), 3486-3489.

17.5 Additional analyses

This chapter broaden results of published article. These results represent influence of resonator geometry on maximum value of strain where 2D material is positioned. Higher maximum value of strain allows better modulation of 2D material properties. Influence of other materials that can be possibly used on stretchable part will be subject of “GJ18-06498Y: Modulation of graphene physical properties due to controlled induced mechanical strain” project. Polymer materials enable to reach higher values of strain but it complicates the preparation procedure. Individual fabrication steps will have to exclude O_2 plasma for purification and descum. Nevertheless, it will be possible to prepare such structures even if some parts of fabrication process are changed. Following simulation is pointed on change of length and width of resonator part but other parts of geometry stayed preserved (see **Figure 38**).

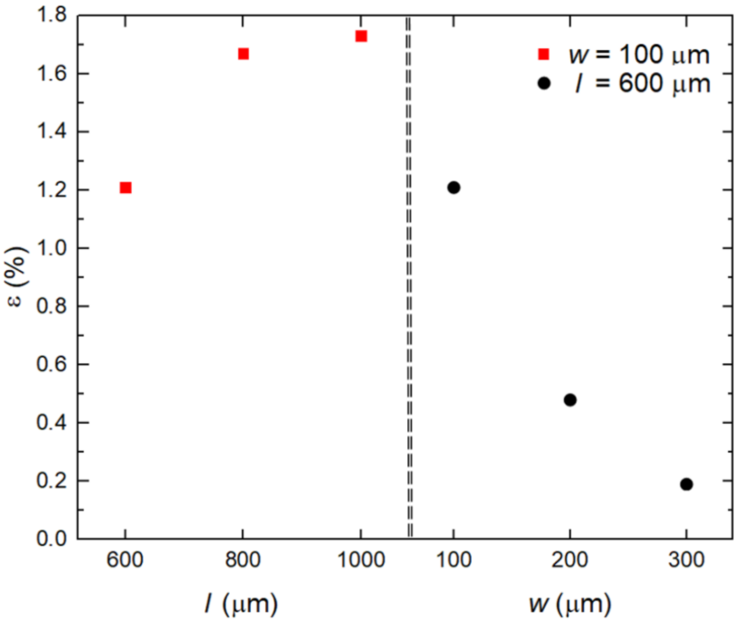

Figure 38: Influence of resonator geometry on maximum value of strain on position where 2D material is deposited and shaped.

Graph of first resonance mode depicted in **Figure 38** shows the longer is the resonator, the highest strain occurs in area were graphene is placed. The opposite results are for the change of resonator width with preserved length. All simulations were realized at sine wave signal with amplitude of 30 V. Experiments proved that with increasing length of resonator, increased strain as well. The highest strain value of ≈ 1.7 % was achieved for resonator with dimensions of 1000 × 100 with preserved materials and their thicknesses.

Variable fabrication technology would allow preparing different structures, for example stretchable part between two cantilevers. If these cantilevers would work with opposite phase, it could lead to increasing strain, too. However, some theoretical models with larger dimensions need to be corrected with practice due to possible presence of low residual stress in layers. Residual stress becomes evident at devices with larger dimensions. Thus, it can cause cracking in the material which can lead to tearing of the stretchable part from one of the cantilevers.

18 Conclusion

This dissertation work proposes the idea of strain inducing into 2D materials using MEMS piezoelectric resonator. Experimental part of research was focused on optimization of thin films deposition processes, FEM simulations, design and fabrication of testing device which was challenging due to 10 lithography steps.

A lot of steps needed to be optimized because this device is sophisticated. Low-stress SiO_2 can be easily prepared with PECVD processes, thus this work is not dedicated to its optimization. On the other side, optimization of other layers was necessary. All PVD depositions were provided using single or dual RFICP Kaufman ion-beam source setup. This method gives a possibility to achieve layers with better quality in comparison to other methods such as e-beam or thermal evaporation or magnetron sputtering. Layers prepared via RFICP Kaufman ion-beam source have usually better crystallography, lower roughness and higher purity which influence their mechanical and electrical properties. Unfortunately, this process is very often accompanied with compressive stress so optimization of this procedure was necessary.

Ti layer was chosen as the bottom electrode of piezoelectric resonator [56] and its deposition process was optimized in the first step [53,54]. This layer plays also a role as a seed layer for subsequent deposition of piezoelectric AlN layer. After all optimization processes, layer with excellent crystallographic and electrical properties was achieved. As prepared layer had (001) preferential orientation, very low misorientation of ≈ 4.4°, stress-free with very low roughness of ≈ 0.58 nm and minimal average crystallite size of ≈ 30 nm. This layer had also excellent electrical properties, namely $\rho = (9.2 \pm 0.1)\cdot 10^{-7}\ \Omega\cdot\mathrm{m}$ and $\alpha = (2.6 \pm 0.2)\ \mathrm{K}^{-1}$ which are very good values for layer with thickness of 80 nm. The resulting layer reached much better parameters in comparison to conventional PVD methods. Additionally, these layers were used for fabrication of microbolometer demanding stress-free thin film and good electrical properties, mostly α [55].

AlN piezoelectric layer was deposited on prepared Ti (001) layer. Properties and quality of AlN layer are highly dependent on underlayer. When AlN was deposited on another types of substrates than Ti (001) thin film, results of experiments confirmed that AlN layer quality and properties are dependent on underlayer. Deposition process of AlN layer was more difficult than deposition of Ti (001) thin film and it demanded utilization of dual RFICP Kaufman ion-beam source. This attitude allowed to reach stress-free layer with high quality crystallography and low roughness. AlN layer had (001) preferential orientation with significant recognition of $K_{\alpha1}$ and $K_{\alpha2}$ diffraction peaks from XRD analysis. Prepared layer with thickness of 1 μm evinced misorientation only ≈ 1.9°. Ellipsometric analysis of direct bandgap was provided with the result of 6.1 eV. The value of d_{33} coefficient is influenced by above mentioned parameters which was confirmed via quasi-static method. Measured value of d_{33} coefficient was $(7.33 \pm 0.08)\ \mathrm{pC\cdot N^{-1}}$.

As prepared materials were used for fabrication of simple piezoelectric cantilever beam and the goal was to match the simulation with real behavior of structure. Parameters of simulation were defined according to general table values, thickness measurements of layers and d_{33} value.

Simulation results were different only of 3% in comparison to measured values of resonance frequencies. These resonant frequencies were measured mechanically using vibration shaker and electrically using impedance analyzer.

A simple experiment to prove the functionality of resonator in practice was provided. Resonator was exhibited to sine wave signal from loudspeaker at resonance and non-resonance frequencies. Movement was measured via oscilloscope because resonator behaved as energy harvester and generated charge. This measurement proved the possibility that these structures can be utilized for fabrication of cantilever arrays which are used for development of cochlear implants.

A final device that joined piezoelectric cantilever beam with stretchable part including Hall Bar/FET structure was produced and simulated. Fabricated structure was practically without stress. SEM images confirmed absence of bending structure without enclosed voltage on electrodes of resonator. Simulations of this structure showed maximum strain value of ≈ 0.36 % which should be sufficient to change electrical properties of graphene or other 2D materials [64,65]. This value can be changed by modifying geometry, mostly proportions of piezoelectric resonator to stretchable part ratio. Simulation showed that the value of strain may reach ≈ 1.7 % if same materials would be used. The highest strain was achieved for resonant frequencies. Thus, it was a necessity to provide the measurement using lock-in amplifier. Method of this measurement was published in the article for measurement of microbolometer [62] via Wheatstone bridge [63].

Simple structures suitable for basic characterization of 2D materials were fabricated simultaneously with fabrication and characterization of FET resonator. Problematic preparation and transfer of graphene led to simple option of drop-coating graphene oxide from suspension with subsequent drying and annealing. Measured dependence of current on voltage correlated with results in literature.

I participated on the fabrication of nanostructured gold microelectrode arrays which are suitable for functionalization of piezoelectric resonators [60]. These arrays have high sensitivity thanks to their active surface in comparison to gold thin film without modification. Another structure appropriate for functionalization of piezoelectric resonators are microfluidic channels with single-step lithography [61]. The main advantage of microfluidic channels is high variability which is possible due to their dimensions from units to hundreds of micrometers and they are also CMOS compatible. These structures can be used for mass sensing of living cells or physical and chemical phenomena inside cells which affect their mass or temperature change.

Benefit of this work lies in innovation of controlled stretching of 2D materials on a chip which allows modulation of their electrical properties. This phenomenon can be exploited for fabrication of highly sensitive sensors with increased selectivity.

Solution proposed within this work opens the opportunity to make versatile devices integrated on a single chip with sensor arrays and sophisticated circuits for smart and wearable applications. The advantage of this structure is its potential applications at room temperature measuring and monitoring toxic, explosive, greenhouse gases, chemical vapors, cells, enzymes, amino acids, DNA, RNA, etc.

Optimization of these structures with subsequent fabrication and characterization will be realized within project “GJ18-06498Y: Modulation of graphene physical properties due to controlled induced mechanical strain”. The first step will be devoted to optimization according to the simulations with consequent fabrication of final structures and deposition of 2D material on stretchable part with Hall Bar/FET. The most important step will be modification of geometry to achieve maximum possible strain. Concept of device design has to take into consideration that functionality of resonator must be preserved. High driving voltage can cause excessive mechanical strain of material which can lead to mechanical damage of structure.

Another possibility how to increase the strain of stretchable part is to use another material such as high elastic polymers compatible with fabrication technology. A good example is parylene which evince high elasticity and is a very good electrical insulator.

References

[1] MALUF, N. a WILLIAMS, K. *Introduction to Microelectromechanical Systems Engineering*. Artech House, 2004. pp. ISBN 9781580535915.

[2] MATTOX, D. M. Chapter 1 - Introduction. In MATTOX, D.M. *Handbook of Physical Vapor Deposition (PVD) Processing (Second Edition).* Boston: William Andrew Publishing, 2010, pp. 1-24.

[3] PIERSON, H. O. 1 - Introduction and General Considerations. In PIERSON, H.O. *Handbook of Chemical Vapor Deposition (CVD) (Second Edition).* Norwich, NY: William Andrew Publishing, 1999, pp. 25-35.

[4] PIERSON, H. O. 2 - Fundamentals of Chemical Vapor Deposition. In PIERSON, H.O. *Handbook of Chemical Vapor Deposition (CVD) (Second Edition).* Norwich, NY: William Andrew Publishing, 1999, pp. 36-67.

[5] NGUYEN, N.-T. Chapter 4 - Fabrication technologies. In NGUYEN, N.-T. *Micromixers (Second Edition).* Oxford: William Andrew Publishing, 2012, pp. 113-161.

[6] GAD-EL-HAK, M. *MEMS: Applications*. CRC Press, 2005. pp. ISBN 9781420036558.

[7] HUSÁK, M. *Mikrosenzory a mikroaktuátory*. Academia, 2008. pp. ISBN 8020014780.

[8] ACAR, C. a SHKEL, A. M. An approach for increasing drive-mode bandwidth of MEMS vibratory gyroscopes. *Journal of microelectromechanical systems,* 2005, vol. 14, no. 3, pp. 520-528. ISSN 1057-7157.

[9] JUDY, J. W. Microelectromechanical systems (MEMS): fabrication, design and applications. *Smart materials and Structures,* 2001, vol. 10, no. 6, pp. 1115. ISSN 0964-1726.

[10] YE, T. a CHRISTIAN, D. Facile Fabrication of Single-Crystal-Diamond Nanostructures with Ultrahigh Aspect Ratio. *Advanced Materials*, 2013, vol. 25, no. 29, pp. 3962-3967.

[11] VASHIST, S. K. A review of microcantilevers for sensing applications. *J. of Nanotechnology*, 2007, vol. 3, pp. 1-18.

[12] LANG, H. et al. Nanomechanics from atomic resolution to molecular recognition based on atomic force microscopy technology. *Nanotechnology*, 2002, vol. 13, no. 5, pp. R29. ISSN 0957-4484.

[13] BRIDLE, H. et al. Static mode microfluidic cantilevers for detection of waterborne pathogens. *Sensors and Actuators A: Physical,* 2016, vol. 247, pp. 144-149. ISSN 0924-4247.

[14] MATSUDAIRA, K. et al. MEMS piezoresistive cantilever for the direct measurement of cardiomyocyte contractile force. *Journal of Micromechanics and Microengineering,* 2017, vol. 27, no. 10, pp. 105005. ISSN 0960-1317.

[15] SANG, S. et al. Surface stress-based biosensors. *Biosensors and Bioelectronics*, 2014, vol. 51, pp. 124-135. ISSN 0956-5663.

[16] NEETHU, K. a SUJA, K. Sensitivity Analysis of Rectangular Microcantilever Structure with Piezoresistive Detection Technique Using Coventorware FEA. *Procedia Computer Science*, 2016, vol. 93, pp. 146-152. ISSN 1877-0509.

[17] BOUCHAALA, A. et al. Mass and position determination in MEMS mass sensors: a theoretical and an experimental investigation. *Journal of Micromechanics and Microengineering*, 2016, vol. 26, no. 10, pp. 105009. ISSN 0960-1317.

[18] ILIC, B. et al. Attogram detection using nanoelectromechanical oscillators. *Journal of Applied Physics*, 2004, vol. 95, no. 7, pp. 3694-3703. ISSN 0021-8979.

[19] PANG, W. et al. Piezoelectric microelectromechanical resonant sensors for chemical and biological detection. *Lab on a Chip*, 2012, vol. 12, no. 1, pp. 29-44. ISSN 1473-0197.

[20] ZHANG, W. et al. Adaptive vibration control of micro-cantilever beam with piezoelectric actuator in MEMS. *The International Journal of Advanced Manufacturing Technology*, 2006, vol. 28, no. 3, pp. 321-327. ISSN 1433-3015.

[21] CLEMENT, M. et al. *Frequency characterization of AlN piezoelectric resonators*. Frequency Control Symposium, 2007 Joint with the 21st European Frequency and Time Forum. IEEE International. IEEE, 1424406463.

[22] CHEN, Y. et al. Chemiresistive and gravimetric dual-mode gas sensor toward target recognition and differentiation. *ACS applied materials & interfaces*, 2016, vol. 8, no. 33, pp. 21742-21749. ISSN 1944-8244.

[23] ZHOU, Q. et al. *The study of adsorption behavior of small molecules on stanene: A search of superior gas sensors*. Electronic Packaging Technology (ICEPT), 2016 17th International Conference on. IEEE, 1509013962.

[24] XU, P. et al. Advanced nanoporous materials for micro-gravimetric sensing to trace-level bio/chemical molecules. *Sensors*, 2014, vol. 14, no. 10, pp. 19023-19056.

[25] GUO, D. et al. Theoretical insight into structure stability, elastic property and carrier mobility of monolayer arsenene under biaxial strains. *Superlattices and Microstructures*, 2016, vol. 100, pp. 324-334. ISSN 0749-6036.

[26] BOUSA, M. et al. Stress and charge transfer in uniaxially strained CVD graphene. *Physica Status Solidi B-Basic Solid State Physics*, 2016, vol. 253, no. 12, pp. 2355-2361. ISSN 0370-1972.

[27] SCHEDIN, F. et al. Detection of individual gas molecules adsorbed on graphene. *Nature Materials*, 2007, vol. 6, no. 9, pp. 652-655. ISSN 1476-1122.

[28] OHNO, Y. et al. Chemical and biological sensing applications based on graphene field-effect transistors. *Biosensors & Bioelectronics*, 2010, vol. 26, no. 4, pp. 1727-1730. ISSN 0956-5663.

[29] ARASH, B. et al. Detection of gas atoms via vibration of graphenes. *Physics Letters A*, 2011, vol. 375, no. 24, pp. 2411-2415. ISSN 0375-9601.

[30] YAO, Y. et al. Graphene oxide thin film coated quartz crystal microbalance for humidity detection. *Applied Surface Science*, 2011, vol. 257, no. 17, pp. 7778-7782. ISSN 0169-4332.

[31] BASU, S. a BHATTACHARYYA, P. Recent developments on graphene and graphene oxide based solid state gas sensors. *Sensors and Actuators B-Chemical*, 2012, vol. 173, pp. 1-21. ISSN 0925-4005.

[32] QIAN, Z. et al. Graphene–aluminum nitride NEMS resonant infrared detector. *Microsystems & Nanoengineering*, 2016, vol. 2, pp. 16026. ISSN 2055-7434.

[33] YI, J. et al. Vertically aligned ZnO nanorods and graphene hybrid architectures for high-sensitive flexible gas sensors. *Sensors and Actuators B-Chemical*, 2011, vol. 155, no. 1, pp. 264-269. ISSN 0925-4005.

[34] WALLACE, P. R. The Band Theory of Graphite. *Physical Review*, 1947, vol. 71, no. 9, pp. 622-634. ISSN 0031-899x.

[35] NOVOSELOV, K. S. et al. Electric field effect in atomically thin carbon films. *Science*, 2004, vol. 306, no. 5696, pp. 666-669. ISSN 0036-8075.

[36] ALLEN, M. J. et al. Honeycomb Carbon: A Review of Graphene. *Chemical Reviews*, 2010, vol. 110, no. 1, pp. 132-145. ISSN 0009-2665.

[37] FIORI, G. et al. Electronics based on two-dimensional materials. *Nat Nano*, 2014, vol. 9, no. 10, pp. 768-779. ISSN 1748-3387.

[38] NOVOSELOV, K. S. et al. A roadmap for graphene. *Nature*, 2012, vol. 490, no. 7419, pp. 192-200. ISSN 0028-0836.

[39] ANG, Y. S. et al. Nonlinear optical response of graphene in terahertz and near-infrared frequency regime. *Frontiers of Optoelectronics*, 2015, vol. 8, no. 1, pp. 3-26. ISSN 2095-2759.

[40] BOOTH, T. J. et al. Macroscopic graphene membranes and their extraordinary stiffness. *Nano Letters*, 2008, vol. 8, no. 8, pp. 2442-2446. ISSN 1530-6984.

[41] ZHANG, Z. H. et al. Tunable electronic and magnetic properties of two-dimensional materials and their one-dimensional derivatives. *Wiley Interdisciplinary Reviews-Computational Molecular Science*, 2016, vol. 6, no. 4, pp. 324-350. ISSN 1759-0876.

[42] ZHANG, X. Y. et al. How the Orientation of Graphene Is Determined during Chemical Vapor Deposition Growth. *Journal of Physical Chemistry Letters*, 2012, vol. 3, no. 19, pp. 2822-2827. ISSN 1948-7185.

[43] BIRO, L. P. et al. Graphene: nanoscale processing and recent applications. *Nanoscale*, 2012, vol. 4, no. 6, pp. 1824-1839. ISSN 2040-3364.

[44] ROLDAN, R. et al. Strain engineering in semiconducting two-dimensional crystals. *Journal of Physics-Condensed Matter*, 2015, vol. 27, no. 31. ISSN 0953-8984.

[45] LEE, C. et al. Measurement of the Elastic Properties and Intrinsic Strength of Monolayer Graphene. *Science*, 2008, vol. 321, no. 5887, pp. 385.

[46] LINDAHL, N. et al. Determination of the Bending Rigidity of Graphene via Electrostatic Actuation of Buckled Membranes. *Nano Letters*, 2012, vol. 12, no. 7, pp. 3526-3531. ISSN 1530-6984.

[47] YOON, D. et al. Negative Thermal Expansion Coefficient of Graphene Measured by Raman Spectroscopy. *Nano Letters*, 2011, vol. 11, no. 8, pp. 3227-3231. ISSN 1530-6984.

[48] DING, F. et al. Stretchable Graphene: A Close Look at Fundamental Parameters through Biaxial Straining. *Nano Letters*, 2010, vol. 10, no. 9, pp. 3453-3458. ISSN 1530-6984.

[49] SI, C. et al. Strain engineering of graphene: a review. *Nanoscale*, 2016, vol. 8, no. 6, pp. 3207-3217. ISSN 2040-3364.

[50] FISCHER, A. C. et al. Integrating MEMS and ICs. *Microsystems & Nanoengineering*, 2015, vol. 1, pp. 15005.

[51] GRAYSON, A. C. R. et al. A BioMEMS review: MEMS technology for physiologically integrated devices. *Proceedings of the Ieee*, 2004, vol. 92, no. 1, pp. 6-21. ISSN 0018-9219.

[52] WISTRELA, E. et al. Impact of the substrate dependent polarity distribution in c-axis oriented AlN thin films on the etching behaviour and the piezoelectric properties. *Microsystem Technologies*, 2016, vol. 22, no. 7, pp. 1691-1700. ISSN 1432-1858.

[53] GABLECH, I. et al. Preparation of (001) preferentially oriented titanium thin films by ion-beam sputtering deposition on thermal silicon dioxide. *Journal of Materials Science*, 2016, vol. 51, no. 7, pp. 3329-3336. ISSN 0022-2461.

[54] GABLECH, I. et al. Stress-free deposition of 001 preferentially oriented titanium thin film by Kaufman ion-beam source. *Thin Solid Films*, 2017, vol. 638, pp. 57-62. ISSN 0040-6090.

[55] GABLECH, I. et al. *Preparation of [001] Oriented Titanium Thin Film for MEMS Applications by Kaufman Ion-beam Source*. Nanocon 2017: 9th International Conference on Nanomaterials - Research & Application. Ostrava: Tanger Ltd.

[56] GABLECH, I. et al. *Influence of Underlayer on Crystallography and Roughness of Aluminum Nitride Thin Film Reactively Sputtered by Ion-Beam Kaufman Source*. Nanocon 2015: 7th International Conference on Nanomaterials - Research & Application. Ostrava: Tanger Ltd, 978-80-87294-63-5.

[57] SANDBERG, R. et al. Temperature and pressure dependence of resonance in multi-layer microcantilevers. *Journal of Micromechanics and Microengineering*, 2005, vol. 15, no. 8, pp. 1454. ISSN 0960-1317.

[58] CLEMENT, M. et al. *Frequency Characterization of AlN Piezoelectric Resonators*. 2007 IEEE International Frequency Control Symposium Joint with the 21st European Frequency and Time Forum. May 29 2007-June 1 2007. 2327-1914.

[59] ŽÁK, J. et al. Model-based design of artificial zero power cochlear implant. *Mechatronics*, 2015, vol. 31, pp. 30-41. ISSN 0957-4158.

[60] PODESVA, P. et al. Nanostructured Gold Microelectrode Array for Ultrasensitive Detection of Heavy Metal Contamination. *Analytical Chemistry*, 2018, vol. 90, no. 2, pp. 1161-1167. ISSN 0003-2700.

[61] GABLECH, I. et al. Fabrication of buried microfluidic channels with observation windows using femtosecond laser photoablation and parylene-C coating. *Microfluidics and Nanofluidics*, 2018, vol. . ISSN 1613-4982.

[62] SVATOS, V. et al. In situ observation of carbon nanotube layer growth on microbolometers with substrates at ambient temperature. *Journal of Applied Physics*, 2018, vol. 123, no. 11, pp. 7. ISSN 0021-8979.

[63] SVATOŠ, V. et al. Precise determination of thermal parameters of a microbolometer. *Infrared Physics & Technology*, 2018, vol. 93, pp. 286-290. ISSN 1350-4495.

[64] GABLECH, I. et al. Monoelemental 2D Materials-based Field Effect Transistors for Sensing and Biosensing: Phosphorene, Antimonene, Arsenene, Silicene, and Germanene go beyond Graphene. *TrAC Trends in Analytical Chemistry*, 2018. ISSN 0165-9936.

[65] GABLECH, I. et al. *A new method for 2D materials properties modulation by controlled induced mechanical strain*. In Proceedings of XXXII International conference Eurosensors 2018. Austria.

Author’s publications

Impacted papers

GABLECH, I.; SOMER, J.; FOHLEROVÁ, Z.; SVATOŠ, V.; PEKÁREK, P.; KURDÍK, S.; FENG, J.; FECKO, P.; PODEŠVA, P.; NEUŽIL, P. Fabrication of buried microfluidic channels with observation windows using femtosecond laser photoablation and parylene-C coating. *Microfluidics and Nanofluidics*, 2018, ISSN 1613-4982

PODEŠVA, P.; GABLECH, I.; NEUŽIL, P. Nanostructured Gold Microelectrode Array for Ultrasensitive Detection of Heavy Metal Contamination. *Analytical Chemistry,* 2018, vol. 90, no. 2, p. 1161-1167. ISSN: 1520-6882.

GABLECH, I.; PEKÁREK, J.; KLEMPA, J.; SVATOŠ, V.; SAJEDI-MOGHADDAM, A.; NEUŽIL, P.; PUMERA, M. Monoelemental 2D Materials-based Field Effect Transistors for Sensing and Biosensing: Phosphorene, Antimonene, Arsenene, Silicene, and Germanene go beyond Graphene. *TRAC-TRENDS IN ANALYTICAL CHEMISTRY,* 2018, vol. 105, no. NA, p. 251-262. ISSN: 0165-9936.

SVATOŠ, V.; GABLECH, I.; PEKÁREK, J.; KLEMPA, J.; NEUŽIL, P. Precise determination of thermal parameters of a microbolometer. *INFRARED PHYSICS & TECHNOLOGY,* 2018, vol. 93, no. NA, p. 286-290. ISSN: 1350-4495.

SVATOŠ, V.; GABLECH, I.; ILIC, B; PEKÁREK, J.; NEUŽIL, P. In situ observation of carbon nanotube layer growth on microbolometers with substrates at ambient temperature. *Journal of Applied Physics,* 2018, vol. 123, no. 11, p. 0-0. ISSN: 1089-7550.

SVATOŠ, V.; SUN, W.; KALOUSEK, R.; GABLECH, I.; PEKÁREK, J.; NEUŽIL, P. Single Measurement Determination of Mechanical, Electrical, and Surface Properties of a Single Carbon Nanotube via Force Microscopy. *Sensors and Actuators,* 2018, vol. 271, no. NA, p. 217-222. ISSN: 0924-4247.

GABLECH, I.; CAHA, O.; SVATOŠ, V.; PEKÁREK, J.; NEUŽIL, P.; ŠIKOLA, T. Stress-free deposition of [001] preferentially oriented titanium thin film by Kaufman ion-beam source. *Thin Solid Films,* 2017, vol. 638, no. NA, p. 57-62. ISSN: 0040-6090.PEKÁREK, J.; PROKOP, R.;

SVATOŠ, V.; GABLECH, I.; HUBÁLEK, J.; NEUŽIL, P. Self-compensating method for bolometer– based IR focal plane arrays. *Sensors and Actuators,* 2017, vol. 265C, no. NA, p. 40-46. ISSN: 0924-4247

GABLECH, I.; SVATOŠ, V.; CAHA, O.; HRABOVSKÝ, M.; PRÁŠEK, J.; HUBÁLEK, J.; ŠIKOLA, T. Preparation of (001) preferentially oriented titanium thin films by ion- beam sputtering deposition on thermal silicon dioxide. *Journal of Materials Science,* 2016, vol. 51, no. 7, p. 3329-3336. ISSN: 0022- 2461.

PŘIKRYLOVÁ, K.; DRBOHLAVOVÁ, J.; SVATOŠ, V.; GABLECH, I.; KALINA, L.; PYTLÍČEK, Z.; HRDÝ, R.; HUBÁLEK, J. Fabrication of highly ordered short free- standing titania nanotubes. *Monatshefte für Chemie,* 2016, vol. 147, no. 5, p. 943-949. ISSN: 1434-4475.

PRÁŠEK, J.; TRNKOVÁ, L.; GABLECH, I.; MAJZLÍKOVÁ, P.; DRBOHLAVOVÁ, J.; CHOMOUCKÁ, J.; ADAM, V.; KIZEK, R.; HUBÁLEK, J. Optimization of Planar Three-Electrode Systems for Redox System Detection. *International Journal of Electrochemical Science,* 2012, vol. 7, no. 3, p. 1785-1801. ISSN: 1452- 3981.

Indexed conference papers

GABLECH, I.; PEKÁREK, J.; KLEMPA, J.; SVATOŠ, V.; VYROUBAP, P.; NEUŽIL, P.; A new method for 2D materials properties modulation by controlled induced mechanical strain. In *Proceedings of XXXII International conference Eurosensors 2018*. Austria

GABLECH, I.; CAHA, O.; SVATOŠ, V.; PRÁŠEK, J.; PEKÁREK, J.; NEUŽIL, P.; ŠIKOLA, T. Preparation of [001] Oriented Titanium Thin Film for MEMS Applications by Kaufman Ion-beam Source. In *Proceedings of 9th International conference Nanocon 2017.* 1. Ostrava: Tanger, 2017.

NEUŽIL, P.; PEKÁREK, J.; SVATOŠ, V.; PROKOP, R.; GABLECH, I.; PAVLÍK, M.; FUJCIK, L.; HUBÁLEK, J. A Self- Compensating System for Fixed Pattern Noise Reduction of Focal Plane Arrays of Infrared Bolometer Detectors. In *Proceedings of XXX Eurosensors 2016. Procedia Engineering.* Hungary: Elsevier, 2016. p. 1007-1011. ISSN: 1877-7058.

GABLECH, I.; SVATOŠ, V.; PRÁŠEK, J.; HUBÁLEK, J. Influence of Underlayer on Crystallography and Roughness of Aluminum Nitride Thin Film Reactively Sputtered by Ion-Beam Kaufman Source. In *Proceedings of 7th International conference Nanocon 2015.* 1. Ostrava: Tanger, 2015.

GABLECH, I.; PRÁŠEK, J.; MAJZLÍKOVÁ, P.; HUBÁLEK, J. Gas Sensor Based on Tin Dioxide– Carbon Nanotubes Nanocomposite Film for Isobutane Detection. In *Proceedings of 6th International conference Nanocon 2014.* Ostrava: Tanger, Ltd., 2014. p. 441-446. ISBN: 978-80-87294-53-6.

Other conference papers

GABLECH, I.; PRÁŠEK, J.; MAJZLÍKOVÁ, P.; HUBÁLEK, J. Semiconductive SnO_2/ MWCNTs Gas Sensor. In *XIV. Pracovní setkání fyzikálních chemiků a elektrochemiků*. Brno: LITERA BRNO, 2014. p. 200-202. ISBN: 978-80-210-6842-1

GABLECH, I.; PYTLÍČEK, Z.; PRÁŠEK, J.; HUBÁLEK, J. Tin dioxide sensor for methane detection. In *XII. Pracovní setkání fyzikálních chemiků a elektrochemiků.* Brno: LITERA BRNO, 2012. p. 54-56. ISBN: 978-80-7375-618-5.

PYTLÍČEK, Z.; GABLECH, I.; PRÁŠEK, J.; HUBÁLEK, J. Zařízení pro automatickou charakterizaci polovodičových senzorů plynů. In *XII. Pracovní setkání fyzikálních chemiků a elektrochemiků.* Brno: LITERA BRNO, 2012. p. 197-199. ISBN: 978-80-7375-618-5.

List of figures

Curriculum Vitae

PERSONAL INFORMATION

Ing. Imrich Gablech

📍 Naměstí SNP 1132/24, 613 00 Brno (Czech Republic)
☎ +420 777 966 824
✉ imrich.gablech@ceitec.vutbr.cz

Sex Male | Date of birth 27/01/1989 | Nationality Czech

WORK EXPERIENCE

01/2012–Present

Smart Nanodevices - technical/office staff

Brno University of Technology - Central European Institute of Technology (CEITEC)
Purkyňova 123, 612 00 Brno (Czech Republic)

Fabrication and characterization of piezoelectric MEMS resonators for sensing applications:

- material depositions: PVD (evaporation, sputtering), CVD (LPCVD, PECVD, ALD, MOCVD)
- material analyses: XRD, XPS, AFM
- FEM analyses (ANSYS Workbench)

01/2012–Present

Department of Microelectronics - technical/office staff

Brno University of Technology - Faculty of Electrical Engineering and Communication
3058/10 Technická, 616 00 Brno (Czech Republic)

Fabrication of microfluidic channels in silicon wafers:

- surface and bulk microfabrication techniques
- CVD deposition of polymer materials

Fabrication and characterization of MEMS bolometers for IR detection:

- CVD deposition of absorption materials
- electric and thermal measurements
- FEM analyses (ANSYS Workbench)

ADDITIONAL INFORMATION

Projects

Grant Agency of Czech Republic (2018–2020) - Modulation of graphene physical properties due to controlled induced mechanical strain

Technology Agency of Czech Republic (2017–2019) - Experimental development of MOCVD apparatus for high temperature growth of A(III)B(V) semiconductors and applied research of metal-nitrides epitaxial thin film growth

Internal Grant Agency (2017) - Modulation of graphene physical properties due to controlled induced mechanical strain

European Union H2020 (2016–2019) - Advancing Smart Optical Imaging and Sensing for Health (ASTONISH)

Grant Agency of Czech Republic (2016–2018) - Microfludics-based Ultra Fast Differential Scanning Fluorimetry for Drug Discovery (μDSF)

Ministry of Interior (2015–2019) - Unique versatile security camera based on nanotechnologies

Grant Agency of Czech Republic (2015–2017) - Formation and properties of TiO2-based nanocolumn arrays via porous-alumina-assisted anodizing of doped titanium layers

Grant Agency of Czech Republic (2013–2015) - New nanostructured system for detection of infrared radiation (NanoIR)

EDUCATION

09/2015–08/2018

Doctoral Study of Advanced Nanotechnologies and Microtechnologies

Brno University of Technology - Central European Institute of Technology (CEITEC), Brno (Czech Republic)

Full-time study

06/2012–06/2014

Master Study of Microelectronics

Brno University of Technology - Faculty of Electrical Engineering and Communication - Brno (Czech Republic)

Full-time study

06/2009–06/2012

Bachelor Study of Microelectronics and Technology

Brno University of Technology - Faculty of Electrical Engineering and Communication - Brno (Czech Republic)

Full-time study

PERSONAL SKILLS

Mother tongue(s) Czech

Foreign language(s)

	UNDERSTANDING		SPEAKING		WRITING
	Listening	Reading	Spoken interaction	Spoken production	
English	B2	B2	B2	B2	B2
German	A2	A2	A2	A2	A2
Spanish	A1	A1	A1	A1	A1

Driving licence B